AN EXPERIMENTAL INVESTIGATION INTO VORTEX BREAKDOWN AND VORTEX BREAKDOWN CONTROL

Submitted by

Sammy Khalil

B.Eng.(Hons) Monash University, Clayton, Australia

Submitted to fulfil the degree of

Doctor of Philosophy

Department of Mechanical Engineering
Faculty of Engineering

Monash University
Clayton, Victoria,
Australia 3800

February 2006

Contents

Nonclemanture

a	Acceleration or constant in equation (3.2).
A	Area.
b	Constant in equation (3.2).
c	Chord length.
C_D	Drag coefficient.
C_s	Suction Coefficient.
C_μ	Blowing Coefficient.
d	Diameter.
D	Nozzle diameter.
d_a	Point response function of the particle diameter.
d_{GI}	Geometrical image diameter.
d_l	Distance from object plane to test section wall.
d_o	Distance from object plane to camera lens.
DOF	Depth of Field.
dt	Time interval.
f	Frequency.
$f^\#$	Ratio of lens diaphragm diameter to focal length.
FFT	Fast Fourier Transform.
g	Gravitational acceleration at the surface of the earth.
Gr_z	Grashof number.
H	Total head.

k	Axial wave number.
L	Test tank width.
LEXs	Leading Edge Extensions.
LDA	Laser Doppler Anemometry.
m	Azimuthal wave number (mode) or mass.
$\dot{m}$	Mass flow rate.
M	Magnification factor.
m_v	Peak Mass Flow Variation (PMFV).
Pr	Prandtl number.
PIV	Particle Image Velocimetry.
PTV	Particle Tracking Velocimetry.
QCA	Quasi-Cylindrical Approximation.
r	Radial distance (based on a Cartesian coordinate system).
R	Nozzle radius.
r_c	Viscous core radius.
Ra_z	Rayleigh number.
R_e	Reynolds number.
Ri	Richardson number.
S	Swirl number defined by equation (1.13).
S_c	Critical swirl number for vortex breakdown to occur.
ΔS_c	Percentage difference between the critical swirl number when a temperature difference is imposed, compared to the critical swirl number when no temperature difference is imposed.
S_{ca}	Critical swirl number for the appearance of vortex breakdown.
S_{cd}	Critical swirl number for the disappearance of vortex breakdown.
$S_{crit\text{-}th}$	Critical theoretical swirl number.
Si	Swirl number defined by equation (1.14).
SPIV	Stereo Particle Image Velocimetry.
St	Strouhal number.
St_n	Natural (un-forced) Strouhal number.
t	Time.

T	Period (Chapter 3) or temperature (Chapter 4).
ΔT	Temperature difference.
T_f	Average film temperature.
T_r	Response time.
u	Convective boundary layer velocity.
U	Velocity.
$\|U\|$	Velocity magnitude.
U_1	Constant in equation (4.10).
U_r	Radial velocity.
U_z	Axial velocity.
U_θ	Azimuthal (out of plane) velocity.
V	Constant in equation (4.8).
x	Cartesian coordinate.
$\vec{x}_p$	Particle displacement.
y	Cartesian coordinate.
z	Axial (Vertical) distance (based on a Cartesian coordinate system).
z_0, z_1	Locations along the vortex axis.
z_a	Axial location of the breakdown stagnation point at $S = S_c$.
z_d	Axial location of the breakdown stagnation point just before its disappearance.
Z_b	Axial location of the un-forced breakdown stagnation point.
Z_{bp}	Axial location of the forced breakdown stagnation point.
ΔZ_{bp}	Fractional difference between the axial location of the forced breakdown stagnation point, compared to that of the un-forced.
α	Thermal diffusivity.
β	Volume expansion coefficient.
γ	Helix angle.
Γ	Circulation.
δ	Boundary layer thickness.

θ	Azimuthal (out of plane) distance (based on a Cartesian coordinate system).
λ	Lens focal length.
Λ	Swirl parameter.
μ	Dynamic viscosity.
ν	Kinematic viscosity.
ω	Angular Velocity.
Ω	Angular velocity (Chapter 1).
ω_I	Instability growth rate.
ω_θ	Azimuthal vorticity.
ρ	Density.
σ	Error.
τ_{rz}	Axial shear stress.
$\tau_{r\theta}$	Azimuthal shear stress.

Subscripts

0, 1	Locations along the vortex axis.
amb	Ambient room properties.
B	Blowing.
c	Central vortex filament.
conv	Convection.
crit	Critical.
F	Fluid.
i	Image.
J	Jet.
jet	Jet.
lam	Laminar.
max	Maximum.
min	Minimum.
p	Particle.

R	Ratio.
s	Suction (Chapter 1) or seeding (Chapter 2).
st	Stagnation point.
T	Theoretical.
turb	Turbulent.
w	Wall.
wing	Wing.
∞	Surrounding working fluid.

Superscripts

$\dot{}$	Derivative with respect to time.
$\bar{}$	Mean.
$\vec{}$	Vector.

List of Figures

Figure 3.13: **Instantaneous SPIV data at R_e = 600, S = 1.36, showing streamtraces of the transitional bubble including. A central cross-sectional cut of the tilted toroidal vortex ring is highlighted by the red lines.**

Figure 3.14: **Instantaneous SPIV data at R_e = 600, S = 1.36, showing streamtraces of the transitional bubble and contours of velocity magnitude for all three velocity components, (a) U_z, (b) U_θ, (c) U_r and (d) magnitude of the 3-D velocity vector $|\mathbf{U}| = \sqrt{U_r^2 + U_z^2 + U_\theta^2}$, equation (3.4).**

Figure 3.15: **Flow visualisation showing streamlines of the transitional bubble including the internal structure at R_e = 600, S = 1.36 at two different times during its upstream movement. More than one tilted internal vortex ring can exist during the breakdowns upstream movement with the location of the vortex ring coinciding with the exterior shear layer shedding axial positions.**

Figure 3.16: **Flow visualisation at R_e = 600 showing the different diameter bubbles which result when changing the swirl from (a) S = 1.35 $\rightarrow$ 1.39 and (b) S = 1.37 $\rightarrow$ 1.39. Note that the rate of change of rotational velocity was the same in each case. (b) shows a 45% larger diameter than that of (a).**

Figure 3.17: **Flow visualisation at R_e = 600, showing the different diameter bubbles which result when changing the rate of change of the rotation rate of the vortex generator from (a) $\dot{U}_\theta = 6.2\text{x}10^{-4}\,\text{rad/s}^2$ and (b) $\dot{U}_\theta = 1.24\text{x}10^{-3}\,\text{rad/s}^2$. For the same increment in swirl S = 1.37 $\rightarrow$ 1.4, (b) shows a 45% larger diameter than that of (a).**

Figure 3.18: **Instantaneous SPIV data at R_e = 600, S = 1.34, showing streamtraces of the steady state cone, clearly visible is the thinning conical sheet.**

Figure 3.19: **Instantaneous SPIV data at R_e = 600, S = 1.34, showing streamtraces of the steady state cone, and contours of velocity magnitude for all three velocity components, (a) U_z, (b) U_θ, (c) U_r and (d) magnitude of the 3-D velocity vector $|\mathbf{U}| = \sqrt{U_r^2 + U_z^2 + U_\theta^2}$, equation (3.4).**

Figure 3.20: **Flow visualisation at R_e = 600, S = 1.34, showing the variance in cone structure with a ±1% (m_υ = 1%) sinusoidal variation in mass flow rate. Each image (1) - (5) corresponds to the mass flow rate as shown in the bottom left graph.**

Figure 3.21: **Instantaneous SPIV data streamline plots at R_e = 900, S = 1.37, showing the asymmetry of high Reynolds number breakdown as can be seen by (a) the breakdown structure resembling a bubble on the right and cone on the left, and vice versa in (b), which shows the structure at a different time after it has precessed through 180°.**

Figure 3.22: **Flow visualisation in the (a) vertical plane and (b) horizontal plane at z/R = -2, of an off-axis dye filament revealing a helix structure during the development of breakdown at R_e = 600, S = 1.32.**

Figure 3.23: **Volume flow visualisation at (a) R_e = 300, S = 0.61 and (b) R_e = 600, S = 1.23 and planar flow visualisation at (c) R_e = 900, S = 0.3 and (d) R_e = 600, S = 1.32, showing the shear layer shedding associated with swirling jets.**

Figure 3.24: **FFT performed on the time varying vorticity data at the point of shear layer shedding. Planar PIV data consisted of 1500 frames, at R_e = 600, S = 0.6.**

Figure 3.25: **Axial shear layer Shedding frequency at z/R = -2, shows that shedding frequency is independent of swirl ($0 \leq S \leq 1.45$) and Reynolds number within two standard deviations as indicated by the vertical error bars.**

Figure 3.26: **Horizontal flow visualisation at R_e = 600, S = 1 and z/R = -4, revealing an azimuthal mode, m = +2, over a half cycle (180°), rotating in a clockwise fashion in the same direction as the swirling jet.**

Figure 3.27: **Horizontal flow visualisation at R_e = 900 revealing: (a) Axisymmetric mode, m = 0, at S = 1.2 and z/R = -2. (b) Mode, m = +2, at S = 1.2 and z/R = -4. (c) Competition between modes, m = +1 and m = +2, at S = 1.35 and z/R = -1.**

Figure 3.28a: **Steady state azimuthal vorticity plots at a fixed Reynolds number of R_e = 900 (representative of, $300 \leq R_e \leq 900$, for $S < S_c$), and various swirl numbers, (a) S = 0, (b) S = 0.25, (c) S = 0.76, (d) S = 0.95, (e) S = 1.08, (f) S = 1.17, (g) S = 1.24. Note: the scale of the colour contour levels are adjusted for each image in order to capture the entire range and not flood the image. Data were obtained via SPIV with an average of 100 images.**

Figure 3.28b: **Azimuthal vorticity plots at R_e = 600, representative of, $300 \leq R_e < 725$, for $S \geq S_c$. The development of breakdown is shown at selected times, (a) 3 min, (b) 5 min and (c) 9 min after the swirl is abruptly increased from S = 1.25 to S = 1.32 in 1 second. Vorticity plot (d) shows the transitional bubble when swirl is increased from S = 1.32 to S = 1.36 in 1 second, before settling to a**

the mass flow rate at St = $4St_n$ and m_v = 15%. Flow is from top to bottom and as the flow is symmetrical only the left portion is shown. The vorticity contour plot is equi-spaced with max = 0.37 s^{-1} and min = -0.37 s^{-1}. Images are at $\dot{m} = \overline{\dot{m}}$.

Figure 5.4: **Instantaneous SPIV data showing a comparison of unforced (left), and forced (right) vortex breakdown at R_e = 300 and S = 1.32 by a vector plot (a), which is accompanied by its associated streamtracers (b), in conjunction with a vorticity plot (equi spaced, max = 0.4 s^{-1} and min = -0.4 s^{-1}) (c). The forced case was conducted at a fixed PMFV value of m_v = 15% and St = St_n, with the instantaneous image taken at $\dot{m} = \overline{\dot{m}}$. The vorticity plot (c) was scaled equally for the unforced and forced cases.**

Figure 5.5: **Instantaneous SPIV data showing a comparison of unforced (left), and forced (right), vortex breakdown at R_e = 600 and S = 1.32 by a vector plot (a), which is accompanied by its associated streamtracers (b), in conjunction with a vorticity plot (equi spaced, max = 0.9 s^{-1} and min = -0.9 s^{-1}) (c). The forced case was conducted at a fixed PMFV of m_v = 15% and St = St_n, with the instantaneous image taken at $\dot{m} = \overline{\dot{m}}$. The vorticity plot (c) was scaled equally for the unforced and forced cases.**

Figure 5.6: **Instantaneous SPIV data showing a comparison of unforced (left), and forced (right) vortex breakdown at R_e = 900 and S = 1.35 by a vector plot (a), which is accompanied by its associated streamtracers (b), in conjunction with a vorticity plot (equi spaced, max = 2.05 s^{-1} and min = -2.05 s^{-1}) (c). The forced case was conducted at a fixed PMFV of m_v = 15% and St = St_n, with the instantaneous image taken at $\dot{m} = \overline{\dot{m}}$. The vorticity plot (c) was scaled equally for the unforced and forced cases.**

Figure 5.7: **Flow visualisation (left) in conjunction with instantaneous PIV data in the form of vector (middle) and streamtracer (right) plots showing a cross-section at z/R = -2 of a swirling jet undergoing cone breakdown at R_e = 600, S = 1.32, during shear layer shedding. The top row of figures are representative of the unforced case, while the bottom row, of the forced case conducted at a PMFV of m_v = 15% and St = St_n, with the instantaneous image at $\dot{m} = \overline{\dot{m}}$.**

Figure 5.8: **Instantaneous PIV data in the form of vector (left), and streamtracer (right) plots showing a cross-section at z/R = -1, of an unforced (top), and forced**

Abstract

The experimental investigation undertaken explores the response of low Reynolds number ($300 \leq R_e \leq 900$) unconfined swirling jets undergoing vortex breakdown. A parametric study describing the most prominent features of breakdown is revealed along with the effects of temperature in-homogeneities resulting in convection. A pneumatic control technique in the form of superimposed sinusoidal axial pulsing was employed in an attempt to alter the structure and examine its effects on vortex breakdown. Particle visualisation in conjunction with 2-D Particle Image Velocimetry (PIV) and Stereo PIV (SPIV) has allowed a detailed examination of the three mainstream topics investigated within this PhD thesis and a comparison to the literature.

The characterisation of a swirling jet at fixed Reynolds numbers with the swirl increased in small incremental steps was investigated in order to examine the dominant features and instabilities which result in each of the four identified regimes. Results show that this particular isolated or screened vortex promotes both axisymmetric centrifugal instability and a Kelvin-Helmholtz instability causing a destabilisation of the azimuthal modes, and eventually vortex breakdown. Vortex breakdown is found to occur at a Swirl number range of $1.31 \leq S \leq 1.35$ with the existence of hysteresis below a Reynolds number range of 650 - 725. The three main Reynolds number dependent breakdown states identified are the transitional bubble, steady state cone and asymmetric breakdown structure. An examination into the shedding frequency of the shear layer has shown a constant axial shedding Strouhal number. An analysis of azimuthal wave number modes has revealed that the dominant modes for symmetric breakdown are m = 0, +2, while asymmetric breakdown consists of modes m = 0, +1, +2, with their appearance dependent

on the axial location. The development of a swirling jet was also examined in terms of azimuthal vorticity plots. This revealed an internal vorticity sign swap within the viscous core of the swirling jet as a prerequisite for breakdown, in agreement with Althaus et al. (1995), Brown and Lopez (1990).

A theoretical and experimental investigation into free convection has allowed insight into the magnitude and effects of both global and local temperature differences in low Reynolds number flows inside relatively large tanks. Results show that even minute temperature differences between the experimental tank wall and inner working fluid can cause free convective flow to be the dominant over forced convection. A study of the effects of local temperature differences (i.e. between the swirling jet and working fluid) has shown that if the swirling jet is of a temperature lower than that of the surrounding fluid, a cone breakdown will be suppressed and a more closed bubble-type breakdown will be encouraged to form with a lower downstream location of the stagnation point. For the case in which ΔT is positive, the formation of the open cone-type breakdown is enhanced, in which the extremities of the conical sheet move upstream, and a wider apex angle exists in the vicinity of the stagnation point along the axis. A theoretical criterion for the critical swirl number required for breakdown to occur when a temperature difference exists was derived and experimentally verified. Results show that a negative temperature gradient, in which negative buoyancy assists the downstream motion of the vortical core and suppresses breakdown, while a positive temperature gradient advances breakdown and enlarges the breakdown bubble or cone.

An experimental investigation into the effects of low level sinusoidal forcing of a swirling jet undergoing breakdown was also conducted. Extremely promising results have emerged especially when the frequency of pulsing is set to that of the natural shear layer shedding frequency of the swirling jet. The breakdown location can be delayed or even completely destroyed with low amplitude perturbations (in the order of 6 - 10% of the mean mass flow rate). The delay in breakdown position is a function of the swirl number, Reynolds number, amplitude and frequency of pulsing. Bursts of increased vorticity concentrations at regular intervals, as a result of axial pulsing, cause a reduction in the jet diameter in the vicinity of the shedding vortex ring. The intensified shedding is also enough to transfer the momentum in the shear layer to the central core of the vortex. As a

result, the axial and azimuthal velocity profiles are effectively modified in such a way as to lower the average swirl number over a period of time and delay the onset of breakdown and/or shift the breakdown structure downstream. An added benefit of this particular means of forcing is the ability to promote axisymmetry within the swirling jet and breakdown structure.

Declaration

This thesis contains no material which has been accepted for the award of any other degree or diploma in any university or other institution and, to the best of my knowledge it contains no material previously published or written by another person, except where due reference is made in the text of the thesis.

Sammy Khalil
February 2006

Acknowledgements

First and foremost, this PhD would not have been possible without God almighty, to whom I am eternally grateful.

I would like to express my gratitude for the support of my supervisors Prof. Kerry Hourigan and A/Prof. Mark Thompson. I would also like to thank all the assistance of the technical staff within the mechanical engineering department for being such a great help and manufacturing the experimental rig.

This research was supported by an Australian Post-Graduate Award, which I am grateful for.

I would like to express my gratitude and show my appreciation for the support and help which my family has given me over the years. In particular I would like to thank my mum, Zeinab Khalil for her continued nagging, my father, Samy Khalil for his continual distractions and Sister, Sherene Khalil for making me laugh at her lack of common sense. Last and not least, I would like to thank my wife, Kate Powell for her love and support during the most critical time of this PhD, thankyou.

Chapter 1

Literature Review

Background

1.1 Introduction

Experimental research into vortex breakdown and vortex breakdown control techniques has been undertaken for the past half century. The understanding of this phenomenon and how to control it is of immense importance in several areas such as heat exchangers, particle and heat separators, combustion control, but none more pronounced than in the aeronautical industry. Swirling flows are also widely present and of critical importance in many natural flows such as cyclones. It is their importance and complexity which has required such extensive research over the past few decades, and will do so for years to come.

Vortex breakdown and vortex breakdown control is an extremely broad topic which has been reviewed by several authors including Delery (1994), Escudier (1988), Green (1995), Lucca-Negro and O'Doherty (2001), Mitchell and Delery (2001), Stuart

(1987), just to name a few. For an in depth review of all aspects of vortex breakdown, both experimentally or numerically determined, the reader is referred to the above mentioned reviews. The most relevant portions of the literature to this PhD thesis are covered herein. A concise summary of breakdown states and their features including the mechanisms behind their evolution will be covered, along with mechanical and pneumatic control techniques which have been implemented in the past.

1.2 Vortex Formation

Vortices can be created during the separation process at a boundary, during which vorticity that was previously confined in the boundary layer near the body surface moves away from the surface and forms vortical structures, often called "vortices". Vortices can have both an axial velocity component and an azimuthal velocity component which provides the swirling motion about its axis. There exist two types of vortices: jet-like vortices, in which the maximum axial velocity occurs along the axis of the vortex; and wake–like vortices, in which the maximum axial velocity occurs at the boundary of the vortex viscous core. Examples of a jet-like vortex are those which occur over delta wings, while wake-like vortices can be seen in the trailing wake of bluff bodies. These two types of vortices are also referred to as leading and trailing edge vortices respectively.

1.3 Instabilities in Swirling Jets which lead to Vortex Breakdown

The following is a summary of the various theoretical, experimental and computational studies of vortex instabilities leading up to breakdown, i.e. $S < S_c$, where, the swirl number S is defined as twice the ratio of maximum azimuthal velocity to maximum axial velocity, and the critical swirl number S_c was found to equal 1.3 - 1.4 by Billant et al.

(1998) in a previous experimental study on vortex breakdown. A description of the dynamics of instability waves in swirling jets is given.

1.3.1 Non-Swirling Jets

Extensive studies on non-swirling jets (see for example O'Neill et al. (2004)) have revealed that ring vortices are the dominant feature in all non-swirling jets at moderate to high Reynolds numbers due to Kelvin-Helmholtz shear instability. Temporal evolution of the jet shows that a secondary instability is responsible for the formation of counter rotating vortex pairs which occur in the intertwining tails of the vortex rings and are responsible for inducing asymmetry in what was previously a symmetrical jet. Lin and Corcos (1984), Neu (1984) have shown that the secondary instability causes the vortices in the braid region to collapse into stream-wise vortices. These structures appear as mushroom type structures in vertical plane visualisations while in the horizontal plane they appear as tangential deformations in the initial stages of their development.

1.3.2 Theoretical Investigations into the Development of Primary Instability when a Swirl Component is added to a Jet

1.3.2.1 Columnar Vortex: Azimuthal Velocity Component Only

According to the works of Rayleigh (1916), the axisymmetric mode (i.e. m = 0, where m is the azimuthal wave number or mode) will be subject to a centrifugal instability if the following necessary and sufficient criterion is found to be true:

$$\frac{d}{dr}(rU_\theta)^2 > 0. \qquad \textbf{(1.1)}$$

Loiseleux and Chomaz (2003) stated that the above criterion means that "a vortex is unstable with respect to axisymmetric perturbations if and only if the circulation decreases as the radial distance increases".

1.3.2.2 Columnar Vortex: Azimuthal and Axial Velocity Components

Howard and Gupta (1962) found a criterion for columnar vortices with axial flow. The following condition is necessary but not sufficient on its own to predict axisymmetric instabilities (m = 0):

$$\frac{d}{dr}(rU_\theta)^2 < \frac{1}{4}r^3\left(\frac{dU_z}{dr}\right). \qquad \textbf{(1.2)}$$

A condition for the stability of columnar vortices to helical disturbances ($m \neq 0$) was established as a sufficient condition for instability by Leibovich and Stewartson (1983):

$$\frac{d}{dr}\left(\frac{U_\theta}{r}\right)\left[\frac{d}{dr}\left(\frac{U_\theta}{r}\right)\frac{d}{dr}(rU_\theta)+\left(\frac{dU_z}{dr}\right)^2\right] < 0. \qquad \textbf{(1.3)}$$

1.3.2.3 Batchelor Vortex: Theoretical Inviscid Linear Stability Analysis

A theoretical approach in which the eigenvalues are determined was adopted by Lessen et al. (1974) to ascertain the inviscid linear stability of a Batchelor vortex. This was implemented theoretically by applying minuscule non-axisymmetric Fourier disturbances of the type $e^{i(kx+m\theta-\omega t)}$ to the flow while continuously increasing the swirl number from 0 to 2 (i.e. the maximum azimuthal velocity is equal to the maximum axial velocity). Results showed that at small swirl numbers with an azimuthal wave number (m) equal to +1, the applied disturbances "die out quickly". However, for negative azimuthal wave numbers (m = -1), the "amplification rate increases and then decreases", and the disturbances only began to die out when the swirl number is increased beyond 3. All the remaining negative helical modes ($m \leq -2$) become unstable to the applied perturbations.

Their results can be summarised as follows for a vortex with a velocity profile similar to that of a Batchelor vortex:

- **No swirl:** All positive and negative modes (including the axisymmetric mode m = 0) are stable with the exception of m = ±1.
- **Increased swirl:** All negative helical modes (m < 0) now become unstable with a magnification in the instability at m = -1, while all positive modes remain stable and the previously unstable m = +1 mode now becoming quickly damped.
- **Instability growth rates ω_I = (m, S):** The growth rates are a function of the mode and swirl number, with maximum growth rates ω_{Imax}(m, S) increasing as the azimuthal wave number modulus |m| increases. Maximum instability growth rates occur at S ≅ 0.85, then decrease for S > 0.85, and drop to negative growth rate values (i.e. damping) for S ≥ 1.5.

1.3.2.4 Batchelor Vortex: Theoretical Viscid Linear Stability Analysis

A follow up study of the viscid linear stability of a Batchelor vortex was conducted by Khorrami (1991), Lessen and Paillet (1974). In a fashion similar to the inviscid study, they found, as expected, viscous modes in which the instability growth rates were a great deal smaller than the inviscid case due to the damping effects of viscosity. The axisymmetric mode (m = 0) did not experience any instability for cases with or without swirl. It is for this reason that Loiseleux and Chomaz (2003) suggests that "the Batchelor vortex is in a sense inadequate: it does not properly reproduce the strong shear in the axial direction observed in jet or swirling jet experiments", as observed by Billant et al. (1998), Panda and McLaughlin (1994).

1.3.2.5 Rankine Vortex: Theoretical Inviscid Linear Stability Analysis

The stability of a Rankine vortex with a superimposed axial plug flow was examined by Loiseleux et al. (1998). In general they found that although there is only one unstable Kelvin–Helmholtz mode for each azimuthal wave number or mode (m), there are an

infinite number of "neutrally stable inertial waveguide modes composed of inertial waves bouncing off the core boundary at r = R". The following results were obtained from their theoretical analysis:

- **No swirl:** The Rankine vortex experiences instability in the axisymmetric mode m = 0 and all helical modes $|m| \neq 0$.
- **Increased swirl:** Unlike the Batchelor vortex analysis above, the Rankine vortex (with and without swirl) is found to experience instability in the axisymmetric Kelvin–Helmholtz mode (m = 0) for all axial wave numbers (k). For helical modes ($|m| \neq 0$) the initiation of swirl breaks the rotational symmetry of the vortex and time dependent instabilities which affect the positive and negative modes differently with respect to their growth rates. The effect of small amounts of swirl at low axial wave numbers (k) causes an interaction between the unstable Kelvin-Helmholtz mode and the inertial waveguide modes, in the form of direct resonance. According to the authors this has the effect of producing "neutrally stable wave number bands separated by bubbles of instability". Low swirl levels at high axial wave numbers destabilize both negative and positive helical modes, while high swirl levels are at all times stabilizing for both helical mode types. A critical limitation to the Rankine vortex model was put forward by Loiseleux and Chomaz (2003) who stated that, "high wave numbers always remain unstable due to the infinitely thin shear layer thickness of the axial velocity profile."
- **Instability Growth rates ω_I = (m, S):** For a Rankine vortex with swirl, the instability growth rate of the axisymmetric mode $\omega_I(0, S)$ decreases as the swirl is increased even though it is unstable for all axial wave numbers. The instabilities present for helical modes $|m| \neq 0$ become time dependent as swirl is increased along with an increase in instability growth rates, with the negative helical modes increasing at a faster rate then the positive modes. However, it should be noted that their growth rates may not necessarily be larger than in the case without swirl. At "high wave numbers negative helical mode growth rates are enhanced for small swirl and decrease continuously for large swirl, while positive helical mode growth rates monotonically decrease

with increasing swirl". The highest growth rates occur at m = 0 and m = -∞ for low axial wave numbers and high axial wave numbers, respectively. While the lowest growth rates occurred for |m| = ∞ and m = 0 for low axial wave numbers and high axial wave numbers, respectively.

1.3.3 Comparison of the Batchelor and Rankine Vortex Theoretical Stability Analysis to that Observed Experimentally

Experimental observations of swirling jets by researchers such as Billant et al. (1998), Panda and McLaughlin (1994) have found that the circulation rapidly decreases as you move further away from the vortex axis. This experimentally observed property of swirling jets shows that the theoretically examined Rankine vortex and Batchelor vortex are not truly representative of the experimental case, due to the fact that they remain centrifugally stable and hence do not experience a rapid decrease in circulation as you move further away from the vortex axis.

1.3.4 Further Theoretical Studies

A study which highlighted the competition and interaction of centrifugal and Kelvin-Helmholtz instabilities was performed by Martin and Melburg (1994). Their investigation looked at the theoretical inviscid stability of swirling jets in the form of a central vortex filament of circulation Γ_c, which is surrounded by a vortex sheet with its circulation equal to $\Gamma_c - \Gamma_\infty$ (where Γ_∞ is the surrounding circulation), which is superimposed with a plug flow axial velocity profile. The two main cases investigated were the centrifugally stable ($\Gamma_c - \Gamma_\infty < 0$) and unstable ($\Gamma_c - \Gamma_\infty > 0$) cases. In the centrifugally stable case the flow becomes destabilized by initially minute Kelvin–Helmholtz waves. The Kelvin-Helmholtz instability was maintained via the supply of vorticity from the azimuthal and axial vorticity components, with negative helical modes being the most unstable.

However for the centrifugally unstable case, the most unstable modes are the positive helical modes.

In general centrifugal instability dominates when the flow contains long axisymmetric waves while Kelvin–Helmholtz instability in the azimuthal direction dominates when the flow contains long helical waves. As the axisymmetric or helical waves decrease in wavelength the instability becomes purely dominated by Kelvin–Helmholtz instability which feeds off the azimuthal vorticity.

1.3.5 Experimental Observations of Vortex Instability Modes

Singh and Uberoi (1976) were among the first to experimentally investigate the instability modes of vortices. Their observations of a laminar flow wing tip vortex revealed the existence of the two primary modes of instability, namely, an axisymmetric mode ($m = 0$) and a helical or bending mode $|m| = 1$.

A more specific study of vortex instabilities was conducted by Panda and McLaughlin (1994) in which they concentrated on the development of Kelvin-Helmholtz instability waves. The Swirling air jet was investigated in the Reynolds number range of $2 \times 10^4 \leq R_e \leq 6 \times 10^4$. A unique acoustic forcing function was setup by arranging speakers around the circumference of the vortex and run at various phase differences. Forcing in this manner was able to reveal the axisymmetric ($m = 0$) and helical ($|m| = 1$) instability modes. From their study they concluded that swirling the flow reduces the amplification rate of the various instability modes.

A recent follow on study by Loiseleux and Chomaz (2003) experimentally investigated the instabilities found in swirling jets leading up to, and at the onset of breakdown in the swirl range of $0 \leq S \leq S_c$. The vortex velocity profiles were the same as an earlier study on vortex breakdown conducted by Billant et al. (1998). There has been found to be three distinct ranges (along with a transitional zone) of swirl number in which different instabilities affecting the vortex core occur:

1. **$0 < S < 0.6$:** At the lower end of this range the jet is predominantly affected by the same axial mode instabilities as a non-swirling jet in that the axisymmetric

vortex rings are generated due to axial shear stresses. The frequency at which these vortex rings are shed is independent of the swirl number and occurs at a fixed Strouhal number. As the swirl is increased the influence of the axial mode instability is reduced while a secondary instability appears in the form of secondary co-rotating vortical structures which are generated at a location where the shed vortex ring merges or interlaces with the emerging vortex ring. The horizontal transfer of momentum caused by these secondary vortical structures creates a tangential wave which propagates downstream in a helical fashion. The speed at which these waves propagate is proportional to the tangential velocity of the vortical core.

2. **S ~ 0.6:** At this transitional region of swirl the axial shear stresses reappear as the dominant feature in the form of axisymmetric vortex rings, while the helical travelling wave is no longer visible.
3. **0.6 < S $\leq$ 1:** This swirl range consists of two dominating instabilities, a tangential and axisymmetric type. Unlike earlier axial instability modes where a single vortex ring was formed at a set Strouhal number, the vortex rings are now shed simultaneously along the extremities of the vortex core. This simultaneous shedding of vortex rings causes multiple helical waves (of azimuthal wave number, m = 2) to be produced and interact with one another. Again the velocity of the propagating waves increases in proportion to the swirl, but at a much higher rate than that for lower swirl values.
4. **1 < S < 1.3:** In this regime there is a greater interaction between the tangential waves and the axisymmetric vortex rings. The most striking feature of this flow regime is the emergence of a bending mode m = 1 propagating with a high negative phase velocity.

Liang and Maxworthy (2005) experimentally examined the instabilities present during the evolution of a "plug" flow exiting from a rotating tube into a large reservoir as the swirl is increased from zero. The centrifugally unstable swirling jet was examined at a Reynolds number of $R_e = 1000$. It was found that for non-swirling jets, Kelvin-Helmholtz instability in the axial shear layer, generated by the axial velocity and leading to vortex ring formation, dominated the flow. The introduction of swirl caused an interaction

between the axial and azimuthal shear layers, creating an instability which they claim is a modified form of Kelvin-Helmholtz instability. This results in the appearance of tilted vortex rings which travel downstream for low swirling jets. For high swirling jets (i.e. just before the onset of breakdown), the vorticity in the azimuthal shear layer, formed by the azimuthal velocity continued to grow until it was of comparable size to the vorticity in the axial shear layer. In this regime the flow is asymmetric due to the presence of strong helical waves of azimuthal wave numbers, m = +2 or +3 replacing the previously dominant vortex rings (m = 0). Once breakdown had occurred, a dominant m = +1 mode appeared which interacted with a secondary less influential m = +2 mode. The coexistence of strong helical waves with m = +1 and +2 appeared. The phase speed and direction of these helical modes was the same as the rotation rate and direction of the tube. Liang and Maxworthy (2005) believe that "the helical wave m = +2 for strongly swirling jets before vortex breakdown and m = +1 after breakdown were self-excited/globally unstable and brought about by a region of local absolute instability within the wake region of the breakdown structure and is identified as a super-critical Hopf bifurcation".

1.3.6 Numerical Investigations into Vortex Stability

Although the study of vortex stability has mainly been theoretical along with a limited number of experimental studies, there have still been numerous numerical studies undertaken. Caflisch et al. (1993) performed a numerical study on vortex instabilities with and without axial flow along with the effects of applying axisymmetric and helical disturbances to the flow. In the zero axial velocity case, equal strength counter rotating vortex pairs have been observed. When axisymmetric forcing is added at high swirl levels, one vortex ring is augmented while the other is reduced in strength and size due to the Kelvin–Helmholtz instability arising from the addition of an axial velocity component. By further applying an azimuthal perturbation to the flow, the Kelvin-Helmholtz instability now feeds off the stream-wise vorticity component and creates concentrated stream-wise vortices of opposite sign, being indicative of a centrifugal

instability. It is interesting to note that in the non-swirling case they found that the stream-wise vortices are of the same sign. It was again found that the determining factor in the vortex development was the amplitude ratio of the azimuthal to axial perturbations. A small amplitude ratio produces counter rotating vortex rings due to the dominating centrifugal instability. At medium ratios, stream-wise vortices appear in the braid regions. At higher ratios, the counter rotating vortex rings are suppressed while the stream-wise vortices grow at a high rate between the co-rotating vortex rings which are induced by the Kelvin-Helmholtz instability. At the highest levels of swirl tested (i.e. just before the onset of breakdown), they observed a disappearance of all vortex rings and only rapidly growing stream-wise vortices remained.

Martin and Meiburg (1996) conducted inviscid three-dimensional numerical simulations in a follow on study with the same vortex properties as their previous theoretical study, Martin and Melburg (1994). As previously mentioned their vortex consisted of a central line vortex of circulation Γ_c which is surrounded by a vortex shear layer with both azimuthal and stream-wise vorticity with circulation equal to Γ_c - Γ_∞ (where Γ_∞ is the surrounding circulation) which is superimposed with a plug flow axial velocity profile. For this study they set the surrounding circulation (Γ_∞) to zero. Their simulations helped to reveal the non-linear interaction and competition between the centrifugal instability and Kelvin–Helmholtz instabilities with the latter feeding on both axial and azimuthal vorticity. The addition of swirl led to the creation of counter-rotating vortex rings. Due to the inviscid model assumption, the associated circulation of these vortex rings grew continuously without limit, however scaling laws were applied to the growth of these rings. As the vortex rings are shed the local jet diameter decreases dramatically. Similar results to that of Caflisch et al. (1993) were obtained. By applying both axisymmetric and azimuthal disturbances to the flow, "the nonlinear evolution of the flow depends strongly on the initial ratio of the azimuthal and axisymmetric perturbation amplitudes". The consequential steady state jet structures consist of counter-rotating or co-rotating vortex rings connected by stream-wise braid vortices, or by wavy stream-wise vortices alone.

Sun et al. (2002) performed a time dependent, Direct Numerical Simulation (DNS) to examine the stability and temporal evolution of a swirling jet. The jet was

characterised by a centrifugally unstable Taylor vortex-like azimuthal velocity which induced a dominant Kelvin-Helmholtz instability at low axial wave numbers a dominant centrifugal instability at high axial wave numbers. It was shown that linear stability theory matched up well with the DNS evolutionary results. For small vortex cores with high axial wave numbers, it was found that the centrifugally unstable azimuthal velocity profile causes the containment of negative axial vorticity within the core and inhibits the formation of secondary vortex ring pairs with opposite vorticity. However, for large vortex cores, the negative axial vorticity is situated far from the central core region.

1.4 General Description of Vortex Breakdown

1.4.1 Vortex Breakdown States

Vortex breakdown is a highly significant phenomenon associated with vortical flows, and was first identified by Werle (1954). Vortex breakdown is a phenomenon that is found in both naturally occurring and man-made flows such as cyclones and delta wing vortices, respectively. Vortical flows display characteristic axial and azimuthal (or swirling) velocity components, they also contain a radial velocity component that is generally negligible until breakdown begins to occur. Vortex breakdown has been observed to occur in many forms. However its common main features include an abrupt deceleration of the flow near the axis as the vortex core abruptly widens into a new stable coherent structure. This leads to the formation of a stagnation point, as if a solid obstacle had been introduced into the flow (Billant et al. (1998)). A region of reversed axial velocity along the core is created and which contains a viscous recirculation region with the downstream wake region being characterised by large scale velocity fluctuations and turbulence as seen in Figure 1.1. Vortex breakdown has been observed to occur when a simple measure, being the ratio of azimuthal to axial velocity (otherwise known as the swirl ratio or swirl number) exceeds a certain threshold value. However, according to Mitchell and Delery (2001), it is “a mechanism still not fully understood”.

Experimental investigations of vortex breakdown in free swirling jets have mainly been conducted at high Reynolds numbers with the central focus being on velocity distributions and their associated turbulence fluctuations (see, for instance, Farokhi et al. (1988), Panda and McLaughlin (1994)). Experiments on vortex breakdown have been carried out over delta wings by Lambourne and Bryer (1961a), Peckham and Atkinson (1957), Klute et al. (2005), Deng and Gursul (1996), Gursul and Xie (2001), Guy et al. (1999), Guy et al. (2000a), Hebbar et al. (1994), Maines et al. (1999), Mitchell et al. (2000), Nawrocki (1995), Owens and Perkins (1995), Pelletier and Nelson (2000), Rao et al. (1995), Shih and Ding (1996), Vorobieff and Rockwell (1996), Wang et al. (2003), Wood and Roberts (1988), in confined tubes by Bruecker (1993), Bruecker and Althaus (1992), Bruecker and Althaus (1995), Escudier et al. (1982), Escudier and Zehnder (1982), Faler and Leibovich (1977a), Faler and Leibovich (1977b), Faler and Leibovich (1978), Garg and Leibovich (1979), Harvey (1962), Panda and McLaughlin (1994), Sarpkaya (1971a), Sarpkaya (1971b), Sarpkaya (1974), Sarpkaya (1995), Ozgoren et al. (2002), Rockwell et al. (2002), Akilli and Sahin (2001), Mitchell et al. (2000), Pelletier and Nelson (2000), Wang et al. (2003), Adams et al. (1999), Althaus et al. (1995), Brown and Lopez (1990), Bruecker (1993), Bruecker (2002), Bruecker and Althaus (1992), Bruecker and Althaus (1995), Goldshtik and Hussain (1998), Jones et al. (1998), Jones et al. (1999), Khorrami (1995), Sotiropoulos and Ventikos (2001), in a cylindrical container with a rotating end wall by Bhattacharyya and Pal (1998), Escudier (1984), Spohn et al. (1998), Thompson and Hourigan (2003), Husain et al. (2003), Liu et al. (2003), in a tornado generator by Shtern and Hussain (1993), Khoo et al. (1997) and in a relatively unconfined free swirling jet by Billant et al. (1998), Farokhi et al. (1988), Panda and McLaughlin (1994), Serre and Bontoux (2002), Loiseleux and Chomaz (2003), to name a few.

The two principal breakdown configurations, namely the bubble and the spiral, were first identified in the tip vortices generated by flow over delta wings by Lambourne and Bryer (1961a). Flow visualisation with the introduction of dye on the vortex axis was the main method of distinguishing between breakdown states. In the case of the bubble type breakdown, it was found that the filament of dye spreads symmetrically, outlining the stagnant point, while as the name suggests for spiral type breakdown, the dye filament

is deformed into a spiral structure surrounding a stagnation point. It is consequently assumed that in the case of spiral breakdown, an oscillatory disturbance is what forces the particles to take different paths as they proceed past the stagnant zone.

Figure 1.1: Vortex breakdown over a slender delta wing (sourced from Mitchell and Delery (2001)).

Even though many interesting findings regarding vortex breakdown can be made through the flow over delta wings, the complete properties of the vortical structures cannot be determined as the swirl and axial velocities are fixed for any particular geometry and angle of attack. Therefore a major disadvantage of delta wing experiments is that the axial and azimuthal velocities cannot be varied independently. As a result, many subsequent experiments on vortex breakdown were conducted with a separate control mechanism for both the axial and azimuthal velocities. Experiments on vortex breakdown over delta wings soon adopted an adjustable downstream outflow nozzle in order to vary the pressure gradient and hence vary the axial velocity accordingly (see for example Delery (1994)). Sarpkaya (1971b) used another method of controlling both velocity components, which consisted of a straight or slightly diverging confined tube with swirl imparted by 32 upstream guide vanes. Using this experimental setup, a controversial third type of breakdown state was observed, named the double helix. However as pointed out by Leibovich (1978), this breakdown state does not contain a stagnation point and therefore does not rigorously fulfil the criteria to qualify as a

breakdown state. Nevertheless visualisations via dye injection into the working fluid (water) enabled Sarpkaya (1971b) to classify the various types of breakdown that occurred as the azimuthal velocity was varied, i.e. for differing swirl ratios. The classifications include:

- **Low swirl velocity:** A double Helix type breakdown (see Figure 1.2) is observed in which the filament of dye defining the vortex core becomes sheared in the form of a helix which performs several rotations before breaking into turbulence.
- **Higher swirl velocities:** Observations similar to that observed by Werle in 1954 of flow over delta wings were seen. It was found that a spiral type breakdown appears and is characterised by a stagnation point appearing at the breakdown location causing the dye filament to immediately deviate from its path and begin to spiral about the structures axis.
- **Even higher swirl velocities:** A bubble type breakdown appears, characterised by its closed axisymmetric bubble (see Figure 1.3) formation, seen as the dye filament symmetrically spreads around the stagnation point.

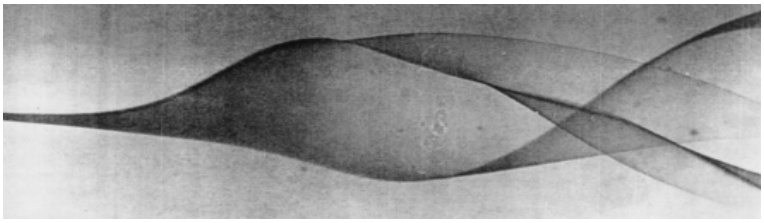

Figure 1.2: Double helix breakdown (sourced from Sarpkaya (1971a)).

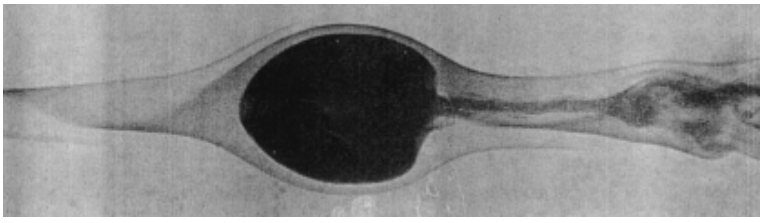

Figure 1.3: Axisymmetric bubble (sourced from Sarpkaya (1971b)).

The first reliable quantitative measurements using Laser Doppler Velocimetry (LDV) were conducted by Faler and Leibovich (1977a), Faler and Leibovich (1978),

Mitchell and Delery (2001) in which a similar experimental set-up was used to identify breakdown states. Using water as the working fluid, the experiments were conducted with a diverging vortex tube with 32 vanes which imparted the swirl motion. This set-up produced a recirculating bubble structure consisting of four recirculating cells. A centre axis cross section of such a structure indicates that the streamlines show four saddle points and centres.

Faler and Leibovich (1977a) have managed to compile a more complete classification of the types of breakdown states in comparison to Sarpkaya (1971b). Six classes of breakdown have been identified via the visualisation of dye injection upstream of breakdown. The breakdown states are various configurations of bubbles or spirals, with two new distinct breakdown states found, namely a bubble which is flattened in a steady preferred plane (type 4) and a state sharing the characteristics of both the spiral breakdown and the flattened bubble (type 3). The complete vortex breakdown type classification according to Faler and Leibovich (1977a) is:

- **Type 0:** Typically known as the recirculating bubble with a quasi-steady axial location, which begins with an upstream stagnation point on the vortical axis. This causes the flow to deviate in such a way that dye filament visualisations show an almost fully axisymmetric bubble which envelops a low frequency recirculating fluid interior, followed by a reformation of the vortical structure before a spiralling tail which ends in turbulence further downstream.
- **Type 1:** This breakdown type resembles type 0, however with some distinct differing features, such as a slightly asymmetric upstream bubble tip. The bubble appears more ragged and no longer possesses a noticeable emptying bottom extremity along with an ambiguous vortex reformation directly after the bubble structure. In this case the bubble structure is directly followed by large scale turbulence without the distinct spiral tail observed in type 0.
- **Type 2:** Typically known as the spiral type breakdown, the appearance of a stagnation point causes the dye filament to kink and form a coiled structure which proceeds downstream for a number of cycles before its break up into large scale turbulence (see Figure 1.4).

- **Type 3:** This structure contains a combination of attributes from both a flattened bubble and spiral structure, which quickly becomes disorganised. It initially starts as a spiral type breakdown.
- **Type 4:** Typically known as the flattened bubble with it beginning at a stagnation point causing the off-axis deflection and shear of the dye filament. The lower edge rolls up and forms an array of small, compact spirals which dissipate into small scale turbulence. Its open ended downstream extremity structure encases a recirculating region which exhausts fluid at its base.
- **Type 5:** Typically known as the double helix, it does not develop an upstream stagnation point, only a deceleration of flow causing the filament of dye to depart from the structure centre-line by staying in the meridian plane and expanding into a sheet which wraps around the central axis.

There is however doubt as to whether all the breakdown types identified by Faler and Leibovich (1977a), Sarpkaya (1971a) actually exist. The bubble and spiral breakdown structures have for years been a point of controversy as to whether or not they are the same or a different phenomenon; this topic is discussed further in section 1.4.2.

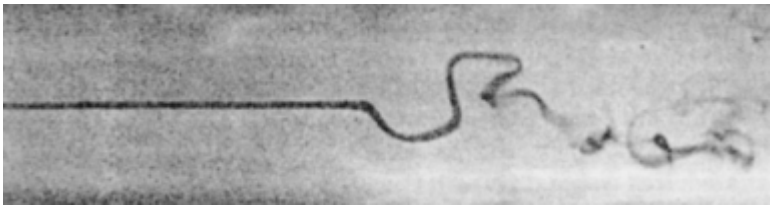

Figure 1.4: Spiral breakdown (sourced from Leibovich (1978)).

Billant et al. (1998) have also conducted investigations into vortex breakdown; however unlike most previous investigations, their experimental technique has used an improved method of independently controlling the axial and azimuthal velocity components of the vortical structure. This was achieved by imparting swirl to the flow via a motor that sets a honeycomb into rotational motion within a settling chamber and controlling the axial flow by using constant head tanks. They adopt a swirling jet experimental set-up where confinement effects are negligible since the jet exhausts into a comparatively large water tank. Their experimental setup also had the ability of

visualising perpendicular cross-sections of the jet axis, hence allowing the authors to clearly determine whether the swirling jet and its associated breakdown state are axisymmetric or not. Such a set-up has allowed the identification of a new breakdown configuration in the form of a conical sheet or cone breakdown structure (see Figure 1.5), which according to the authors is clearly distinct from the previously documented open bubble state. A quantitative investigation into the presence and exact properties of hysteresis was also examined by systematically varying the swirl parameter near threshold, significantly increasing the knowledge in this area when compared with earlier quantitative and qualitative work. It was possible for the authors to ascertain that the cone experiences secondary temporal dynamics and that recirculating motions are present within the stagnant region.

Khoo et al. (1997), Sarpkaya (1995) have also reported observing a conical vortex breakdown structure, however Billant et al. (1994), Billant et al. (1998) believe that "the flow structure discovered during their experiments is qualitatively different from these authors' observations". It is the latter authors' view that "the conical state reported by Sarpkaya (1995), which occurs for very high Reynolds numbers of order 10^6, is in fact a bubble whose turbulent conical wake has come so close to the stagnation point that the whole structure looks like a cone". This can be verified by the observation of a transformation of the common bubble structure at a Reynolds number of 5×10^4 to a turbulent conical bubble at a Reynolds number of 20×10^4. Billant et al. (1998) also provide similar remarks about the conical breakdown structure observed at higher Reynolds numbers ($3200 \leq R_e \leq 3600$) than the bubble or spiral as reported by Khoo et al. (1997). The authors went on to say that this conical breakdown state is simply the wake of the bubble state as it evolves to its turbulent state as the Reynolds number is increased. Furthermore, Sarpkaya (1995) reported the cone opening angle of 20 ° and Khoo et al. (1997) reported an angle of 40 ° while Billant et al. (1994), Billant et al. (1998) found a cone which, unlike those observed by previous authors, is laminar and observed for the same Reynolds number and swirl ratio as the bubble, it is also characterised by an opening angle of 90°. Theoretical investigations into vortex breakdown by Long (1961), Shtern and Hussain (1993) have concluded that conical flows (similar to that seen by Billant et al. (1998)) with a velocity field that is inversely

proportional to the distance from the origin are common and a distinct form of breakdown. By solving the Navier-Stokes equations Goldshtik (1979) showed that theoretically both the cone and bubble can exist at the same Reynolds number and swirl ratio, within a certain parametric range.

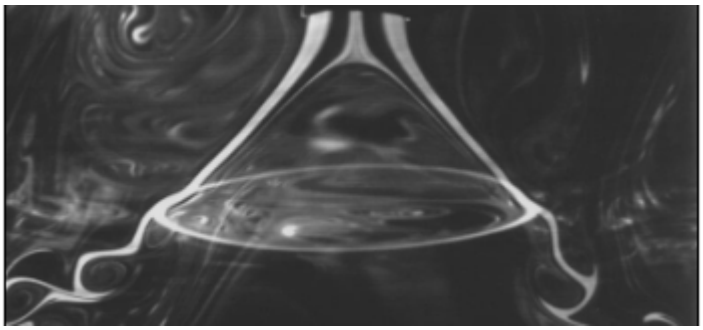

Figure 1.5: Axisymmetric Cone breakdown at R_e = 606 and S = 1.37 (sourced from Billant et al. (1998)).

1.4.2 Discrepancies among Various Studies Regarding the Existence of the Bubble and Spiral Breakdown States

1.4.2.1 Bubble Breakdown as the Basic Form

It is thought by some researchers that the different vortex breakdown features observed are simply different aspects of the same phenomenon. For example some investigators believe that the two breakdown types are the one phenomenon, with the bubble type breakdown being the basic form, and the spiral type being a consequence of the instability of the bubble form. Escudier (1988) verifies this by his findings of asymmetric disturbances in most experiments on this phenomenon. Lambourne (1965) found that the bubble breakdown structure is initially axisymmetric but due to asymmetric instabilities changes to a spiral. Escudier and Keller (1983), Escudier and Keller (1985) believed that the two breakdown forms were in fact two different aspects of the same axisymmetric phenomenon, and axisymmetry is lost due to azimuthal instabilities. These instabilities according to the authors were not generated from the breakdown process and caused the

shear layer surrounding the bubble breakdown to disengage and roll up, resulting in a precession of the stagnation point and surrounding fluid about the axis, hence the spiral appearance. Experimental results of breakdown structures by Escudier and Zehnder (1982) support this theory as their data correlate regardless of the breakdown type. Escudier and Keller (1983) supported their theory by the argument that if the spiral is in fact asymmetric in nature then it would not rotate with the vortex, instead remaining stationary, as was shown to be the case by Keller and Escudier (1980) in asymmetric standing waves in hollow core vortices.

Ruith et al. (2003) conducted direct numerical simulations of incompressible vortex breakdown in a semi-confined domain, with both jet-like and wake-like axial velocity profiles. They found that the axisymmetric bubble is the basic form of breakdown and that a transition to a helix is the result of "a sufficiently large pocket of absolute instability in the wake of the bubble, giving rise to a self-excited global mode".

1.4.2.2 Spiral Breakdown as the Basic Form

Although agreeing with the above mentioned researchers that the spiral and bubble breakdown types are the one phenomenon, some researchers believe that the spiral breakdown is the fundamental mode of vortex breakdown, from which the secondary bubble state develops. An investigation into leading edge vortices by Jones (1964), Lowson (1964) showed that breakdown is always initially a spiralling axial filament which progresses and develops into an axisymmetric bubble. Sarpkaya (1971a) observed similar results in a diverging tube with his results suggesting that the spiral was the result of instabilities which occur in flows with moderate swirl levels. This observation was further dealt with by Hall (1972) who put forward that at high swirl levels, such instabilities are possibly non-existent, resulting in an axisymmetric bubble breakdown structure. Lessen and Paillet (1974) confirmed this by showing that asymmetric disturbances are only initially destabilised by the swirl component. In a review by Hall (1972), based on Sarpkaya (1971a) results, the progressive pattern of vortex breakdown as swirl is increased was sketched (see Figure 1.6a), with an initial asymmetric spiral structure then finally progressing to an axisymmetric bubble structure at high swirl. As

the adverse pressure gradient is increased (by increasing the vane angle), the dye filament distorts and reverses back upstream towards the kink, eventually giving rise to an open bubble structure.

Payne et al. (1988)'s study of vortex breakdown over delta wings produced similar explanations of the phenomenon. The vortical core was observed to form a bubble breakdown structure by expanding around the oval shaped recirculating region (see Figure 1.6c). The downstream portion of the bubble sheds vortex rings at its exit, which travel downstream with the oncoming bulk flow. According to the authors, these vortex rings were in fact a result of a tightly wound spiral which commences from the downstream portion of the bubble (see Figure 1.6c). The observed structure sometimes gradually changed from a bubble to a spiral mode of breakdown (see Figure 1.6b) and vice versa, hence confirming their interpretation that the vortex rings were a result of the spiral. As expected, there was an associated change in the mean axial position of each type of breakdown, with the spiral's location being further downstream than that of the bubble.

Laser Doppler Anemometry (LDA) by Faler and Leibovich (1977b), Uchida et al. (1985) and Particle Tracking Velocimetry (PTV) by Bruecker (1993), Bruecker and Althaus (1992), Bruecker and Althaus (1995) have provided quantitative velocity measurements and a detailed picture of the internal structure of the bubble. The topology of spiral type breakdown observed by Bruecker (1993) indicates a profound similarity with the bubble except that the stagnation point is not located on the vortex axis but travels around it. Bruecker (1993) went on to say that, "the slope, winding and diameter of the spiral vortex core determine the different observable forms". Bruecker found that the asymmetric reversed flow region's strength and position depended on the angle at which the vortical core was deflected about the upstream point at which breakdown occurs, hence causing the stagnation point to move off-axis as seen in Figure 1.7. He believed that bubble breakdown was simply a compressed spiral which appears as the swirl level is increased, bringing about a more axisymmetric reversed flow region and a more stable and centred stagnation point. The dye filaments would spread around the outer shear layer and inner recirculating region of the bubble, unlike the spiral form in which the dye filaments are deflected as a whole. The bubble's compression of the

spiralling vortex core causes the azimuthal vorticity to converge into a vortex ring like structure, unlike the separated vortices seen in a spiral type breakdown. The concentrated vorticity within the vortex ring causes an increase in the reversed flow and hence causes the movement of the structure further upstream until a point is reached were the flow forces reach the new equilibrium state. Further experiments by Brucker (2002) into vortex breakdown in confined tubes produced similar conclusions, that the bubble and spiral breakdown "patterns do not represent different fundamental modes of breakdown". He came to this conclusion as it was possible to force a bubble type breakdown to a spiral by inducing a small asymmetric disturbance. This was also confirmed in an experimental investigation by Kurosaka et al. (2003) which is discussed in more detail later in this chapter in section 1.7.9.

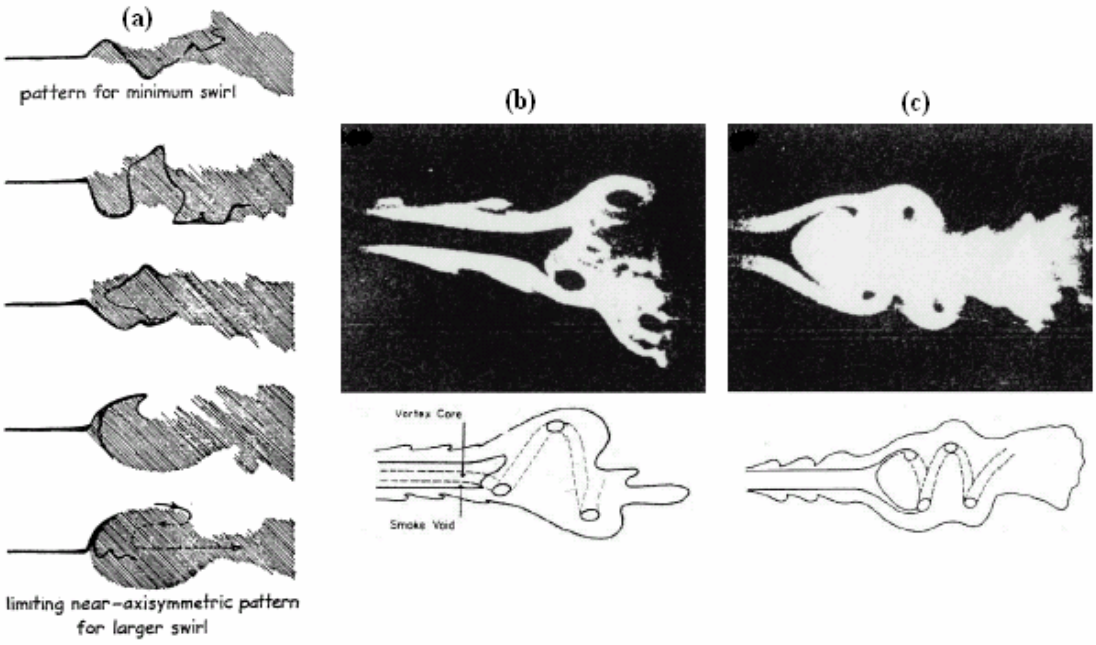

Figure 1.6: **(a) A sketch by Hall (1972) based on Sarpkaya (1971b)'s results of the evolution of vortex breakdown as the swirl is increased. Flow visualisation over a delta wing by Payne et al. (1988) of (b) spiral breakdown and (c) bubble breakdown with an accompanied sketch below each picture.**

High Reynolds number (in the order of 3 x 10^5) vortex breakdown over delta wings was investigated using LDA by Novak and Sarpkaya (2000). They found that of all

the observed breakdown forms, “the spiral emerges as the most fundamental breakdown form”. The progression from the spiral to other forms of breakdown such as the bubble and double helix was highly dependent on Reynolds number and local turbulence properties.

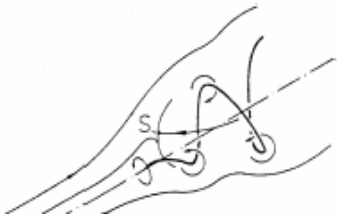

Figure 1.7: A sketch by Bruecker (1993) of the off-axis stagnation point present in a spiral breakdown.

1.4.2.3 Axial Position as a Determining Factor

The differing opinions as to whether the spiral and bubble breakdown structures are the same or different phenomena are sometimes based on the axial positions of each breakdown state. The axial position of the bubble with respect to the spiral breakdown is still an aspect of breakdown which has received differing observations. Leibovich (1983) suggested that the two types of breakdown structure were different to one another due to the larger core expansion associated with the bubble breakdown and the different axial location of each breakdown type. Billant et al. (1998) have observed that the asymmetric bubble is located in the same range of axial positions as the symmetric bubble. These authors have also found that the symmetric bubble turns into an asymmetric bubble as the Reynolds number is increased, which is also confirmed by the experiments of Althaus et al. (1995), Bruecker and Althaus (1995). However in sharp contrast, experiments in confined tubes by Faler and Leibovich (1977a), Garg and Leibovich (1979), Sarpkaya (1971a) have reported that the spiral breakdown state appears at locations downstream of the symmetric bubble and that, as the Reynolds number is increased, the spiral develops into a bubble. It is the geometrical differences that stand out by far as the most likely factor causing these discrepancies; the work of Jones et al. (2001) suggests that the symmetric bubble will appear at sufficiently low Reynolds numbers in a cylindrical

container with a rotating lid as opposed to its appearance at high Reynolds numbers as found in diverging tubes and delta wing experiments.

1.4.2.4 Effects of Different Visualisation Techniques

Another opinion arises concerning the spiral and bubble breakdown structures. Billant et al. (1998) believe they are the one fundamental breakdown mode, with the discrepancy in observation occurring due to the visualisation technique used. Billant et al. (1998) believes the spiral breakdown identified by Bruecker (1993) is simply an asymmetric bubble with an off-axis stagnation point that rotates around the vortex axis. They believe the spiral was previously thought of as a separate type of breakdown due to the visualisation technique used. For example, when a single dye filament is injected on the vortex axis of an asymmetric bubble, its path deviates due to the rotating off-axis stagnation point which results in the visualisation of the spiral structure. Delery (1994) has a similar opinion to Billant et al. (1998) and states that, "It is legitimate to think that the introduction of a swirl component will not significantly change the essence of the phenomenon…… The front stagnation point is a focus for the streamlines constituting the stream surface bounding the bubble. A streamline close to the axis, which has a helicoidal shape, will be distorted when arriving in the vicinity of the stagnation point to adopt a spiral shape. Thus the observations of the bubble or spiral would be due to the behaviour of the dye introduced to visualise the breakdown…… Also there are strong theoretical arguments in favour of the existence of several types of breakdown. However, the existence of a stagnation point on the structure centre-line is universally accepted as the characteristic feature of the breakdown, this stagnation point is not incompatible with a spiralling motion."

A numerical study by Hourigan et al. (1995) considered the errors associated with off-axis dye injection for the particular case of steady swirling flows within closed cylinders. Their results showed that visualisations of the swirling flow structure were highly dependent on the radial offset of the dye injection from the centreline. In summary their results revealed that even minor radial offsets (in the order of less than 1% of the cylinder radius) of the dye injection location was enough to produce a predictable spiral

pattern. In agreement with Delery (1994) and Billant et al. (1998), Hourigan et al. (1995) conclude that even axisymmetric breakdown can display deceptive asymmetrical visualisations (in the form of a spiral) if dye injection is not precisely released along the centreline of the swirling structure.

1.4.2.5 Resolving Discrepancies

Unfortunately it is difficult to come to a conclusion regarding the progression of forms of the breakdown states due to the conflicting observations made by researchers. For example, Bruecker and Althaus (1995), Escudier and Zehnder (1982), Lambourne (1965) report that the fundamental breakdown type is the bubble and a spiral breakdown subsequently develops due to instabilities caused by helical disturbances. It was also noted that the rotation of the spiral is opposite to the primary vortex as it proceeds downstream. Conversely, Faler and Leibovich (1977a), Sarpkaya (1971a), Novak and Sarpkaya (2000) have observed that the spiral type is the fundamental breakdown state from which the secondary bubble state develops. Another contrasting observation by these authors was that they observed a co-rotation of the spiral and primary vortex. It seems that this question of breakdown forms is still a mystery and far from being a topic of unanimous agreement.

1.4.3 The Existence of Hysteresis

Billant et al. (1998) investigated the existence of a hysteresis loop for a cone type breakdown which they claim to have identified. They did this by examining the stagnation point axial location (z/D) as the swirl number (S) was increased and then decreased. They found that as the swirl is increased, breakdown will appear when the critical swirl number ($S_c = S_a$) is reached and the final breakdown location is set $z = z_a$. Above the critical swirl number ($S_c = S_a$), an increase in swirl will cause the stagnation point to move upstream and a decrease in swirl will cause it to move back down stream along the same spatial parameter path (S, z). If the swirl is reduced further, below the critical swirl value, breakdown is still observed with the stagnation point located further

downstream, below z_a. This pattern continues until the swirl number reaches a critical value ($S_c = S_d$) at which the stagnation point and vortex breakdown disappears at a certain axial location z_d and reverts back to its original swirling jet state. Figure 1.8 gives some idea as to the extent of hysteresis inherent in this phenomenon. Similar results were also obtained for the bubble. By solving the Navier-Stokes equations Goldshtik (1979) derived a genus of non-unique conical solutions, which exhibit hysteresis.

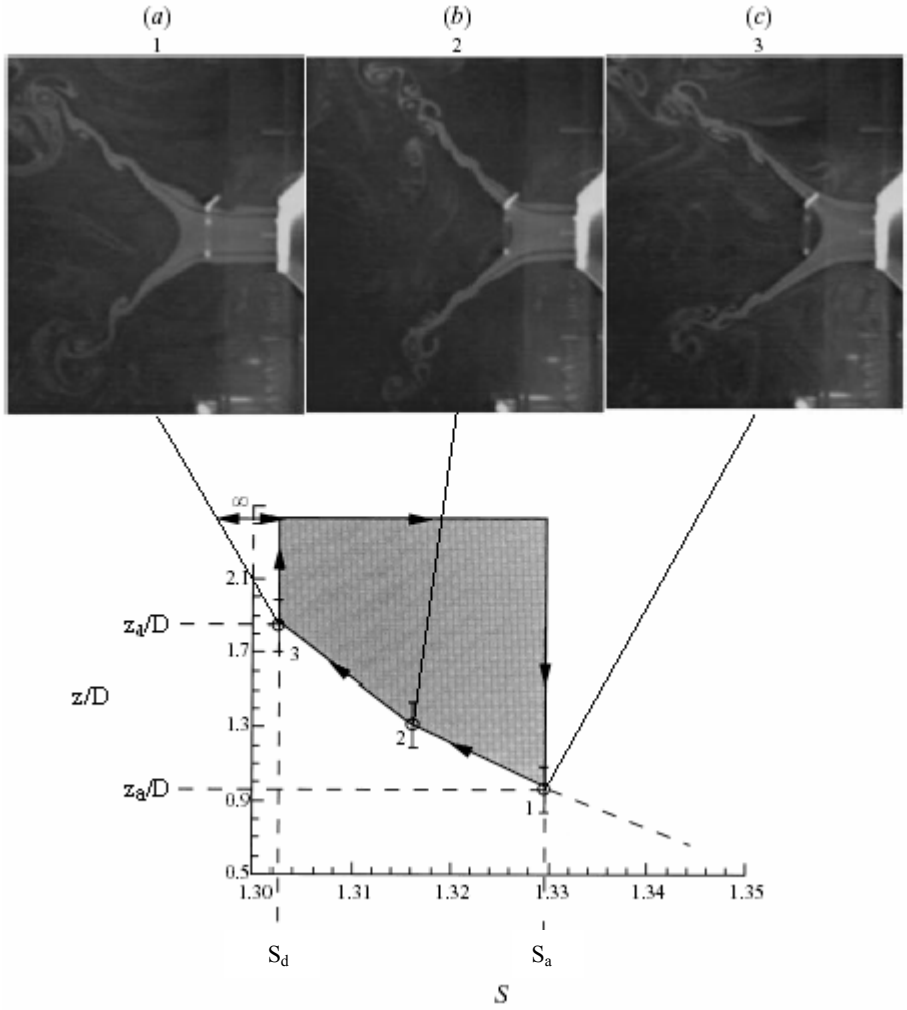

Figure 1.8: Hysteresis loop of a cone at $R_e = 752$ (sourced from Billant et al. (1998)).

While confirming that hysteresis did actually exist, Billant et al. (1998) applied a finite-amplitude perturbation to the flow by slightly constricting the flexible exit pipe of the tank, which produced a pressure wave and slowed the axial velocity of the swirling jet undergoing breakdown. They found that applying "sufficiently strong perturbations" to

the bubble and cone in a swirl range greater than the critical swirl number for breakdown ($S > S_a$) "succeeded in temporarily suppressing breakdown but breakdown ultimately reappeared after a finite time". In the so called "metastable" range ($S_d < S < S_a$), applying similar perturbations caused the bubble to be "swept away and it never reappeared within the next half hour". By applying a different type of perturbation (by the same means, however details were not mentioned regarding the amplitude or frequency of perturbation) Billant et al. (1998) were also able to regain the breakdown structure due to the induced reduction in axial velocity. Similar results for the cone were obtained in the metastable range; however unlike the bubble, a re-formation of the cone breakdown via perturbations was unachievable. This indicated that the cone is a difficult state to reach in the metastable range. Overall this technique of applying perturbations to the flow at a set frequency and amplitude shows great promise in the ability to control vortex breakdown.

1.4.4 Bi-Stability

Several investigations reveal that vortex breakdown exhibits bi-stability behaviour. The most common example of bi-stability can be seen in a photograph by Lambourne and Bryer (1961a), which displays the spiral and the bubble type breakdown occurring simultaneously on opposite sides of a delta wing, in which the same flow conditions exist. Another example of bi-stability was observed by Leibovich (1978), Sarpkaya (1971a) in confined tube experiments, in which the spiral and the bubble were highly unstable and the flow structures continually changed over time from one to the other. This also agrees with similar observation by Escudier and Zehnder (1982). Such stability issues and unpredictability could be due to the role played by helical disturbances in the dynamics of breakdown. However this is a controversial issue with two main points of view having emerged. Ludwieg (1962) was the first to put forward the notion that the development of helical disturbances in swirling flows are the main cause of breakdown, of which Leibovich (1978), Leibovich (1983), critically reviews and outlines the importance of asymmetry in breakdown. While Escudier (1988) believed that vortex

breakdown was an independent phenomenon and that helical disturbances were a by-product of breakdown, hence they were able to coexist.

1.4.5 Confinement Effects

Confinement effects imposed by tubes with various angles of divergence that create an adverse pressure gradient is found to significantly control the occurrence of breakdown, as observed by Althaus et al. (1995), Escudier et al. (1982), Sarpkaya (1974). These authors found that such tubes cause breakdown to occur at lower Reynolds numbers when the pipe flare angle is increased. This feature can be attributed to the fact that as the tube expands, the local pressure increases and the axial velocity component decreases, hence lowering the local swirl ratio until such a point that the swirl ratio reaches a critical value and breakdown occurs. However, confinement effects do not seem to have an effect on the various types of vortex breakdown states as shown by Khoo et al. (1997), who have observed and identified the same six modes of vortex breakdown in their unconfined tornado generator as in the confined tube configuration of Faler and Leibovich (1977b).

Several numerical simulations of vortex breakdown in pipes have been undertaken by Grabowski and Berger (1976), Kopecky and Torrance (1973), Krause et al. (1983), in which both steady and unsteady axisymmetric incompressible Navier-Stokes equations were solved by numerical integration. Althaus et al. (1995) have comprehensively reviewed time-dependent three-dimensional simulations that have reproduced the unsteadiness and asymmetry of the internal flow within the bubble, as found by Spall et al. (1990), along with the spiral type breakdown as found by Gatsky and Spall (1991).

1.4.6 Temporal Dynamics of Vortex Breakdown

Vortex breakdown is generally an unsteady, time dependent phenomenon. The bubble mode of breakdown is also accompanied by asymmetric recirculating regions within the stagnation zone. Bruecker and Althaus (1992), Sarpkaya (1971a), describe this phenomenon which involves a gyrating tilted vortex ring. Fluid is injected into and ejected out of the internal region by an emptying and filling process taking place in the downstream part of the bubble. While Bruecker (1993), Faler and Leibovich (1978), Lambourne and Bryer (1961a) observe the spiral type breakdown to proceed as a solid body about the central axis in the same direction as the upstream vortex. Adding to the phenomenon's complexity, Faler and Leibovich (1977a) also found that the breakdown states display secondary temporal dynamics in the form of random axial motions both upstream and downstream.

1.4.7 Effect of Reynolds Number, Jet-Like and Wake-Like Velocity Profiles on Vortex Breakdown

As previously mentioned, Ruith et al. (2003) conducted direct numerical simulations of incompressible vortex breakdown in a semi-confined domain, with both jet-like and wake-like axial velocity profiles. They found that at low Reynolds numbers a bubble or helix type breakdown were non-existent, even at very high swirl numbers. High Reynolds number flows at high swirl numbers can sustain a bubble, helical or double-helical type breakdown, in which jet-like axial velocity profiles promote axisymmetry, while wake-like profiles cause the flow to be helically unstable and lead to asymmetric breakdown. The theory that vortex breakdown is analogous to a hydraulic jump, proposed by Benjamin (1962), is confirmed in these simulations with a transition from super-critical to sub-critical flow, accurately predicting breakdown. Benjamin's theory was found to only hold for flows with supercritical inflow profiles. The inherent azimuthal wave numbers (or modes) for the helix breakdown were found to be m = -1 and m = -2, with

the minus sign indicating a counter-rotation to that of the main flow. This is in agreement with the previously mentioned experimental study by Novak and Sarpkaya (2000).

1.4.8 Vortex Breakdown Theories and a Theoretical Vortex Breakdown Criterion

In this section, we will examine several theoretical models which attempt to account for and describe the observed vortex breakdown structures and the mechanisms which control them. From this initial analysis, we will proceed to derive a simple vortex breakdown criterion which holds for all types of breakdown and imposed conditions. The following section will use a cylindrical co-ordinate system (r, z, θ), where r is the radial distance from the central axis, z is the axial distance downstream of the breakdown conception point (e.g. nozzle exit) and θ is the out of plane azimuthal angle component. The respective velocities in the corresponding directions are denoted as; U_r, U_z, U_θ.

Many conflicting theories regarding vortex breakdown have emerged over the years, with theories including hydrodynamic instability, flow stagnation, conjugate states and two-stage transition theory, to name a few. A comprehensive review of these theories can be found in Althaus et al. (1995), Delery (1994), Escudier (1988), Escudier and Keller (1983), Hall (1972), Leibovich (1978), Leibovich (1983), Stuart (1987).

Benjamin (1962) provided an analogy between vortex breakdown and hydraulic jump theory, which he called conjugate flow analysis. The theory is based on the premise that vortex breakdown is a dissipative axisymmetric jump-like transition between two distinct inviscid states. Similar to a hydraulic jump, there exists an upstream (supercritical) state where no upstream propagation may occur and only minuet downstream travelling waves can exist and a downstream (subcritical) state where standing waves can occur. Using the hydraulic jump analogy, Benjamin (1962) argued that the axial momentum flux in the downstream region must always be greater than its corresponding upstream region. Vortex breakdown and the associated downstream turbulence are seen in this case to account for the difference in axial momentum flux associated with the supercritical to subcritical transition at the critical transition region.

Billant et al. (1998) found that Benjamin (1962)'s conclusion that the transition is always dissipative is contradictory since a smooth transition with no evidence of dissipation is observed in their experiments. Benjamin (1962)'s conclusion was shown to be incorrect by Escudier and Keller (1983), Escudier and Keller (1985), Keller et al. (1985) in the first stage of their two-stage transition theory. Escudier and Keller (1983) demonstrate that the difference in axial momentum flux between the two states can disappear without the requirement of turbulence due to breakdown, as their analysis allowed for hollow core flows and arbitrary downstream velocity profiles. By assuming uniform upstream and hollow downstream vortex states separated by a transition region, it is possible to derive a criterion for breakdown with the condition that the axial momentum flux be conserved, with the assumption that the cavity of the downstream hollow vortex is at stagnation pressure with negligibly small velocity inside (Billant et al. (1998)).

Escudier and Keller (1983), have shown that vortex breakdown is a transition between two individual states which is non-dissipative and axisymmetric in nature and contains negligible velocities within the stagnation zone. Hall (1966) was able to obtain a criterion for vortex breakdown, for the general case of a free vortex undergoing conical breakdown with negligible confinement effects. Hall's basic idea is based on the conservation of circulation which means that if the radius of the vortex increases as it travels downstream in the z direction, an axial increase in pressure within the vortex core results, creating an axial deceleration. This process will continue until a point at which the pressure reaches a certain level as to bring the axial velocity to zero, resulting in a stagnation point and vortex breakdown.

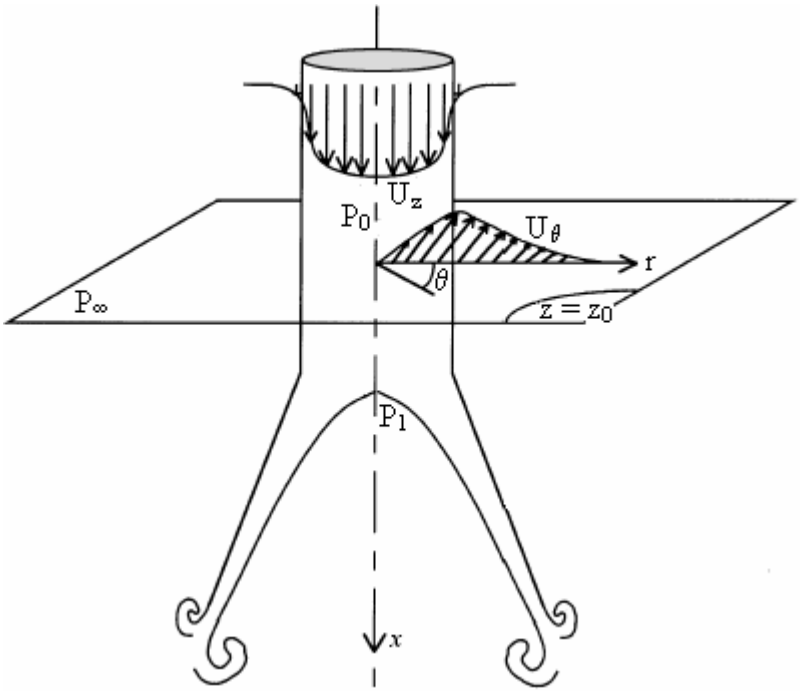

Figure 1.9: Schematic of a swirling jet undergoing cone breakdown (sourced from Billant et al. (1998)).

As covered in Hall (1966) and again in Billant et al. (1998), an examination of the following equations governing the flow of a free vortex which undergoes a cone type breakdown due to the emergence of a downstream stagnation point along the vortex axis (see Figure 1.9) will aid in a theoretical determination of a criterion for vortex breakdown. The total head can be found by applying Bernoulli's equation for total head along the vortical axis (i.e. r = 0) streamline:

$$H = \frac{P}{\rho} + \tfrac{1}{2}\left(U_z^2 + U_r^2 + V_\theta^2\right). \qquad \textbf{(1.4)}$$

Applying this equation along the vortex axis streamline (r = 0) and between points 0 and 1 (i.e. between $z = z_0$ and $z = z_1$) gives:

$$H = \frac{P_0}{\rho} + \tfrac{1}{2}U_z^2(r = 0, z = z_o) = \frac{P_1}{\rho}, \qquad \textbf{(1.5)}$$

where z_0 is the axial location, well upstream of the stagnation point, P_0 is the upstream (at $z = z_0$) pressure along the vortex axis ($r = 0$), ρ is the fluid density (assumed the same for the jet and surrounding fluid), $U_z(r = 0, z = z_0)$ is the upstream vortex axis velocity (assumed to be unaffected by the presence of the stagnation point) and P_1 is the pressure at the stagnation point. It is assumed that $U_r \approx 0$ along the vortex axis (i.e. along $r = 0$, the radial velocity is negligible along the vortex axis and may be assumed equal to zero, however this assumption does not hold in the breakdown region where radial velocities are significantly higher) and $V_\theta \approx 0$ along the vortex axis (i.e. $r = 0$).

Far upstream of the stagnation point, the radial pressure gradient is balanced by the centrifugal force, consequently:

$$P_0 = P_\infty - \int_0^\infty \rho \frac{U_\theta^2(r, z = z_0)}{r} dr, \qquad \textbf{(1.6)}$$

where $U_\theta(r, z = z_0)$ is the azimuthal velocity far upstream and P_∞ is the ambient pressure far upstream as $r \to \infty$.

Escudier and Keller (1983) assume that the velocities within the stagnation region are zero; even some weak internal recirculation from instabilities and viscosity effects may be approximated to be zero with reasonable accuracy. The stagnation zone in the breakdown region of the cone is open to the surrounding fluid which is at rest as $r \to \infty$. Instead of using Escudier and Keller (1983)'s technique of obtaining the stagnation pressure P_1 from the conservation of axial momentum, the following derivation will be along the same lines as Billant et al. (1998)'s reasoning. As confirmed by Farokhi et al. (1998)'s pressure measurements of a free swirling jet, it can safely be assumed that stagnation zone pressure is the same as that of the ambient pressure ($P_1 = P_\infty$) as there is negligible fluid exchange between the stationary surrounding fluid and the stagnation zone. By using this assumption along with equations (1.5) and (1.6), it is possible to eliminate the pressure terms in order to obtain the following ratio which relates the axial and azimuthal velocities of a vortex undergoing an open cone type core expansion:

$$\frac{\int_0^{\infty} \frac{U_\theta^2(r, z = z_0)}{r} dr}{U_z^2(r = 0, z = z_0)} = \frac{1}{2}. \qquad \textbf{(1.7)}$$

Equation (1.7) must be satisfied for a stagnation point to develop and a cone type vortex breakdown to exist for any type of vortex velocity distribution.

It is worthwhile considering the common case of a Rankine vortex (solid body rotation, with angular velocity, Ω) undergoing breakdown. However before discussing its properties, it is now appropriate to define the viscous core radius (r_c), which is defined as the radial distance from the centre line to the point of maximum azimuthal velocity $U_{\theta(max)}$. A typical Rankine vortex is described by the following properties far upstream of breakdown and the stagnation point (i.e. at $z = z_0$):

- Solid body rotation (for $r < r_c$):

$$U_\theta(r) = \Omega r \quad \text{and} \quad U_z = \text{const}. \qquad \textbf{(1.8)}$$

- Irrotational flow (for $r > r_c$):

$$U_\theta(r) = \frac{\Omega r_c^2}{r} \quad \text{and} \quad U_z = 0. \qquad \textbf{(1.9)}$$

- Maximum azimuthal velocity (for $r = r_c$):

$$U_{\theta\,max}(r = r_c) = \Omega r_c. \qquad \textbf{(1.10)}$$

Using the properties of a Rankine vortex at $z = z_0$, reduces equation (1.7) to:

$$\frac{U_{\theta\,max}(r = r_c)}{U_z(r = 0)} = \frac{1}{\sqrt{2}} \qquad \text{at} \quad z = z_0. \qquad \textbf{(1.11)}$$

Equation (1.11) was also obtained by Escudier and Keller (1983), and shows that at or above this critical value, vortex breakdown will occur for a Rankine vortex with negligible confinement effects.

When considering the case of a closed end bubble type breakdown, it is no longer possible to assume that the stagnation zone pressure is equal to the ambient pressure ($P_1 = P_\infty$) as the two regions are no longer connected. Instead this previous assumption should be replaced by the more suitable inequality, $P_1 \leq P_\infty$. The same derivation used to obtain equation (1.7) still holds for the bubble type breakdown state, except for the replacement of the previous equality with the now more appropriate inequality. Hence the general criteria for a bubble type breakdown is:

$$\frac{\int_0^{\infty} \frac{U_\theta^2(r, z = z_0)}{r} dr}{U_z^2(r = 0, z = z_0)} \geq \frac{1}{2} \qquad \textbf{(1.12)}$$

Criteria 1.12 clearly shows that for a bubble state breakdown to arise, the above ratio has a lower limit of 1/2.

1.4.9 Critical Swirl Number at which Vortex Breakdown Occurs

Several parameters have been put forward in an attempt to accurately predict the onset of breakdown. Although there are several ideas behind the mechanism of vortex breakdown, there is yet to be one that can explain all of the observed features of this phenomenon. Several theories all hold true to certain observed characteristics of vortex breakdown. Criticality theory holds for vortex breakdown in which all the observed vortical flows were supercritical upstream of breakdown and subcritical downstream, along with the fact that downstream conditions greatly affected the entire process. A stagnation point is another common characteristic of breakdown along with the existence of instabilities. Due to each theory having its own merits, it was an obvious advancement to combine these theories for a more complete explanation of the mechanisms behind this phenomenon. Shi (1985) showed the link between criticality and stagnation. Randall and Leibovich (1973) combined the ideas of wave propagation and hydrodynamic instability to produce the theory of wave trapping. Escudier et al. (1982) and Maxworthy et al.

(1985a), Maxworthy et al. (1985b) described the process of vortex breakdown by criticality theory and stability as a secondary mechanism. Even though limiting themselves only to the bubble breakdown, Brown and Lopez (1990) proposed a theory based on the development of negative azimuthal vorticity while also using stability theory as a secondary mechanism. They believed that vortex breakdown was a result of the axial vorticity tilting (due to the azimuthal component of the swirling jet) into negative azimuthal vorticity. This transfer of vorticity from the axial to azimuthal planes would continue at an increasing rate due to a positive feedback mechanism until such point that a stagnation point appears and vortex breakdown occurs. Bruecker (1993) proposed that the different forms of observed breakdown were primarily due to the angle at which the vortex core is deflected off- axis, the winding characteristics and diameter of the vortex core.

There have been many attempts to define a swirl parameter which can accurately predict the occurrence of breakdown. Some definitions of the swirl parameter, based on axial fluxes of azimuthal and axial momentum, are commonly used in the literature on swirling jet flows (see, for instance, Farokhi et al. (1988), Panda and McLaughlin (1994)). However, Farokhi et al. (1988) have shown that this definition is inappropriate for studying vortex breakdown. This is due to the fact that two swirling jets with different exit velocity profiles may then have the same value of the swirl parameter value although only one experiences breakdown. However Billant et al. (1998) went further to say that "the essential feature of all the definitions is the inclusion of a measure of the ratio of azimuthal to axial velocities". The most accurate way of predicting the occurrence of breakdown is via the swirl number S (also known as the swirl ratio or inverse Rossby number), which if it locally at any point in the vortical structure reaches or surpasses a critical swirl number value (i.e. $S \geq S_c$ where S_c = 1.3 - 1.4 according to Billant et al. (1998)) then breakdown will occur:

$$S = \frac{2U_{\theta max}}{U_{z max}}, \qquad \textbf{(1.13)}$$

where $U_{\theta max}$ is the maximum azimuthal velocity at the nozzle exit and U_{zmax} is defined as the maximum axial velocity at the nozzle exit.

The factor of 2 in front of the swirl number is sometimes omitted; however, for easy comparison in latter work it will be retained. The importance of the swirl number (or swirl angle) as a predictive parameter for the onset of vortex breakdown was also pointed out in experiments by Pagan and Molton (1990). Another more precise definition of the swirl number is:

$$Si = \frac{\left(\int_0^{\infty} \frac{U_\theta^2(r, z=0)}{r} dr \right)^{1/2}}{U_{z\,max}}, \qquad \textbf{(1.14)}$$

where $U_\theta(r,z = 0)$ is the azimuthal velocity profile at the nozzle exit. This definition was compared with that of equation (1.13) by Billant et al. (1998) using different velocity profiles such as that used by Farokhi et al. (1988). They found that equation (1.13) "applied to profiles measured close to the nozzle exit correctly predicts the observations of these authors. This further confirms the validity of the breakdown criterion".

Billant et al. (1998) have used this criterion (equation (1.13)) and reproduced many other experimental and numerical results. Their results agree well with the progression of breakdown forms previously described, and verify the accuracy of this parameter in the prediction of breakdown. The different forms of breakdown are attributed to the different Reynolds number and swirl number ranges which control the observed breakdown structure. The criterion for breakdown was clearly observed to occur at a critical swirl ratio of $S_c = 1.3 - 1.4$ and was found to be independent of the Reynolds number and nozzle diameter (see Figure 1.10). This could in fact be in contradiction to Mitchell and Delery (2001) who state that "The Reynolds number has nearly no direct effect on the phenomenon, except at very low Reynolds numbers well below any practical values." but do not go on to say how low a Reynolds number. Billant et al. (1998) compared this critical value with that of Escudier and Keller (1983)'s theory on three dimensional vortical flows, and it was found to be in good agreement.

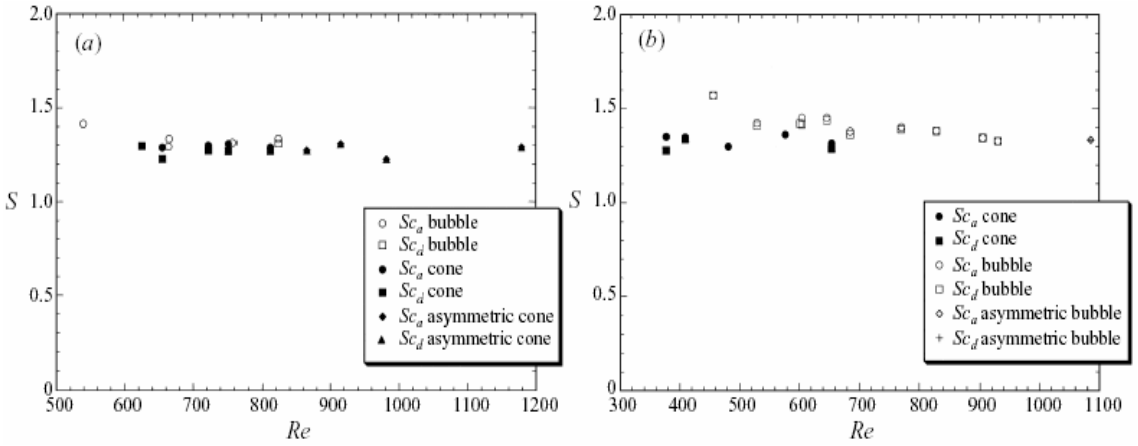

Figure 1.10: Billant et al. (1998)'s results showing the critical swirl number for the appearance Sc_a, and disappearance Sc_d, of breakdown at various Reynolds numbers and 2 different nozzle diameters, (a) D = 40mm and (b) D = 25mm.

Delery (1994) have mentioned that many experiments especially those using delta wings use another form in which the swirl number is expressed as a helix angle:

$$\gamma = \tan^{-1}\left[\frac{U_{\theta\max}}{U_{z\max}}\right], \qquad \textbf{(1.15)}$$

which at a critical value (approximately 43° to 46° according to Faler and Leibovich (1977a)) also indicates the onset of breakdown. Delery (1994) states that a common ratio which characterises the strength of the vortex and can predict the onset of breakdown is the swirl parameter:

$$\Lambda = \frac{\Gamma_{z=0,U_{\theta\max}}}{r_{U_{\theta\max}} U_{z\max}}, \qquad \textbf{(1.16)}$$

where $\Gamma_{z=0,U\theta max}$ is the circulation (ie. integrated vorticity $\omega_z = \nabla \times \vec{U}$) at the nozzle exit at a radial location where the azimuthal velocity is a maximum ($r_{V\theta max}$). It is interesting to note that the circulation for a Rankine vortex is equal to $2\pi r U_\theta$ and is independent of the axial location.

However all of these parameters (see equations (1.13) to (1.16)) are able to be related to one another making for easy comparison between various experiments and results. Relating these parameters for a Rankine vortex gives:

$$\Lambda = \frac{\Gamma_{z=0,U_{\theta\,max}}}{r_{U_{\theta\,max}} U_{z\,max}},$$

$$\Lambda = 2\pi S,$$

$$\Lambda = 2\pi \tan\gamma. \qquad \textbf{(1.17)}$$

1.5 Detailed Description of the Various Breakdown States

The following four principles and unique breakdown states and their inherent properties have been identified:

1. **Spiral:** Identified as an asymmetric spiral which is characterised by an upstream stagnation point which precesses about the axis.
2. **Bubble:** Identified by its symmetric recirculating bubble structure consisting of four recirculating cells and the existence of a stagnation point on the vortex axis.
3. **Cone:** Identified by its symmetric laminar open core structure and the existence of a stagnation point on the vortex axis.
4. **Asymmetric cone and asymmetric bubble:** The asymmetric cone is identified by its asymmetric cone structure and the existence of a co-rotating off-axis stagnation point, while the asymmetric bubble is identified by an asymmetric recirculating region and the existence of a co-rotating off-axis stagnation point.

1.5.1 Spiral Breakdown

This structure's distinctive traits include the appearance of a stagnation point causing a kink in the axially injected dye filament which forms a coiled structure that proceeds downstream for a number of cycles before its break-up into large scale turbulence. It was found that the period of rotation of a spiral was directly related to the swirl imparted to the upstream vortical structure. More specifically, an increase in the axial Reynolds number or swirl causes an increase in the rate of rotation of the spiral structure.

The spiral breakdown from leading edge vortices over delta wings identified by Lambourne and Bryer (1961a) produced a similar structure to that reported in Chanaud (1965), who in addition found that the spiral type breakdown frequency is linked to the angular velocity of the upstream vortical structure, from which it also obtains its energy due to hydrodynamic instabilities. Chanaud (1965) also mentioned that the upstream stagnation need not maintain a fixed position in the temporal domain. Comparing the vortex core expansion downstream of the breakdown region, observed in both the bubble and spiral breakdown states, shows that the vortex core expansion associated with the spiral is considerably smaller than that of the bubble.

Cassidy and Falvey (1970) also observed a steady helical structure at low Reynolds numbers and the spiral type breakdown as the Reynolds number was increased, unlike Harvey (1962) who did not observe any spiral type structure. This could possibly be attributed to the different vortex generation mechanisms used by each of the authors; the latter author used variable angle guide vanes while the prior using angled water inlet jets.

The spiral's rotational direction with respect to the upstream vortical flow has been a point of controversy and contradictory observations among researchers. Faler and Leibovich (1977a) in agreement with Sarpkaya (1971a), Sarpkaya (1971b) observed the spiral to rotate and wind in the same direction as the upstream vortex. A contrary observation by Escudier and Zehnder (1982) who witnessed the spiral's rotational direction was the same as the upstream vortex while the winding direction was "unmistakably opposite" to that of the upstream vortex. A similar observation was found

via vortex breakdown experiments over delta wings, as conducted by Lambourne (1965), Lambourne and Bryer (1961a).

There have been many explanations put forward as to the experimentally observed discrepancies in the winding direction of the spiralling flow with respect to the rotational direction of the upstream swirling flow and spiral from which it was generated. Some explanations/theories have been discounted through experiments while others have yet to be investigated thoroughly and be either confirmed or rejected. The following will outline the main explanations some of the researchers, along with any observations which contradict their theories.

Leibovich (1983) suggested that the primary factor in determining the spiral's rotational direction was dependent on the experimental setup and, more specifically, the way in which the azimuthal velocity (or swirl) was generated. He suggested that swirling flows generated via tangential entry devices like that of Escudier and Zehnder (1982) rather than vane devices like those used by Faler and Leibovich (1977a), Sarpkaya (1971a), had a closer resemblance to leading edge vortices created over delta wings. However this theory was countered by experiments by Bruecker (1993), who used a guide vane vortex generator and found that the spiral does rotate in the same direction as the upstream vortex; however the winding of the spiral is in the opposite direction.

Gursul (1996) carried out experiments to support his theory that the axial velocity profile is what determines the spirals winding direction. His experiments consisted of exciting helical mode instabilities of the vortex breakdown, which showed that the flow is most sensitive to helical mode disturbances rotating in the same direction as the mean swirl for wake-like axial velocity profiles and in the opposite direction for jet-like axial velocity profiles. He found that for jet-like axial velocity profiles that the spiral would wind in the direction opposite to the upstream vortical structure while the wake-like velocity profile would have a spiral winding in the same direction. This is contradictory to Faler and Leibovich (1977a)'s observations who found that their jet–like axial velocity profile produced a spiral which winds in the same direction as the upstream vortex.

Escudier and Zehnder (1982) suggested that the main factor was a "pre-breakdown" disturbance that would appear for circulation numbers below approximately

six. This had the observed effect of causing the rotation and winding direction of the spiral to be the same as that of the upstream swirling flow.

Dye filament visualisations of the spiral by Lambourne and Bryer (1961a) found that even though the filament took the form of a spiral, individual particles were deflected from the spiral path and would continue downstream at an equivalent radial distance from the vortex axis as the spiral but with little azimuthal "winding" velocity about the vortex axis. An attempt to explain this observation was put forward by Hall (1972), who hypothesized that the deflected particles were in fact following the fluid close to the central axis which has diminutive angular momentum and hence cannot follow the spiral path.

Klute et al. (2005) utilized Particle Image Velocimetry (PIV) to investigate leading edge vortex breakdown over a delta wing. A detailed mapping of the evolution of spiral vortex breakdown along the vortex axis revealed that the vorticity swaps sign at the onset of vortex breakdown. This is in agreement with previous experimental and numerical results.

1.5.2 Bubble Breakdown

Faler and Leibovich (1977a), Sarpkaya (1971a) have comprehensively documented the bubble breakdown structure in confined tube experiments. The axisymmetric bubble contains a recirculating region, which exchanges fluid between the interior and exterior at the base of the bubble. Sarpkaya (1971b) also discovered a toroidal vortex ring with a fixed frequency rotation in the downstream region of the bubble. The simultaneous filling and emptying of the bubble was explained by Sarpkaya, who believed that the instabilities at the wake of the bubble caused the vortex ring to absorb fluid from its downstream portion while expelling the internal fluid from its upstream portion. While agreeing with the filling and emptying mechanism of the bubble via the vortex ring as suggested by Sarpkaya, a contradictory observation was put forward by Faler and Leibovich (1977a) who believed that the emptying and filling process was the exact

reversal of Sarpkaya's observations (i.e. the vortex ring expelled fluid at its base while absorbing fluid at its upstream region).

The fully axisymmetric bubble which envelops a low frequency recirculating fluid interior was examined by Faler and Leibovich (1977a), Sarpkaya (1971a), Sarpkaya (1971b), who attributed this low frequency motion to the trading of fluid between the interior and exterior at the base of the bubble. LDA measurements by Faler and Leibovich (1978), conducted on the breakdown bubble within confined tubes, identified a twin cell internal structure which was later reproduced using unsteady three-dimensional numerical simulations by Spall et al. (1990).

The re-formation of vortex core, observed in the wake region of the bubble, appears less intense with a reduction in axial velocity and has an expanded core in comparison to the original upstream vortical structure. The reformed vortical structure was found to digress from the central axis before it forms a spiral tail which breaks up into turbulence further downstream. Garg and Leibovich (1979), Leibovich (1983) pointed out that these observations are similar/analogous to those found in the wake regions behind bluff bodies. At low Reynolds numbers, Faler and Leibovich (1977a) found that on some occasions, the reformed vortical core would split into two distinct spiralling tails with opposing azimuthal directions.

Sarpkaya (1971a) found that the axisymmetric bubble would develop directly from the swelling of the vortical core, or indirectly, by evolving from the spiral or double helix formation. The path to the bubble's creation, either directly or indirectly by evolving, depended on the exact combination of swirl and Reynolds numbers used. The direct formation of the axisymmetric bubble via vortex core expansion was found to occur only at high Reynolds and swirl numbers as shown by Escudier (1988)'s evolutionary photographs.

Sarpkaya (1971a) observed the creation of a series of up to 3 bubble breakdowns as the swirl was increased for an axisymmetric bubble breakdown state with a spiralling tail. Increasing the swirl beyond this point causes the spiralling tail to move further upstream, and destroys a series of bubbles except for the one furthest upstream which seemed to move upstream with the spiral tail. The upstream bubble was symmetric during its initial formation and grew in size by drawing in fluid from its bottom end as the swirl

was increased. The bubble's upstream movement and growth stopped at an upstream axial point which coincides with the location of a similar breakdown structure occurring at the same swirl number.

A discrepancy in results arises when comparing LDA measurements by Bornstein and Escudier (1984) which reveal similar results to Sarpkaya (1971a) with the exception of not displaying a closed bubble with two internal stagnation points. This has been an issue that has persisted over the years with no feasible explanation as to whether the bubble is open or closed or whether each state is different and depends on the imposed conditions.

Particle Tracking Velocimetry (PTV) measurements of an open ended breakdown bubble within a confined tube was conducted by Bruecker and Althaus (1992). Their volume mapping of the structure at R_e = 150 revealed an unsteady and asymmetric interior. The internal fluid motion was found to be governed by a tilted vortex ring at the open end rear portion of the bubble (see Figure1.11) in agreement with Sarpkaya (1971a).

Billant et al. (1998) found that the vortex core suddenly expands after the appearance of a stagnation point located half a nozzle diameter (D) from the nozzle exit in the axial direction, with the inner surface of the upstream breakdown point consisting of a parabolic cross-section. The vortex expansion in the shape of a bubble had radial and axial dimensions of 1.5D to 2.5D in diameter which enclosed a slow moving, oval cross-section recirculating region. The bubble consists of two distinct regions, the axisymmetric upstream bubble region and the asymmetric downstream segment in which the bubbles tail takes the shape of a twin limb spiral. The temporal dynamics of the bubble structure is also spatially dependent in that the location of the upstream stagnation point and the bubble diameter are very nearly static; however, the downstream tail region is unsteady and even further downstream the flow structure is highly chaotic. The inner surface of the bubble is characterised by an upstream parabola shape near the stagnation point, while its downstream region takes the form of a cone.

Billant et al. (1998)'s visualisations were complemented by LDA measurements of the axial and azimuthal velocity contours. They found that the azimuthal and axial velocities are particularly weak within the internal zone of the bubble in comparison to that of the surrounding flow. The internal zone has two distinct recirculating regions as

indicated by axial velocity contours. The near axis region consists of fluid which is expelled and passed into the outer perimeter region of the internal structure. LDA measurements also showed that the bubble type breakdown experienced typical velocity fluctuations about the mean velocities of 17% in the downstream region of the bubble and 4% in the upstream region within the stagnation expanse.

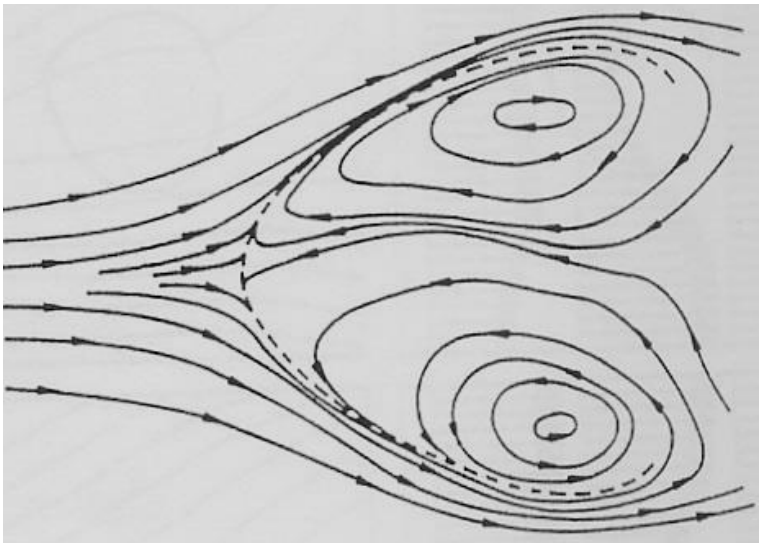

Figure 1.11: Instantaneous streamlines of an open ended bubble by Bruecker and Althaus (1992).

1.5.3 Cone Breakdown

According to Billant et al. (1998), the cone type breakdown which they have identified has not previously been observed (see figure 1.5). The following is a summary of their reported findings. The cone breakdown profile is characterised by the expansion of the vortical structure at the stagnation point in the form of a laminar conical sheet. Unlike the bubble state, the cone is an open ended structure which does not contract in the downstream region and enclose the stagnation point.

The conical sheet thickness is inversely proportional to the downstream distance from the stagnation point, up to an axial distance of 2 to 3 vortex core diameters downstream, at which point instabilities cause the breakdown of structure and the bottom

edge of the cone rolls up into small scale vortices prior to its destruction into weak turbulence. These instabilities are most likely caused by a combination of axial shear and azimuthal shear within the conical sheet along with centrifugal instability due to the azimuthal motion within the conical sheet. The secondary recirculating flows within the cone are considerably slower and weaker than those present within the bubble. The cone angle varies with time in a regular and well-defined fashion while the stagnation point wanders back and forth along the jet axis.

According to Billant et al. (1998), below the critical swirl number for onset of breakdown S_c, i.e. when $0 \leq S < S_c$, the swirling jet is highly asymmetric and takes the shape of a steady helix, while above breakdown onset, cross-section visualisations indicate that the cone and the bubble are axisymmetric, except at high Reynolds numbers. The cone is observed to undergo slow oscillations induced by secondary recirculating motions that are independent of confinement effects.

1.5.4 Asymmetric Cone and Asymmetric Bubble Breakdown

The axisymmetric cone and bubble appear at lower Reynolds numbers than their corresponding evolutionary configurations which appear as an asymmetric cone (see Figure 1.12a) and asymmetric bubble (see Figure 1.12b), respectively. Both the symmetric and asymmetric configurations are visually similar, except for the behaviour of the stagnation point which co-rotates about the vortex axis and is one of the main differing features present in both of the asymmetric configurations, as observed by Billant et al. (1998). The asymmetric configuration can be identified by its off nozzle axis stagnation point, which is seen to move in a regular manner about the nozzle axis and is evident when flow visualisations are conducted. Other distinguishing/differing features include more intense recirculation flows and a more open ended bubble for the asymmetric bubble case than for the symmetric bubble.

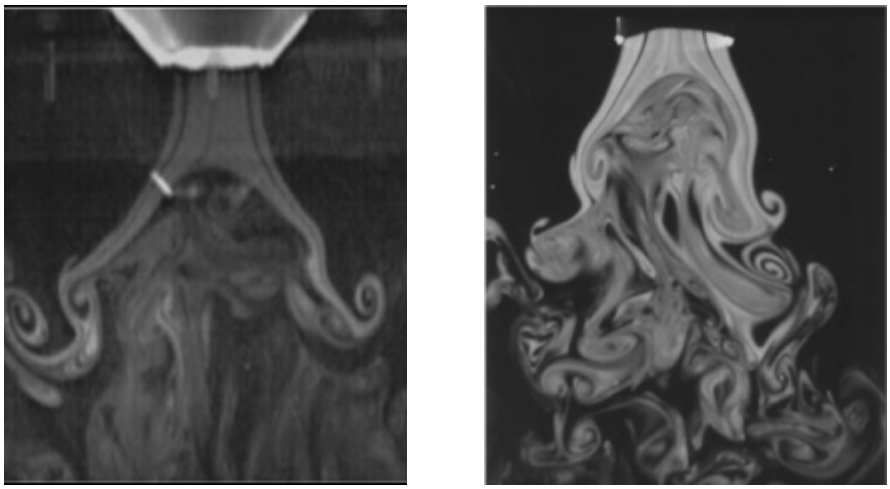

Figure 1.12: (a) Asymmetric cone at R_e = 916, S = 1.31 and (b) asymmetric bubble at R_e = 1022, S = 1.35 (sourced from Billant et al. (1998)).

The occurrence of the asymmetric breakdown structures at higher Reynolds numbers than their symmetric predecessors means that any instability within the structure is magnified. The magnification of these instabilities has the effect of producing more intense recirculating regions and causing the breakdown structure to break up further upstream (closer to the stagnation point). For example the asymmetric cone breakdown structure breaks up into turbulence after approximately 1 to 1.5 nozzle diameters downstream from the stagnation point in comparison to 2 to 3 nozzle diameters for the symmetric cone according to Billant et al. (1998).

The asymmetric bubble of Billant et al. (1998) and the 2-D velocity field relating to the spiral breakdown observed by Bruecker (1993) show that both are similar to the asymmetric bubble seen here, with the main feature being the regular movement of the stagnation point about the nozzle axis. The latter author has also found that the stagnation point moves about the nozzle axis in the same direction as the azimuthal velocity of the swirling jet. As indicated by Billant et al. (1998), the spiral breakdown identified by Bruecker (1993) is simply an asymmetric bubble with an off-axis stagnation point that rotates around the vortex axis. The spiral was previously thought of as a separate type of breakdown due to the visualisation technique used. For instance, when a single dye filament is injected on the vortex axis of an asymmetric bubble, its path deviates due to the rotating off-axis stagnation point which results in the visualisation of the spiral

structure. The spiral filament structure can exist without the presence of a stagnation point due to the helical instabilities to which vortical flows are so highly prone.

There are still differing observations and opinions present regarding some critical aspects of vortex breakdown. For example, Billant et al. (1998) have observed that the asymmetric bubble is located in the same range of axial positions as the symmetric bubble. These authors have also found and that the symmetric bubble turns into an asymmetric bubble as the Reynolds number is increased, which is also confirmed by the experiments of Althaus et al. (1995), Bruecker and Althaus (1995). In sharp contrast however, experiments in confined tubes by Faler and Leibovich (1977a), Garg and Leibovich (1979), Sarpkaya (1971a) have reported that the spiral breakdown state appears at locations downstream of the symmetric bubble and that, as the Reynolds number is increased, the spiral develops into a bubble. Such conflicting arguments need to be investigated carefully in order to find why such critical differences occur. In comparing the different methods of observation, vortex generation mechanisms and geometrical differences of the various experiments, it is the geometrical differences that stand out by far as the most likely factor causing these discrepancies.

1.6 Overview of Experimental, Numerical and Theoretical Investigations

As was seen throughout this discussion, various breakdown states have been identified at different combinations of Reynolds and circulation (or swirl) numbers. The breakdowns dependence on Reynolds number is considered a vorticity effect rather than a viscosity effect according to Lucca-Negro (1999), Mitchell and Delery (2001).

All the breakdown forms identified have been asymmetric in the azimuthal direction and periodic in motion. The majority of experimental apparatus produce a jet-like axial velocity profile vortical structure, which transforms into a wake-like axial velocity profile downstream of the breakdown. This downstream region is also characterised by a greater degree of turbulence and stronger periodic motions than that of

the upstream region. Such a flow field resembles that of a bluff body placed in a channel flow.

At high Reynolds numbers, the only breakdown structures which appear are the asymmetric bubble and spiral. The bubble form contains a stagnation point followed by a recirculating bubble which exchanges fluid between the interior and exterior flow via a single tilted ring-like structure which rotates around the vortex centre line. The bubble fills from the downstream portion of the tilted vortex ring and empties from the upstream portion. The spiral breakdown is characterised by an off-axis stagnation point, which causes a rapid deceleration of the upstream flow, leading to an abrupt kink in the vortex followed by a spiralling of the vortical core. The spiral is observed to rotate as a whole structure with reference to the base flow. The direction of winding of the spiral is a point of difference amongst investigators, with some observing the winding direction of the spiral the same as the vortex rotation direction (e.g. Faler and Leibovich (1977a), Sarpkaya (1971a), Sarpkaya (1971b)), while others observe the opposite direction (e.g. Bruecker and Althaus (1992), Escudier and Zehnder (1982), Lambourne (1965)). This point requires further investigation/research, as to date there is still no explanation for the differing observations. The second discrepancy is regarding the downstream core size below the breakdown structure. Researchers' observations of their experiments vary once more, Garg and Leibovich (1979), Leibovich (1983) believe that the vortex core weakens and expands (with expansion being significantly larger for a bubble than for a spiral breakdown), while Bruecker and Althaus (1992) believe the axial vorticity is increased with a reduction in the vortex core size.

There is a distinct sequence of vortex breakdown modes/types and locations as the swirl is increased. The spiral always occurs at swirl velocities lower than that required for a bubble breakdown. The breakdown location is also linked to the swirl, in that the higher the swirl, the further upstream the breakdown occurs, hence the bubble occurs further upstream than that of the spiral. Evolutions between breakdown states may also occur depending on the combination of Reynolds and circulation (or swirl) numbers. The bubble may either evolve indirectly from a bubble or directly from vortex core swelling, while in specific ranges of the flow settings, the bubble and spiral may spontaneously transform from one to the other.

The type of breakdown and its axial position along the tube depends on the flow rate (Reynolds number), swirl (or circulation), the externally imposed pressure gradient, the expansion rate of the vortex, the upstream and downstream flow conditions and a strong dependence on confinement effects among other system variables as observed by Hall (1972), Sarpkaya (1971a), Sarpkaya (1971b), Sarpkaya (1974).

These experimental studies have given researchers insight into many of the mysteries behind vortex breakdown. Vortex tube wall pressure measurements by Sarpkaya (1971a) have shown that the amplitude and frequency of fluctuation increases with increasing swirl. The two-celled asymmetric bubble structure has been documented with velocity and vorticity measurements revealing a positive axial velocity along the vortex centre line. The two cells consisted of an outer tilted ring which was responsible for the fluid exchange between the interior and exterior of the bubble along with an inner cell of flow reversal near the vortex centre line. There are two main trains of thought as to whether the bubble and spiral structures are separate entities or different aspects of the same phenomena.

Numerical solutions have progressed over the years and have become more and more complex in order to be able to capture the complexities of the flow structures associated with vortex breakdown. The simplest approach was to indicate the position of breakdown for different flow conditions using Quasi-Cylindrical Approximation (QCA). The need for more detailed solutions was necessary to study the breakdown structure and consequently led to the next step of finding solutions to the Navier-Stokes equations.

Vortex breakdown was seen experimentally to be periodic and three dimensional in nature. As a result, the restraints on computational abilities and the complexity of the problem limited early numerical studies to laminar, incompressible, steady and axisymmetric flows (see for example Grabowski and Berger (1976), Kopecky and Torrance (1973)). It was not until after the mid 1980's in which unsteady flow was also considered, (see for example Hafez et al. (1987), Krause and Menne (1987), Salas and Kuruvila (1989), Shi (1985)). Due to the unrealistic restrictions, such as axisymmetry, the numerical solutions were in disagreement with some of the experimentally observed attributes, however they still captured some similar features.

The first three-dimensional, time-dependent simulation was proposed by Spall and Gatski (1987), who noticed from their simulations that the redistribution from axial to radial and azimuthal vorticity components was undertaken as the flow reached the stagnation point for the bubble structure along with a total increase in local vorticity in the same region. The breakdown was unstable and appeared to move upstream towards the inflow boundary as time proceeded. Further three-dimensional and time-dependent simulations were conducted by several investigators (see for example Breuer and Hanel (1989), Breuer and Hanel (1993), Krause (1990a), Krause (1990b), Spall and Gatski (1990), Spall et al. (1990)).

It is readily concluded from both experimental and numerical investigations that the type of breakdown is dependent upon the imposed adverse pressure gradient. The transition between the breakdown forms appears gradually. In general the attributes agree well with experimental results, with more specific examples including the double ring bubble structure similar to Faler and Leibovich (1978), which temporally evolves into a the bubble structure as experimentally observed by Bornstein and Escudier (1984).

In the numerical study of turbulent vortex breakdown Spall and Gatski (1995), it was found that the axial vorticity upstream of breakdown decays more rapidly for the laminar rather than the turbulent case, while the axial vorticity downstream of the turbulent breakdown is only positive and is up to three times lower than that of the laminar case and much simpler in structure.

Although there are several proposed mechanisms for vortex breakdown, there is yet to be one that that can explain all of the observed features of this phenomenon. Several theories all hold true to certain observed characteristics of vortex breakdown. Criticality theory holds for vortex breakdown in which all the observed vortical flows were supercritical upstream of breakdown and subcritical downstream, along with the fact that downstream conditions greatly affected the entire process. A stagnation point is another common characteristic of breakdown along with the existence of instabilities. Due to each theory having its own merits, it was an obvious advancement to combine these theories for a more complete explanation of the mechanisms behind this phenomenon. Shi and Shan (1987) showed the link between criticality and stagnation. Randall and Leibovich (1973) combine the ideas of wave propagation and hydrodynamic

instability to produce the theory of wave trapping. Escudier and Keller (1983), Maxworthy et al. (1985a), Maxworthy et al. (1985b) described the process of vortex breakdown by criticality theory and stability as a secondary mechanism. Even though limiting themselves only to the bubble breakdown, Brown and Lopez (1990) proposed a theory based on the development of negative azimuthal vorticity while also using stability theory as secondary for the mechanism causing vortex breakdown. Bruecker (1993) put forward that the different forms of observed breakdown were primarily due to the angle at which the vortex core is deflected off-axis, the winding characteristics and diameter of the vortex core.

Although these theories (even the combined theories) are still unable to fully describe the mechanisms behind vortex breakdown, they have given researchers more insight into the flow structures which appear and a possible path for future investigations.

1.7 Control of Vortex Breakdown

1.7.1 Requirement for the Control of Vortex Breakdown

Vortex breakdown is a naturally occurring phenomenon which can be seen as an abrupt area change and the sudden emergence of a stagnation point at a critical point within the flow of a swirling jet or from the rolling up of a shear boundary layer. This phenomenon can have both adverse and/or beneficial effects, depending on the design application and industry. The aerospace industry is one such industry in which vortex breakdown can play a critical role in the design of aircraft and the engines which power them. The ability to accurately predict, control and in some cases eliminate vortex breakdown is of immense importance in aiding the design of the next generation of aircraft, automobiles, engines, rockets, control surfaces, mixing chambers and almost all three dimensional bodies, just to name a few design situations where vortices exist.

Keeping in mind that vortex breakdown is the destruction of a vortical structure, it would be advantageous to provoke such a phenomenon to our advantage when trying to

destroy hazardous vortices originating from the tips of aircraft or to enhance air and fuel mixing in combustion chambers. The most significant advantages and disadvantages of vortices and vortex breakdown occur in the aerospace industry. Leading edge vortices are an important factor in producing non-linear lift for delta wing aircraft, however they also pose they also pose controllability issues for other aircraft in their wake. If vortex breakdown occurs over the wings, as is the case with highly swept aircraft wings at high angles of attack, then a reduction in lift and manoeuvrability occurs along with increased noise, structural vibrations and fatigue due to pressure fluctuations. Other disadvantages of vortex breakdown include its asymmetric nature over each wing, creating a difference in lift which induces a roll moment and destabilises the aircraft. Vortices can also be created from points on the fuselage and nose of aircraft at high angles of attack which in itself can create handling problems. If the vortex undergoes vortex breakdown, the situation is further complicated and made even more hazardous. The internal aerodynamics of machines such as jet engines may also require vortex breakdown control. A typical situation is one were a vortex generated on the aircraft structure undergoes breakdown and is directed into the engine, causing dangerous levels of flow unsteadiness and vibration. It is clear that there are an almost endless array of situations in which the study of vortex breakdown and its control are essential in either delaying or avoiding this phenomenon.

The major control mechanisms which have been investigated in the past include steady or periodic, mechanical and pneumatic devices. Although these techniques have not shown any major advantage in effectiveness or efficiency over each other, they do provide a unique approach to the control of vortex breakdown depending on the desired outcome. However the control of vortex breakdown faces many other obstacles such as the oscillating breakdown position which is already difficult to quantify and identify in well controlled experimental conditions. Added adversity arises when trying to implement these processes in situations such as aircraft in mid-flight. The lack of effectiveness of control techniques is greatly due to the inadequate knowledge of the breakdown process and the mechanisms behind the phenomenon. According to Mitchell and Delery (2001), “When considering the relative success of the large number of studies into vortex breakdown and their control, it is clear that decisive progress in this domain

will require further basic investigations to clearly elucidate the physics of the phenomena and to improve the predictive capability.”.

The obvious solution in avoiding vortex breakdown is to avoid the formation of a vortex in the first place. This requires the ability to control the surfaces from which the flow separates and vortices emanate. Mitchell and Delery (2001) proposed that in order to achieve this type of control mechanism, two possible control techniques would be required: either contouring the surface or using small lifting surfaces or pneumatic devices. The authors went on to suggest that this method of controlling vortex breakdown by the suppression of the vortex would be almost impossible due to the fact that “vortices are intimately linked to lift and the higher the lift the more intense the vortices”.

We have seen that the occurrence of vortex breakdown is linked to the swirl number and stabilising a vortex or reversing the breakdown process may be achieved by lowering the swirl number by either reducing the azimuthal velocity or increasing the axial velocity component. This can have a stabilizing effect by delaying vortex breakdown, or even lead to the recreation of the vortical core after breakdown has occurred. However, it should be kept in mind that the transition to the breakdown state is hysteretic and to re-establish the pre-breakdown state may require the swirl number to drop well below the critical value for the onset of breakdown. Currently in practice, this is achieved by altering the flow characteristics by either mechanical or pneumatic devices which are designed to increase the axial velocity via the injection of additional stream-wise momentum, hence lowering the swirl number and delaying breakdown. Since the pressure field also influences the breakdown process, it is possible to also use mechanical and pneumatic devices to change the entire pressure field and avoid adverse pressure gradients which slow the axial velocity and induce breakdown. As used in boundary layer separation control devices, suction can be used to control the position of the vortical structure and its associated breakdown state. By altering the local swirl number by imposing pressure gradients by means of diverging nozzles, Althaus et al. (1995), Escudier et al. (1982), Sarpkaya (1974) found that they could significantly control the occurrence and location of breakdown.

Unfortunately many reported studies contain mixed objectives. This leads to a situation in which the desired outcomes may be achieved but cannot be directly attributed

to only one of the many implemented mechanisms causing its occurrence. Hence, we require the need for a much more basic focused study with a great degree of control over a limited number of parameters. In addition Mitchell and Delery (2001) state that "often inspired by two dimensional reasoning, the identification or control action may be inadequate when applied to the three dimensional case in which the physics behind the flow is not yet well understood". This echoes what was previously found in vortex breakdown studies that two dimensional approximations may prove inadequate and as a result basic three dimensional vortex breakdown control studies are essential.

As the conditions which cause vortex breakdown are well known, when controlling a vortical flow, it is far more efficient and effective to apply a local rather than global action to manipulate the flow. In order to avoid breakdown, the implemented control mechanism must change the velocity distribution in such a way as to decrease the local swirl number. This is achieved by either increasing the axial velocity component by means of fluid injection, and/or decreasing the azimuthal swirling component by introducing a swirling flow in the opposite direction. It is however a lot more difficult to control the manipulation of vortices in comparison to controlling a boundary layer. This is due to the fact that boundary layers are attached to the surface, hence the area of concern is limited to a 2D plane whereas vortical structures are generally far from the surface from which they emanate, and therefore the area of concern is now in the confines of a 3D volume.

Mitchell and Delery (2001) stated that "vortex breakdown can be viewed as a brutal amplification of disturbances leading to an expansion of the flow structure (more or less like boundary layer transition). A promising way to control the phenomenon could be to introduce well-defined perturbations into the flow field by implementing unsteady blowing techniques. If a spectacular effect is to be obtained, the frequency of this pulsating action must be carefully adjusted to coincide with the natural frequencies of the vortex instabilities (eigen-frequencies). Interesting investigations of this type are currently being conducted with various authors having claimed to achieve control of the phenomenon with a reduced energy cost compared to continuous control techniques. The design of effective pulsating techniques requires a careful analysis of the fluctuating properties of vortical flows and of their stability limits in order to identify phenomena

that can be used as indicators for the application of a specific control technique." The focus of current investigations is to minimize the adverse effects of vortices by avoiding, delaying or repositioning their formation.

1.7.2 Effects of Pressure Gradients

As mentioned previously, many researchers (see for example Sarpkaya (1971a), Faler and Leibovich (1977a), Faler and Leibovich (1978), Mitchell and Delery (2001)) imposed a pressure gradient by confining the swirling jet within a diverging tube. The imposed pressure gradient is another factor upon which vortex breakdown is highly dependent. An adverse pressure gradient destabilises an otherwise stable vortex (i.e. vortex which is below the critical swirl number, and is not undergoing breakdown) as it causes a reduction in the axial velocity (due to the increase in pressure) and an increase in the local swirl number, which can cause breakdown if the critical swirl number is reached or exceeded. As expected, a favourable pressure gradient has the effect of stabilising the vortical flow even if it was previously unstable. The reverse effects of an adverse pressure gradient occur, such that even a vortex undergoing breakdown may be reversed and the reformation of the vortical structure occurs. However research has shown that the reformation process is subject to a high degree of hysteresis (see Billant et al. (1998), for example).

1.7.3 Effects of Temperature Gradients

Vortical flows and more so in flows experiencing vortex breakdown are found to be extremely sensitive to temperature gradients. Billant et al. (1998) reports that temperature differences of as little as 0.1°C between that of the vortical core and surrounding fluid has considerable effects on the resulting breakdown structure. This was also later confirmed in further experiments by Loiseleux and Chomaz (2003) who found that temperature

gradients can lead to a premature lose of axisymmetry of the swirling jet and alter the dominant mode from the axisymmetric m = 0 mode to m = +1 mode.

Herrada and Shtern (2003b), Herrada and Shtern (2003c) ran numerical simulations in an attempt to investigate the effects of temperature gradients in a closed container with a spinning lid. It was found that axial temperature gradients enabled either suppression or advancement of breakdown. A positive temperature gradient in which the convection assists the downstream motion of the vortical core suppresses breakdown while a negative temperature gradient advances breakdown and enlarges the breakdown bubble. Temperature gradients are found to have more of an effect on breakdown than increasing the Reynolds number.

Herrada and Shtern (2003a) conducted axisymmetric numerical simulations to examine the effects of applying an axial temperature gradient to a compressible ideal gas swirling flow undergoing a bubble type vortex breakdown in a closed cylinder with a rotating bottom disk. By varying the temperature gradient, Mach number, Froude number, Reynolds number and aspect ratio, they showed the prominent effects of temperature gradients on vortex breakdown. They found that a positive vertical temperature gradient (i.e. inducing thermal convective flow opposite to that of the base flow) causes the breakdown bubble to reduce in size and eventually disappear. However, negative vertical temperature gradients (i.e. inducing thermal convective flow in the same direction to that of the base flow) enlarge the bubble breakdown and causes unsteadiness in the flow. The mechanism which they attribute to this control method is centrifugal and/or gravitational convection due to density variations induced by the temperature gradients. The effects of temperature gradients are quite major with the authors stating that “these effects of centrifugal convection become more prominent with increasing Mach and Reynolds numbers and are more important for vortex breakdown control than those induced by the increase in Mach number”.

1.7.4 Control of Vortex Breakdown Over Delta Wings

Since most vortex breakdown control mechanisms have been experimentally implemented for the cases of swept wings or slender delta wings, it is beneficial at this point to describe the flow over such configurations and how the vortex forms. This will enable a greater understanding of the flow field to which the vortical structure and its subsequent breakdown state are subjected. It will also enable a more in-depth understanding of how the control mechanisms work and how they are affected by the flow field over a delta wing.

Generally the flow over swept wings or slender delta wings can be described as follows. Once the angle of attack passes a certain value, the flow travelling from the under-side (or high pressure side) of the wing to the upper most side (or low pressure side) of the wing, separates along a separation line located on the wing apex at critical points. This results in the rolling up of the separation surface and forms the primary vortex, which is fed by the vorticity which was previously contained in the boundary layer along the wing surface. As the vortex proceeds downstream along the wing, it continues to develop and intensify by the continuous injection of vorticity into the core, until the structure reaches the trailing edge. At an approximate angle of incidence of 20°, the maximum azimuthal velocity is approximately the same as the free-stream velocity. This high amount of swirl also induces an acceleration of the axial flow along the vortex core and the velocity can reach up to four times that of the free-stream velocity. The intense low pressure region caused by swirling motion on the low pressure side of the wing is what provides the additional lift known as vortex lift. When the angle of attack (α) is increased beyond a certain critical value (α_c), the primary vortex undergoes breakdown, which occurs at the trailing edge of the wing where an adverse pressure gradient is met. As the angle of attack is increased, the breakdown structure moves further upstream towards the leading edge. As with all types of vortex breakdown, the breakdown structure depends on free-stream conditions, the surrounding geometry (in this case the wing shape) and externally induced disturbances (such as the perturbations from the engine of an aircraft).

The primary vortex is found to be only slightly dependent on the Reynolds number as separation usually occurs along the leading edge of the wing. It should be noted that secondary and tertiary vortices are also created but are far less intense and have negligible influence on the primary vortex. However they are Reynolds number dependent due to the separation of the boundary layer, which gives rise to these vortices, occurring on the low pressure surface side of the wing. Hence the vortices depend on the local properties of the boundary layer at the point of separation (Mitchell and Delery (2001)).

In order to be able to advance to an effective closed loop system of vortex breakdown control, we require an understanding of the phenomenon's characteristics and the mechanisms which cause its occurrence and control its behaviour. This will enable researchers to find the critical parameters for which feedback systems may be based in order to achieve maximum efficiency and reliability. This requires an array of focused studies into the phenomenon and its control. Although countless studies have been conducted on vortex breakdown, there still remain points of controversy as to the differing observations and theories regarding this complex phenomenon which need to be resolved. Also from the control point of view, several open loop studies have been conducted, however the sheer amount of studies with mixed objectives leaves some doubt as to the individual effect(s) of the implemented control mechanisms.

1.7.5 Experimental Techniques to Control Vortex Breakdown

As mentioned previously, the majority of vortex breakdown over delta wing experiments utilising vortex breakdown/flow control techniques have had mixed objectives. As a consequence several of these studies do not directly distinguish what the exact effects on the vortical structure are when implementing the control mechanism(s). Instead, their analysis may be limited to the overall effects on aircraft performance such as the effects on the lift to drag ratio and stability. It is therefore essential to take care when comparing results as several factors may be in play and indistinguishable due to the complexity of some setups. Therefore only studies which directly refer to the effects of the control

mechanism on the vortex breakdown properties will be mentioned in order to maintain a basic and fundamental analysis. Where possible, an attempt will be made to clarify the exact effects on the flow field and breakdown properties which the control mechanism achieves.

Werle (1960) implemented four different techniques on the suction side of the wing to control the vortex breakdown location over delta wings, they include:

1. **Placing an obstacle downstream** of breakdown which moved the breakdown position upstream, due to the induced adverse pressure gradient.
2. **Applying suction downstream** of breakdown which delayed or eliminated breakdown from occurring by inducing a favourable gradient.
3. **Blowing upstream** in the opposite direction to the free-stream, had the effect of slowing the axial velocity of the vortex and causing breakdown to occur further upstream.
4. **Along the core blowing** delays breakdown by increasing the axial velocity.

Werle used a dimensionless momentum coefficient:

$$C_{\mu} = \frac{\dot{m}_b U_z}{P_{\infty} A_{wing}}, \qquad \textbf{(1.18)}$$

where m_b is the blowing mass flow rate, U_z is the jet exit velocity, P_∞ is the free-stream dynamic pressure, and A_{wing} is defined as the wing area, in order to quantify the amount of momentum added to the vortex by blowing. However it was found that the value of the momentum coefficient required to alter the breakdown location varied greatly ($10^{-3} \leq C_{\mu} \leq 10$) depending on the location and orientation of the applied along the core blowing. Other observations included the effectiveness of how both steady and unsteady control depended on the angle of attack (the induced pressure field) and wing properties (surrounding geometry).

Current methods of controlling vortex breakdown on aircraft are in the form of mechanical or pneumatic mechanisms or both. These control processes generally aim to alter the location of the critical points at which the vortices form, however as seen previously, vortices are also able to be controlled by altering the surrounding pressure

field or swirl number (i.e. velocity distribution). Examples of such devices include mechanical; strakes, canards, filets, leading edge extensions (LEXs), flaps and vortex fences and pneumatic; various configurations of suction and blowing both continuous and pulsed such as span wise blowing, azimuthal blowing, leading edge blowing, along the core blowing, trailing edge blowing, leeward surface suction, leading edge suction and suction along the vortex core.

1.7.6 Mechanical Devices

Mechanical devices for the control of vortices and vortex breakdown have been most predominantly used in the aircraft industry. Canards and strakes have been implemented on the Saab Viggen (Behrbohn (1965)) and F-16 (Smith et al. (1979)) aircraft, respectively. The vortical structures over the suction side of aircraft wings are essential in the production of non-linear lift.

1.7.6.1 Flaps and Variable Sweep Delta Wings

Rao (1979), Rao (1980) performed experiments on the effectiveness of leading edge flaps (see Figure 1.13) in the control of vortices. Rao (1980) stated that the "suction effect of coiled vortices generated via controlled separation over leading edge flap surfaces is utilised to produce an aerodynamic thrust component". Rao (1979) found that vortex flaps can be "an effective flow manipulator which can influence the efficiency and controllability of slender wings when operating in an aerodynamic environment governed by vortical flow structures". This shows that directly controlling the source of generation or altering the surrounding flow field of the vortex are effective means of controlling the phenomenon. Marchman and Grantz (1982) performed similar experiments using tapered leading edge flaps and confirmed Rao (1979), Rao (1980)'s results that leading edge flaps cause the vortex to form on that surface. Therefore the placement of protruding objects (e.g. flaps) at specific points in the flow field can allow the selective location of the formation of vortices.

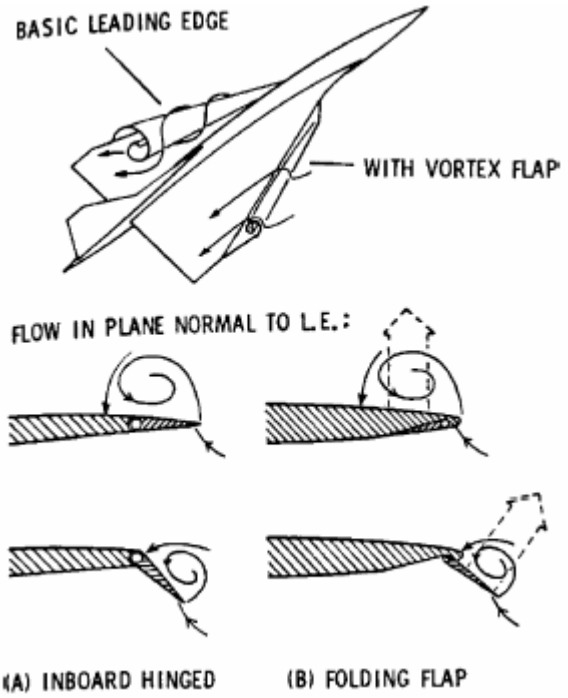

Figure 1.13: Two leading edge flap configurations used by Rao (1979), Rao (1980).

Rao and Buter (1983) performed experiments on an apex flap which is able to rotate about a span wise hinge (see Figure 1.14). An increase in the vertical deflection of this flap would increase the strength of the vortex, which formed at the apex of the flap. Pressure measurements along the wing surfaces showed that as the angle of attack of the apex flap is increased, the two vortices (one on each wing) merge together. Once again the altering of the pressure flow field and the point at which the vortical structure is created is an effective means of controlling the phenomenon and breakdown location. This study was extended by Klute et al. (1993) who also examined the effects of apex flaps at negative angles with respect to the wing surface. Their research found that both positive and negative apex flap angles produce a substantial delay in vortex breakdown, with maximum delay occurring at negative 15 degrees. This shows that increasing the favourable pressure gradient in the vicinity of the vortex causes an increase in axial velocity and a delay in the vortex breakdown formation and location.

Cavity flaps on delta wings, which consist of a flap that extends from the leading edge of the delta wing (see Figure 1.15) were investigated by Schaeffer et al. (1993). Cavity flaps delayed the vortex breakdown location and shifted the structure towards the

inboard location, by altering the axial and span wise pressure field. The cavity flaps were found to be more effective in steady flow cases, than unsteady cases and in both flow cases provided a stabilising effect on vortical structures.

Trailing edge flaps on a 55 degree sweep angle delta wing were investigated by Pilkington and Wood (1994), with both a fixed flap configuration of ±10 degrees and oscillating flap configuration of ±5 degrees. From pressure measurements along the wing surface, they found that positive flap angles caused the breakdown location to move further upstream, due to an increase in the adverse pressure gradient. They concluded from their studies that trailing edge flaps could produce strong local pressure gradients while having little effect on the overall flow field.

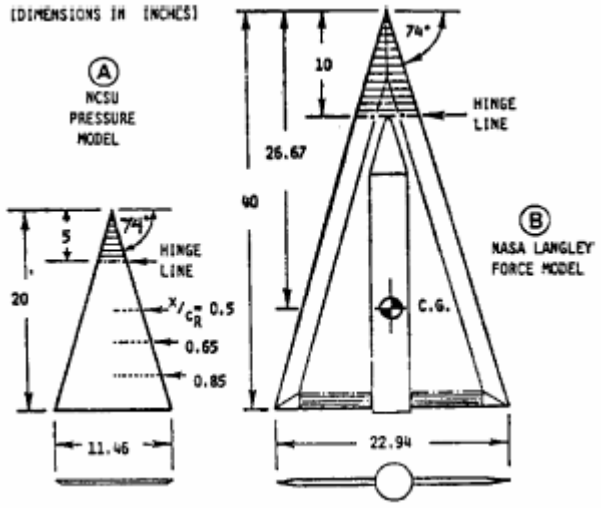

Figure 1.14: Apex Flap as used by Rao and Buter (1983).

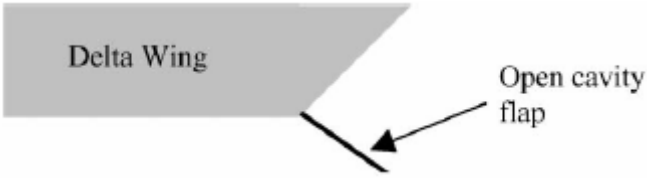

Figure 1.15: Cavity flap used by Schaeffer et al. (1993).

Gursul et al. (1995b) also tested oscillating flaps, however the difference in this case was that they were leading edge flaps with a positive and negative angle of deflection of 180 degrees rather than trailing edge flaps (see Figure 1.16). They also went

on to test a mechanical configuration which allowed the sweep angle of a delta wing to vary from 60 to 70 degrees (see Figure 1.16). Gursel et al. found that leading edge devices were the most appropriate in controlling vortex breakdown and stated that "all vorticity of the leading edge vortices originates from the separation point along the leading edge; therefore, leading edge devices are attractive tools to influence the strength and structure of these vortices". The flaps create an adverse pressure gradient in the span wise direction, hence increasing the size of the breakdown structure. The oscillating flaps produce a time lag response similar to that seen on pitching delta wings. Experiments using the variable sweep angle design showed that the breakdown location could be varied monotonically with the sweep angle (Mitchell and Delery (2001)).

Gursul et al. (1995a) took a further step in the development of the variable sweep angle design by implementing a closed loop control which used the pressure at 90% of the root chord as the feedback variable. The closed loop controller's task was to maintain constant pressure amplitude at the pressure transducer location by varying the sweep angle, which controlled the vortex breakdown location.

Deng and Gursul (1996) used Laser Doppler Velocimetry (LDV) to find the exact effects of leading edge flaps. They found that by varying the angle of the leading edge flaps they were able to control the breakdown location. The flaps produced an adverse pressure gradient in the span wise direction by altering the region at which the flow separates.

Panton (1990) conducted experiments on a 65 degree delta wing with an apex extension of a greater sweep angle than that of the basic delta wing. This configuration enabled them to test the influence of a decrease in the total pressure or increase in the vorticity of the vortex core. This leading edge modification increases the core vorticity and delays vortex breakdown. They also found that decreases in total pressure in the core caused vortex breakdown to occur further upstream.

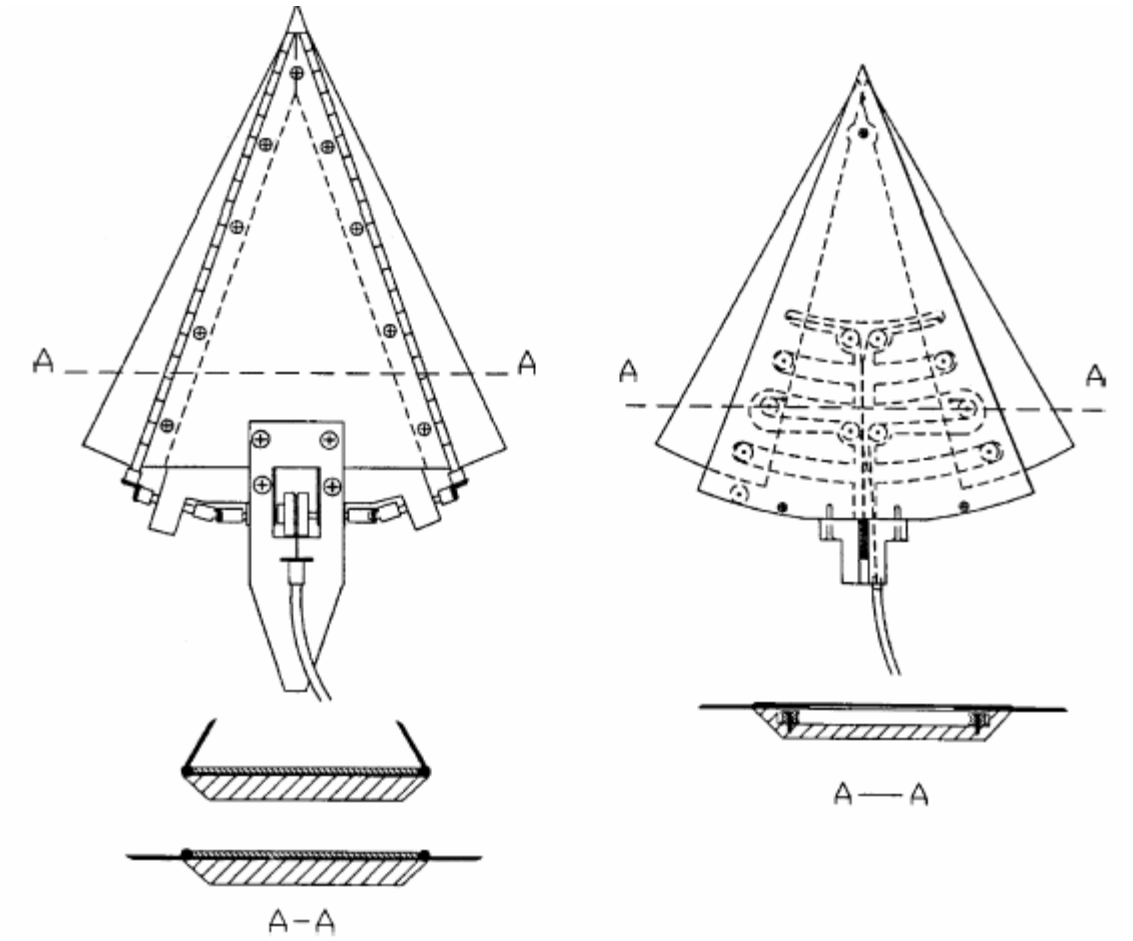

Figure 1.16: Leading edge flaps (Left) and variable sweep delta wing (right) designs used by Gursul et al. (1995b).

Cheng and Lu (1993) tested the forced oscillation of leading edge vortex flaps on delta wings as a means of suppressing vortex breakdown. Their water tunnel flow visualisation reveals that, under forced disturbances, there are two types of concentrated vortex breakdowns, which in turn can be divided further into six patterns. The unsteady concentrated vortex breakdown may involve a process of switching among several breakdown patterns, with the effects of vortex flap oscillations on vortex breakdown being closely related to the sweep angle of the delta wing. An increase in the sweep angle leads to this control technique being less effective and possibly having adverse effects. The oscillations of the vortex flap were found to delay breakdown for delta wings with a sweep angle of 50 degrees, while for a sweep angle of 70 degrees the oscillations would become detrimental to the vortex breakdown and advance the breakdown position further

upstream. Overall the vortex flap was found to alter the vortex breakdown state and shift the path of the vortical core so as to align it parallel to the leading edge.

Schaeffler et al. (1993) tested vortex cavity flaps as a means of delaying vortex breakdown over delta wings at high angles of attack. Surface pressure measurements at various angles of attack revealed along with LDV mapped out the flow field over the delta wing at an angle of attack of 35 degrees. It was found that for a 70 degree swept delta wing, cavity flaps can delay the appearance of vortex breakdown over the wing to higher angles of attack than the uncontrolled case.

Xu and Wang (2002) experimentally examined the effectiveness of apex flaps to control the vortex breakdown on a 70 degree sweep angle delta wing. The angles of attack ranged between 30 and 50 degrees. The two main factors which control the effectiveness of this technique include the flap angles and their length. Flow visualisation results show that vortex breakdown can be delayed by drooping the apex flap which effectively lowers the angle of attack. They found that the larger the flap, the more effective it was at delaying breakdown.

Kuo and Rockwell (1991) studied one degree sinusoidal perturbations of the angle of attack of the aircraft. The study concentrated on investigating the vortical flow structure upstream and downstream of vortex breakdown over a delta wing with controlled wing motion via qualitative flow visualisation in conjunction with quantitative velocity measurements. They found that this technique can substantially alter the vortical flow structure of the leading edge vortices above a highly swept delta wing. The change in the vortex structure and breakdown location is dependent upon the “instability of the separating shear layer that feeds into the large scale leading edge vortex at different exciting frequencies, variations of the magnitude and phase distributions of the fluctuating axial and swirl velocity components across vortex core, alteration of spectral content of the vortex core in the pre-and post-breakdown region”.

Lowson and Riley (1995) examined the effects of various delta wing geometries on the vortex breakdown location. They found that the Reynolds number had little effect and it was the geometry of the wings, particularly the apex, which is the most important factor in determining the position of vortex breakdown.

1.7.6.2 Strakes, Wing Fillets and Co-Axial Wires

Hebbar et al. (1994) examined the influence of strakes and wing fillets on vortex core trajectories and vortex breakdown locations in water tunnel tests using double delta wing models. Their results showed that if both strakes and wing fillets are introduced then the vortex cores are found to interlace at low angles of attack, while at high angles of attack the vortices maintain their separate paths. Diamond fillet configurations proved to be the most effective means of delaying the vortex breakdown location and vortex interaction of all the fillet configurations tested.

Akilli et al. (2003) used a small diameter wire (1% of the vortex core diameter) which was tethered from the apex of a delta wing and aligned with the centreline of the leading edge vortex to control the location and onset of vortex breakdown. PIV results allowed him to come to several conclusions on the effectiveness of this technique. At several angles of attack ranging from 15° - 35°, it was possible to displace the vortex downstream by as much as one chord length. The movement in breakdown position downstream, was highly dependent on the length of the wire up to a length ratio (defined as the length of the wire to the wing chord length) of 1.1 was attained, at which point further increases in the tethered wire had no effect. For cases in which breakdown had not yet occurred, the tethered wire had the effect of causing the azimuthal vorticity to switch sign and induce a wake-like region in the downstream portion of the vortex core.

1.7.6.3 Mechanical Controls in Confined Flows

A vortex breakdown control study in a closed cylindrical container set up (see Figure 1.17) in which a rotating end disc drives the base flow was conducted by Husain et al. (2002). The control technique consisted of applying an independently co-rotating or counter-rotating thin cylindrical rod on the vortex axis with the with rod radius << disk radius. They found that “co-rotation is adequate to totally suppress vortex breakdown, whereas counter-rotation increases the number and size of vortex breakdown "bubbles" and makes the flow unsteady”. They extended this limited case to say that their results “suggest that an additional co-rotation or counter-rotation, applied near the vortex axis, can be effective in suppressing or enhancing vortex breakdown in practical flows”.

Mununga et al. (2004) used a small rotating disk in a closed cylindrical container with a rotating lid to successfully control the occurrence and structure of breakdown. Co-rotation of the small bottom disk was found to prematurely induce the onset breakdown, shift the breakdown structure further upstream and increase the dimensions of the bubble, both axially and radially. Counter-rotation caused a delay in the onset of breakdown and reduced the size of the bubble. Counter-rotation had the ability to shift the bubble downstream or even completely suppress it.

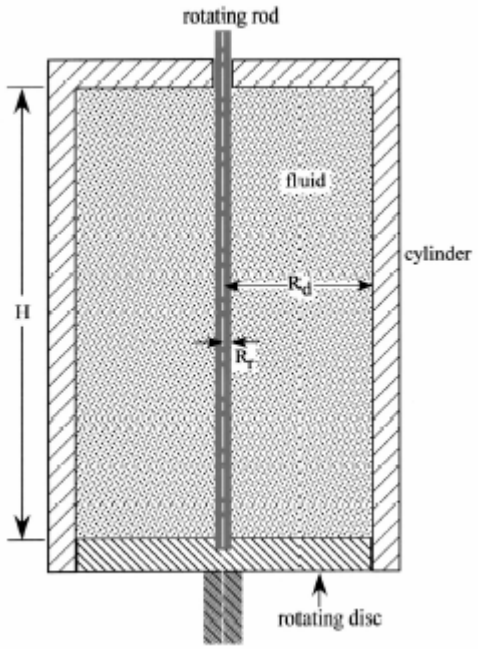

Figure 1.17: Closed cylinder with a rotating end wall and independently rotating rod used by Husain et al. (2002).

1.7.7 Pneumatic Techniques

This section covers several different pneumatic control techniques which involve blowing and suction at different locations, combinations and angles to the free-stream flow and vortex. Werle (1954) was the first to pioneer a variety of pneumatic control techniques in an attempt to control vortical flows and their locations. Werle found that blowing downstream along the core delayed or eliminated breakdown, while blowing upstream

caused breakdown to impulsively occur or to move further upstream. He demonstrated that the type of blowing or suction and its direction are critical in the control of breakdown, among other factors which include:

- Mass flow rate of the blowing or suction (generally expressed in terms of the non-dimensional momentum coefficient, C_μ , or suction coefficient, C_s).
- The type of blowing or suction (pulsed or continuous) and the combination and geometrical arrangement and dimensions of the suction and/or blowing holes.
- The surrounding flow field and boundary conditions.

The pneumatic techniques implemented over the years are generally classified into four distinct groups; suction, blowing, steady and unsteady.

1.7.7.1 Suction

Lambourne and Bryer (1961b) used suction as a means of controlling the vortex breakdown location over sharp edged swept wings. These experiments verified earlier results by Werle that by applying suction at the trailing edge of the wing, it is possible to eliminate breakdown entirely due to the induced favourable pressure gradient which suction at that location provides. This favourable pressure gradient was verified by pressure measurements conducted by (Hummel 1967) on a similar configuration, which utilised suction at the trailing edge to control the breakdown location. The favourable pressure gradient caused an increase in the axial velocity of the vortical core which lowered the local swirl number and inhibited breakdown from occurring Mitchell and Delery (2001).

After observing Dixon (1969)'s experiments of span wise blowing, Cornish (1970) stated, "the vortex downstream of a separation point could be fixed and not shed if sufficient vorticity could be removed from its core". This led to the possibility of applying suction at the wing/flap junction as a means of delaying breakdown. However instead of applying suction, he applied span wise blowing in an attempt to provide the required suction via entrainment. Cornish showed that pulsed or continuous suction was an effective means of stabilising vortex cores and delaying or eliminating breakdown. Cornish (1983) went on in a later paper to say that "if it is possible to use a power source

such as compressed air, suction, vibration, or even acoustics, then it is possible to obtain an impressive degree of control of vortex flow".

Parmenter and Rockwell (1990) applied localised suction downstream of vortex breakdown and found that this delayed the breakdown location by stabilising the vortex. They also studied the time response of the vortex and breakdown structure once suction was suddenly applied. They non-dimensionalised their results by a so called suction coefficient (similar to the momentum coefficient) defined as:

$$C_s = \left(\frac{U_s}{U_\infty}\right)^2 \left(\frac{A_s}{A_{wing}}\right), \qquad \textbf{(1.19)}$$

where U_s is the suction velocity, U_∞ is the free-stream velocity, A_s is the suction area and A_{wing} is defined as the wing area.

The suction coefficient required to stabilise and delay breakdown was dependent upon the distance from the vortex breakdown, i.e. the closer the suction to the breakdown, the lower the required suction coefficient. The response time of the breakdown state was defined as the time from the application of suction until the vortical structure was stabilised. Parmenter and Rockwell (1990) also analysed the response time for a sudden end in the suction until the vortical structure was stabilised. They used the following time response parameter:

$$T_r = \left(\frac{tU_\infty}{c}\right), \qquad \textbf{(1.20)}$$

where, t is the period of time suction is applied, U_∞ is the free-stream velocity and c is defined as the root chord length. As found in several studies of vortex breakdown structures, there was a large degree of hysteresis which in this case was linked to the amplitude of the suction coefficient, found by Parmenter and Rockwell (1990).

Owens and Perkins (1995) proposed another definition for the suction coefficient which they defined as the ratio of mass flux through the suction holes to that of the free-stream velocity. By applying suction to the boundary layers of delta wings (see Figure

1.18), they were able reduce the adverse pressure gradients in these regions and displayed the ability to control both the point at which the vortex is formed and its corresponding breakdown location. The results showed greatest promise when suction was applied upstream of breakdown along the leading edge and downstream of breakdown along the trailing edge.

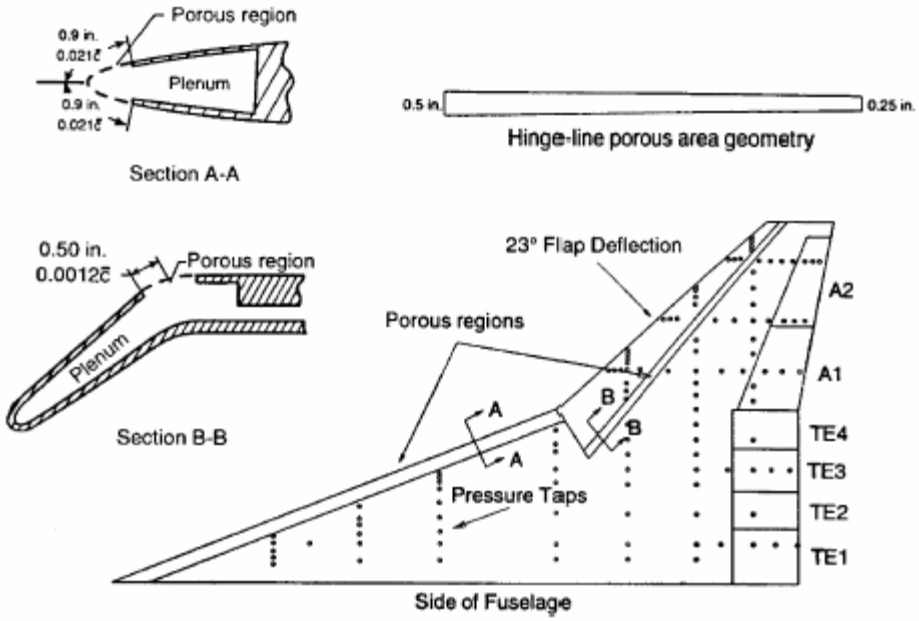

Figure 1.18: Delta wing model with suction ports used by Owens and Perkins (1995).

Controlling vortices and breakdown via suction was also implemented by McCormick and Gursul (1996) on the leading edge of delta wings. They found that by applying suction near the point of vortex conception (i.e. where the shear layer separates) caused a change in the vortex structure (i.e. velocity distribution) and a movement in the breakdown position further downstream as suction was increased. However the effects of suction were only capable of controlling the breakdown location and were limited to certain spatial limitations at which point any further increase in suction no longer moved the breakdown location further downstream. The limited spatial effects of suction were also demonstrated when the authors applied suction to only one side of the delta wing and found that it had no effect on the vortex on the opposite side, from which they concluded that suction can be used independently to control each separate breakdown structure.

Suction altered gradients in all three Cartesian planes causing the structure to also move in all three planes. Velocity measurements showed that as the suction was increased, axial vorticity also increased. This increase in axial vorticity was due to the reduction in vortex core size when suction is applied and is an expected effect when considering that angular momentum must be conserved. Suction was also applied to a location further downstream than the leading edge and showed adverse effects in that the breakdown location moved further upstream as the suction was increased, due to an increase in the adverse pressure gradient. Interpreting these results reveals that the optimum location of suction can be anywhere upstream of breakdown or at the point of vortex formation and anywhere downstream of breakdown in order to induce a favourable pressure gradient.

McCormick and Gursul (1996)'s results were also verified by Maines et al. (1999), who performed similar experiments by applying suction from the leading edge of a delta wing all the way downstream to 68% of the wing chord via an arrangement of holes. The arrangement also applied suction to both the suction side and pressure side of the delta wing. As expected from McCormick and Gursul (1996)'s results, it was found that applying suction on the suction surface caused breakdown to move further upstream while applying suction to the pressure side had the opposite effect and moved downstream. The effectiveness of suction in the control of breakdown was highly dependent on the angle of attack (i.e. the imposed surrounding pressure field) along with the spacing of the holes from the leading edge. Their results showed that for the same mass flow rate, suction applied to the first 18% of the wing chord was more effective at controlling vortex breakdown than applying suction along the entire 68% of the chord. Maines et al. (1999) attributed this finding to the fact that for the same mass flow rate, the suction momentum would increase if applied through fewer holes.

1.7.7.2 Trailing Edge Blowing

Trailing edge blowing has been investigated by Legendre (1954) who found that the mass flow rate and the angle of the jet were crucial parameters in the effectiveness of such a configuration. He also examined the extent of the flow region in which the jet could provide some influence, and found that jets were only effective in the immediate region

near the exit, while away from this region the jet flow velocity quickly dissipated into the free-stream flow.

Werle and Fiant (1964) modelled a Concorde in a water tunnel with its turbojet engines represented as water nozzle jets at the trailing edge of its wings. They conducted these experiments at several nozzle jet velocity ratios which they defined as the ratio of jet velocity to free-stream velocity. They found that the engine's exhaust (i.e. trailing edge blowing) delayed the formation of the leading edge vortex (and secondary vortices) along with the elimination of breakdown on the suction side of the wing. This confirms the idea that trailing edge blowing can provide significant control of both vortices and their corresponding breakdown states.

Another investigation into trailing edge blowing (or jets) on delta wings by Helin and Watry (1994) was conducted in order to examine its effects on the vortex breakdown location. The jets (located on the trailing edge of the delta wing) came from 2 rectangular nozzles with an aspect ratio of 8:1 and the velocity ratio (as previously used by Werle and Fiant (1964) was varied between 0 and 8. Helin and Watry (1994) found that the breakdown location moved further downstream (a maximum of 18% of the vortex core) as the velocity ratio was increased while the vortex core remained along the same spatial path regardless of the velocity ratio. Using the same delta wing model and velocity ratios, Nawrocki (1995) experimented with the effect of changing the angle of the jets between ±45° upward or downward with respect to the trailing edge. Results showed that the breakdown could be delayed to a position equivalent to 40% of the wing chord at an upward jet angle of +45° and velocity ratio of 8, due to its increased effects of decreasing the adverse pressure gradient. These results were confirmed by Shih and Ding (1996) who conducted similar experiments on a 60 degree sweep angle delta wing with two rectangular nozzles (aspect ratio 9.6:1) at the trailing edge with velocity ratios ranging between 0 and 7.3. They investigated the effects of changing the jet angle (between 30 degrees upwards and 45 degrees downward with respect to the trailing edge) on vortex breakdown. They found that even at a zero degree jet angle, the vortex breakdown was delayed by 10% of the wing chord regardless of the angle of attack. For the same mass flow rate, even better results were obtained as the downward jet angle is increased. In fact the effect was so significant that the breakdown location was moved

downstream by 58% of the root chord at a downward jet angle of 45 degrees and a velocity ratio of 7.3. The authors stated that trailing edge blowing lowered the adverse pressure gradient at this location, which is the primary cause for breakdown to occur.

Trailing edge blowing via jets on a 75 degree sweep angle delta wing was investigated by Mitchell et al. (1999a) as a means of controlling the vortex breakdown location. The authors experimented with angles of attack ranging between 20 and 40 degrees and velocity ratios of 0 to 15. Although similar to previous investigations, they were able to control the breakdown location via this method of control, they found that the highest velocity ratio of 15 had an adverse effect and caused the breakdown location to move upstream. Mitchell et al. (1999a) believed that this was due to the fact that a high jet velocity of this magnitude created an "obstacle like effect" causing an adverse pressure gradient which overcame the advantages of entrainment effects that jets provide. As was previously found in experiments on suction by McCormick and Gursul (1996), Mitchell et al. (1999a) also established that blowing can independently control the breakdown location on one side of the wing without affecting the flow field on the other side of the wing.

1.7.7.3 Leading Edge Blowing

Alexander (1963) attempted to control secondary vortices on a 70 degree sweep angle delta wing by applying leading edge blowing at an upward angle of 40 degrees from the wing surface. The jets were configured in such a way as to linearly increase the momentum along the leading edge, with zero momentum at the wing apex. He non-dimensionalised the momentum added to the flow by creating the blowing momentum coefficient (as previously defined). Alexander (1963) found that by applying blowing on the suction surface of the wing, he was able to eliminate the creation of the secondary vortices by eliminating the separation of the flow. However there was a minimum threshold of the blowing momentum coefficient required to attain this control and increased with angle of attack. This technique showed only minimal effects on the primary vortices which are generally of most concern. Leading edge blowing over delta wings was also implemented by Spillman and Goodridge (1972), with the jets orientated

at 40 degrees to the free-stream. Their results verified that of Alexander (1963) and it was found that they could control the axial velocity and swirl velocity of the vortex by adjusting the jet momentum and angle.

LDV measurements examining the effects of leading edge blowing on the vortical structure was conducted by Visser et al. (1988). Their results revealed that the swirl angle (or swirl number) of the vortical core was reduced for high jet mass flow rates which caused an increase in the axial velocity along the outer radial region of the vortex core and decrease in the azimuthal velocity. The optimum nozzle location and angle were found to be at a point close to the wing apex where the vortex originates and at an angle parallel to the leading edge. Several blowing momentum coefficients were examined at this location. It was found that as the blowing momentum coefficient is increased so too is the downstream distance at which breakdown occurs, hence verifying the results of similar previous investigations outlined in the literature. They also verified the existence of a time delay between the implementation of blowing and its effect on the breakdown structure and its location.

1.7.7.4 Span Wise Blowing

Dixon (1969) experimented with span wise blowing over the suction side of the wing, which he believed could control the vortex motion, as the span wise jets would be entrained in the vortex and alter the angle at which the vortex proceeds downstream in proportion to the momentum added to the flow. The most effective nozzles were those which provided high exit velocities, which were achieved by the use of small nozzle cross sections or by providing high pressure jets. The ability to control the vortex dynamics and associated breakdown state was also found to be highly dependent upon the position and orientation of the nozzles. Dixon et al. (1978) went further and found that the most effective jet was one which had an exit velocity equal to the free-stream velocity normal to the jet. They also found that at transonic speeds the blowing momentum required to control vortex breakdown was similar to that required at lower speeds, hence there was added energy cost.

Testing of span wise blowing using small high velocity jets on a 60 degree sweep angle delta wing was implemented by Satran et al. (1985). Their experiments revealed the ability to control the primary vortex and breakdown structure. By adjusting the mass flow rates through the jets along with the axial location and symmetrical nature of the jets, they were able to increase the strength of the vortex and delay vortex breakdown. The vortex breakdown location moved further downstream as the mass flow rate through the jets was increased.

Hites et al. (2002) studied the effects of oscillatory jets (suction and blowing) exiting through span wise slots along a NACA 0015 airfoil. By examining the pressure and lift coefficients along with the wake velocity profiles at fixed oscillatory blowing momentum coefficients and various frequencies, they were able to gain insight into the advantages of pulsed blowing. Their results demonstrated "the effectiveness of pulsed blowing as a tool to increase lift and reduce drag (by enhancing the wake profile), especially when compared to the relative ineffectiveness of steady blowing under similar conditions". Several other investigators (such as Hong et al. (1996)) investigated span wise blowing and concluded that this control technique has the ability to delay vortex breakdown and is a function of the blowing momentum coefficient.

Johari et al. (1995) investigated recessed angled span wise blowing in a water tunnel on a bevelled 60 degree delta wing. The blowing configuration consisted of three pairs of blowing ports, located on the suction side of the wing and beneath the vortex core, which were canted upward in the span wise direction such that the injected flow was parallel to the bevelled edge. Flow visualisations using dye injection revealed that they could delay the vortex breakdown location by up to 15% of the chord, at an angle of attack of 22 degrees and a blowing coefficient of 0.05 with the blowing ports located downstream of breakdown at 43% of the chord. They found that "blowing from a port downstream of the natural burst location delayed vortex breakdown, whereas blowing upstream of the natural burst prompted vortex breakdown at the blowing port". They believed the findings could be explained via Rayleigh's stability criterion for circular flow.

1.7.7.5 Span Wise Blowing Parallel to the Leading Edge

A similar technique to span wise blowing was implemented by Bradley and Wray (1974) in which blowing was applied over the delta wing surface at an angle parallel to the leading edge. Their results showed that this technique delays vortex breakdown at high angles of attack and its effectiveness increases as the jet momentum is increased. This method is able to stabilise the vortex by increasing the axial velocity and hence lower the swirl number, which is especially necessary near the trailing edge of the wing where the flow is met with an increasing adverse pressure gradient.

Span wise blowing parallel to the leading edge over delta wings of various sweep angles was also conducted by Campbell (1976). The positioning of the jet was found to be crucial in the ability to optimally control the vortex and breakdown structure. Campbell found that the optimal position of the jet is that which coincides with the point at which the vortex originates, due to the jet's ability to control the flow at close proximity before its quick dissipation.

Seginer and Salomon (1983) also experimented with span wise blowing parallel to the leading edge on a 60 degree sweep angle delta wing model. They found that varying the vertical position of the nozzle had little effect, while the optimum stream-wise position was found to be 10% of the root chord from the leading edge. This study was extended by Er-El and Seginer (1986) who found that the effectiveness of the blowing jets was inversely proportional to the distance between the jet and the vortical core. They found that if the nozzle exit was close to the vortical core then the jet entrained within the vortex core and the added momentum stabilised both the vortex and breakdown structure. This stabilising effect was reduced as the nozzle distance from the vortex increased as the dissipating jet now enclosed the vortex core. This behaviour was investigated via pressure measurements on the surface of the wing which revealed that the jets created a low pressure region below the vortical structure and caused a reduction in the size of the vortical core.

Iwanski et al. (1989) used LDV to examine the effects of span wise blowing parallel to the leading edge on the vortical structure at various blowing momentum coefficients. The model consisted of a 70 degree sweep angle delta wing at an angle of incidence of 30 degrees. The results showed that this technique was able to delay

breakdown by altering the swirl angle of the vortex as the added momentum increased the axial velocity and decreased the swirl velocity, as previously seen in similar experiments. The vortex core was also found to increase in size due to its entrainment of the blowing jet.

Both steady and pulsed span wise blowing parallel to the leading edge was conducted by Johari and Moreira (1996) in an attempt to control leading edge vortices over delta wings. The nozzles were located at 40% of the root chord downstream of the leading edge. This technique not only delayed breakdown but also damped the oscillations of the breakdown structure, as well as enlarging the size of the vortex which encased the blowing jet. Pulsed blowing proved to be far greater in effectiveness than continuous blowing when it came to delaying breakdown both in static and pitching delta wing cases. Pulsed blowing delayed breakdown by 20% of the root chord in comparison to only 11% via continuous blowing for the static wing case. The most effective pulsing frequency in delaying breakdown was that which matched the natural shedding frequency of the shear layers. The response of the breakdown was also found to lag the pulsing jet. Further advantages of unsteady pulsing or blowing include reduced energy use and the ability to maintain an unchanged mean jet momentum or mass flow as required/desired.

1.7.7.6 Along the Core Blowing

As mentioned in a review paper by Mitchell and Delery (2001), Werle was the first investigator to implement blowing as a means of controlling breakdown. Werle found that along the core blowing delayed or eliminated breakdown while blowing upstream caused the breakdown to occur or move further upstream. Further experiments by Werle in 1971 investigated along the core blowing by placing a probe at the mid chord of a delta wing downstream of the vortex breakdown. Werle found that as he applied along the core blowing, the breakdown structure either moved further downstream, or was eliminated with the re-formation of the vortex which aligned itself with the direction of blowing (see Figure 1.19). A similar experiment by Reynolds and Abtahi (1989) was conducted in an attempt to control the location of vortex breakdown by using a probe to apply along the

core blowing to the vortex structure. Breakdown was found to move downstream of the applied blowing and never passed upstream of the blowing jet.

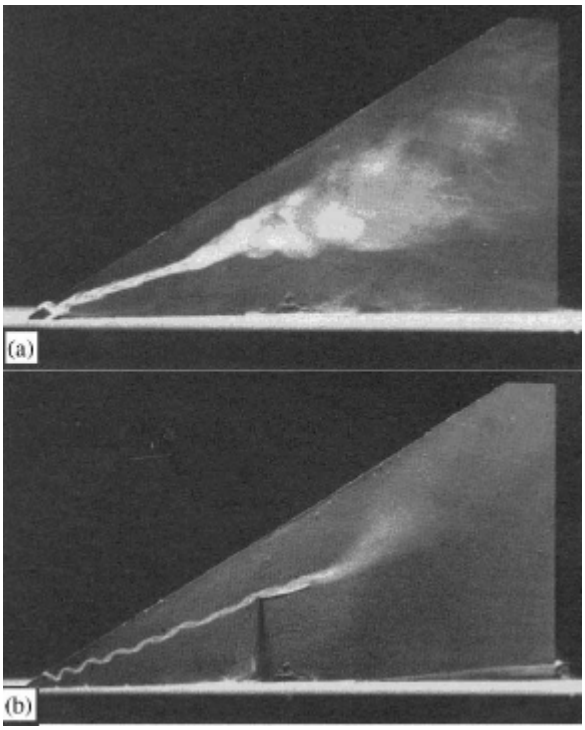

Figure 1.19: (a) No blowing case and (b) along the core blowing via a probe situated at mid chord of a 60 degree delta wing with C_μ = 0.5, as used by Werle (1971).

Along the core blowing was conducted on a 45 degree sweep angle delta wing in a water tunnel running at a free-stream velocity of 11cm/s by Owen and Peake (1986) to test its effect on vortex breakdown. They experimented with various momentum coefficients ranging from $0 \leq C_\mu \leq 0.14$. It was found that for a momentum coefficient of less than 0.05, breakdown was delayed or reversed by stabilising the vortex, through the addition of axial momentum which is in deficit and is the initial cause of breakdown. Another interesting finding was that at the optimal blowing momentum coefficient of 0.5, the periodic fluctuating motion of the reversed flow region just downstream of breakdown was eliminated and the swirl velocity of the vortex core was halved, hence reducing the swirl number dramatically and creating a profound stabilising effect. However, adverse effects on the vortex and breakdown location were experienced for

along the core blowing with $C_\mu > 0.05$, due to the creation of a radial instability in the vortex core.

The effects of along the core blowing in controlling vortex breakdown over a delta wing was investigated by Pagan et al. (1988) and Pagan et al. (1990) using flow visualisation techniques, pressure probes and LDV to quantitatively and qualitatively characterise the observed flow field. Three different nozzle diameters were used (see Figure 1.20a) along with three different nozzle configurations (see Figure 1.20b). Their results show that for the same mass flow rate, faster exit velocities from the along the core blowing jet had the greatest effect in delayed breakdown by providing the maximum reduction in the swirl angle (i.e. the smaller diameter nozzles were the most effective in the delay of breakdown). The technique of along the core blowing was also found to have only a minor effect on the azimuthal velocity profile. Two of the nozzle configurations used by Pagan et al. included blowing perpendicular to the vortex core, both in the same direction as the rotation of the vortex and in the opposite direction. This was achieved by using four nozzles directed at 90 degrees to each other. Normal blowing was also implemented by using two nozzles pointed in the opposite direction to one another. All three cases showed that blowing normal to the vortex core caused breakdown to move further upstream due to their effect of lowering the axial velocity of the vortical core. This effect was much more pronounced for jets orientated in the same rotational direction as the vortex.

Further investigation into along the core blowing was conducted by Pagan and Molton (1990) using a model similar to the aforementioned experiment and analysed using LDV. They characterised the various blowing mass flow rates via the blowing momentum coefficient. Results showed that low blowing momentum coefficients ($C_\mu \leq 0.05$) had negligible effect on the vortex while $C_\mu > 0.4$ increased the axial velocity of the vortex core dramatically (by up to 12%), hence delaying breakdown by lowering the local swirl number (or swirl angle). In all cases of along the core blowing, the azimuthal velocity profile was unaffected. This experiment also verified the importance of the ratio of the azimuthal to axial velocity (or swirl angle) as a prognostic parameter for the onset of breakdown, by showing that an increase in the axial velocity stabilised the vortical structure and delayed breakdown.

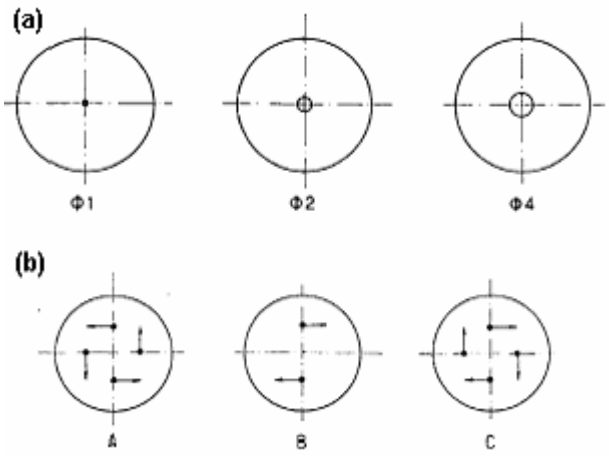

Figure 1.20: (a) Various nozzle diameters (mm) and (b) Various nozzle configurations; A: Co-rotation and B & C: Counter-rotation as used by Pagan et al. (1988) and Pagan et al. (1990).

The effects of along the core blowing on a leading edge vortex formed over a 70 degree sweep angle delta wing was investigated by Afchain and Deluc (1992), Laval-jeantet (1993). The blowing nozzle was placed in the wing apex region at 14% of the root chord downstream from the leading edge. They characterised the flow field via three dimensional LDV and laser sheet visualisations. Their results showed that by implementing along the core blowing, the vortex breakdown structure would move downstream in proportion to the blowing momentum coefficient used. Hence their results agree with previous investigations and show that this control technique is an effective means of controlling vortex breakdown.

Along the core blowing along a 75 degree sweep delta wing was investigated using LDV and pressure taps along the wing surface by Kuo et al. (1997). The jet was located at the wing apex at the wing fuselage junction and the jet momentum was non-dimensionalised by their definition of the blowing momentum coefficient (a similar definition to that of Parmenter and Rockwell (1990)'s suction coefficient) defined as:

$$C_{\mu} = \left(\frac{U_j}{U_{\infty}}\right)^2 \left(\frac{A_{wing}}{A_j}\right), \qquad \textbf{(1.21)}$$

where U_j is the jet exit velocity, U_∞ is the free-stream velocity, A_j is the jet exit area and A_{wing} is defined as the wing area. They also used a similar definition to Parmenter and Rockwell (1990)'s time response parameter to define their convective time scale (c/U_∞, where c is the root chord length) to aid in characterising the vortex structures temporal and spatial development as blowing is applied. The angle of attack was set to 40 degrees and along the core blowing was applied as an impulse function with a blowing momentum coefficient of 0.008 and lasted 0.6 of the convective time scale. Results showed that once the impulse is applied, the breakdown structure moves downstream before gradually returning to its original undisturbed position. Throughout this process, the breakdown structure oscillates axially. The authors found that the vortical structure upstream of breakdown is easily influenced by along the core blowing and is more effective than applying blowing to the outer extremities of the vortex. This is mainly due to the fact that the strongest adverse pressure gradient exists along the vortex core, therefore along the core blowing adds axial momentum to this region and overcomes the velocity deficit due to this pressure gradient. The authors stated that "the vortex core before breakdown, served as a transmitting vessel that steadily delivered the supplied momentum to overcome the strong adverse along the core pressure gradient".

Kuo and Lu (1998) went further to examine the effects on the axial and swirl velocities when brief bursts of along the core blowing are applied. Their results were obtained via LDV at various planes perpendicular to the flow. Kuo and Lu showed that the axial velocity within the vortical core reaches a local maximum then minimum as soon as the blowing was applied and stopped, while the swirl velocity experienced negligible change throughout the whole process. However it is interesting to note that the maximum swirl angle before, after and during blowing did not change significantly, even as the breakdown structure moved downstream.

Another investigation of along the core blowing was conducted by Guillot et al. (1998) on a half model 60 degree delta wing and fuselage model (see Figure 1.21). The aim of this study was to ascertain the most effective jet location, angle and blowing momentum coefficient to obtain a maximum delay in the vortex breakdown location. Axial velocity measurements obtained via one dimensional LDV revealed that the most effective jet angle was 12 degrees inboard of the vortex core. This optimum angle

achieves the greatest delay in breakdown as the "azimuthal velocity of the vortex at the surface of the wing deflects the jet towards the leading edge. If the jet is initially rotated slightly inboard of the vortex core, the azimuthal flow of the vortex will bring the jet into the core where it is most effective". The most effective nozzle location was near the apex of the wing, and the most effective blowing momentum coefficient was 0.007 for this particular set up. This optimum setup produced a delay in breakdown by up to 35%. Yet again, along the core blowing proved to be an effective means of delaying breakdown and stabilising the vortex core, but did not considerably alter the vortex path.

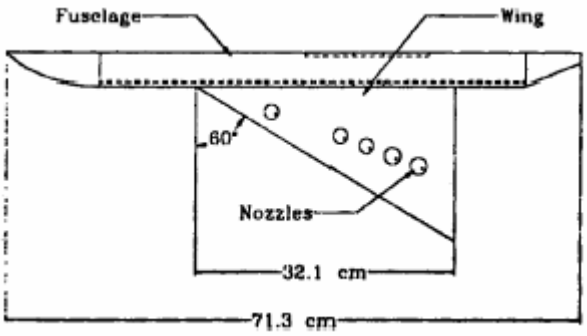

Figure 1.21: Along the core blowing model used by Guillot et al. (1998).

Mitchell et al. (2000), Mitchell et al. (1999b) also conducted an extensive study into the use of along the core blowing on a 70 degree swept delta wing (see Figure 1.22) in an attempt to control leading edge vortices and delay or eliminate their associated breakdown location. LDV was used to characterise the controlled and uncontrolled vortical structures. The nozzle exit points where located 14% of the root chord downstream from the leading edge on each side of the suction surface of the wing. This nozzle location was believed to be the optimal position as pointed out in a previous study by Visser et al. (1988). The jet was angled 5 degrees inboard of the vortical structure (which was chosen on the basis of Guillot et al. (1998) findings of the optimal orientation) and 15.6 degrees vertically from the upper wing face. In order to gain a better understanding of the effects of the implemented control technique, an initial study of the axial oscillations of the uncontrolled vortex and breakdown structure was conducted. Mitchell et al. (1999b) experimented with asymmetric blowing by using only one nozzle to apply the blowing. They found that the uncontrolled vortex location was hardly

affected, while the controlled vortex experienced a downstream shift in the breakdown location by 10-20% in agreement with the earlier experimental results of Pagan (1990), Laval-Jeantet (1993). The implementation of symmetric blowing was found to delay breakdown considerably and its effectiveness increased as the blowing mass flow rate was increased. Mitchell et al. (2000), Mitchell and Delery (2001) have also shown that for high Reynolds number ($2 \times 10^6 \leq R_e \leq 20 \times 10^6$) vortex breakdown, the natural Strouhal frequencies are "similar to those determined at much lower Reynolds numbers" giving the ability for similar low Reynolds number studies to give insight into much higher Reynolds number domains.

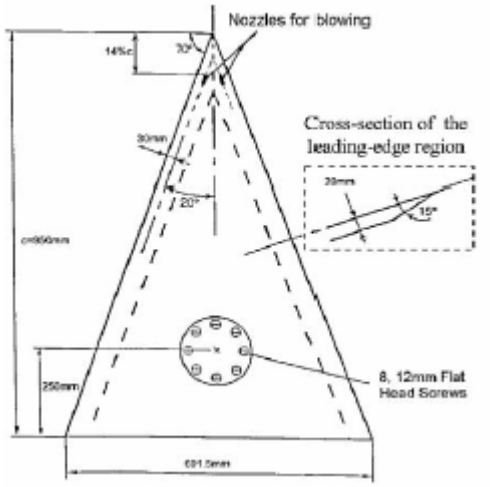

Figure 1.22: Along the core blowing configuration used by Mitchell et al. (2000).

The vortical structure under along the core blowing conditions experienced a jet-like acceleration the axial flow along the vortex core, with maximum velocities obtained along the vortex centre line. This was found to occur along the entire vortex core up to the breakdown location. The breakdown location displayed typical qualities; a stagnation point which caused a deceleration of the axial velocity component followed by a recirculation region of fluid and expanded vortical core structure and wake-like axial velocity profile. Although the breakdown location moved considerably with an increase in the blowing momentum coefficient, it had little effect on the vortex structure and recirculating region, which showed negligible change. In order to gain an understanding of the mechanisms behind the ability of along the core blowing to control the breakdown

location, the authors studied the effects of the various blowing mass flow rates on the velocity profiles upstream of breakdown. Figure 1.23 shows non-dimensional plots of the axial and azimuthal velocity components at two span wise locations (z/c = 0.53 and 0.63) and three different along the core blowing coefficients along with the no blowing case.

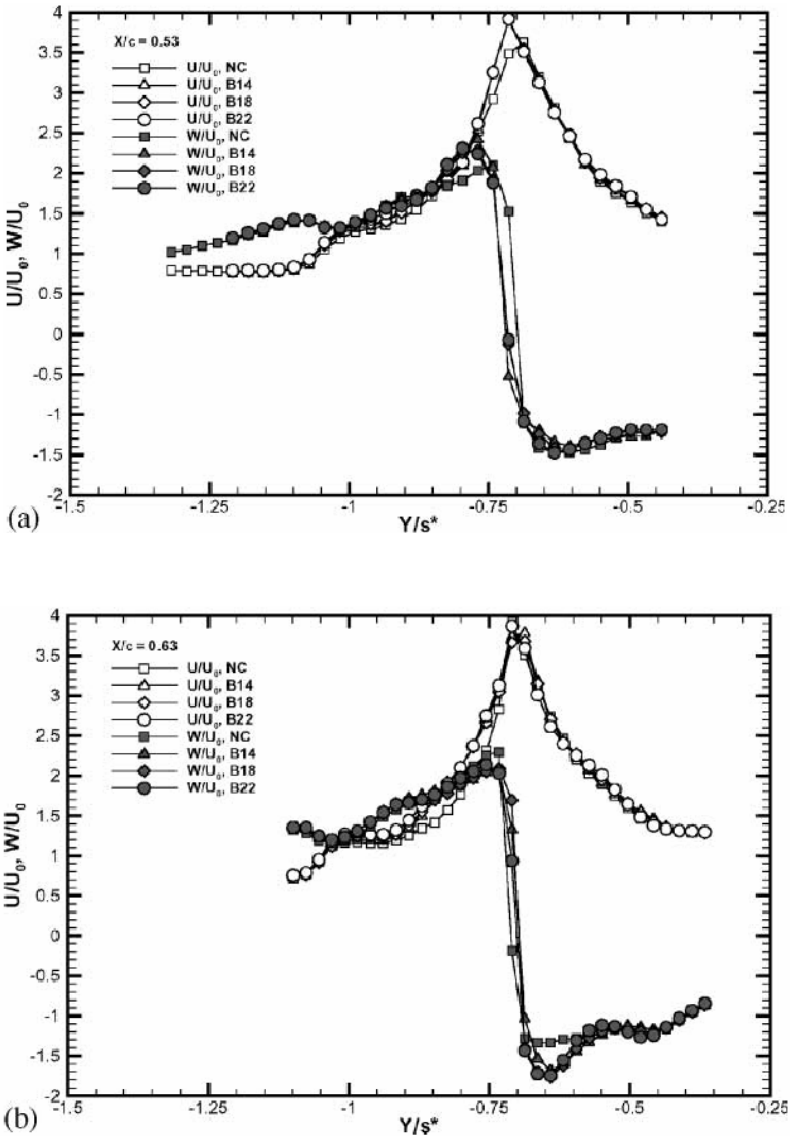

Figure 1.23: Velocity profiles at various blowing momentum coefficients (C_μ = 0, 0.004, 0.005 and 0.006) at (a) z/c = 0.53 and (b) z/c = 0.63, from Mitchell et al. (2000).

These plots show no significant difference in the axial velocity, azimuthal velocity or span wise location of the vortex structure when along the core blowing is applied. To further prove this point, the authors took similar LDV measurements at a plane located z/c = 0.02 upstream of the breakdown stagnation point for the non-blowing and two blowing cases (see Figure 1.24). Figure 1.24 clearly shows the almost identical profile of the two velocity components for blowing and non-blowing cases at a set distance upstream of the stagnation point.

Mitchell et al. (2000) concluded from their investigation that along the core blowing provides additional momentum to along the vortex core to overcome the adverse pressure gradient (which results from the flow field generated by the trailing edge) and delays breakdown. They further added that along the core blowing does not alter the vortical structure upstream of breakdown. The only downside to this technique according to Mitchell et al. is the large amounts of energy required for its effective implementation. Several other investigators (such as Miller and Gile (1992)) have also concluded (from qualitative and quantitative results) that along the core blowing delays vortex breakdown.

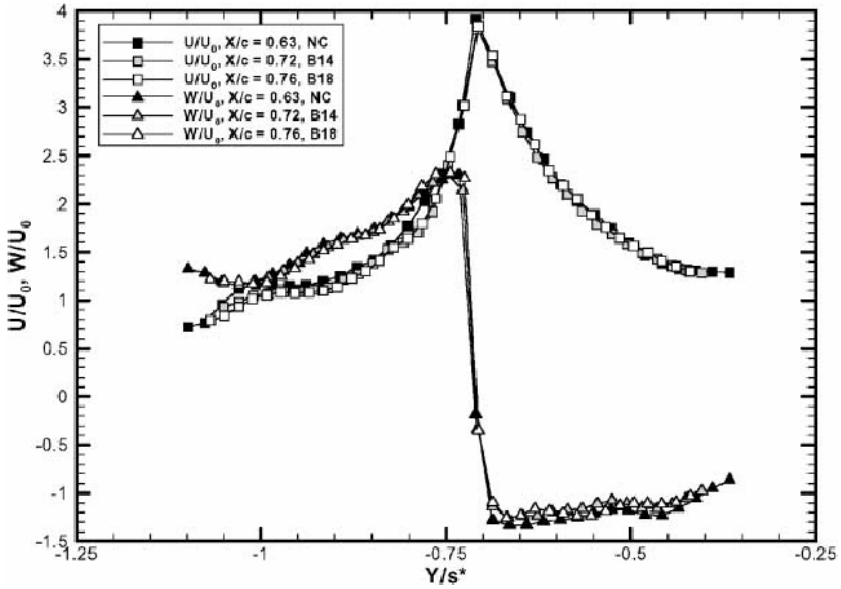

Figure 1.24: Velocity profiles at various blowing momentum coefficients with C_μ = 0 at z/c = 0.63, C_μ = 0.004 at z/c = 0.72 and C_μ = 0.005 at z/c = 0.76, from Mitchell et al. (2000).

1.7.7.7 Azimuthal Leading Edge Blowing

A variation of leading edge blowing was used by Wood and Roberts (1988) on a 60 degree sweep angle delta wing model. Their model consisted of a blowing slot situated on the round leading edge of the delta wing so that the air was blown out perpendicular to the leading edge and flowed onto the suction surface of the delta wing (see Figure 1.25). They called this technique azimuthal leading edge blowing. Their qualitative results and pressure measurements showed that this technique offered a great deal of control over the vortical structure as it directly controls the separation point (i.e. the point of vortex conception) and its inherent properties (eg. velocity distribution, etc). This efficient technique was dependent upon the angle of attack (i.e. imposed pressure gradient) and the blowing momentum coefficient. Control over the vortical structure increased as the angle of attack was decreased, to such a point that at low angles of attack the formation of the vortex was eliminated by eliminating boundary layer separation. Wood et al. (1988) extended this study and examined the effects of this technique on the time response of the vortex for varying blowing momentum coefficients on a 50 degree sweep angle delta wing. They found that the time response of the vortex to blowing increased as the blowing momentum coefficient was lowered and/or the angle of attack increased (i.e. the adverse pressure gradient).

Experiments on the effects of azimuthal leading edge blowing on vortex breakdown were continued by Wood and Roberts (1988) with the use of both continuous and transitory blowing. They examined the dynamic response of the vortex at various angles of attack. The authors found that this control method could reverse the breakdown process altogether (i.e. the breakdown state reformed into the original vortex) or move the breakdown structure further downstream. The authors believed that azimuthal leading edge blowing is an efficient and effective technique at controlling breakdown. This is confirmed when comparing this method to control techniques which require the restoration of the original vortex structure and the identification of "the momentum required and the necessity to know the location of the breakdown which results in an inefficient solution" to the control of vortex breakdown. Wood and Roberts believed that the control technique’s effectiveness originated from its ability to control the vortex point of conception by controlling the boundary layer separation point on the wing surface.

Further investigations into asymmetric and symmetric blowing cases revealed that at low angles of attack, asymmetric blowing had little effect on the vortex while symmetric blowing had a greater influence on the vortex structure due to a superposition effect. At high angles of attack the effects were amplified greatly with symmetric blowing showing the greatest amount of possible control over the breakdown structures location.

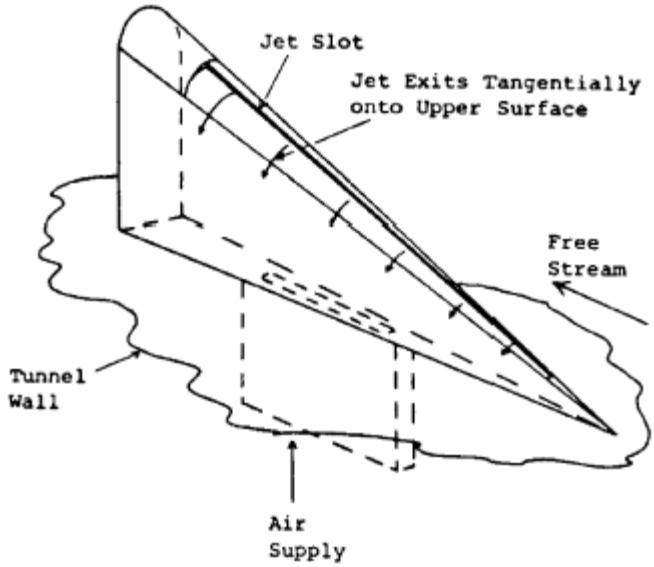

Figure 1.25: Azimuthal leading edge blowing via a jet slot along the leading edge of a half span-delta wing model by Wood and Roberts (1988).

1.7.7.8 Multiple Blowing Technique Studies

Shi et al. (1987) also conducted along the core continuous blowing over a delta wing in water tunnel tests, in addition to span wise continuous and cyclic blowing parallel to the leading edge and continuous blowing perpendicular to the vortex core. All these blowing angles were achieved via a rotating nozzle which was located on the suction side of the wing and nozzles in the fuselage at the same angle as the leading edge of the wing (see Figure 1.26). These authors' results agreed with that of previous investigations (see for example Owen and Peake (1986)), in that along the core blowing delayed vortex breakdown due to "high speed flow transferring momentum to the vortex centre by entrainment and therefore reducing the negative velocity gradient". As expected, along the core blowing (even at small values of C_μ) in the opposite direction to the vortex axial

direction causes breakdown to move further upstream by increasing the negative axial velocity gradient. Blowing in a direction normal to the vortex axis was found to delay breakdown up to a maximum downstream location where the jet met the vortex core. Span wise blowing parallel to the leading edge was found to delay breakdown, stabilise the vortex and actually induce its initial creation. This technique was most effective when the imposed pressure gradients are minimal, i.e. at low angles of attack and low free-stream velocities. In the same configuration, low frequency blowing was also found to delay vortex breakdown, up to an angle of attack of 25 degrees.

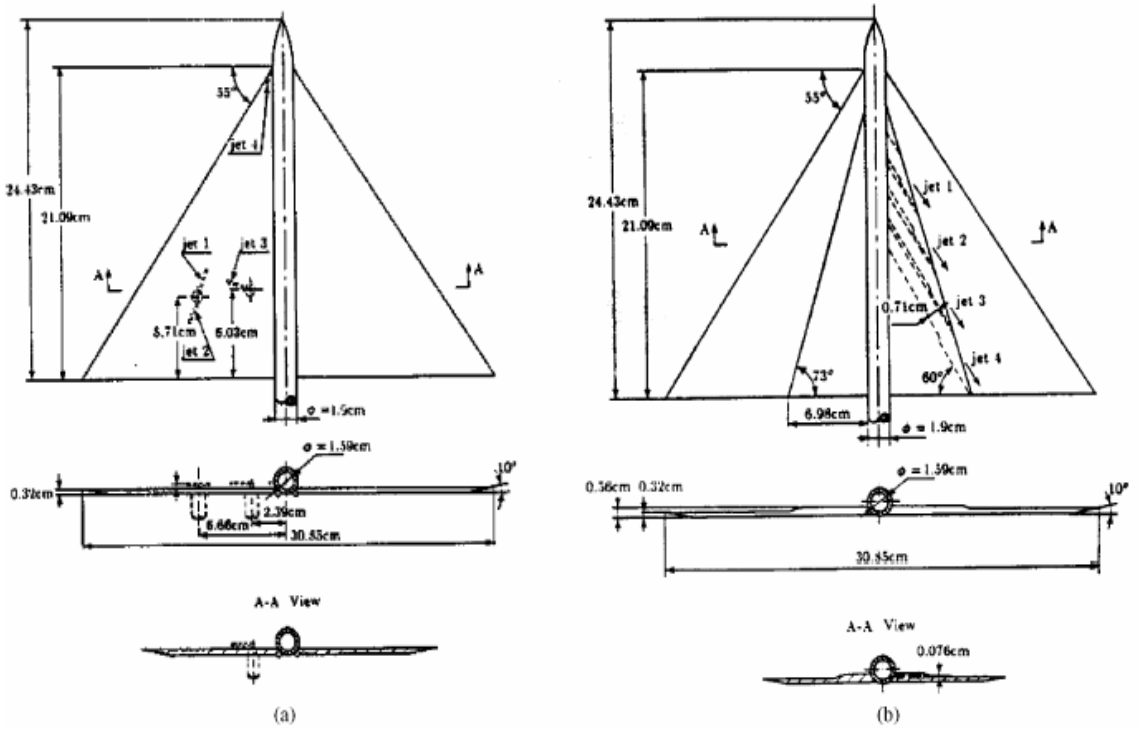

Figure 1.26: Delta wing models with, (a) 4 blowing jets on the suction surface of the wing and (b) 4 blowing jets (from the side of the fuselage) parallel to the leading edge, as used by Shi et al. (1987).

1.7.7.9 Periodic Suction and Blowing

Gu et al. (1993) conducted several experimental investigations into control methods including azimuthal suction and blowing, steady suction, alternate azimuthal suction and blowing all applied along the leading edge. Although all the above mentioned control

techniques delayed breakdown, the most effective was found to be alternating blowing and suction. The optimum period of suction and blowing was found to be equal to one convective time scale. While the full effect of the applied suction and blowing took two convective time scales, it took even longer for its effects to die away after the suction and blowing had been stopped (approximately three convective time scales). The effectiveness of this technique depended upon the frequency and amplitude of the applied perturbation.

Periodic blowing and suction was also examined by Guy et al. (1999) using a 70 degree sweep angle delta wing model. The suction and blowing was applied via slots located on the leading edge of the wing. Their results showed that this technique could delay breakdown by up to 18% of the chord (at an angle of attack of 40 degrees) with the optimum frequency and coefficient of blowing and suction found to be slightly less than one convective time scale (or an equivalent Strouhal number of $St = fc/U_\infty = 1.38$) and $C_\mu = 0.0045$ respectively. This study was furthered by Guy et al. (2000b) who conducted more experiments in order to examine the effects on suction and blowing on the axial component of the leading edge vortex by using one dimensional LDV. Their results showed that the axial velocity within the vortex core was considerably higher in the controlled case than the uncontrolled case.

A highly successful numerical simulation of periodic suction and blowing over a delta wing was conducted by Morton et al. (1999). Their results showed that this control technique moved the breakdown position in both the vertical and lateral directions which caused the breakdown structure to follow an elliptical path. The frequency of suction and blowing was equal to the natural frequency of the flow. At these optimal conditions, breakdown was delayed by 25% of the chord and was in good agreement with similar experimental studies.

1.7.8 Combination of Control Techniques: Mechanical and Pneumatic

Vorobieff and Rockwell (1996) implemented leading edge and trailing edge vortex control mechanisms, both separately and in different combinations with the aim to

provide maximum control of the vortex breakdown location with minimal energy input. The most effective exclusively implemented techniques at delaying breakdown included an upward pitched flap, which was found to delay breakdown by 6% of the root chord by providing a favourable pressure gradient (note: a downward pitched flap caused an adverse pressure gradient and consequently moved the breakdown structure further upstream. The other effective technique was trailing edge blowing at a 30 degree downward angle, also creating a favourable pressure gradient and delayed the breakdown location by 16% of the root chord.

By combining both of the above control techniques, the vortex breakdown location was dramatically increased to a new downstream position of 49% of the root chord. This clearly shows the immense gains that can be achieved by applying control mechanisms both upstream and downstream of the vortical structure. This indicates, as expected, that any control technique has a limited spatial capacity which it can control and create a favourable pressure gradient.

Vorobieff and Rockwell (1996), Vorobieff and Rockwell (1998) experimented with both leading edge flaps and trailing edge blowing (both steady and intermittent) on a half delta wing model (see Figure 1.27). Intermittent blowing during the upward pitching of a delta wing was found to be the most effective means of delaying the vortex breakdown location. They found that there was a phase lag between the intermittent blowing and effect on the vortex breakdown. Intermittent blowing provided a significant advantage in the control of vortex breakdown locations and required a lower blowing coefficient (one order of magnitude less) to achieve the same control levels. PIV measurements showed that intermittent blowing was able to delay breakdown by changing the upstream and downstream flow field in such a way as to reduce the adverse pressure gradient.

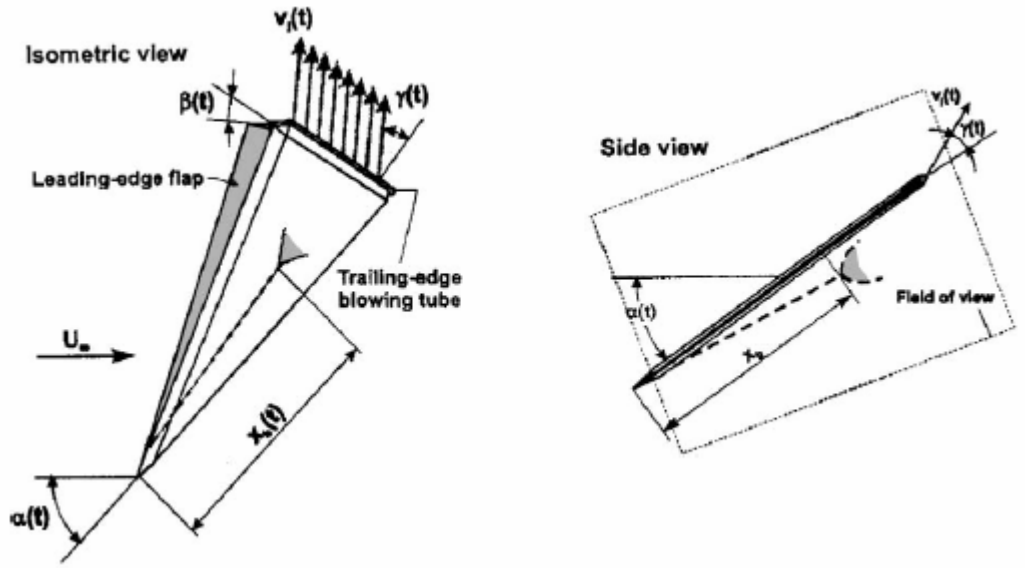

Figure 1.27: Delta wing model with flaps and trailing edge blowing as used by Vorobieff and Rockwell (1996).

1.7.9 Controlling Confined Vortex Breakdown by Imposing Azimuthal Disturbances

Unsteady azimuthal disturbances in the form $e^{(\pm i\theta - i\omega t)}$ have been studied in both confined and relatively unconfined surroundings. A recent experimental study by Kurosaka et al. (2003) in a confined tube was able to transform the breakdown structure from a bubble to a spiral and vice versa by adjusting the azimuthal wave disturbance. The disturbance was implemented by arranging four piston cylinders around the tube in close proximity to the vortex conception point. This arrangement allowed variation in amplitude and the frequency of the azimuthal wave, and also the phase difference between pistons in order to excite different modes i.e. m = 0, ±1 and ±2. This investigation showed forcing an m = 0 mode at the natural Strouhal frequency of $St_n = fR/U_{\theta max} = 0.16 - 0.2$ transforms a spiral into a bubble which moved upstream to its new stable position. While forcing a mode m = 1 disturbance at selective frequencies which lay between $0.85St_n \leq St \leq 1.3St_n$ caused a bubble to move downstream and transform into a spiral. Forcing the negative modes m = -1 and -2 had no effect on breakdown while m = 2 only caused a change in the bubble tail

to look the same as the type 0 two tail bubble breakdown as presented by Faler and Leibovich (1977a). In all cases, once the disturbance was removed the original breakdown structure returned.

A similar experiment performed in a relatively unconfined environment by Gallaire et al. (2004) in which a 6 piston arrangement (with fixed amplitude) at the end of the nozzle enabled the forcing of the following modes, m = (0,-6), (1, -5), (2, -4), (3, -3), (4, -2), (5,-1). It should be noted that this arrangement means that modes can only be forced in pairs as indicated by the brackets. The profound finding from this study was that even when forcing the various modes at various Strouhal numbers ($St_n \leq St \leq 14St_n$), the swirling jet undergoing breakdown vortex breakdown ($S \geq 1.3$) remained unaffected by this forcing method which is in contrast to previous experiments by Kurosaka et al. (2003). Also in contrast, is that breakdown receptivity to azimuthal forcing at the natural Strouhal frequency is negligible both before and after the onset breakdown. However for moderate swirl numbers (S = 0.86), forcing at m=±2, ±3 at frequencies one order of magnitude greater than that of the natural excites these modes within the swirling jet. The unsuccessful manipulation of vortex breakdown by this method was attributed to the fact that the nozzle arrangement only acts on the periphery of the swirling jet whereas all the mechanisms which have been found to cause breakdown occur along the vortex core centre line. According to Wang and Rusak (1997), it is the Kelvin waves (a core mechanism) which is responsible for causing vortex breakdown and hence is unaffected by periphery disturbances. Another explanation given is vortex breakdown is caused by the appearance of negative azimuthal vorticity along the vortex core as shown in a numerical study by Brown and Lopez (1990).

Cho et al. (2000) performed experiments using a swirling jet of air in a confined diverging nozzle which was excited with helical disturbances via an array of 8 speakers close to the vortex conception point and before the nozzle diverged. The swirling jet (not undergoing vortex breakdown) was subjected to two oppositely spinning fundamental harmonic helical waves along with an axisymmetric sub harmonic wave. The sub harmonic wave grows rapidly due to its interaction with the two fundamental helical waves; the initial phase difference between these waves determines the growth rate of the sub harmonic wave along with resulting deformation of the jet cross section.

1.8 Overview of Vortex Breakdown Control Investigations

Vortex breakdown can have beneficial or detrimental effects depending on the application. It is therefore essential that investigations into vortices and their associated breakdown states and how to control them be examined in order to optimise any application in which this natural phenomenon occurs. Although there have been numerous investigations into the control of vortex breakdown over the past half century, the majority of investigations have been conducted using the flow over a delta wing or aircraft. Although this may seem to be advantageous as it is actually implementing the various control methods in a practical situation, it also has its drawbacks. The number of variables to account for, (which in some cases may be inseparable, hence giving a false impression of the real mechanisms responsible or the cause behind the control methods success or failure) along with the need for a greater understanding of the phenomenon results in experiments which display inconclusive or a false interpretation of results. This has resulted in no clear verdict as to whether mechanical or pneumatic control techniques are the most efficient and effective means of controlling this phenomenon.

There have been many mechanical and pneumatic control techniques tested over the years with relatively high success rates at delaying breakdown. The various mechanical control techniques work by changing the flow field and controlling the point of separation (the vortex core conception point). The most recent studies have been focused on pneumatic control methods with a growing interest in along the core blowing and periodic suction and blowing. These two techniques have been shown to be highly effective in delaying breakdown, with the effectiveness of these techniques dependent upon the blowing momentum coefficient along with the frequency of perturbation for the periodic suction and blowing case. There is a slight advantage in using periodic suction and blowing as opposed to along the core blowing, in that it requires less energy to achieve the same delay in breakdown position and can achieve greater maximum downstream shifts in the breakdown position. As Mitchell and Delery (2001) point out, that another “significant advantage of this technique is that the delay in vortex breakdown

can be accomplished with zero net mass". According to Guy et al. (1999), this technique is most effective when applied at the natural shedding frequency of the eddies shed from the boundary layer which separates and creates the vortical structure This is the most efficient method as it allows the maximum transfer of momentum along the vortical core to aid in overcoming the adverse pressure gradient.

There are several difficulties associated with the implementation of the control methods covered. They include the identification or prediction of the breakdown position and the spatial location vortical structure along with the natural frequencies of the instabilities. This along with the various theories behind vortex breakdown makes the implementation of vortex breakdown control mechanisms an increasingly complex task. Vortex breakdown control techniques applied to the flow over delta wings by Er-El and Seginer (1986), Owens and Perkins (1995), Vorobieff and Rockwell (1996) have revealed the most effective positions to implement control mechanisms are those close to the point of vortex conception and downstream of breakdown. The unsteady nature of breakdown, especially at higher Reynolds number, introduces difficulties in positioning a downstream control device; hence, in practice, the optimum control location is upstream of breakdown or at the point of conception of the vortex core. It is clear from the large number of studies concerning the control of vortex breakdown that there is a need for more fundamental experiments in order to clearly identify the mechanisms behind vortex breakdown and the control of this phenomenon.

As a result of compiling and examining this literature review, areas requiring further research and/or clarification justify the aims and objectives of this PhD.

The first aim is to characterise, using flow visualisation, PIV and SPIV, an unconfined swirling jet at fixed Reynolds numbers, as the swirl is increased in small incremental steps up to and beyond the critical threshold swirl number for breakdown. This will enable the identification, examination and classification of dominant features such as instabilities and breakdown states which may arise. Such an objective has many advantages; it is firstly a means of comparing base data from the current experiment with that of reviewed in the literature as to ascertain its validity. Secondly, this base study also enables the confirmation or contradiction of some of the above mentioned theories behind

the mechanisms that cause breakdown and why different breakdown structures are observed with different experimental setups and conditions.

The second aim of this PhD thesis is to examine the effects of thermal convection on vortex breakdown. A theoretical investigation with experimental verification into the effects of temperature difference induced natural convection will be conducted to quantify the global effects of convection in terms of a temperature difference between the tank walls and working tank fluid. The effects of Reynolds number and Grashof number on convective flows in similar experimental setups will also be examined in detail. The influence on breakdown when a temperature difference is imposed or exists between the swirling jet and tank fluid will also be examined in terms of its effect on predicting vortex breakdown and as a means of controlling this phenomenon. This will entail deriving a theoretical criterion to predict the onset of breakdown when convection is taken into account and experimentally verifying its validity. The overall objective is to determine the extent to which breakdown is sensitive to the effects of convection caused by temperature differences.

The third and final aim of this PhD thesis is to study the effects of axial sinusoidal forcing at various frequencies and amplitudes of an unconfined swirling jet undergoing breakdown as a means of controlling this phenomenon. A detailed examination and comparison of the resulting structure and mechanisms behind any change in breakdown to that observed in the base study will be undertaken. This will entail implementing a novel experiment with several controlled parametric studies which are lacking within the literature. The author hopes that these results will contribute greatly to the knowledge within this particular field of fluid mechanics.

Chapter 2

Experimental Setup

Equipment & Data Acquisition

2.1 Introduction

This chapter will present details of the experimental equipment used during this study, which includes data acquisition and examine the various techniques used. The section on the experimental setup is broken up into three main sections, which include descriptions of the vortex generator, test tank, and pulsing flow controllers. In particular, details of the evolution and development of the vortex generation mechanism and ideal "un-confined" surrounding tank will be discussed. Both qualitative and quantitative data acquisition tools, including particle visualisation in conjunction with 2-D and Stereo PIV, will be discussed.

2.2 Experimental Setup

2.2.1 Equipment Overview

A similar method of generating a vortical breakdown structure was used by Billant et al. (1998) and Wu et al. (1992). It consists of a closed loop pressure-driven water jet, which discharges into a large tank. The swirl is imparted by means of an electric motor that rotates a honeycomb which is contained within a settling chamber. A general overview of the entire setup is found in Figure 2.1. A detailed description of each component follows.

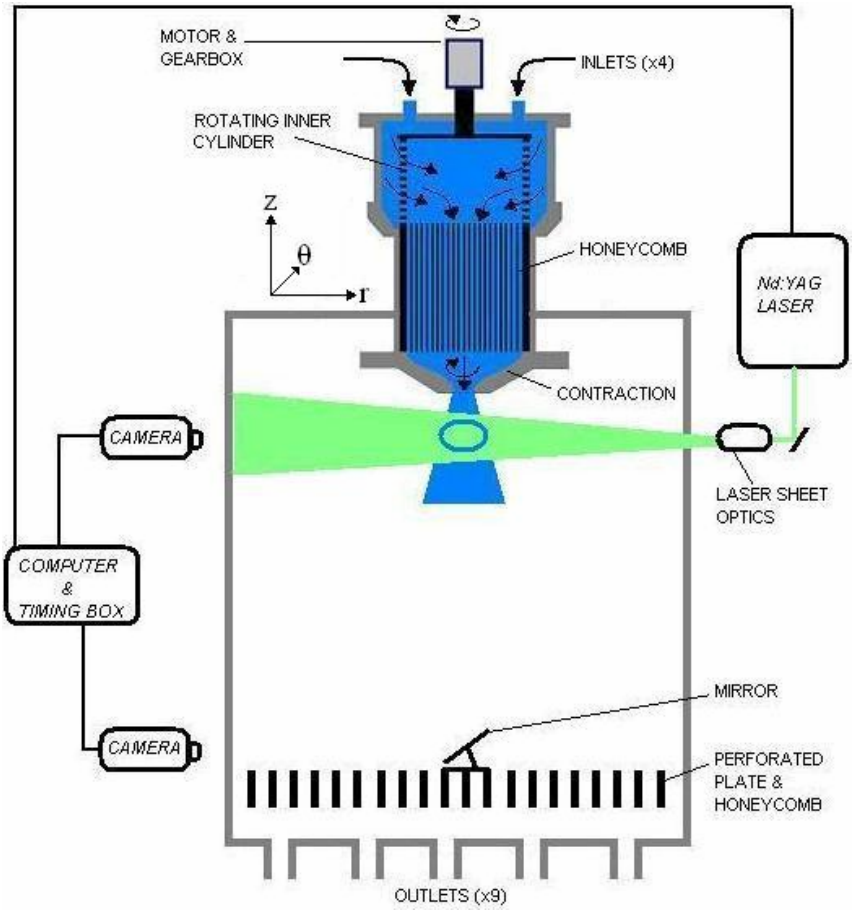

Figure 2.1: **Schematic of the experimental setup. For 2-D planar PIV the Laser sheet is rotated for both horizontal and vertical plane cross-sections, while SPIV was conducted with a fixed vertical laser sheet.**

2.2.2 Vortex Generator

Figure 2.2 is a cross-sectional schematic of the vortex generator and is described in detail below. An azimuthal velocity component is imparted to the flow via a vortex generator. This consists of a servo-motor and two concentric cylinders, similar to that used by Billant et al. (1998) and Wu et al. (1992). The basic principles behind its workings consist of a rotating inner cylinder set within a fixed outer cylinder via cylindrical bearings; this sets the axially flowing fluid into solid body rotation before passing through a contraction. The fluid in the outer cylinder passes through the upper part of the inner cylinder through an arrangement of holes. In order to set the flow into laminar solid-body rotation, (i.e. as a Rankine vortex), the flow is then passed through a honeycomb located in the lower part of the rotating inner cylinder. This also had the benefit of suppressing any upstream turbulence and was designed based on earlier experiments into optimum honeycomb design geometry by Loehrke and Nagib (1976). The dimensions of the honeycomb were 5mm in diameter and 200mm in length with a blockage ratio (defined as the ratio of solid area to total cross sectional area) of 0.2. The swirling jet then passes through a smooth converging nozzle, which is attached to the outer cylinder and is fixed, i.e. non-rotating. In order to avoid flow separation, the contraction zone is designed according to Mikhail (1979)'s optimum contraction design method. The exit diameter of the contraction zone is D = 2R = 39.5mm. The maximum eccentricity (maximum variation in cylindrical radius from the centreline) was very small at less than 1%, due to the computer-based machining process used for its manufacture.

Several high accuracy controllers were incorporated into the experimental rig in order to achieve precise control of the axial and azimuthal velocity of the swirling jet. A frequency inverter drive controls the vortex generator electric servo motor, which is required to maintain a constant frequency of rotation. A closed loop feedback encoder (fixed to the shaft of the motor) relays back a signal to the inverter to monitor and ensure the correct frequency of rotation is attained and maintained by the servo motor, even if loads or conditions vary. This system has an extremely high degree of accuracy, with a maximum error in rotation rate of only ±0.5%.

A smooth axial velocity is generated by a laminar pulse-less disc pump. The disc-pump achieves its pulse-less flow by using the viscous friction which exists between the fluid and a set of closely spaced circular rotating discs in conjunction with centripetal force to set the fluid into motion. This is a clear advantage over blade type or positive displacement pumps; unlike such pumps, it has no inherent blade passage or piston frequency superimposed on the flow. The disc-pump directly supplies the fluid to the outer cylinder via four symmetric pipes at the top of the 'vortex generator' which feeds the water to the upper part of the inner cylinder through a symmetric arrangement of holes. The desired flow rate, which in turn determines the axial velocity in this closed circuit design, is set via a frequency inverter drive that controls the electric servo pump motor. This configuration is also closed loop, with the encoder feedback signal coming from an inline electronic flow meter. This too means that the flow can be set to a specific flow rate and it will be maintained to a high degree of accuracy (±0.1%) regardless of the changing conditions. It should also be noted that the changing conditions which are present during pulsing experiments require an open loop configuration for the flow rate, which is easily set via the frequency inverter drive.

There are several important factors which were considered to ensure a smooth laminar swirling jet. The vortex generator was sealed and ensured to be air tight, as air within the system can cause significant turbulence and even inhibit breakdown from developing. Before each experiment was run, the nozzle exit would be blocked off using a plug while the pump was still working, and a series of air release valves situated at the top of the vortex generator would allow any air within the unit to be expelled. Air release valves were situated throughout the whole system and ensured that no air was trapped within any section of the closed loop system.

Any asymmetry within the vortex generator could also cause premature asymmetry within the breakdown structure by causing the stagnation point to rotate off-axis while still in the laminar breakdown regime. The inlet pipes at the top of the vortex generator are symmetrically placed with a symmetric four to one manifold equalising the pressure between all inlet ports. All components of the vortex generator were accurately manufactured to the required specifications using a CAD based N-C machine, hence minimising human error.

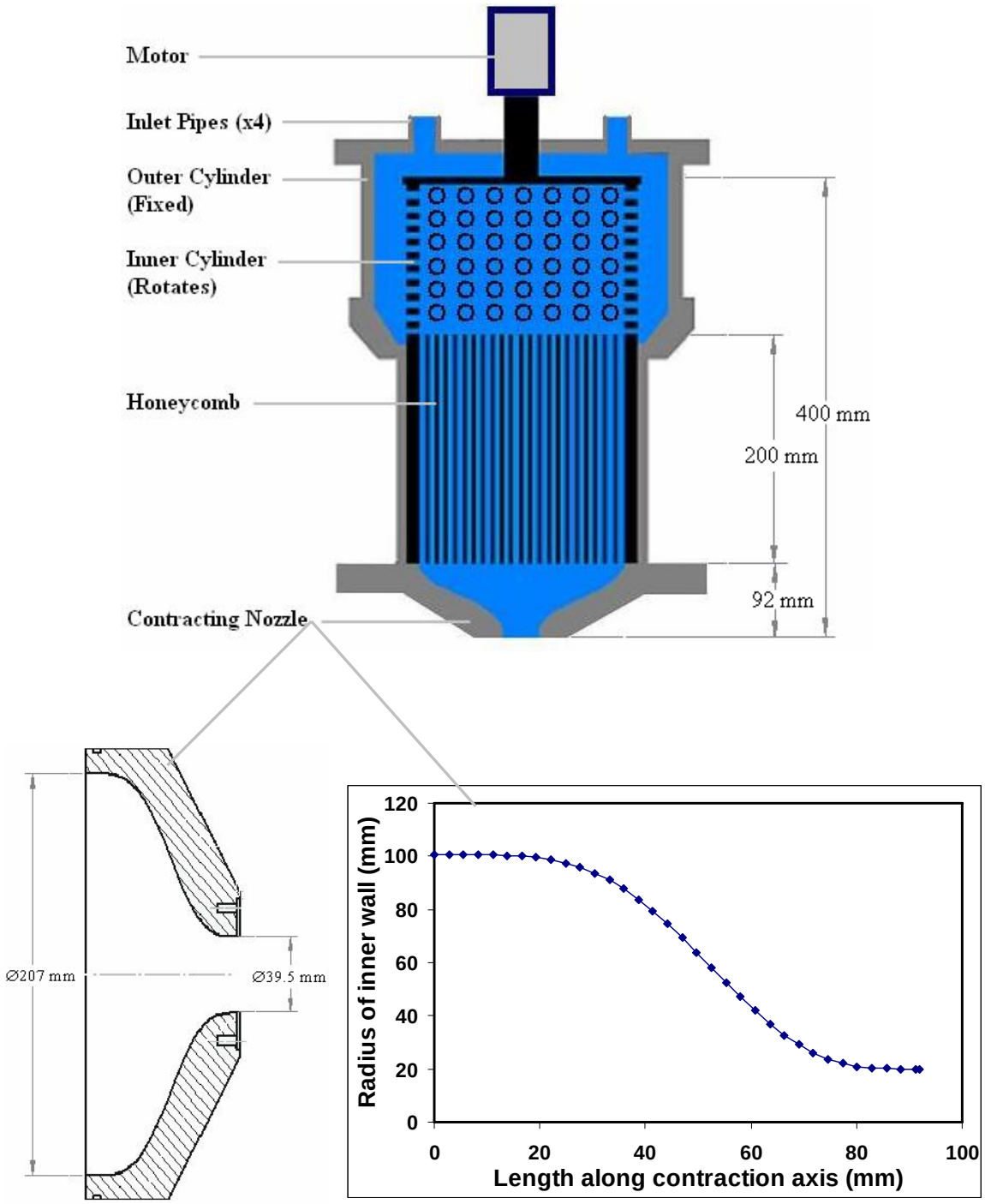

Figure 2.2: **Detailed view of the vortex generator (above), including the contraction and inner wall contraction profile (below).**

2.2.3 Test Tank

The vortex generator is partly submerged in a large square transparent Perspex test tank (650mm x 650mm x 1500mm) into which the swirling jet is discharged. The relatively large area ratio of tank to jet of approximately 345:1 minimises confinement effects and almost entirely eliminates recirculating currents (which were found to be almost non-existent).

To overcome the distortion effects associated with diffraction when shining laser light through the walls, Perspex was chosen as the wall material due to the refractive index being similar to that of water (within 11.5%, taking Perspex as 1.495 and water at a light wavelength of 500nm as 1.34 according to International Association for the Properties of Water and Steam (1997), Lynch and Livingston (2001)). In order to ensure slow-moving outlet flow, and to minimise pressure gradients caused by the outlet pipes, a perforated plate, acting as a honeycomb, is placed at the bottom of the test tank. This also had the advantage of retarding any whirlpool effect from occurring by smoothing out the fluid flow and inhibiting tangential motion before the flow's exit through a symmetrical nine hole manifold setup.

Water consistency and temperature uniformity was vigilantly monitored with highly sensitive thermometers at specific symmetrical locations around the whole circuit and within the vortex generator immediately above the contraction. The maximum temperature difference between any location both vertically or horizontally across the tank was found to be less than 0.1°C at all times. Maximum temperature difference present between the swirling jet and fluid within the test tank was found to be $\Delta T \approx 0 \pm 0.1$ °C. The room in which the experiment was run had air-conditioning which maintained the ambient room temperature constant at 20°C. A theoretical and experimental investigation into the effects of imposed temperature differences between the tank wall and tank fluid and temperature difference between the jet and tank fluid is considered in Chapter 4 of this PhD thesis.

The closed loop system consisted of a flexible piping network with large radial curves (where possible) to avoid high head losses and increased turbulence. Flexible piping also allows for easy interchange of selected sections which allows flexibility and

minimal time to alter the configuration. The experimental apparatus is connected to a bypass filtration loop consisting of a particle and carbon filter in series. This was left running when the equipment was not in use. Filtration was always turned off at least 24 hours before the commencement of experiments to allow the temperature throughout the whole circuit to equalise. During the actual experimental runs no filtration process is conducted to maintain uniform temperature through the circuit and due to the fact that the insertion of foreign particles is a requirement.

A copper-core fin and tube heat exchanger setup was also incorporated to ensure minimal temperature gradients within the tank and jet, to avoid thermal convection. Figure 2.3 (a) shows the experimental configuration used when uniform tank and jet fluid temperature is required. This particular configuration required that the cooler outflow from the exit of the test tank enter the stainless steel heat exchanger casing and pass over the copper core heat exchanger which contained the warmer fluid from the pump head outlet. This would cool the flow sufficiently before entry into the vortex generator. The heat exchanger was a necessary and essential component of this system and without it the effects of natural convection due to temperature differences between the jet and quiescent tank fluid would have been too great to achieve accurate results (see Chapter 4 for convection effects). The introduction of the heat exchanger had a quite profound effect, prior to its implementation the swirling jet temperature was higher than that of the surrounding tank fluid, exceeding it by as much as 0.1°C to 0.5°C, depending on the heat energy input from the pump and solenoid valve. Once the heat exchanger was used and the system was left to stabilise over night an indistinguishable temperature difference of 0±0.1°C existed between the jet and quiescent fluid.

Figure 2.3 (b) shows the heat exchanger configuration used to impose a temperature difference between the jet and quiescent fluid. It was achieved by using fluid of different temperatures from a chiller or heater unit rather than from the tank outflow, during the temperature variation tests (see Chapter 4). The electric compressor-type chiller and electric coil-type heater unit allowed us to impose a temperature difference between the jet and tank fluid of -5°C to +10°C, with an accuracy limited to ±0.1°C, set by the accuracy of the thermometers used. Due to the large energy input or removal from the heater and chiller, respectively, experiments had to be stopped when an increase or

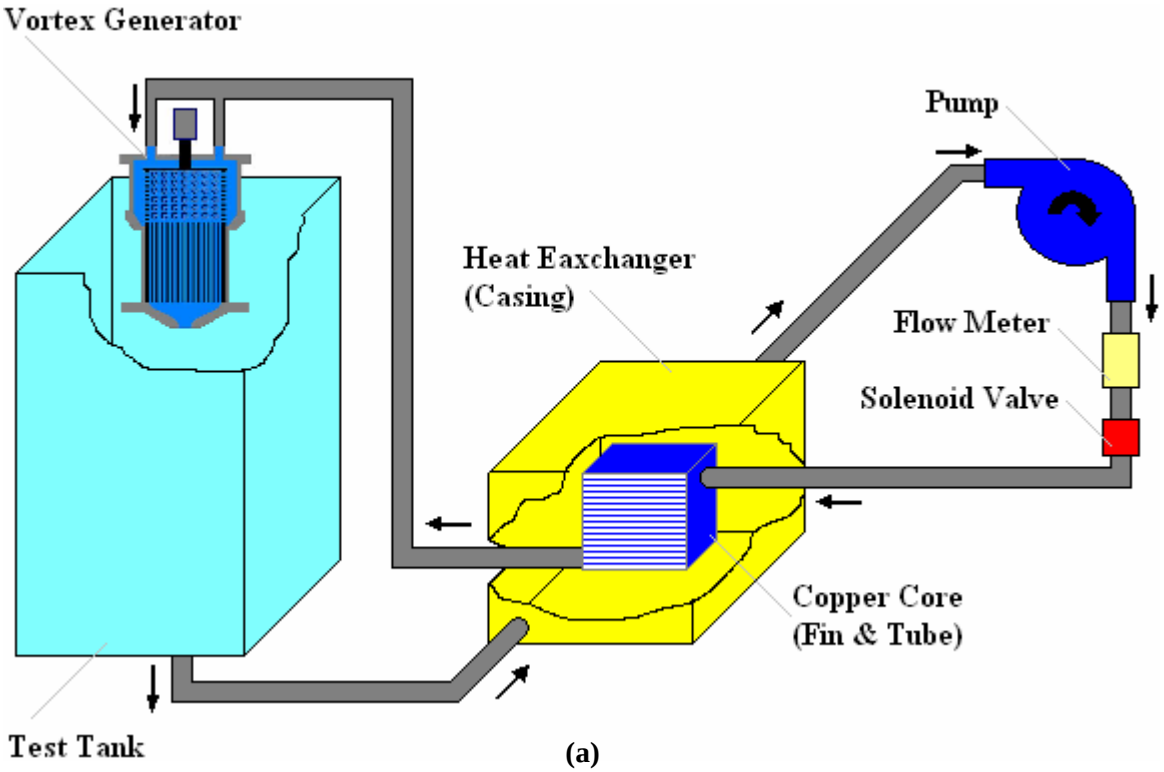

(a)

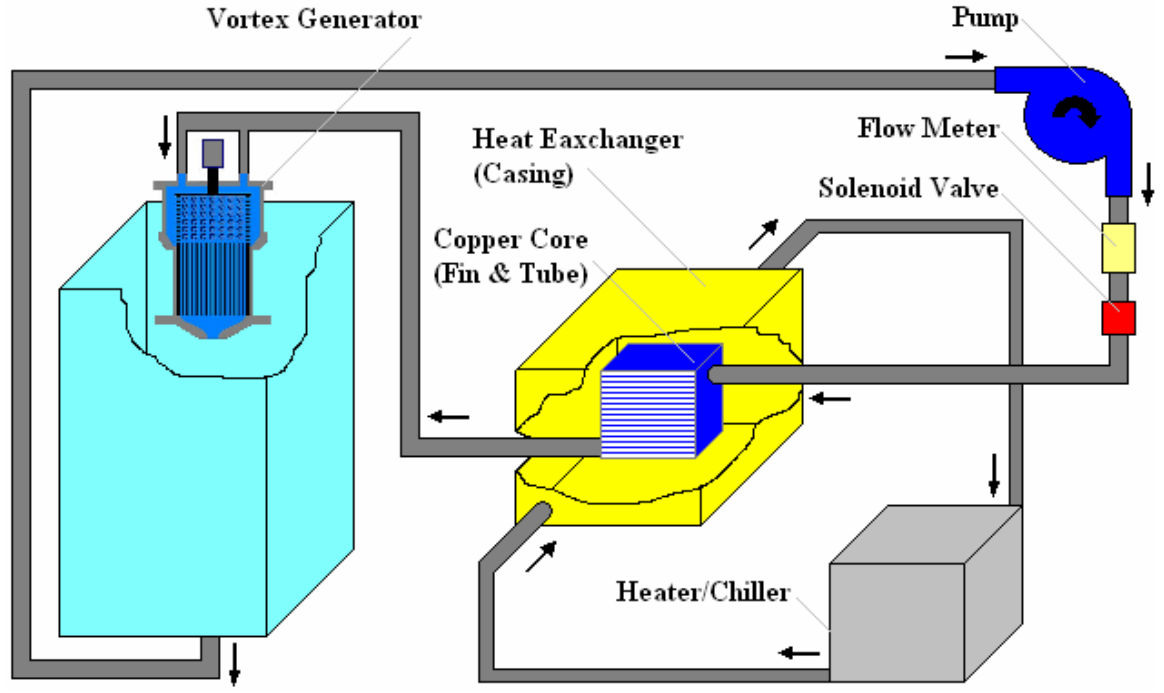

(b)

Figure 2.3: **Heat exchanger configuration used when no temperature difference was required (a), and when an imposed temperature difference was required (b).**

decrease in the bulk fluid temperature in the tank was sensed (i.e. ±0.1°C). Experiments generally only resumed after several hours or the next day when the fluid within the circuit had time to come back to an equilibrium state (i.e. ambient room temperature).

2.2.4 Pulsing Flow Controls

Previous studies (see Mitchell and Delery (2001)) have examined steady and unsteady suction and blowing of separate flows, which join the vortical flow structure somewhere along its path to control vortex breakdown. This experiment is novel in that we will examine the effects of pulsing the swirling jet undergoing breakdown in the axial direction at the point of generation. The laminar pulse-less disc pump allows a direct closed flow circuit to be achieved without the use of constant head tanks and an overflow tank, such as those used by Billant et al. (1998). In our view this improved direct closed flow circuit design allows for a substantially larger Reynolds number range and a more accurate control of axial flow rates, it also enables the flow to be easily pulsed. This particular setup more realistically simulates the pulsing mechanism, which could be used in combustion chambers or in flight; such a configuration would require a similar type of pump or compressor of some sort.

Pulsing of the mass flow rate about the mean is achieved in two ways; the first method is via an inline computer-controlled proportional-lift solenoid valve and the second method is also via a valve but is now driven by a frequency-inverter controlled variable-length scotch-yoke mechanism. Both methods produce a sinusoidal variation of the mass flow rate $\dot{m}$, about the mean mass flow rate $\overline{\dot{m}}$ in the form:

$$\dot{m} = \overline{\dot{m}} + (\dot{m}_{max} - \overline{\dot{m}})\sin(2\pi f\ t), \qquad \textbf{(2.1)}$$

where f (hz) is the frequency of pulsing and $\dot{m}_{max}$ is the maximum mass flow rate. Two methods were employed in order to verify the results and method of pulsing. The highly accurate proportional-lift solenoid valve as seen in Figure 2.4 (a) is able to achieve pulsing frequencies in the order of 33 Hz due to its short response time. Computer control

of the proportional lift solenoid valve is achieved by using an inbuilt function generator program in LabView™, which in turn is connected to a digital to analogue card and amplifier which sends the variable voltage signal to the valve. This enables complete control of both frequency and amplitude of the sinusoidal pulsing with an accuracy of ±1.5% (for 0.01 Hz $\leq$ f $\leq$ 10 Hz) and ±2% respectively over the Reynolds number and pulsing amplitude range tested. Figure 2.4 (a) shows that the proportional lift solenoid valve works by simply changing the resistance in the flow by varying the amplitude of piston motion while holding the rotational speed of the pump motor constant. The various maximum, minimum and mean positions of the piston (i.e. the amplitude of pulsing) required to achieve the magnitude of sinusoidal pulsing are determined by the flow meter readings and verified later by Stereo Particle Image Velocimetry (SPIV will be covered later in this chapter) measurements, the details of which are covered in section 3.2 of Chapter 3. A linear relationship between the piston height/valve opening (i.e. input voltage) and flow rate through the solenoid valve exists for the Reynolds number range tested ($300 \leq R_e \leq 900$). This is made possible due to a smooth transition from a circular to a uniform rectangular vertical plane cross section at the entry through to the exit in the region of the valve where the piston reciprocates.

The second method of pulsing, seen in Figure 2.4 (b), consists of the same type of variable restriction valve; however it is now controlled by a variable-length scotch-yoke mechanism rather than a coiled solenoid. The scotch yoke transforms rotational motion into pure linear simple harmonic motion (i.e. sinusoidal in the same manner as the proportional lift solenoid valve). The frequency of rotation is controlled by means of an electric servo-motor and gearbox assembly, which is directly linked to the rotating disk. The servo motor is driven by a frequency inverter with an encoder feedback signal to monitor the shaft rotational speed. This produces a maximum manufacturer's claimed error of ±0.5% (for 0.1 Hz $\leq$ f $\leq$ 10 Hz). The amplitude of pulsing is adjusted by moving the adjustable rotating disk pin to any position r on the disk via a screw-thread guided grooved track. This enables full adjustment of the amplitude of pulsing, however, to minimise the work on the pump, the length from the centre of the rotating disk to the pump body x is also adjustable via a screw-thread guide track in order to achieve the required mean mass flow rate with minimal input from the pump. This also helps to

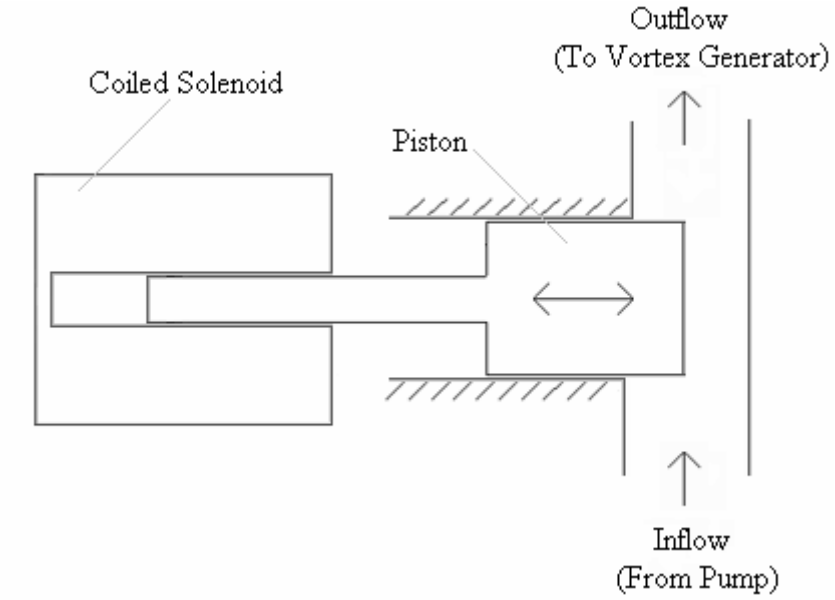

(a)

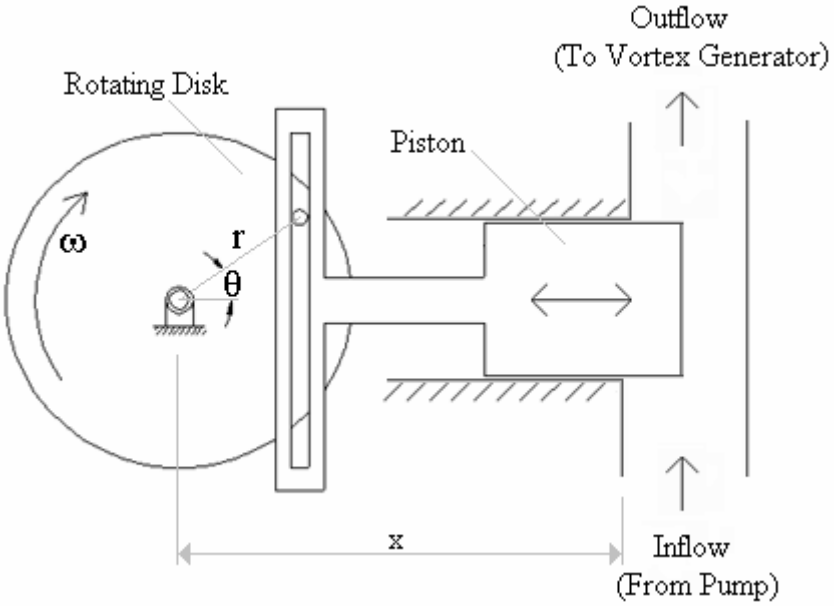

(b)

Figure 2.4: Schematic of the mechanisms used to pulse the mass flow rate by means of (a) an inline computer-controlled proportional-lift solenoid valve and (b) a valve driven by a frequency inverter controlled variable length scotch yoke.

ensure minimal heat input is added to the system as only low rotation rates are required by the pump. In a manner similar to that of the solenoid valve, this setup also has the advantage of having an inherent linear relationship between the piston height/valve opening and flow rate through the solenoid valve for the Reynolds number range tested ($300 \leq R_e \leq 900$). Both methods produced qualitatively identical results, and quantitatively a maximum error of only ±2% for SPIV data and a maximum error of ±1.5% for stagnation point location data (see Chapter 5).

2.3 Experimental Procedure and Control Parameters

In order to explore parameter space, experiments were conducted by varying the rotation rate while maintaining the flow rate constant. When the flow parameters are close to their desired values for breakdown, the rotation rate is varied in small steps with an appropriate transient time lag of 10-15 minutes left between each iteration to ensure a stationary hydrodynamic regime is obtained. The onset of breakdown is detected by flow visualisations. The dynamic response of the breakdown state to an increase or decrease in rotation rate was also examined in a similar manner.

An overriding advantage of this experimental setup is the ability to independently control both of the system variables, namely the axial velocity (flow rate) and azimuthal velocity (rotation rate) of the swirling jet. Both of these variables may be expressed in terms of two non-dimensional parameters, one being the Reynolds number and the other being the swirl ratio or swirl number. The non-dimensional parameters are chosen in order to most concisely describe the resultant flow properties for any imposed flow conditions. The non-dimensional parameters are directly obtained from the flow meter, frequency inverters and various flow data acquisition techniques such as 2-D Particle Image Velocimetry (PIV) and 3-D Stereo Particle Image Velocimetry (SPIV) discussed in detail later in this Chapter.

In order to characterise this experiment, it would be appropriate/logical to adopt a cylindrical coordinate system. However, a limitation with the PIV software being based on a Cartesian coordinate system (see section 2.5.7 of this chapter) has meant that we are

constrained to use this particular coordinate system. As a result, for intuitive purposes we will adopt the symbols used for a cylindrical coordinate system (r, z, θ), however measurements will be based on a Cartesian coordinate system. As we will only consider planar views and not 3-D volumes, this constraint on coordinate system does not pose any problems. The origin of the Cartesian coordinate system is located at the central axis of the nozzle exit. Again, constraints with PIV software has meant that the axial coordinate, z, is taken to be positive in the upward direction, the horizontal coordinate (or loosely speaking, a direction dependent radial coordinate), r, is taken to be positive to the right of the page and the out of plane coordinate (loosely speaking, a direction dependent azimuthal coordinate), θ, is taken to be positive into the page.

The following non-dimensional variables were used throughout this PhD thesis. The swirl number S provides a measure of the ratio of azimuthal velocity U_θ and axial velocity U_z. The swirl number can be expressed in many forms (see for instance Delery (1994)). For comparison purposes, the swirl parameter (or swirl ratio) definition which will be adopted is the same as that used by Billant et al. (1998). To recap, the swirl number is defined as:

$$S = \frac{2U_{\theta(max)}}{U_{z(max)}}. \qquad \textbf{(2.2)}$$

Measurements of the swirling jet, as close as possible to the nozzle exit at z/R = -1 are used, as the swirl definition requires that it should be evaluated at a location far upstream from the stagnation point. This is only of concern once breakdown has occurred as the close proximity of the stagnation point affects the axial and azimuthal velocity profiles, hence producing misleading results. According to Billant et al. (1998), at a critical swirl number of S_c = 1.3 - 1.4, vortex breakdown is found to occur independent of Reynolds number and nozzle diameter.

Trailing edge vortices are characterised by having the maximum axial velocity at the periphery of the swirling jet and minimum along the central axis of the vortex core. In our experimentally generated jet–like vortex (similar to those intense structures found forming over delta wings at high incidence), the maximum axial velocity occurs along the

axis of the swirling jet. The typical tangential velocity profile, induced by the vortex generator, is visually similar to that formed over delta wings and can be seen in Chapter 3 of this dissertation.

The Reynolds number characterises the axial flow component, and is based on the jet diameter D = 2R and average axial velocity $\overline{U}_z$, which is extracted from the mean mass flow rate $\overline{m}$. The Reynolds number is defined as:

$$R_e = \frac{2\overline{U}_z R}{\nu}, \qquad \textbf{(2.3)}$$

where ν is the kinematic viscosity of the working fluid, which in this case is filtered tap water. In practice, the mean axial jet velocity (extracted from the flow-meter reading) is used, as for a fixed Reynolds number it remains constant at any swirl number, in contrast to the peak axial velocity which increases along the centreline of the axis with increasing swirl. The mean axial velocity is not only a more accurate predictor of the swirling jet axial momentum but it also allows for easy comparison of the results obtained from parametric studies.

Furthermore, the Strouhal number is a non-dimensionalised form of the frequency of pulsing f,

$$St = \frac{2fR}{\overline{U}_z}. \qquad \textbf{(2.4)}$$

The sinusoidal variation in mass flow during pulsing is characterised by the Peak Mass Flow Variation (PMFV).

$$m_\upsilon = \frac{\overline{m} - \dot{m}_{min}}{\overline{m}} = \frac{\dot{m}_{max} - \overline{m}}{\overline{m}}. \qquad \textbf{(2.5)}$$

Here, $\dot{m}_{min}$ and $\dot{m}_{max}$ are the minimum and maximum mass flow rates, respectively.

2.4 Flow Visualisation

2.4.1 Particle Type and Injection Location

The same particles used for PIV and SPIV measurements were also used for flow visualisation. The water was seeded with silver coated spherical polyethylene particles with an average diameter of 25μm and an SG of 1.02. The reasons for this choice of particle are discussed later in this chapter under section 2.5.3. For visualisation purposes, a continuous particle injection process was implemented. Three injection points within the circuit were tested to see the effect on results and particle distribution. The first was at the periphery of the vortex generator directly above the contraction via 4 symmetrically mounted 3mm holes, which were joined by flexible hose to a 4:1 manifold. This location of particle injection produced only streak-line flow visualisation. Particle injection had to be conducted with extreme care (i.e. very low flow rates and steady particle injection) in order to prevent a relatively high disturbance to the forming swirling jet within the contraction and to avoid misleading results. This location was only suitable for flow visualisation and could not be used for PIV or SPIV experiments, which require a uniform particle distribution. The second location chosen was directly upstream of the vortex generator located above the junction of the four pipes entering the vortex generator. This location within the flow circuit produced neither a uniform particle distribution nor streak line distribution and, as a result, produced unsatisfactory results for our particular requirements and was no longer used. By far the most suitable location for particle injection was as far upstream as possible, directly after the flow meter and pulsation control devices. This proved to produce the most uniform distribution of particles due to the high amount of available mixing time, making this injection location the most suitable for both flow visualisation, PIV and SPIV. This location also had the advantage of creating minimal disturbance to the flow of the swirling jet as any small scale disturbance had sufficient time to decay.

Particle injection amounts and their associated flow rates were achieved via a piston-controlled injection chamber and a gravity-feed device. The particle-injection flow

rate was negligible in comparison to the main-stream flow rate, being less than 0.5% of the mass flow rate at the lowest Reynolds number tested of 300.

2.4.2 Acquisition Devices and Lighting

To acquire flow visualisation data, a 30 Hz standard digital video camera and 5 mega pixel digital still camera was used. As these devices could not be synchronised with an illumination source a combination of stage lights and spherical lenses were used to create a thin light sheet of 5 mm thickness. A Kodak ES4 CCD 4 mega-pixel camera (2048 x 2048 pixels) in single shutter mode was also used to acquire flow visualisation images when frequencies less than 30 Hz were required for analysis.

The particles were illuminated using a laser sheet generated by a frequency doubled Nd:YAG laser at 532nm and 400mJ in 5ns bursts. The light sheet was produced by projecting a laser beam onto a cylindrical lens directed in the plane of interest with the camera viewing angle being perpendicular to the vertical laser light sheet. For the visualisation of symmetry or asymmetry of the swirling jet, the laser light sheet was directed in a horizontal plane, perpendicular to the axis of rotation of the swirling jet. As previously seen in Figure 2.1, the camera for this case utilised a 45° mirror at the bottom of the tank to acquire the images.

2.5 2-D (Planar) Particle Image Velocimetry (PIV)

2.5.1 Introduction and Theory

Particle Image velocimetry (PIV) allows the velocity of a fluid region illuminated by a two dimensional light sheet to be measured using CCD camera(s). The flow must be seeded with particles which follow the flow and are illuminated by the planar laser light sheet which is created using cylindrical lenses. The particles' motion is used to estimate

the kinematics of the region of flow under consideration. The particles are chosen to be of density similar to the working fluid being observed (i.e. neutrally buoyant). The particle size is chosen small enough to accurately follow the flow while being large enough to efficiently scatter the light.

The motion of the particles is recorded by using a multiple exposure CCD camera. Two images are taken in sequence, at a predetermined time interval (dt). The velocity of the particles is obtained from knowledge of the camera magnification, also required is the time and distance moved by the particles between consecutive images. The subsequent images must be taken at such a rate as to ensure a reasonable spatial separation of images, to ensure accurate velocity measurements.

2.5.2 Photographic Parameters

There are four important parameters which need consideration when estimating an accurate flow measuring system using a PIV configuration and are covered below.

2.5.2.1 Recording the Captured Data

Recording the data can be done in one of two ways, namely via a digital CCD camera or a manual shutter type camera with an electronically controlled shutter. The choice of recording medium is highly dependent on the required resolution, size of the flow field required for analysis and the flow speeds. CCD cameras have the ability to capture up to 30 frames per second and a resolution of 2828 x 2828 (i.e. 8 x 10^6 pixels per image).

Photographic film cameras on the other hand have low numbers of frames per second due to their inherent slower mechanical nature, however the resolution is far greater than that of the CCD camera with (100mm x 125mm) photographic film giving the ability to capture 1.1 x 10^9 pixels per image.

It is the superior speed and ease of analysis due to their digital output that the CCD cameras provide which led to this option being used for this investigation. The cameras used where Pixelfly™ CCD cameras with a 1 mega-pixel resolution (1360 x 1024 pixels).

2.5.2.2 Depth of Field (DOF)

Depth of focus is required knowledge in order to obtain the sharpest particle image possible, by having the seeded particles falling within the depth of field of the cameras. Several approximations have been used for the DOF, for example according to Offutt (1995), DOF = $4(1+1/M)^2 f^{\#2}\lambda$, where M is the magnification ratio of the image on the object plane to the image plane, $f^{\#}$ is the ratio of the diameter of the diaphragm aperture to that of the effective focal length of the lens and λ is the illuminating light sheet wavelength. An appropriate DOF in conjunction with a thin laser sheet helps ensure the sharpest in-focus image possible. Experimentally, it is dependent upon several factors including laser brightness and the degree of out of plane flow.

For the experiments conducted, the most accurate results were obtained at $f^{\#} = 11$. This was found to be the best compromise by enabling a large enough DOF to keep the particles in focus throughout the laser sheet. This was necessary due to the high degree of out of plane motion associated with vortical flows. It also allowed enough light to be reflected from the particles back onto the CCD array for a high quality image.

2.5.2.3 Spatial Resolution

Spatial resolution of an image capture system relates to the number of pixels and the dimensions of the captured area. In general, the experiments conducted had a viewing area ranging from 100 mm x 75.3 mm to 200 mm x 150.6 mm, hence giving a spatial resolution of 13.2 pixels/mm and 6.2 pixels/mm, respectively.

2.5.2.4 Image Size

Image size of the particles depends upon the particle diameter (d_p), lens magnification (M) and the point response function of the lens. According to Adrian and Yao (1985), a good approximation of the image diameter is: $d_I = M^2 d_{GI}^2 + d_a^2$, where the point response function of the particle diameter is $d_a = 2.44(1+M)f^{\#}$, and the geometrical image diameter is defined as $d_{GI} = Md_p$.

This experimental study aimed at having the particle image size a minimum of 2 x 2 pixels at all times in order to give each particle enough character (i.e. a combination of

distinguishing and differently shaded pixels) to be identified and give strong correlation values (in conjunction with correct timing dt) during the analysis stage of the data.

2.5.3 Seeding Density and Particle Dynamics

The seeding density (ρ_s) is the number of particles per unit volume. In this case, the unit volume refers to the planar interrogation area, which is dependent on the FFT size chosen, multiplied by the laser light sheet thickness. The seeding density was kept above 7 for the smallest FFT size. This enabled a high correlation value when performing a cross-correlation type analysis on the data and enabled enough scattered light to reach the CCD array.

The dynamics of the seeded particles is of immense importance when dealing with fluid flows due to the necessity of the particles to follow the flow with as much accuracy as possible. This requires a compromise between particle size and the captured image quality, as smaller particles may follow the flow with much more accuracy than their larger counterparts. However, the resulting reflection may be quite poor and degrade the quality of the image. There is also the possibility of velocity biasing errors occurring if the particles either concentrate (Eaton and Fessler (1994)) or disperse due to local flow conditions within the area of interest.

As outlined by Eaton and Fessler (1994), Grant (1997), in order to consider the motion of seeded particles within flow, we will first consider their motion using Stokes argument in which, for low Reynolds numbers, the inertial forces are ignored and only the drag force of the spherical particle is considered. Using Newton's Law of motion, we can find the velocity of the particle moving through the fluid:

$$\sum F = ma$$

$$\tfrac{1}{2} C_D \frac{\pi d_p^2}{4} \rho_F U^2 = \frac{\pi d_p^3}{6} \rho_P a$$

$$\Rightarrow \qquad U = \sqrt{\frac{4}{3}\frac{d_P}{C_D}\frac{\rho_P}{\rho_F}a}\ , \tag{2.6}$$

where ρ_P is the particle density, ρ_F the fluid density, d_P the particle diameter, U is the particle slip velocity with respect to the fluid and a is the particle acceleration with respect to the fluid. By taking into account that the drag coefficient and drag force on a spherical object are respectively equal to $C_D = 24\mu/(d_P\rho_F U)$ and $D = 3\pi\mu d_P U$, we obtain another expression for the slip velocity of the sphere:

$$U = \frac{d_p^2 \rho_P a}{18\mu}. \tag{2.7}$$

Equation (2.7) enables a comparison of how accurately the particles follow the flow, by comparing the fluid velocity and particle slip velocity. Inertial forces of the particles cause the particles to slip or delay their response as the fluid accelerates, causing measurement errors. Merzkirch (1987), and Tedeschi and Menon (1996) have found that the particles follow the flow as an exponential function of time.

A similar analysis holds for two dimensional swirling flows in which the radial and azimuthal particle accelerations with respect to the fluid motion in cylindrical coordinates are, respectively (Grant (1997), White (1999)):

$$\frac{dU_{rP}}{dt} = \frac{U_{\theta P}^2}{r} + \frac{18\mu}{\rho_P d_P^2}(U_r - U_{rP}), \tag{2.8}$$

$$\frac{dU_{\theta P}}{dt} = -2\frac{U_{\theta P}U_{rP}}{r} + \frac{18\mu}{\rho_P d_P^2}(U_\theta - U_{\theta P}), \tag{2.9}$$

where U_{rP} and $U_{\theta P}$ are the particle radial and azimuthal velocities, respectively. Swirling flows, such as vortices, force the particles to be move outward from the viscous core, with its magnitude being highly dependent upon particle diameter, particle mass, particle

density and the amount of vortex circulation (McComb (1990)). A typical particle seeding picture can be seen in Figure 2.5.

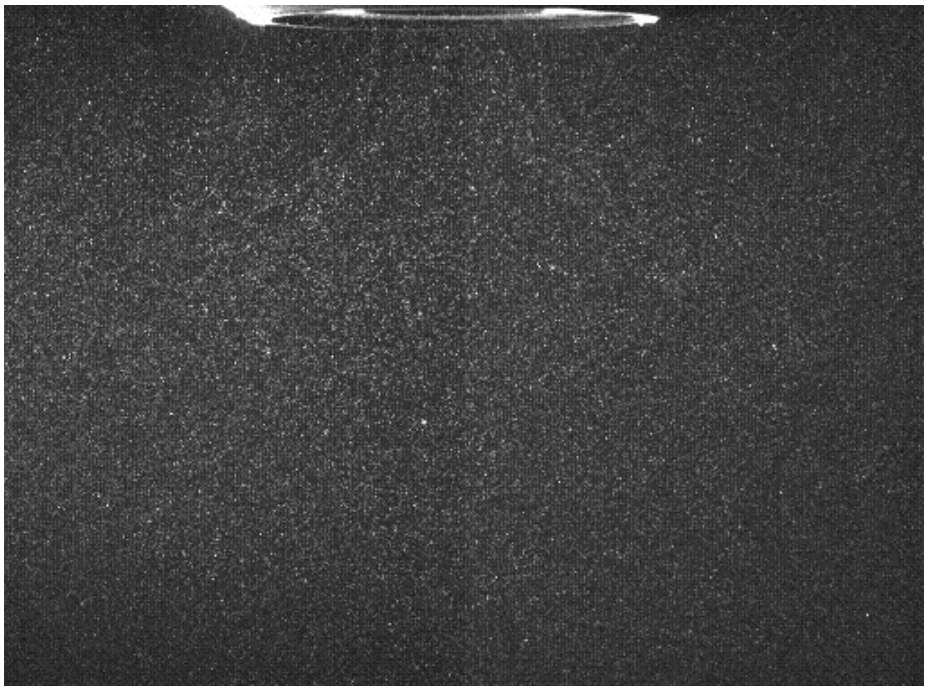

Figure 2.5: Typical particle seeding of a swirling jet undergoing breakdown.

2.5.4 Describing Fluid Motion Using PIV

There are two primary methods of describing fluid motion, namely Eulerian and Lagrangian. The Eulerian method uses a fixed three coordinate, r, z, θ frame of reference and time t, to describe the motion of a fluid at a fixed point in the flow. In the Eulerian method, flow values such as velocity are obtained by point sensors (e.g. Laser Doppler Anemometry) which provide information about the flow at discrete spatial locations in the flow. PIV on the other hand uses the Lagrangian method of obtaining flow velocities throughout the entire area of interrogation. The PIV method monitors the motion of the particles (with each particle being representative of an element of the fluid) by using a moving coordinate system to follow their motion at a set time instance and interval, hence enabling the definition of the flow properties.

Fluid velocity measurements using PIV adopt the assumption that between the two successive images, there is no acceleration of the seeded particles, i.e. the velocity vector (direction and magnitude) is constant. As reviewed by Grant (1997), in cases where the particles are accelerating, the following approximation is used to find the particle's displacement:

$$\Delta\vec{x}_p = \vec{x}_p(t+\Delta t) - \vec{x}_p(t) = \int_t^{t+\Delta t} \vec{U}_P(t)dt\,, \qquad \textbf{(2.10)}$$

where $\vec{x}_p$ is the particle position vector and $\vec{U}_P$ is the particle velocity vector.

2.5.5 Methods for Analysing PIV Images

There are to date three techniques used for the analysis of PIV images; namely Young's fringe analysis method, correlation methods and Optical correlation analysis. The Young's fringe method is generally used in speckle method and high image density PIV. For further reading on this method, the reader is referred to Pickering and Halliwell (1984).

The correlation methods include; auto-correlation and cross-correlation. Auto-correlation uses fringe patterns produced by coherently illuminating (via a laser light sheet) two image pairs (as used by the Young's fringe technique) to produce a spatial auto-correlation function. For further reading on this method, the reader is referred to Adrian (1988). The cross-correlation method is extremely useful and by far the most commonly used method of all due to its ability to produce high signal to noise ratios.

2.5.5.1 Auto-Correlation

This method requires a double exposed image, the convolution theory of Cho and Park (1990) and a 2D FFT to obtain velocity vectors. The entire velocity field is obtained by sweeping a sampling window across the entire captured image. Simpkins and Dudderar (1978) were the first to perform doubly exposed PIV using an auto-correlation technique.

It was found that a serious flaw in the auto-correlation method is its inability to detect small displacements which are found in flows with unsteady flow reversals and is limited by directional ambiguity (Fouras (1997)).

Image shifting is an advancement which has recently been investigated to improve the auto-correlation PIV method, hence enabling the resolution of flow reversals. However this method has disadvantages accompanying its mechanical implementation (Grobel and Merzdirch (1988), Landreth et al. (1988)), which can be overcome by the use of optical polarization methods (Kostas et al. (1996), Lourenco (1991)). The use of optical correlation analysis to analyse PIV images has enabled the process to be undertaken without any digitization, i.e. fully analogue. In this method an auto-correlation function of the particles' displacements is produced by performing a Fourier transform of the amplitude of the Young's fringes. For further reading regarding this method, the reader is referred to Arnold and Hinsch (1989).

2.5.5.2 Cross-Correlation

Cross-correlation does not suffer from the same flaws as the auto-correlation technique, but it is limited due to the need for two images. Hence it is highly dependent upon the acquisition rate of the image capturing equipment. This limits its applicability to relatively low Reynolds number flows as "the time scale of interest is much greater than the interval between exposures" (Fouras (1997)). The two captured images of known time interval are converted to velocity vectors by applying a FFT and then the cross-correlation is applied (note the FFT is not strictly necessary to perform the cross-correlation, however it is almost always used, as computational time is reduced dramatically). In general, "auto-correlation methods have higher temporal resolutions, while cross-correlation techniques have higher accuracy and dynamic range" (Fouras (1997)). It is for these reasons that the chosen form of PIV analysis will be the cross-correlation technique.

Immense improvements in processing power and capabilities over the past few decades have made digital processing the most commonly used method for the analysis of PIV data (Huntley (1989)). Additionally, the many advantages associated with the cross-correlation technique have also made it the most commonly used technique of all the

digital techniques used. Cross-correlation can be used to analyse single, double and multi-exposure PIV images. It is for the above reasons that the cross-correlation method was used in conjunction with high-speed double-exposure Pixelfly™ CCD cameras to perform Digital Particle Image Velocimetry DPIV.

2.5.6 Errors

2.5.6.1 Velocity Measurement Errors

Many researchers have documented the relative velocity errors associated with the PIV technique, some of which will be mentioned below. The three main causes of error are: evaluation error; systematic shift error; and out of plane flow perspective error, according to Raffel and Kompenhans (1994). A description of each error type follows:

1. **Evaluation error:** The round off error associated with the algorithm in determining the exact displacement of the particles.
2. **Systematic shift error:** Any technique requiring shifting applies angular image deflection and has an inherent associated error.
3. **Out of plane flow perspective error:** The error associated with out-of-plane particle motion, and is highly dependent upon the strength of the out-of-plane motion along with the camera setup, such as magnification, image size and focal length.

Evaluation error associated with the algorithm accuracy is also seen to bias the calculated velocities. This error is present when examining interrogation regions in which both high velocities and low velocities exist. In such cases (depending upon the algorithm used and particular settings such as time interval), the low value velocity vectors are biased as the majority of the higher velocity particles have been displaced out of the interrogation region. For further reading and for quantitative results on the various types of errors, the reader is referred to Anders and McCulskey (1994).

2.5.6.2 Vorticity Measurement Error

Vorticity measurements are mainly and directly dependent upon the spatial resolution and measurement accuracy of the velocity vector field. In addition, the algorithm's ability to calculate in-plane motion is also of importance (Fouras (1997)). In addition, errors also arise from the computational method used to produce the vorticity vector field.

The two main methods of obtaining the vorticity vector field are via the adaptive Gaussian window technique or a multi quadratic interpolator with analytic differentiation. Studies by Sinha and Kuhlman (1992) and Spedding and Rignot (1993) have shown that a multi quadratic interpolator with analytic differentiation is superior in terms of accuracy when comparing the two methods. Fouras (1997) has considered the error involved with the accuracy of the vorticity vector field. The effect of velocity error measurements affecting the vorticity calculation is "inversely proportional to the velocity spatial resolution".

2.5.7 Data Acquisition

For PIV measurements, the water was seeded with the same silver coated spherical polyethylene particles with an average diameter of 25μm and an SG of 1.02 used for flow visualisation experiments. For the same reasons mentioned earlier in section 2.4.1, the particles were continuously fed into the flow as far upstream as possible, directly after the flow meter and pulsation control devices. The injection rate was controlled via a piston-controlled injection chamber and a gravity-feed device. Particles were illuminated using a laser sheet generated by a frequency doubled Nd:YAG laser at 532nm and 400mJ in 5ns bursts. The light sheet was produced by projecting a laser beam onto an arrangement of cylindrical lenses directed in the plane of interest, with the camera viewing angle being perpendicular to the vertical laser light sheet. Horizontal planes of the swirling jet were examined with the laser light sheet directed in a horizontal plane, perpendicular to the axis of rotation of the swirling jet. As seen in Figure 2.1, the camera for this case utilised a 45° mirror at the bottom of the tank to acquire the images.

To acquire raw PIV images, a Kodak ES4 CCD 4 mega-pixel camera (2048 x 2048 pixels) in double shutter mode was used. The timing between image pairs was adjusted so that the maximum displacement vector is only one quarter the length of the smallest Sample Window Size (SWS) to ensure high correlation, as shown by Grant (1997). A 9.2Hz sequence between image pairs was the highest possible due to the limitations in synchronised timing between the lasers and the camera. PIV was an essential tool used for quantitative measurements of axial and swirl profiles in order to obtain the swirl number and to examine the breakdown structure.

PIV was performed using an in-house cross-correlation type analysis program as used in Fouras (1997), with the dynamic range enhanced using an iterative approach to select the SWS by starting at 128 x 128 to a final window size of 16 x 16 with an overlap of 50%. By performing the analysis in this fashion, the largest displacement vectors are determined by using a large SWS. The accuracy and spatial resolution is increased by then reducing the SWS and offsetting successive pairs of sample windows by the displacement calculated from the previous iteration. Erroneous vectors are rejected by comparing them to a local fit of the data (in an absolute sense) and any vector which deviates from that fit (by more then 2 pixels in this case) are rejected and replaced by the local fit. Vorticity is calculated using a second-order least-squares fit in X and Y (6 terms) and then analytically differentiating this equation to obtain the derivatives i.e. the vorticity. As mentioned earlier in section 2.3, a constraint of the PIV program is that it is based on a Cartesian coordinate system (with the origin located at the central axis of the nozzle exit) as opposed to a more intuitive/appropriate cylindrical coordinate system for our particular case. Typical errors in the evaluation of the velocity vector field are in the order of 0.1-0.3 pixels as shown by Fouras (1997). Particular care was taken to ensure that the camera was perpendicular to the object plane, as small angles of 5 degrees can cause in-plane errors of approximately 10% when the out of plane flow is of the same magnitude as the in-plane, as shown by Prasad (2000).

2.6 3-D Stereoscopic Particle Image Velocimetry SPIV

2.6.1 Introduction and Theory

Stereoscopic particle image velocimetry (SPIV) uses two cameras. In our particular case, two Pixelfly™, 1360pixels x 1024pixels CCD cameras in double shutter mode were used to simultaneously record tracer particle seeded flows, as opposed to PIV which requires just one camera. The main advantage of SPIV is that the third out-of-plane velocity component can now be calculated from the two camera images, unlike PIV which can only calculate the in-plane displacements. SPIV also increases the accuracy of the in-plane components by removing the perspective error and using this to find the out-of-plane velocity component.

2.6.2 Method

There are two main configurations used for SPIV, the first being the translational system in which the cameras are both perpendicular to the object plane and laterally displaced from each other. The other method used is the rotational system in which the cameras are rotated at a particular angle θ from the perpendicular while utilizing what is known as a Scheimpflug condition to obtain focus across the entire image plane. The rotational system was chosen over the translational due its greater accuracy. The reader is recommended to look at Prasad (2000) for an in-depth review of the advantages and disadvantages along with the associated errors for both methods.

The rotational method requires that two cameras be rotated and their axes intersect at the object plane. This rotation creates a non-uniform magnification across the image along with a vertical central focal strip at which either side remains out of focus. In order to increase the width of the focal strip to get the whole image in focus, the Scheimpflug condition must be met. This condition requires that the CCD array must be further rotated with respect to the lens by an angle α in such a way that the object, image

and lens planes are all collinear as seen in Figure 2.6, a schematic of a rotational SPIV setup. This further rotation of the CCD array amplifies the variation in magnification across the image. Correcting the variation in magnification will be discussed later in this chapter. The angular rotation of the cameras also causes square interrogation spots to be viewed as oppositely stretched trapezoids in the image plane of each camera along with different grid points, as can be seen in Figure 2.7. Before the information from each camera can be combined, the data must be mapped onto a common grid.

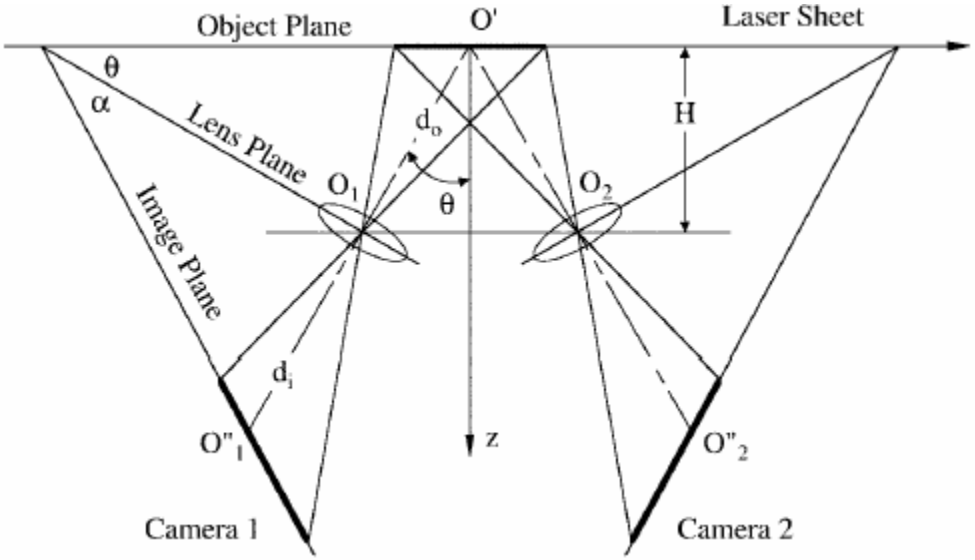

Figure 2.6: Schematic of an angular-displacement SPIV setup as depicted in Prasad (2000).

Another problem which occurs concerns the distortions arising when viewing through a thick liquid layer, which are due to the large off-axis angle associated with SPIV. These aberrations cause a radial distortion of particles within the image and reduce the sharpness of the overall image. The most widely used corrective solution for this problem was proposed by Prasad & Jensen (1995). They showed that through ray tracing, the use of a prism filled with the test section liquid placed up against the test section wall, as depicted in Figure 2.8, is very efficient at reducing these distortions. In this way, both the left and right cameras are perpendicular to the liquid–air interface. The distance from the object plane to camera lens plane in Fig 2.8 is given by:

$$d_o = \frac{1}{\mu}(d_l + d_p)\cos\theta + d_a\,, \qquad \textbf{(2.11)}$$

where μ refers to the index of the test liquid and prism liquid. The equations required to resolve the particle displacements from the left and right cameras are presented in Prasad and Jensen (1995).

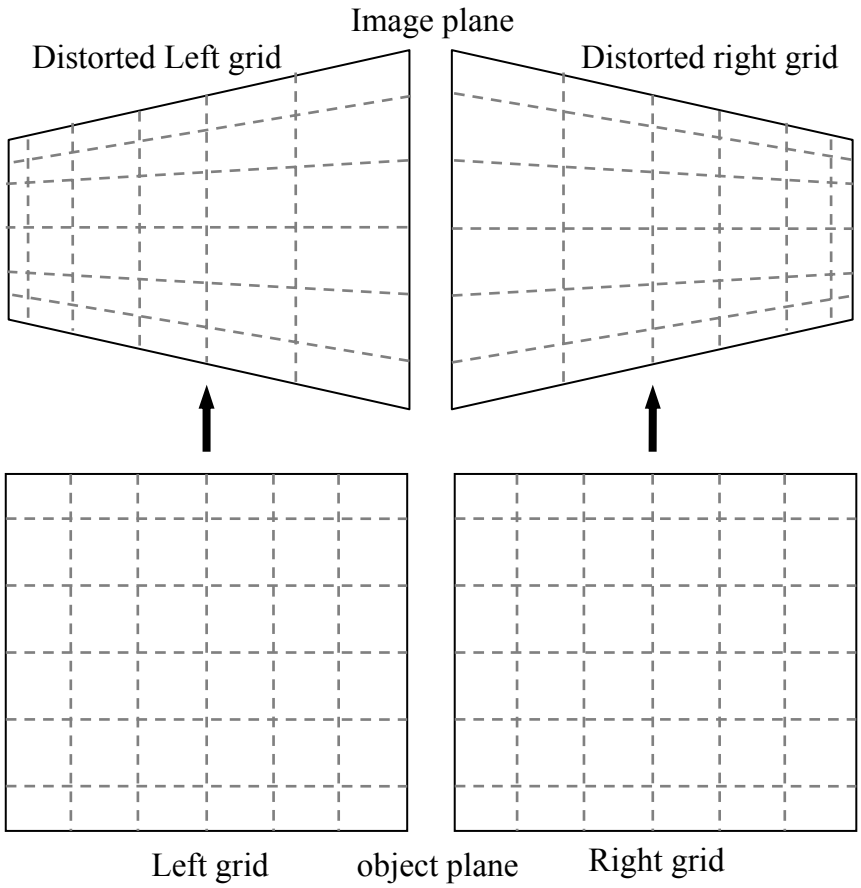

Figure 2.7: **Schematic of the resultant stretching of a Cartesian grid image due to the varying magnification when viewed through the left and right cameras of a rotational SPIV setup.**

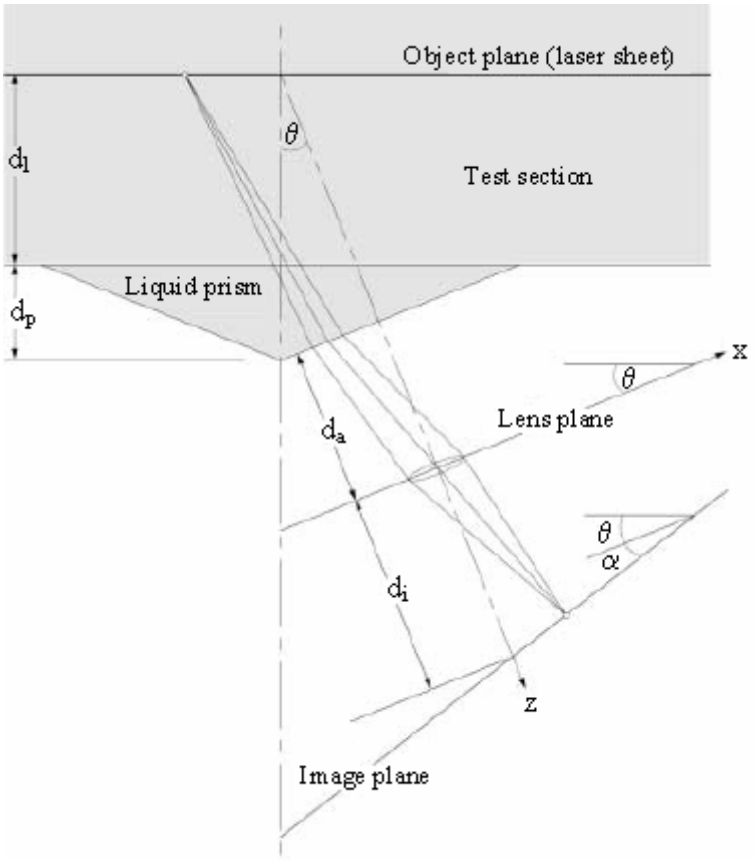

Figure 2.8: Ray tracing of a Scheimpflug stereoscopic setup incorporating a liquid prism from Prasad and Jensen (1995). Note: right camera only is shown.

2.6.3 Errors

Both Zang and Prasad (1997) and Lawson and Wu (1997) have investigated and documented the relative errors associated with SPIV in comparison to planar PIV. The first set of authors presented an error analysis which incorporated the Scheimpflug condition while the latter show the error associated with various rotational angles. With the same convention used in Figure 2.8, Zang and Prasad (1997) showed that the relative error in the out-of-plane component in comparison to the in-plane at x = 0 and y = 0 is equal to $\sigma_{\Delta z}/\sigma_{\Delta x} = \sigma_{\Delta z}/\sigma_{\Delta y} = 1/\tan\theta$, while the absolute value of the in-plane error is $1/\sqrt{2}$ times smaller than that of planar PIV. When we consider that the in-plane component error of Planar PIV is fixed at between 0.1 to 0.3 pixels, it is clear that the associated

error is extremely small. Another advantage is that the stereoscopic method eliminates the perspective error associated with planar PIV and this can be quiet substantial. Lawson and Wu (1997)'s work, as can be seen in Figure 2.9, shows the relative out-of-plane to in-plane error as a function of the off-axis position x/d_o for a rotational SPIV system. It can be seen that the error has a very small dependence on the off-axis position, while the most desirable angle is 45 degrees in order to achieve an error ratio of approximately 1.

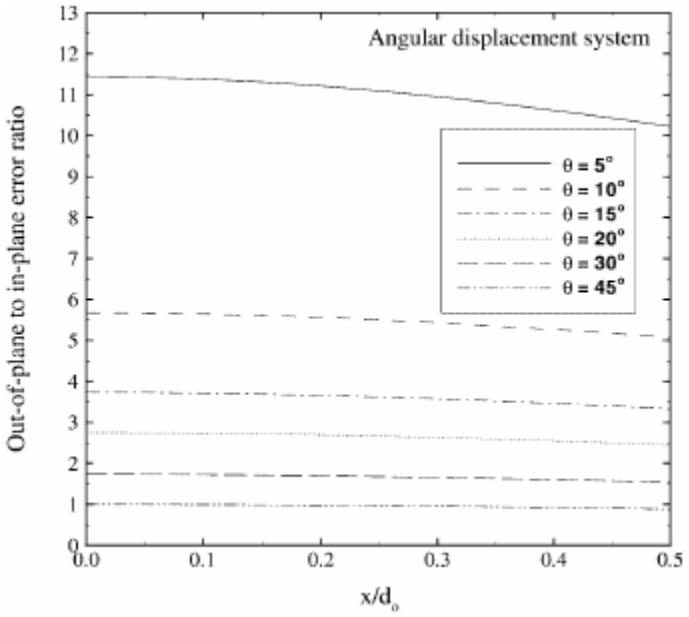

Figure 2.9: Out-of-plane to in-plane error ratio as a function of the off-axis position at y = 0 and z = 0 for rotational (angular displacement) SPIV systems, from Lawson and Wu (1997).

Another source of error known as registration error occurs when the resulting velocities calculated from each camera view are incorrectly combined onto the common grid due to different regions of the image plane being combined. This may occur if the cameras are set up as not to point at the same central point or from misalignment when creating the distorted mapping function. This was overcome by first using markers to mark out the desired viewing window on the calibration plate to ensure the magnification/viewing domain of the head on and angled images were identical. Once the magnification/ viewing window is set, the cameras are then both centred at the centre

point of the calibration plate (also marked out) at which point there is zero distortion by both the left and right camera images.

2.6.4 Reconstruction of Images

Firstly each set of camera images from a stereo pair must be individually analysed via a cross-correlation technique (same analysis as used in the planar PIV section). This is followed by mapping these displacements to a common grid so that the data from both cameras can be combined, or otherwise known as reconstructed. There are two main types of reconstruction methods, one being geometric reconstruction and the other calibration reconstruction. The latter will be discussed and was used throughout the SPIV experiments conducted for this PhD research.

The calibration based reconstruction method is performed in one of two ways, the first being the 2-d based calibration in which some geometry of the system is required and is a simplified geometric reconstruction method. The other method known as 3-d based calibration does not require any geometric information, however it does require that the test target (calibration plate) be traversed across the out-of-plane extremities and centreline of the laser sheet. The 2-d calibration based reconstruction method was used throughout this investigation. For further reading on the other above-mentioned methods, the reader is referred to Prasad (2000) for a review.

2.6.4.1 2-D Calibration Based Reconstruction

A calibration plate/target must be placed in the object plane, i.e. the front surface of the target must be placed along the centreline of the laser sheet. The calibration plate used for these experiments was a transparency of random high-density speckled sand with a black backing (Figure 2.10). Once the target is in place, a zero-degree front-view head-on shot (planar PIV) is taken of the calibration plate. Next, the cameras are brought to their final position (in our case a half angle rotation θ of 30°), an image of the calibration plate is taken for both cameras making sure that the images have the same horizontal-magnification/image-viewing area as the zero-degree front head-on shot and that they are

centred. Due to the calibration plate being a speckled sand image, performing cross-correlation PIV analysis at any FFT window size is possible due to the excellent image quality and density of particles in the image. Hence a cross-correlation is performed between the straight and rotated image for both the left and right cameras in order to obtain a mapping function which shows the particles' image displacement (and the gradient being the magnification) due to the rotation (Figure 2.11).

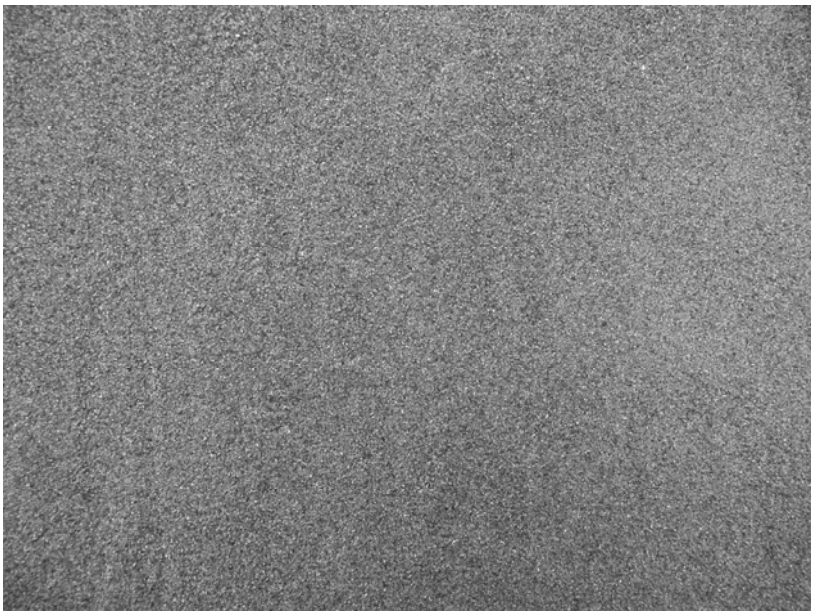

Figure 2.10: Calibration plate, transparency of random high density speckled sand with a black backing.

This mapping now provides a common grid for both cameras between the object plane and image plane (in 2-d). It should be noted that the FFT window size and amount of overlap used to create these mapping functions should be the same as those used later to analyse the images from the left and right cameras. The mapping function is only used to combine the data from both cameras onto a common grid, then the appropriate transformation equations (which also require some geometry information such as the separation between lenses, object distance and the half angle of the cameras, θ) are applied to give the 3-d vector data.

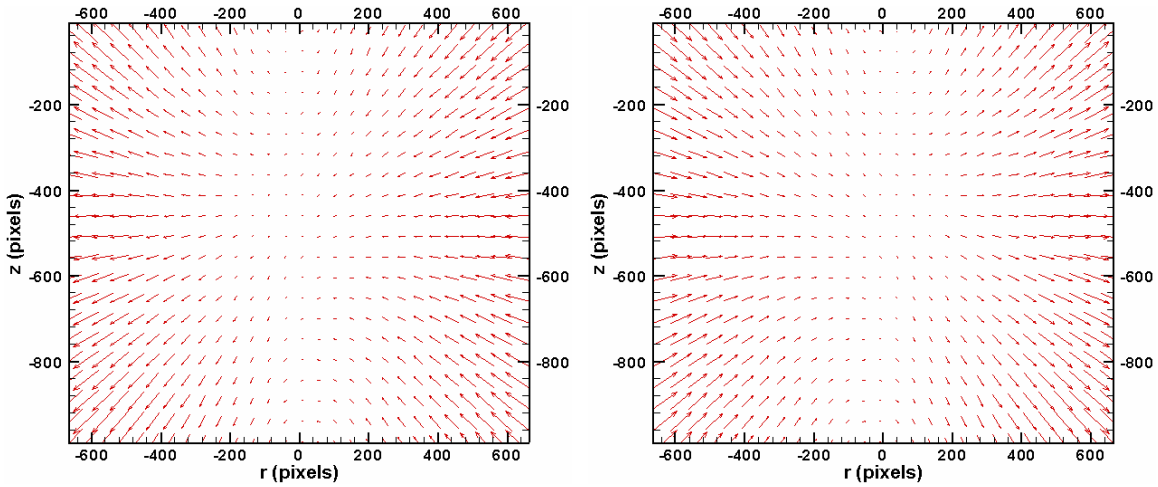

(a)

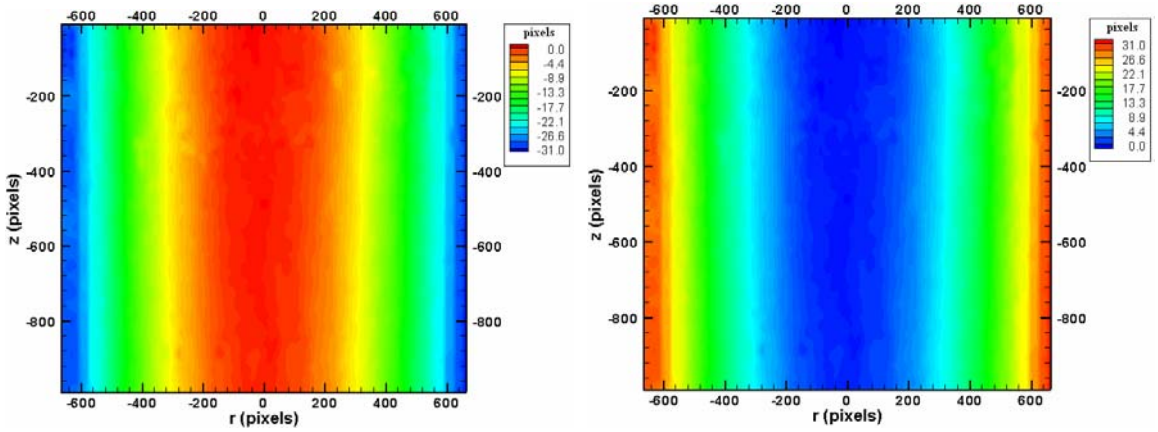

(b)

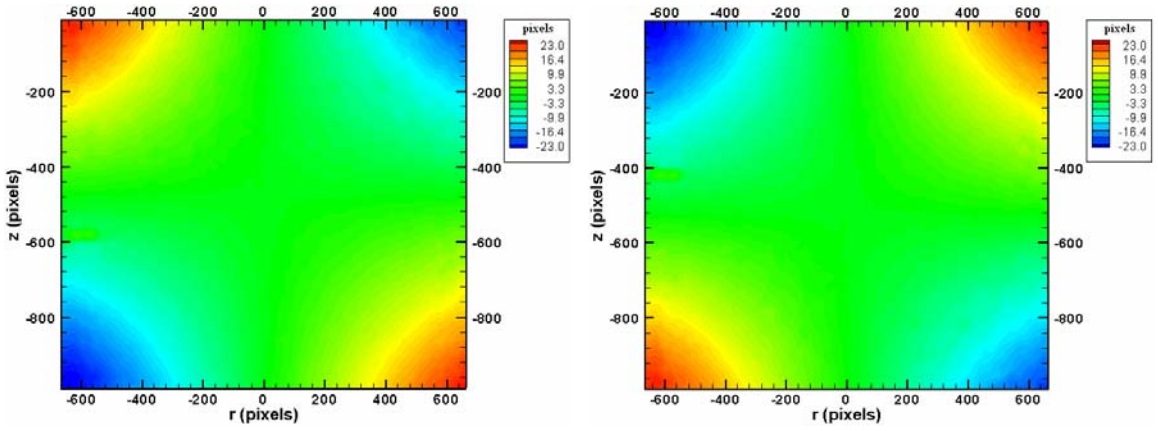

(c)

Figure 2.11: Left and right camera mapping functions which were generated when cross-correlating the zero-degree front head-on view with that of the distorted 30

degree rotated views of the cameras. (a) Vector displacement plot, (b) r (radial) displacement contours and (c) z (axial) displacement contours. All units used on the plots are in pixels and view a 200mm x 150mm calibration plate as seen in Figure 5.

Once the mapping function is created, the calibration target is removed and the stereo images are recorded. The mapping function is used to transform (i.e. account for the variable magnification) displacement data from each camera onto a common Cartesian grid. The final step is to combine the data from both cameras using the standard equations as presented in Prasad and Jensen (1995) to obtain the 3-d data (Δr, Δz, $\Delta \theta$).

Chapter 3

Results & Discussion

Vortex Breakdown

3.1 Introduction

This chapter will present the various breakdown states which arise as part of a parametric swirl and Reynolds number experimental investigation. Operationally, the Reynolds number is set to a fixed value between $300 \leq R_e \leq 900$ while the swirl number is gradually increased. A detailed examination of velocity profiles and the dynamics of breakdown are presented. Both qualitative and quantitative data obtained via flow visualisation, PIV and SPIV will be discussed and compared with the literature. Areas which require further research will also be outlined. This chapter presents the data which will be used as a basis for the work presented in the following chapters.

3.2 Swirling Jet Characterisation

Axial and azimuthal velocity profiles through the jet were obtained via SPIV and planar PIV. Figures 3.1 & 3.2 show SPIV velocity profiles for various fixed Reynolds numbers for a range of swirl numbers at a downstream location of z/R = -1. At S = 0, the jet axial velocity possesses an approximation to a top-hat velocity profile. Increasing the swirl reveals that velocity profiles in both the horizontal and vertical planes interact in a non-linear manner. Billant et al. (1998) attribute this non-linear interaction to the contracting nozzle which causes a pressure decrease along the axis, hence creating an acceleration of the axial flow along the centreline causing an axial velocity overshoot. In order for the jet to maintain an unchanged axial momentum, a deficit in the axial velocity at R_e = 300 occurs between $0.45 \leq r/R \leq 0.95$ and $-0.95 \leq r/R \leq -0.45$, while at R_e = 600 and R_e = 900 the axial velocity deficit occurs between $0.5 \leq r/R \leq 0.75$ and $-0.75 \leq r/R \leq -0.5$, as clearly seen in Figure 3.2.

The axial velocity profiles show a jet-like profile at which the maximum velocity occurs along the jet axis at r = 0. For the azimuthal velocity component, the maximum is at $r/R \cong \pm 0.5$. Hopfinger and Heijst (1993) refer to this type of vortex as being either an isolated or screened vortex due to the almost solid body rotation in the core with a relatively rapid decrease to zero at the outer periphery of the jet, which is characterised by high levels of vorticity at its core periphery due to the associated azimuthal shear. This type of vortex promotes both axisymmetric centrifugal instability and Kelvin-Helmholtz instability, causing a destabilisation of the azimuthal modes.

To verify the accuracy of both the PIV and SPIV measurements, a comparison using a mass flow rate meter was conducted. This mass flow rate meter, over the range tested, is factory calibrated and accurate to 0.1%, hence we consider this to be the base (true) mass flow rate. The mass flow rate from PIV and SPIV data was found by using Simpsons rule to numerically investigate the mass flux to give:

$$\dot{m} = 2\pi\rho \int_{-1.5R}^{1.5R} rU_z dr \,. \qquad \textbf{(3.1)}$$

Note the limits of integration in equation (3.1) are $-1.5R \leq r \leq 1.5R$, as opposed to $-R \leq r \leq R$, to account for the mass flux associated with the slight jet expansion at the point of measurement (z/R = -1) as seen in figures 3.1 & 3.2. A maximum error of the global mass

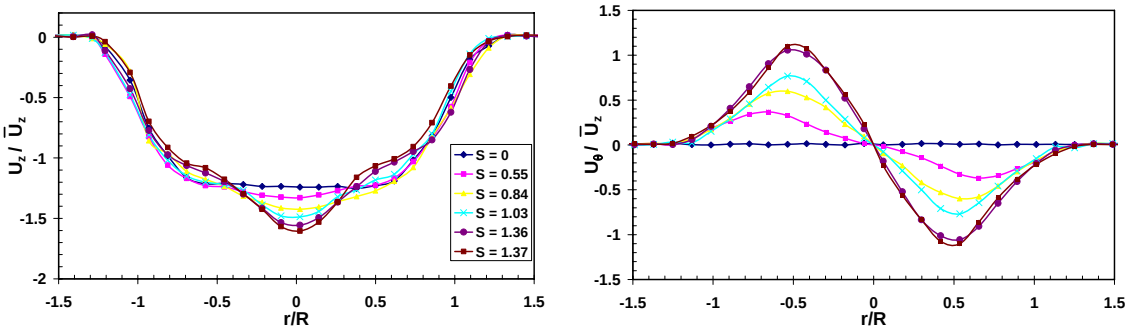

(a) R_e = 300

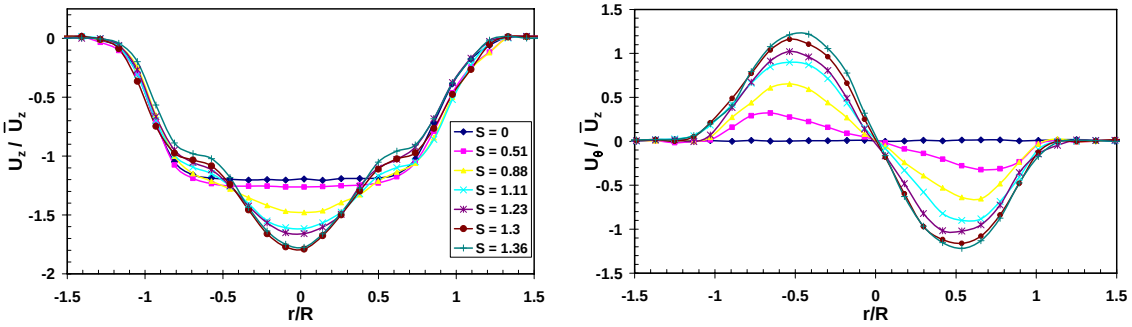

(b) R_e = 600

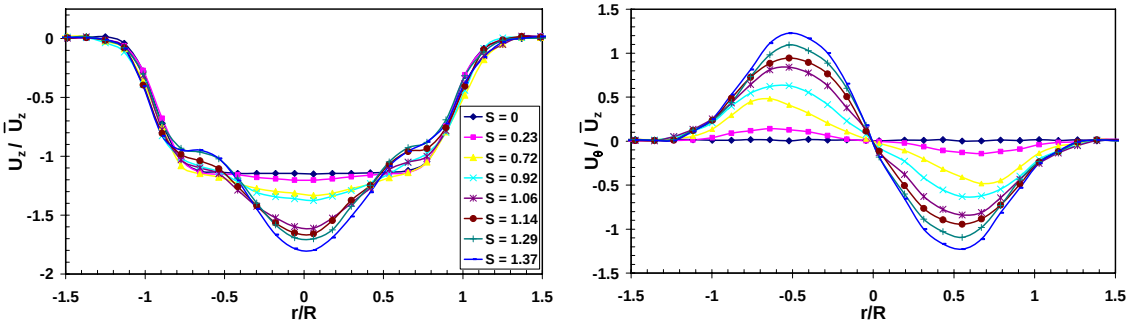

(c) R_e = 900

Figure 3.1: Axial (left) and Azimuthal (right) velocity profiles deduced from SPIV data averaged over 150 frames at (a) R_e = 300, (b) R_e = 600 and (c) R_e = 900 as S is varied. Profiles taken at z/R = -1.

flow rate based on the PIV and SPIV measurements (averaging 150 frames) of approximately 2.5% was found when comparing equation (3.1) to the flow meter reading for a Reynolds number range of $300 \leq R_e \leq 900$.

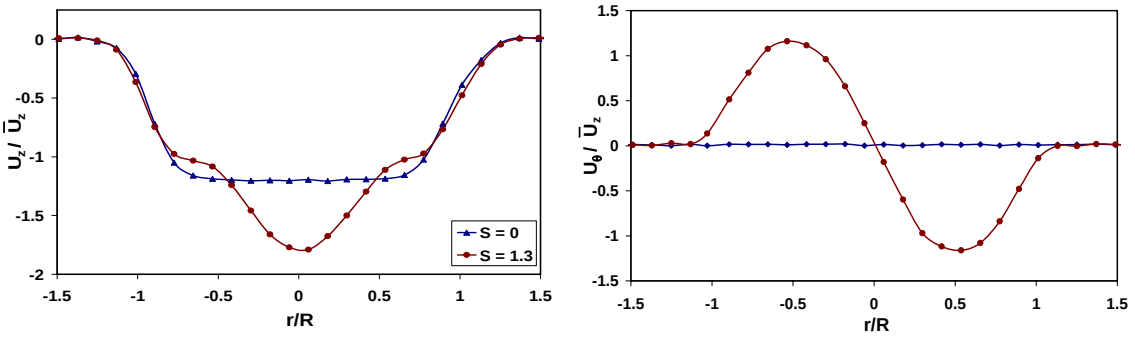

Figure 3.2: **Axial and Azimuthal velocity profiles respectively (at z/R = -1) for S = 0 and S = 1.3 at R_e = 600, showing the exact radial locations in which axial velocity gains and deficits occur at S just below S_c. Profiles are obtained from SPIV data averaged over 150 frames.**

A limitation associated with using the swirl number to characterise the swirling jet arises when vortex breakdown occurs and the stagnation point is close to the nozzle exit. It is necessary for the velocity measurements to be taken at a sufficient distance upstream from the breakdown stagnation point to avoid an altered velocity profile due to the close proximity of the stagnation point. To avoid an erroneous swirl number reading, PIV and SPIV are performed at a series of small incremental steps (5-10%) from zero swirl up to the onset of breakdown. This parametric study enables a least squares fit to the data in the form:

$$S = a(1 - e^{(b\omega)}), \qquad \textbf{(3.2)}$$

where a and b are constants determined from experimental data and ω is the angular velocity of the vortex generator. This same procedure was used by Billant et al. (1998) to predict the swirl number once breakdown had taken place. This enabled an accurate measure of the swirl number; when compared to the PIV data the fitted curves reveal a maximum deviation of only 3%. Figure 3.3 clearly shows the close agreement of the least

squares fit of equation (3.2) with the experimentally determined swirl number. Another interesting feature to note in Figure 3.3 is the extent to which the swirl number plateaus with increasing rotational speed of the vortex generator.

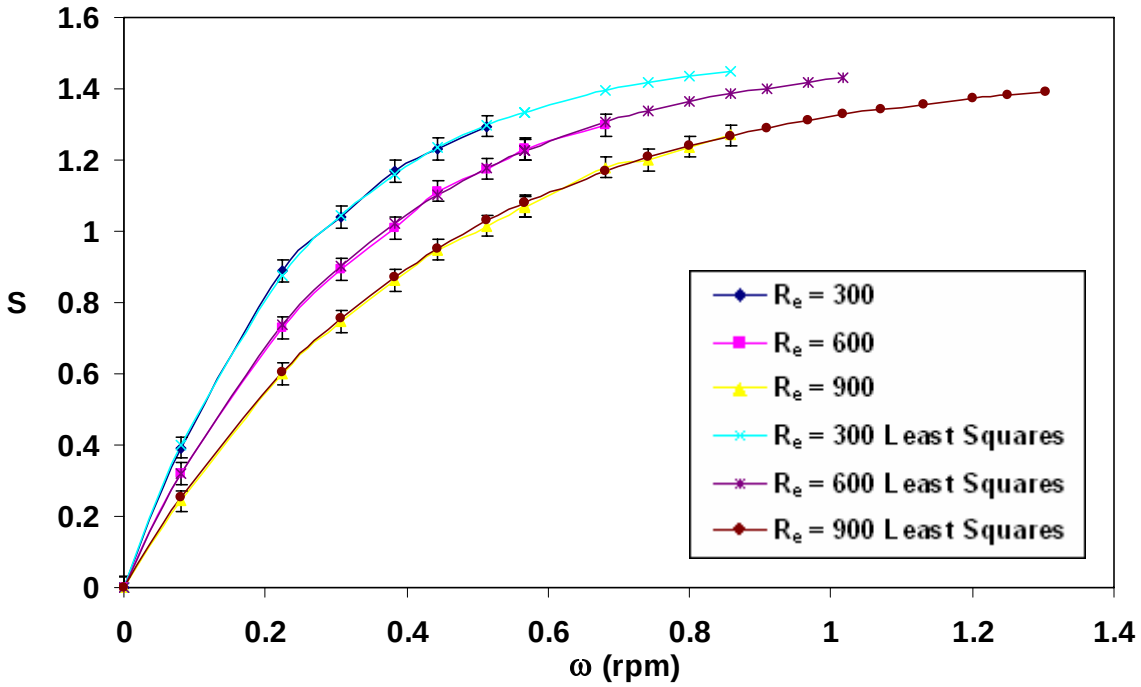

Figure 3.3: **Variation in the swirl number with the rotational speed, ω, of the vortex generator, extracted from SPIV data averaged over 150 frames at various Reynolds numbers with least squares curves fitted to the data using equation (3.2). The swirl number is evaluated at z/R = -1.**

The azimuthal velocity profiles of Figure 3.1 enable the calculation of circulation:

$$\Gamma(r,z) = 2\pi r U_\theta(r,z). \qquad \textbf{(3.3)}$$

A typical example of the radial variation in circulation is shown in Figure 3.4. The circulation increases to a maximum before decreasing to zero. The location of maximum circulation is not constant, and increases with swirl. Similar to the location of maximum azimuthal velocity, as seen in Figure 3.1, the location of maximum circulation is also

swirl number dependent. Increasing swirl values shifts the maximum circulation point closer to the vortex axis (r = 0), up to approximately r/R = 0.7, at which point there is no further movement in the peak location for all Reynolds numbers tested. It is interesting to note that Billant et al. (1998), having a similar experimental setup, also have a slight azimuthal velocity or circulation peak dependency on the swirl number. Figure 3.4 also confirms that no net circulation exists due to the azimuthal velocity component decaying to zero as a consequence of the no slip condition which exists at the nozzle boundary. Billant et al. (1998) note two important points regarding this type of circulation profile. Firstly, the circulation differs greatly from that of a Batchelor or Rankine vortex, which is used in the majority of theoretical studies on trailing line vortices, in that their circulation remains constant and does not decay to zero as in our case. Secondly, the region of decreasing circulation may lead to a centrifugally unstable flow.

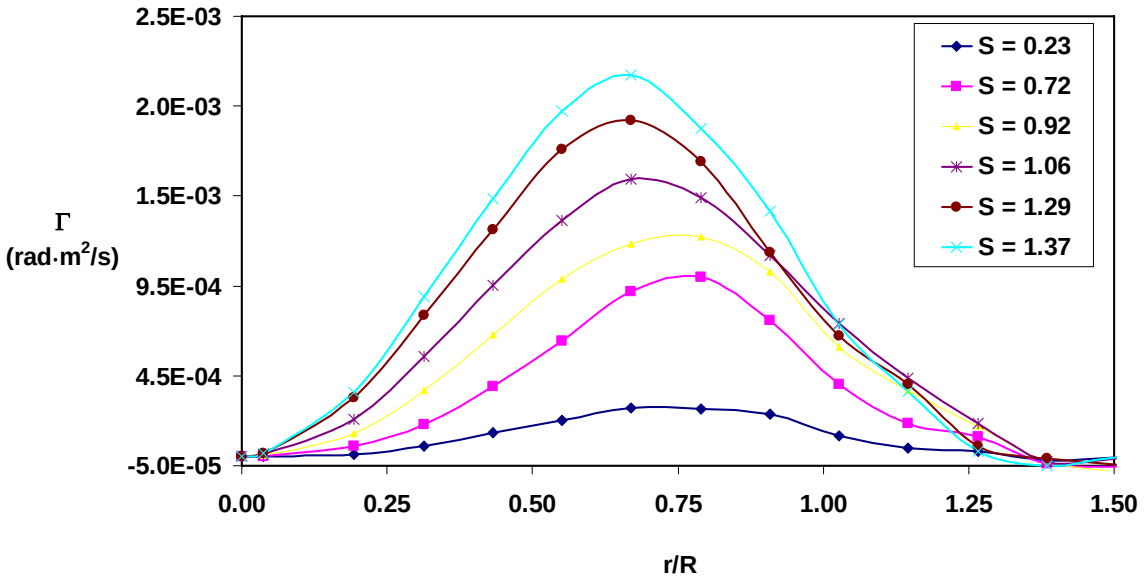

Figure 3.4: **Variation in the circulation, $\Gamma(r,z) = |2\pi r U_\theta(r,z)|$, (equation (3.3)), at R_e = 900 and various swirl numbers. Data was deduced from the azimuthal SPIV data of Figure 3.1 (c).**

In all Reynolds number cases at S = 1.25, i.e. just below the critical swirl number for breakdown, S_c, the swirling jet began to develop a broadening of the vortical core at approximately 2 radii downstream, presumably due to the centrifugal instability as seen

in Figure 3.5. A close look at each of the velocity components as the swirling jet progresses downstream reveals some common features across the entire Reynolds number range tested. As expected, all quantities decrease with increasing downstream distance, approaching zero at a sufficient downstream position. Due to the broadening of the jet, the radial velocity component continues to rise in magnitude before plateauing and then beginning to decrease at $-6 \leq z/R \leq -5$. Quantitatively, all SPIV vector plots are similar along with the initial upstream section of the maximum velocity plots. For example, when velocities are non-dimensionlised in terms of the average axial velocity, $\overline{U}_z$, the axial, azimuthal and radial velocity components all begin at 1.6, 1 and 0.5 respectively, independent of the Reynolds number. However their progression downstream is Reynolds number dependent.

Figure 3.5 shows two distinct patterns, one which is common at low Reynolds numbers, namely $300 \leq Re \leq 725$, and another for higher Reynolds numbers $725 < Re \leq 900$. The lower Reynolds number range shows the two velocity components that determine the swirl number, namely the maximum axial and azimuthal velocity components, gradually decrease at roughly the same rate. There also exists a point at $z/R \cong -3$ where the maximum radial velocity begins to increase rapidly to a maximum at -5 radii downstream, at which point it begins to gradually decrease at a much slower rate. The higher Reynolds number range shows a greater rate of decrease in the maximum axial velocity when compared to that of the azimuthal, resulting in a much shallower incline in the swirl number. The radial component is an increasing function of downstream distance, and reaches a maximum at $z/R \cong -3$ before its gradual descent, with the magnitude of this local maximum only half that of the lower Reynolds number regime.

As mentioned above, for the evaluation of a useful swirl number, velocity measurements must be taken well upstream of breakdown or any downstream effects which propagate upstream. Figure 3.6 shows the relationship between the maximum axial and azimuthal velocity components with swirl number at $R_e = 300$, $R_e = 600$ and $R_e = 900$. Clearly from this figure at approximately $S = 1.35$, once breakdown has occurred and a stagnation point has appeared, the effect is felt well upstream. This is indicated by the beginning of a steep decline in the maximum axial velocity beyond this point. At the

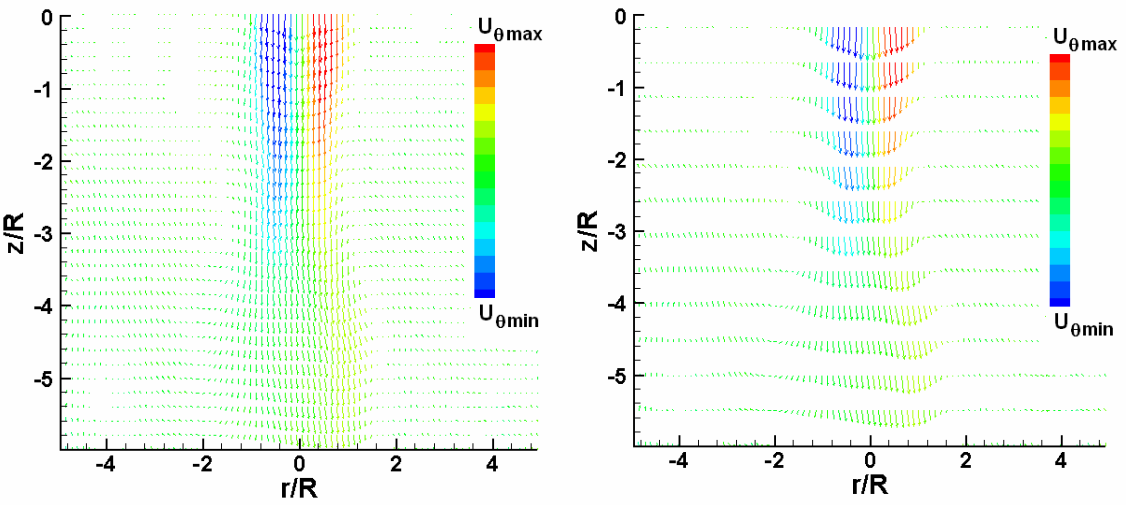
z/R
r/R
$U_{\theta max}$
$U_{\theta min}$

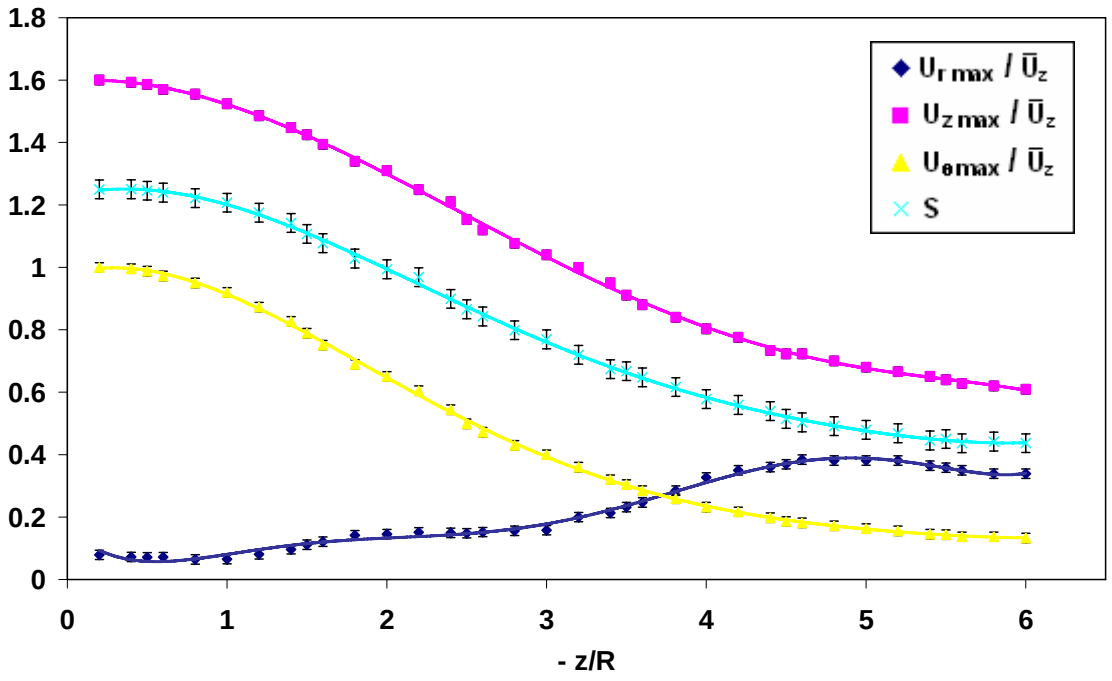
$U_{r\,max} / \bar{U}_z$
$U_{z\,max} / \bar{U}_z$
$U_{\theta max} / \bar{U}_z$
S
- z/R

(a) R_e = 300

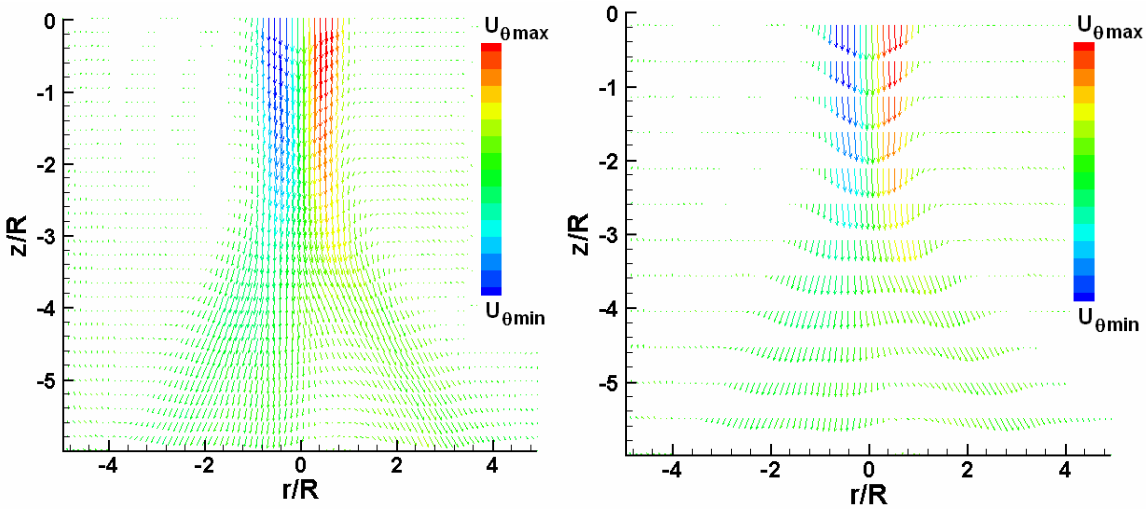
z/R
r/R
$U_{\theta max}$
$U_{\theta min}$

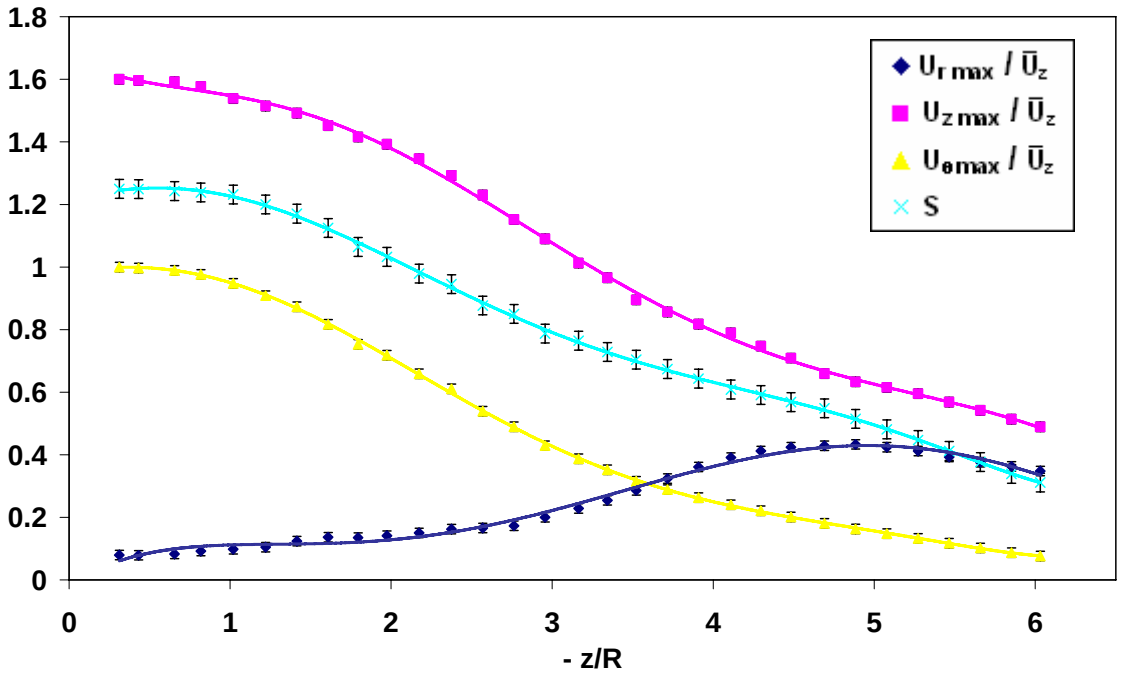
$U_{r\,max} / \bar{U}_z$
$U_{z\,max} / \bar{U}_z$
$U_{\theta max} / \bar{U}_z$
S
- z/R

(b) R_e = 600

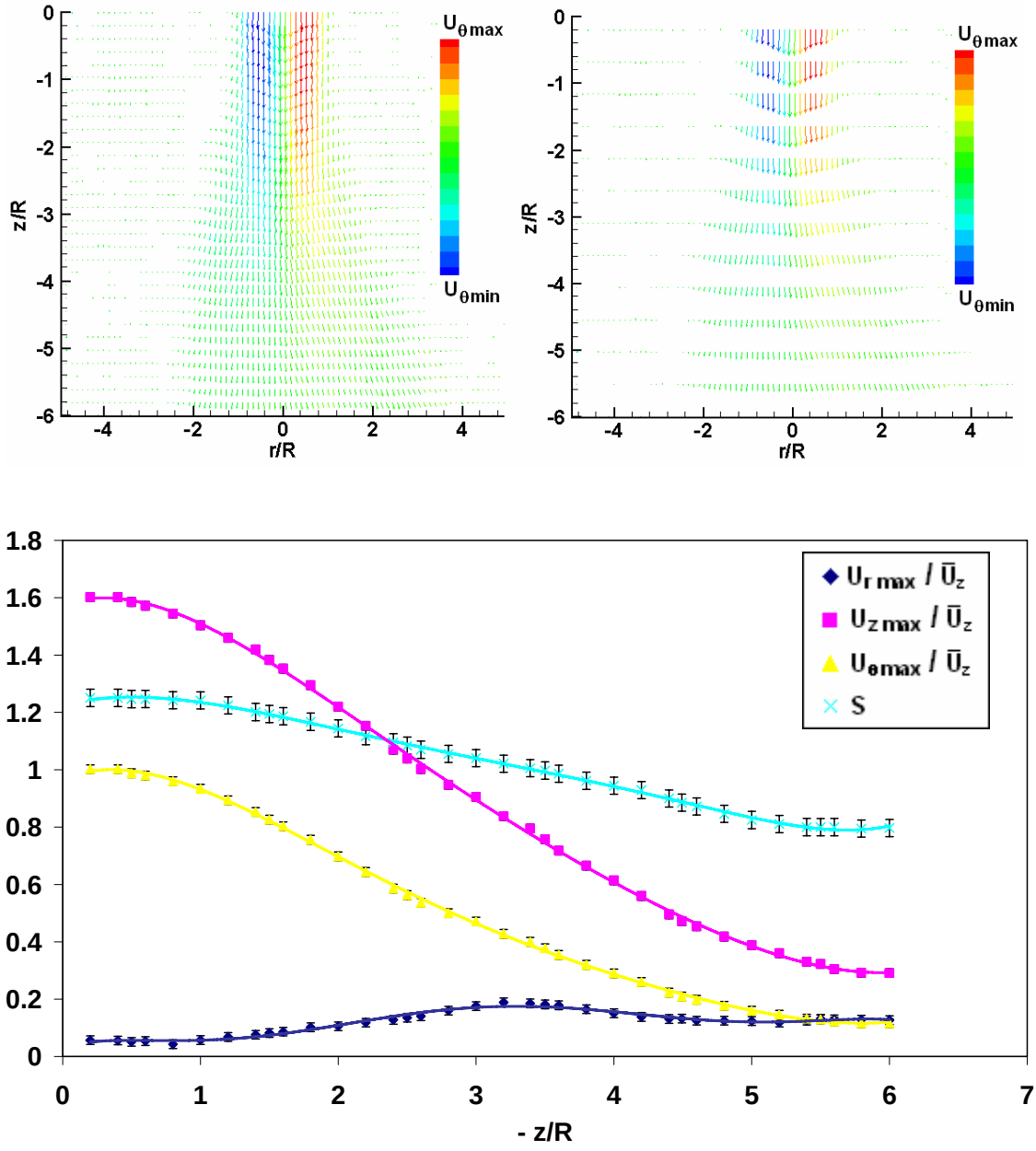

(c) R_e = 900

Figure 3.5: **SPIV velocity profiles (averaged over 150 frames) as a function of the downstream distance z/R. Velocity vector plots qualitatively show the relative velocities with the vector length and direction representing the U_r & U_z velocity components and the colour mapping represents the out of plane velocity magnitude U_θ at (a) R_e = 300, (b) R_e = 600 and (c) R_e = 900 at S = 1.25, i.e. S just below S_c. The maximum velocities and swirl number as a**

function of downstream distance is plotted below each vector plot. Trendlines are least squares fitted polynomials.

same point the azimuthal velocity increases up to approximately S = 1.35 after which point a more gradual decrease results. The reason for this decrease in maximum azimuthal velocity is possibly due to either the complex interaction between the axial and azimuthal velocity or due to the broadening of the vortical core as a result of the close vicinity of the stagnation point. Figure 3.6 also reveals that the rate of increase in the maximum azimuthal velocity is approximately 67% higher than that of the axial velocity when leading up to breakdown but suffers from a lower decrease rate once breakdown has occurred. It is this non-linearity within the maximum velocity that leads to the non-linearity in the swirl number as previously seen in Figure 3.3. The most striking feature of Figure 3.6 is that all Reynolds numbers, $300 \leq Re \leq 900$ coincide and show the same variation in maximum axial and azimuthal velocity (when non-dimensionlised using the average axial velocity, $\overline{U}_z$) versus swirl number.

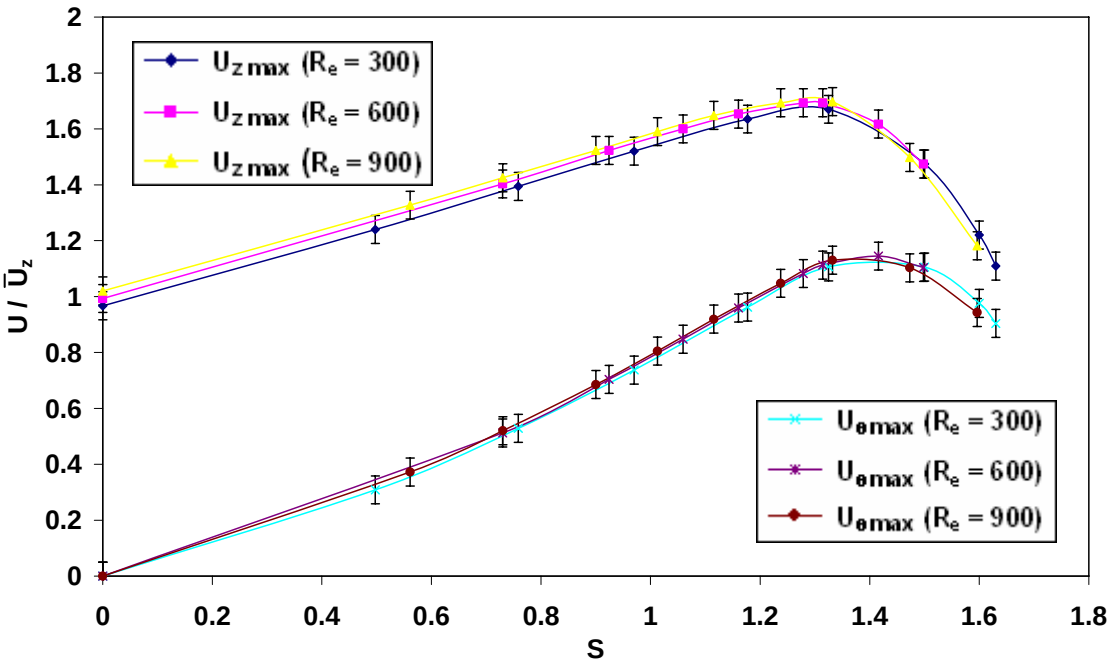

Figure 3.6: **Maximum axial and azimuthal velocity (at z/R = -1) versus swirl number. Results obtained though PIV and SPIV measurements, with an average of 200 image pairs.**

3.3 Vortex Breakdown Onset & Hysteresis

Vortex breakdown can experience hysteresis, which is characterised by the breakdown structure remaining in tact after the swirl number is lowered well below that required to initiate breakdown. There exists a critical swirl number at which breakdown appears, i.e. $S_c = S_a$, and disappears, S_d, due to hysteresis (see Figure 3.7). Above a Reynolds number of approximately 650 to 725, hysteresis no longer exists and is only a low Reynolds number effect. This could be attributed to the unsteady and asymmetric breakdown structure associated with the higher Reynolds number swirling jet. The effects of this asymmetry and unsteadiness are possibly too great to maintain breakdown at such a critical and fragile swirl number, i.e. $S < S_a$.

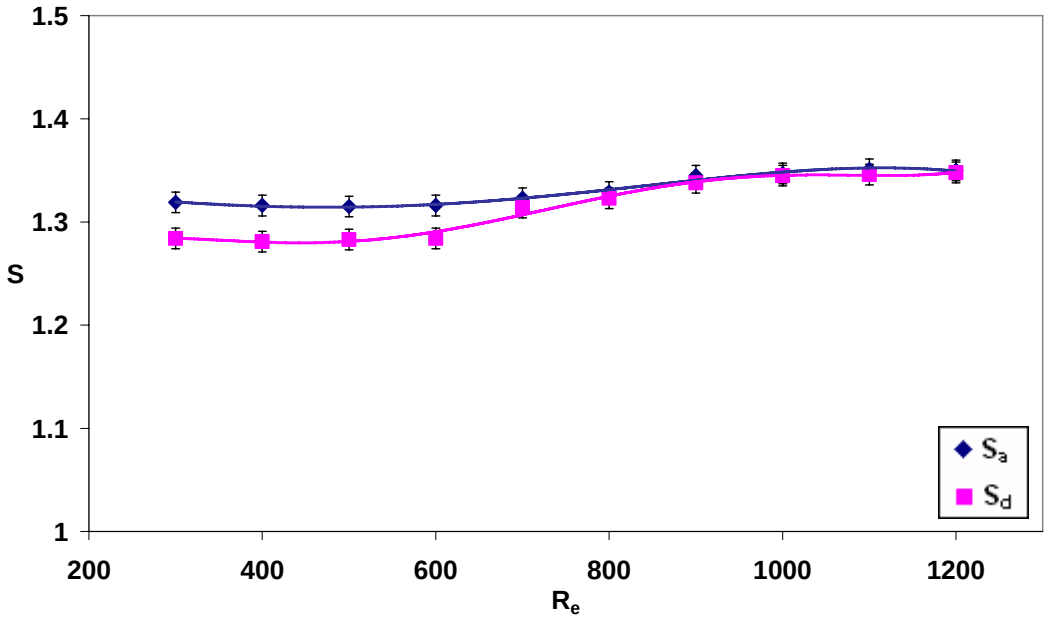

Figure 3.7: **Parametric evaluation (S versus R_e) of the swirl number at which breakdown appears, S_a, and disappears, S_d. Trendlines are least squares fitted polynomials.**

In general, the minimum swirl number for breakdown to occur is in the range of $1.31 \leq S_c \leq 1.35$ for the Reynolds numbers tested ($300 \leq R_e \leq 1200$). There is however a slight increasing trend in the critical swirl number with increasing Reynolds number;

again this could be due to the same reasons of asymmetry and a more unsteady structure associated with higher Reynolds number breakdown. This critical swirl number range ($1.31 \leq S_c \leq 1.35$) is comparable with the experimental results of Billant et al. (1998), who found that vortex breakdown occurs between $1.3 \leq S_c \leq 1.4$. Billant et al. (1998) also states that the critical swirl number for vortex breakdown to occur is "independent of the Reynolds number and nozzle diameter". However as their results show no indication as to the magnitude of the error, there may in fact exist a slight dependency on Reynolds number, whereas Billant et al. (1998) have approximated the critical swirl number as constant. The states experienced at various Reynolds number and swirl number ranges will be examined in detail in section 3.4.

Figure 3.8 shows a more detailed look at the path from S_a to S_d at $R_e = 400$ and $R_e = 600$ and shows the non-linear movement of the stagnation point downstream up to the point of disappearance. Significant downstream movement of the stagnation point, Z_b, is achieved over the hysteretic range with downstream movements in the order of 100% before the disappearance of breakdown. The downstream movement follows an exponential type path for both cases shown and is only offset from one another due to the slight difference in S_a (due to S_a being Reynolds number dependent as mentioned above). Flow visualisations in Figure 3.8 also show that the steady state structure in the hysteretic range is the same as that at $S_c = S_a$, i.e. an open cone type breakdown with an almost stagnant central region (see section 3.4 for more details on this breakdown type).

It will be seen later that the transitional Reynolds number for the occurrence of hysteresis also coincides with the Reynolds number separating axisymmetric and asymmetric breakdown. This boundary lies in the region of $R_e = 725 \pm 19$. It is this coincidence of R_e boundaries which provides the most plausible reason for the disappearance of hysteresis at higher Reynolds numbers. It appears that that the transition to asymmetry and unsteadiness at higher Reynolds numbers is not hysteretic.

As mentioned earlier the azimuthal and axial velocity components interact in a non-linear manner and as a result the swirl number eventually plateaus with increasing rate of rotation. This is consistent with the observation that, for the same increment in swirl, the lower the initial swirl number the higher the upstream axial movement of the stagnation point, Z_b, as can be seen in Figure 3.9. As previously revealed in Figure 3.1 &

3.2, increasing the azimuthal velocity also alters the axial velocity component in a non-linear fashion. This process is also seen to occur in the reverse situation in that if the angular velocity of the vortex generator was kept constant, the azimuthal velocity would increase with increasing Reynolds number (i.e. axial velocity) as seen in Figure 3.10. This is yet another non-linear effect of our experimental setup to which the cause cannot be pinpointed but is most likely due to the contraction, as the vortex core radius remains constant. This is unlike the experiments conducted by Althaus et al. (1995), who also had a similar complex coupling between the velocities in both the horizontal and vertical planes, but was strictly due to the decrease in vortex core radii.

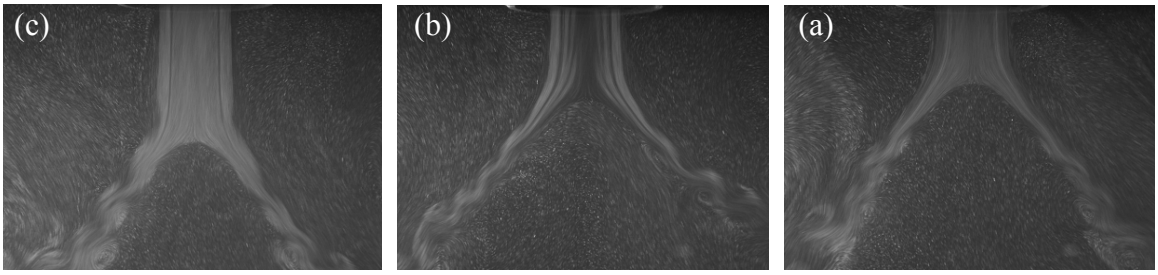

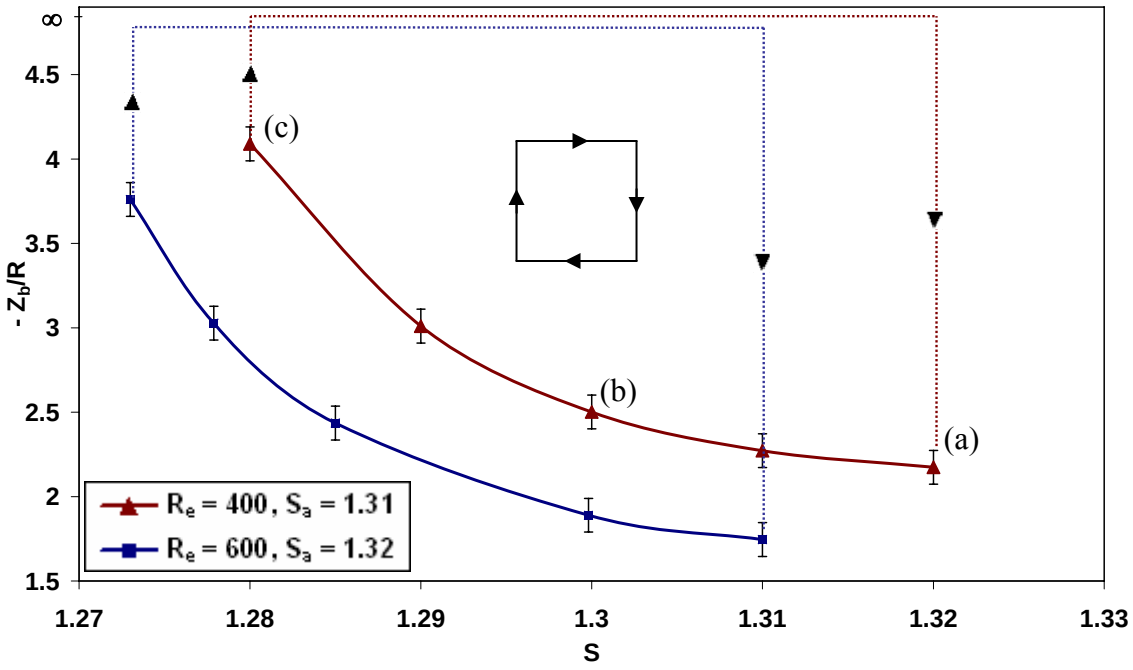

Figure 3.8: **Hysteresis plot of the stagnation point location versus swirl number. Flow visualisations at R_e = 400 accompany the plot, while the arrows indicate that the plot is read in a clockwise manner.**

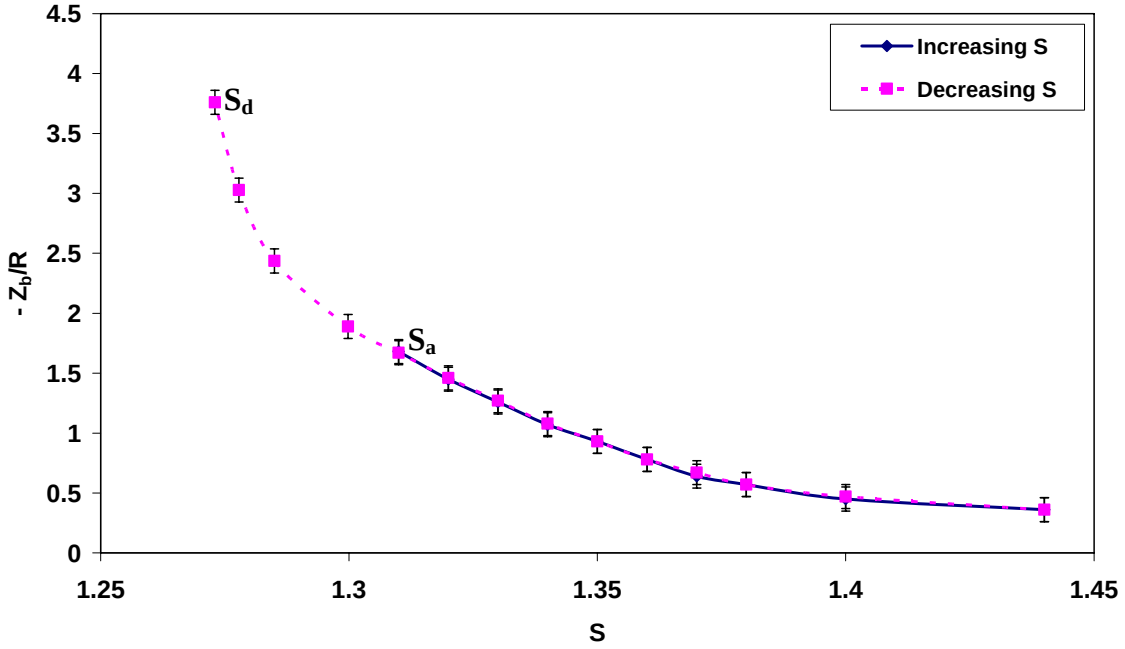

Figure 3.9: **Upstream and downstream movement of the stagnation with increasing and decreasing swirl. Also revealing hysteresis as indicated by S_a and S_d.**

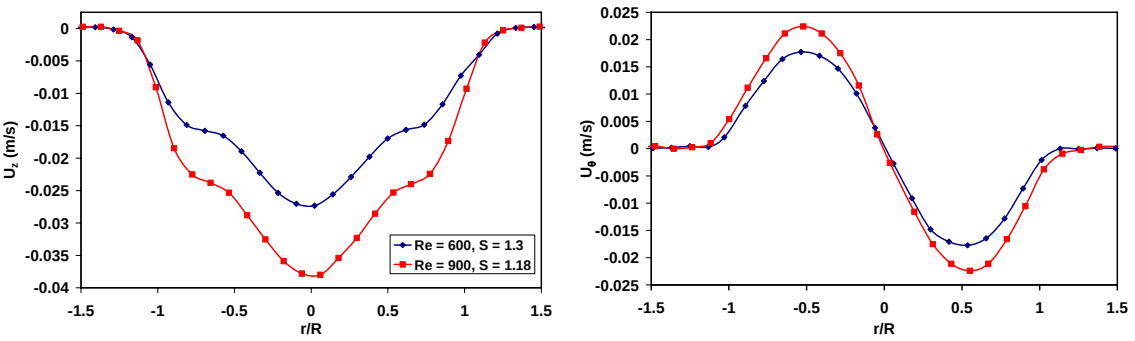

Figure 3.10: **Axial and azimuthal velocity profiles (extracted from an average of 150 SPIV frames at z/R = -1) at R_e = 600 and R_e = 900 when the vortex generator rotation rate is set to ω = 0.682 rpm, showing the complex interaction between the two velocity components.**

3.4 The Evolution of Swirling Jets

By gradually increasing the swirl at all Reynolds numbers tested ($300 \leq Re \leq 900$), a predictable sequence of events occurs which leads to vortex breakdown (see Figure 3.11a

and Figure 3.11b). A general description of the sequence at R_e = 600 (Figure 3.11a) follows. The non-swirling jet (see Figure 3.11a, S = 0) is characterised by the shedding of axisymmetric ring vortices due to the Kelvin-Helmholtz shear instability. The addition of low level swirl (see Figure 3.11a, S = 0.51), causes a tilting of the shed vortex rings (which now appear asymmetric), along with their intensification. At moderate swirl levels (see Figure 3.11a, S = 1), the jet develops asymmetric instabilities downstream, causing its decay into small scale turbulence and a widening of the vortical core. Due to the conservation of both the axial and angular momentum, a further increase in swirl along with an increase in the vortex core radius, results in an increase in pressure within the vortex core, creating an axial deceleration. This process continues until the forces associated with the centrifugal instability outweigh the opposing pressure forces within the vortex core, resulting in a stagnation point and vortex breakdown (see Figure 3.11a, S = S_c = 1.33 (developing)). While the stagnation point begins in the turbulent/disorganised downstream region of the swirling jet, it slowly moves upstream and settles to its new location and final structure (see Figure 3.11a, S = 1.33). The open bubble type breakdown (see Figure 3.11a, S = 1.33 (developing)) appears as a transient/intermediate breakdown structure before settling to an open cone type breakdown (see Figure 3.11a, S = 1.33). Further increases in swirl beyond S_c causes the stagnation point to move further upstream, while again taking the form of a transient open bubble breakdown (see Figure 3.11a, S = 1.37 (developing)). Given sufficient time the breakdown structure settles/transforms back to a steady state open cone breakdown (see Figure 3.11a, S = 1.37) which is more compact than that at lower swirl numbers in that the expansion of the vortex core is smaller and its overall length before breaking up due to turbulence at its tail is reduced.

A closer examination of Figure 3.11a allows the identification of four regimes in which the most dominant features distinguish any regime from any other. The crossover point from one regime to another is not definite and appears to result from the competition between two competing states. At S = 0, strong axisymmetric deformations are the dominant feature with the formation of ring like structures at the jet periphery due to the Kelvin-Helmholtz instability. The jet remains laminar and axisymmetric for more than 8D downstream of the nozzle. The second regime, $0 < S < 1$, a low to moderate swirl

level is introduced which is enough to intensify the shed vortex rings. Khorrami (1995) observed similar behaviour and goes on to state that low levels of swirl increase the entrainment rate of the shear layers. An increase in asymmetric azimuthal disturbances in the downstream region of the jet become apparent and the effects move upstream with increasing swirl. In fact the jet becomes highly unstable between approximately 6D and 7D downstream. Between $1 < S < 1.3$, distinct pinching of the jet occurs downstream and this effect moves upstream with increasing swirl. Above the point of pinching, a broadening of the jet begins to take place, causing its decay into small scale turbulence. Once this balance of asymmetric and axisymmetric instabilities has had sufficient time to reach equilibrium, a coherent and steady trident state (similar to that seen by Billant et al. (1998)) appears before the onset of vortex breakdown in the final regime, $S > 1.3$.

Increasing S above S_c leads to the formation of a stagnation point downstream which gradually travels upstream creating a small open ended bubble in its wake containing a tilted toroidal vortex ring within its internal recirculating flow. Given sufficient time, the instabilities settle and result in a steady cone type breakdown. Further increasing the swirl not only moves the stagnation point further upstream but also gives rise to a much broader transient open bubble type breakdown state which, while in existence, also contains a tilted vortex ring within the internal recirculating flow. The reason for the smaller diameter transient bubble which is seen during breakdown development at $S = S_c$, compared to that at higher swirl numbers, could be attributed to the faster and greater upstream movement which the stagnation point must undergo to settle to its new steady state position. While the stagnation point is moving upstream, there exists a higher average relative velocity difference between the internal and external regions than when it has reached its steady state position. This leads to a pressure difference which counteracts the centrifugal forces and limits the structure's expansion, which only begins to expand into a cone type breakdown once the stagnation point has stopped moving upstream. The above mentioned toroidal vortex ring is responsible for the filling and emptying process by simultaneously expelling fluid from the upstream region and absorbing fluid at its base, which is in agreement with Sarpkaya (1971) and contradictory to Faler and Leibovich (1977b). The stagnation point is still moving upstream, extremely slowly. Once stagnation point movement upstream has ceased a

steady state cone structure reappears. Further increasing the swirl results in the same combination of events, however, the resultant cone breakdown is more compact and breaks into small scale turbulence sooner than at lower swirl numbers. It was also observed that further increases in swirl causes the internal vortex ring of the transient bubble to intensify and gives rise to multiple recirculation regions within the bubble.

Higher Reynolds number flows, as shown in Figure 3.11b, reveals that the sequence of events leading to breakdown are qualitatively very similar to that at lower Reynolds numbers. Mitchell et al. (2000), Mitchell and Delery (2001) have shown that at very high Reynolds numbers ($2x10^6 \leq R_e \leq 20x10^6$) vortex breakdown, the natural Strouhal frequencies are "similar to those determined at much lower Reynolds numbers" suggesting the possibility for similar low Reynolds number studies to give insight into much higher Reynolds number domains. There are, however, very prominent differences in the breakdown structure of the swirling jet for $S > S_c$ due to its more turbulent nature at higher Reynolds numbers. The following sections will provide a more detailed examination of the above mentioned differences, in addition to the presentation of both qualitative and quantitative results, to fully define the flow under investigation.

Results at higher Reynolds numbers, $Re \geq 725 \pm 19$, as can be seen in Figure 3.11b, reveal that although the swirling jet's development is quite similar to that for lower Reynolds numbers, in that the same four regimes still remain, there are still unique features associated with this higher Reynolds number domain. The most noticeable difference in the development process leading to breakdown is the point at which the structure becomes highly disorganised and its dissipation into small scale turbulence occurs further upstream. Once breakdown has occurred, it is asymmetric due to the precession of the off-axis stagnation point about the central axis in the same rotational direction as the vortex core, in agreement with observations by Billant et al. (1998), Bruecker (1993), Bruecker and Althaus (1992).

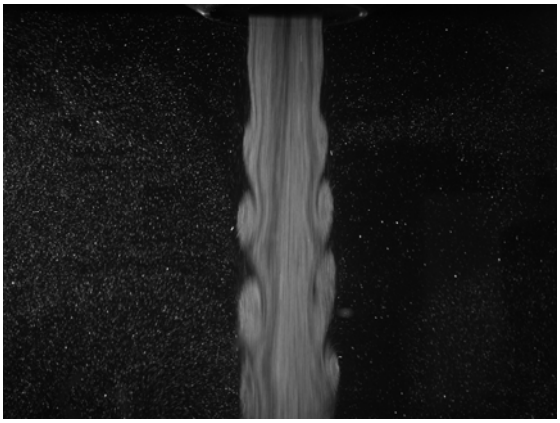

S = 0

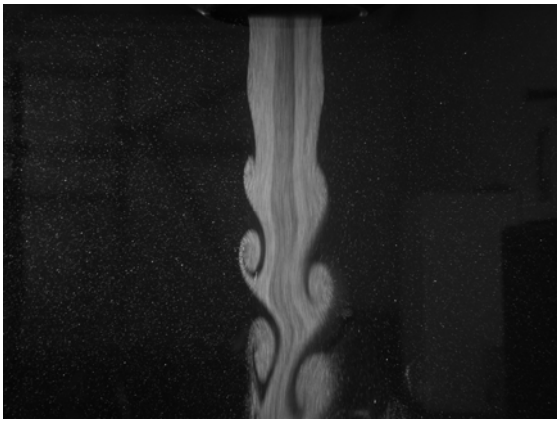

S = 0.51

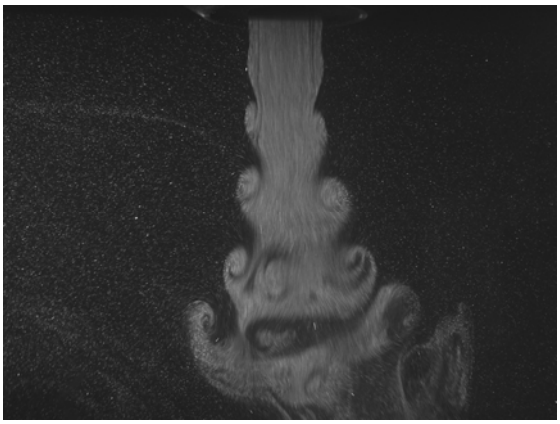

S = 1

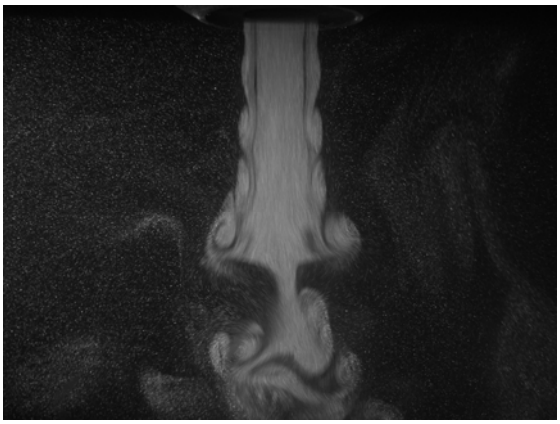

S = 1.23

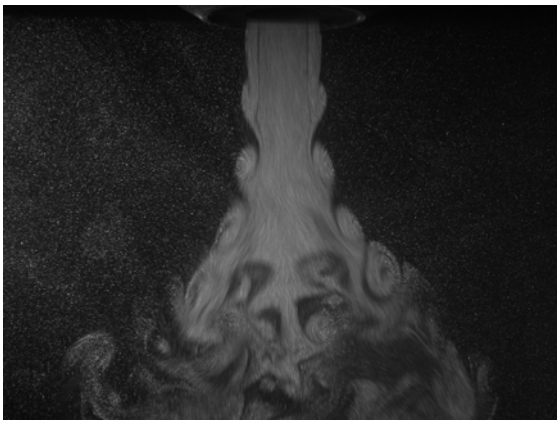

S = 1.3

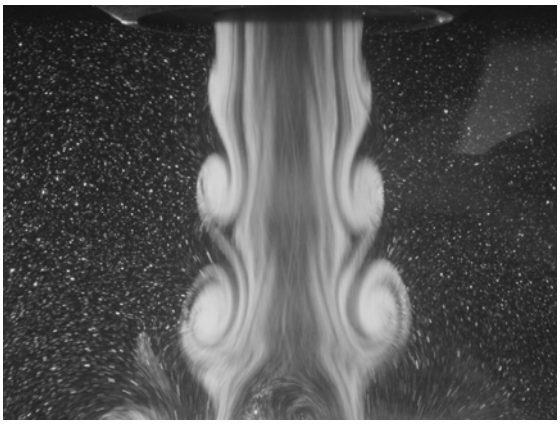

S = 1.33 (developing)

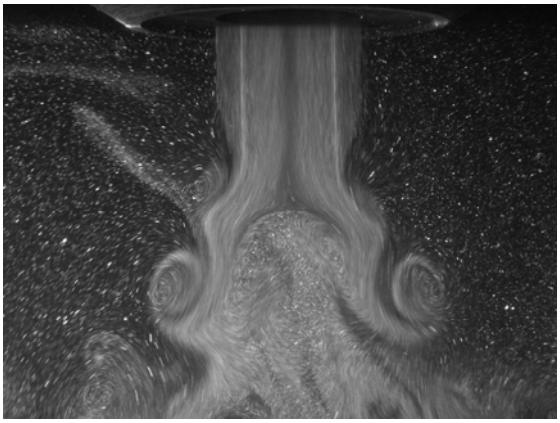

S = 1.33 (developing)

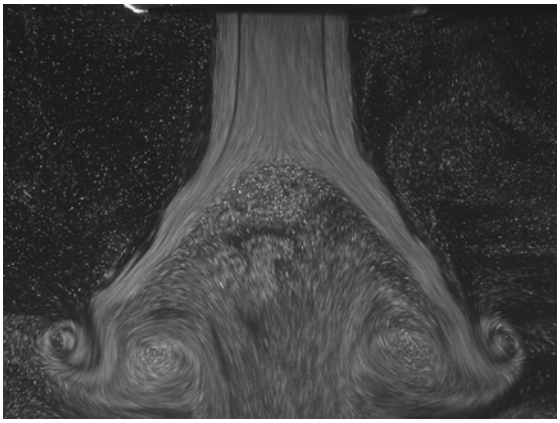

S = 1.33

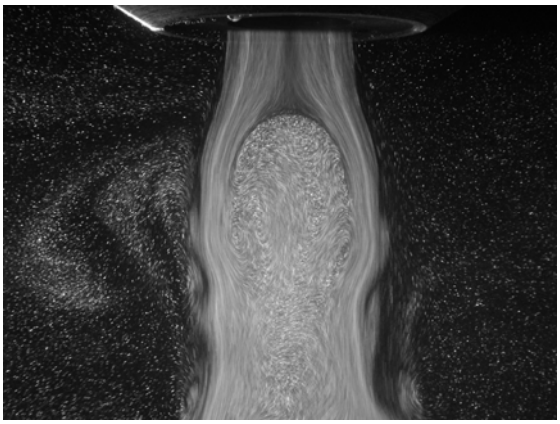

S = 1.37 (developing)

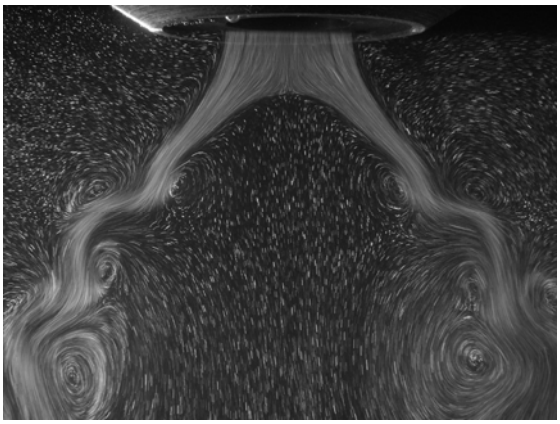

S = 1.37 (developing)

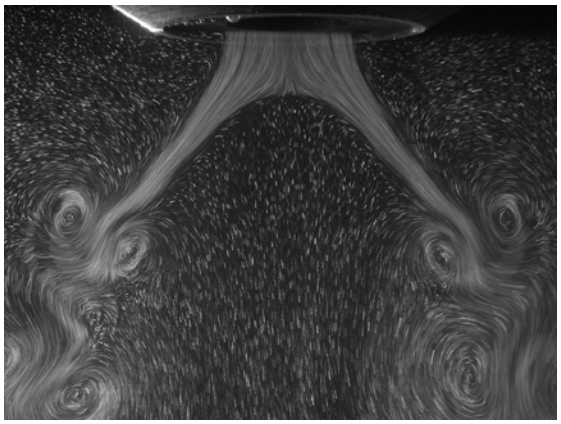

S = 1.37

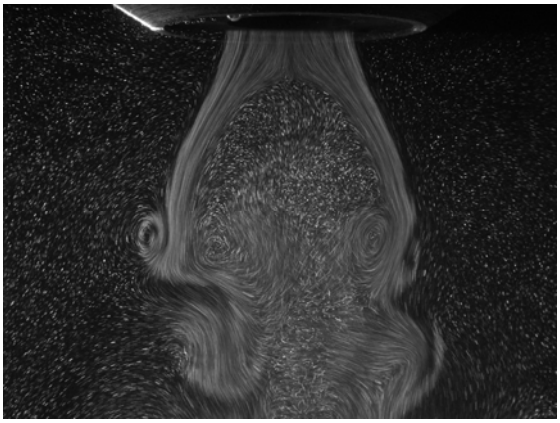

S = 1.4 (developing)

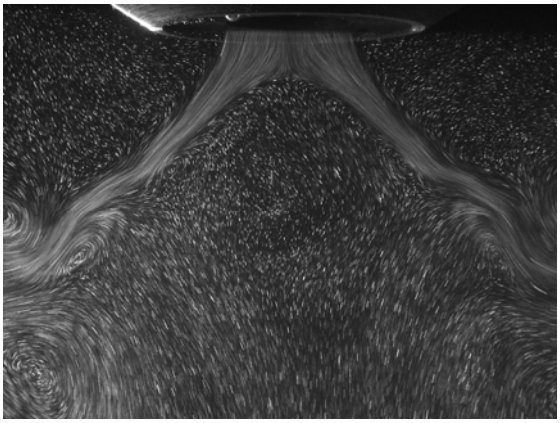

S = 1.4

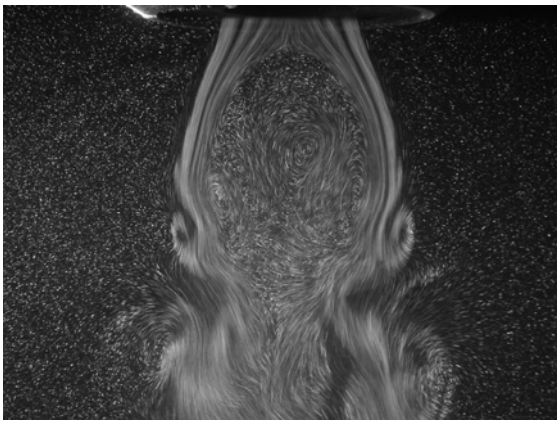

S = 1.44 (developing)

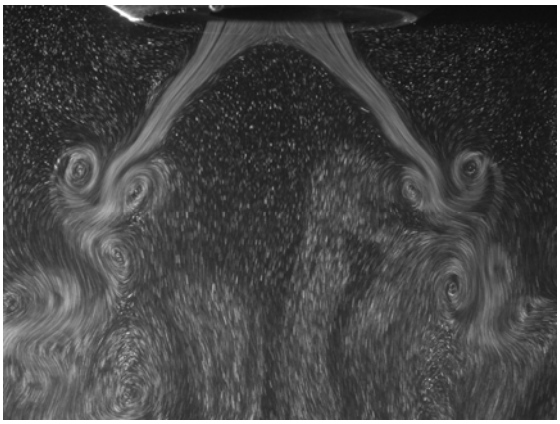

S = 1.44

Figure 3.11a: Evolution of a swirling jet at R_e = 600 (representative of 300 $\leq$ R_e $\leq$ 725), up to and beyond S_c.

Another feature of note at higher Reynolds numbers is a more open ended breakdown state, which is almost a mix of a bubble and a cone state. The transitional bubble state no longer exists. Discounting temperature differences and in turn buoyancy effects (which are considered in Chapter 4 of this thesis), the reason behind this mixed structure, which is neither a cone or bubble breakdown, is attributed to the higher internal velocities that exist along the centreline due to the precessing stagnation point. Again, these higher internal velocities create an opposing pressure gradient to the centrifugal forces which cause the expansion, hence inhibiting the formation of an open cone type breakdown. A closer examination of all the above mentioned breakdown states follows.

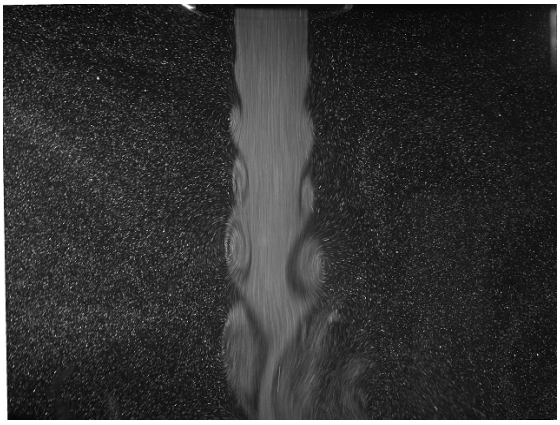

S = 0

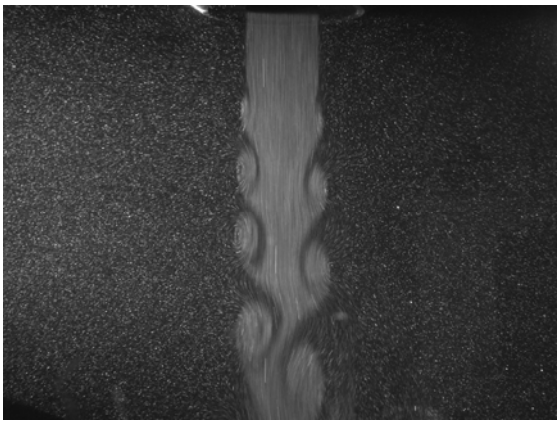

S = 0.23

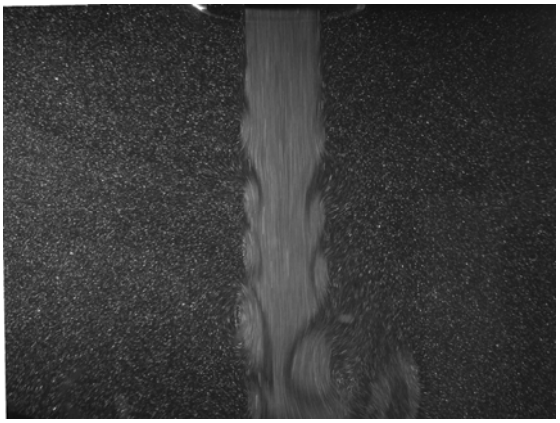

S = 0.82

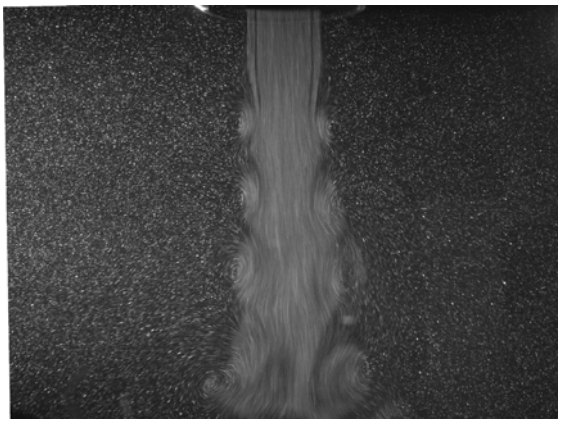

S = 1.04

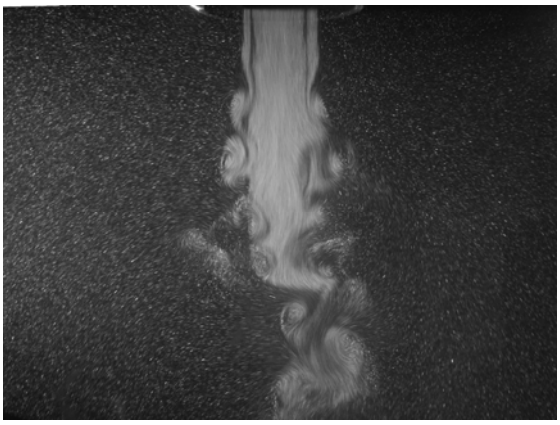

S = 1.22

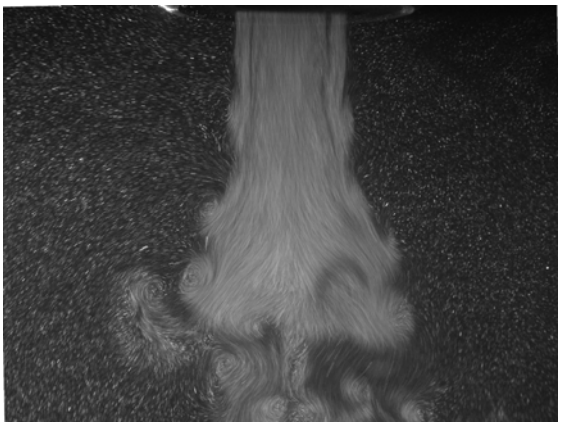

S = 1.3

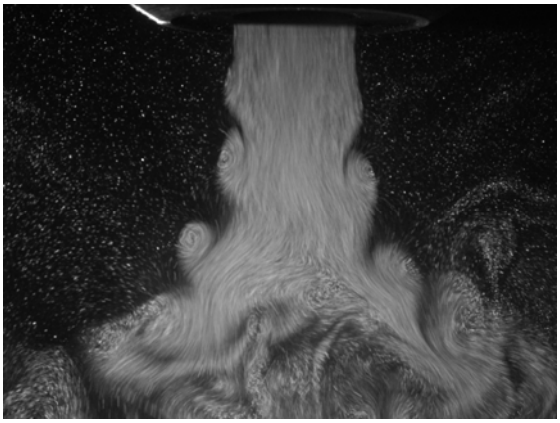

S = 1.32

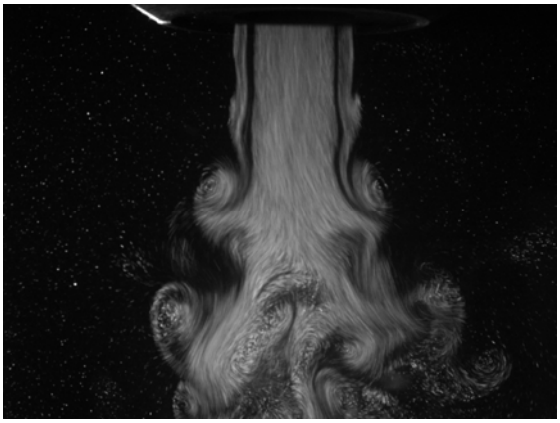

S = 1.34 (developing)

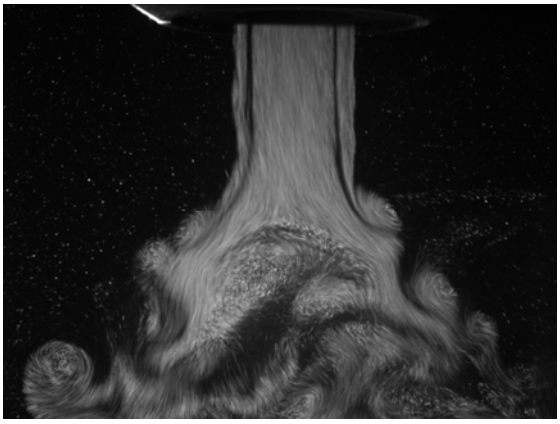

S = 1.34 (developing)

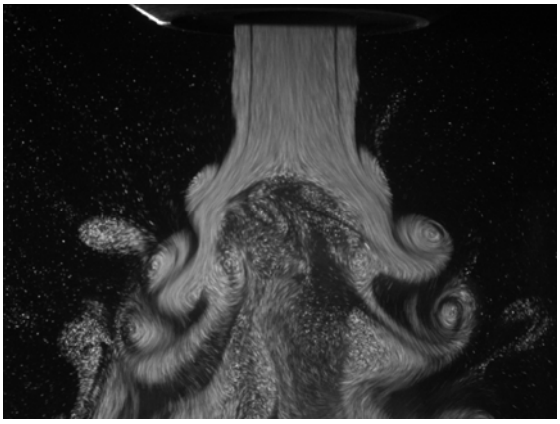

S = 1.34 (developing)

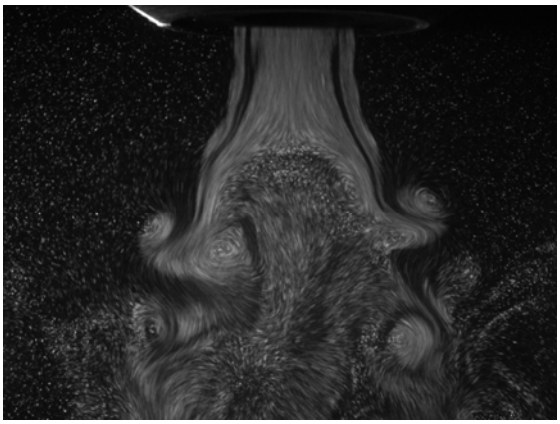

S = 1.34

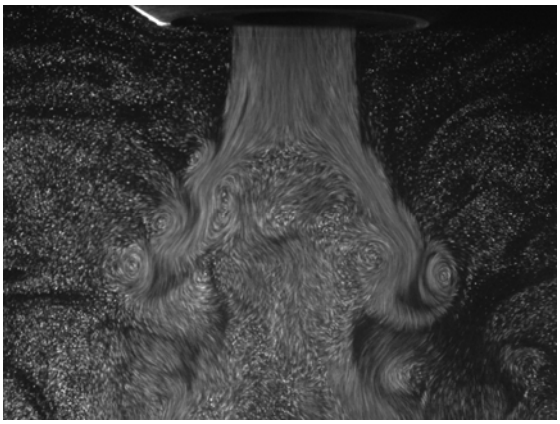

S = 1.34

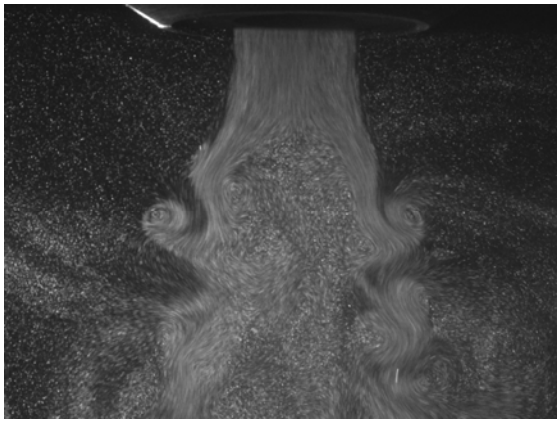

S = 1.36

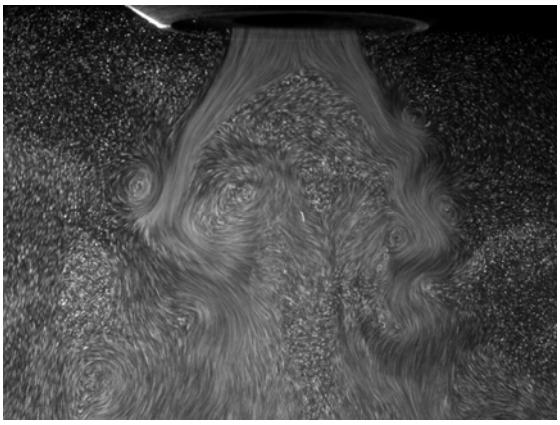

S = 1.39

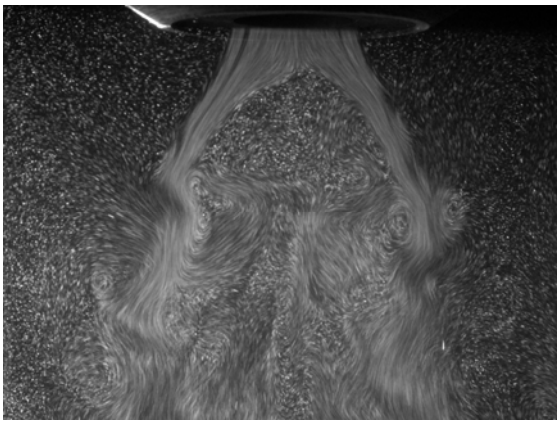

S = 1.39

Figure 3.11b: Evolution of a swirling jet at R_e = 900 (representative of 725 $\leq$ R_e $\leq$ 900) up to and beyond S_c.

3.4.1 Transitional Open Bubble Breakdown

A closer examination of the transitional bubble structure (between 300 $\leq$ R_e < 725 as seen in Figure 3.11a, S = 1.33 (developing), 1.37 (developing), 1.4 (developing) and 1.44 (developing)) at various swirl numbers is presented herein. The expansion of the vortical core due to the appearance of a stagnation point moving upstream creates a parabolic cross-section inner surface in the axisymmetric upstream region, while maintaining an asymmetric turbulent and disorganised downstream tail. It appears as if a solid object

with a profile matching the internal parabola shape was placed along the centreline of the swirling jet. The vortex expansion in the shape of a bubble had radial dimensions of 1D - 2.5D in diameter which enclosed a slow moving, elliptical cross-section recirculating region.

As previously mentioned the internal structure of the transient bubble consists of a tilted toroidal vortex ring, which is responsible for the filling and emptying process. Streak line flow visualisation in Figure 3.12 and streamtraces obtained via SPIV in Figure 3.13 show the internal structure of the transient bubble. SPIV (Figure 3.14) and PIV measurements have also revealed that the internal structure's azimuthal and axial velocities are relatively weak within the internal zone of the bubble in comparison to that of the surrounding flow. The maximum axial and azimuthal velocities associated with the internal recirculating bubble are generally only 40% of the maximum axial and azimuthal velocities of the upstream vortex. Radial velocities in the centre of the bubble are highest at the downstream tip of the tilted toroidal vortex ring. A more general view is provided by the magnitude of the 3-D velocity vector, defined as:

$$\left|U\right| = \sqrt{U_r^2 + U_z^2 + U_\theta^2}\ . \qquad \textbf{(3.4)}$$

For all Reynolds numbers and swirl numbers tested, a maximum velocity magnitude of only 30 % of the upstream vortical core exists within the interior of the recirculating bubble.

A cross-section of the internal region of the bubble, as seen in Figure 3.13, shows a cross-section of the internal tilted vortex ring. Observations from 30 Hz video of the internal tilted toroidal vortex ring have revealed that the near axis region absorbs fluid from the downstream portion flow and expels fluid from the upstream outer periphery of the internal structure. This is in agreement with experiments by Sarpkaya (1971), but contradictory to those of Faler and Leibovich (1977b). Unsteady three-dimensional numerical simulations by Spall et al. (1990) found similar structures within confined tubes, and are in agreement with the internal structure of the transient bubble presented here. The structure appears organised, and besides exhibiting a slight tilt in the vortex ring due to the swirl component travelling downstream in a helical fashion, the structure

is almost symmetrical. Increasing swirl levels lead to a more asymmetric internal structure containing a much more disorganised recirculating internal region (see for example Figure 3.11a, S = 1.44 (developing)). The position of the internal tilted vortex ring coincides with the point of Kelvin-Helmholtz type vortex shedding on the external shear layer surface. Hence, the internal shear layer roll up appears as a tilted toroidal vortex ring.

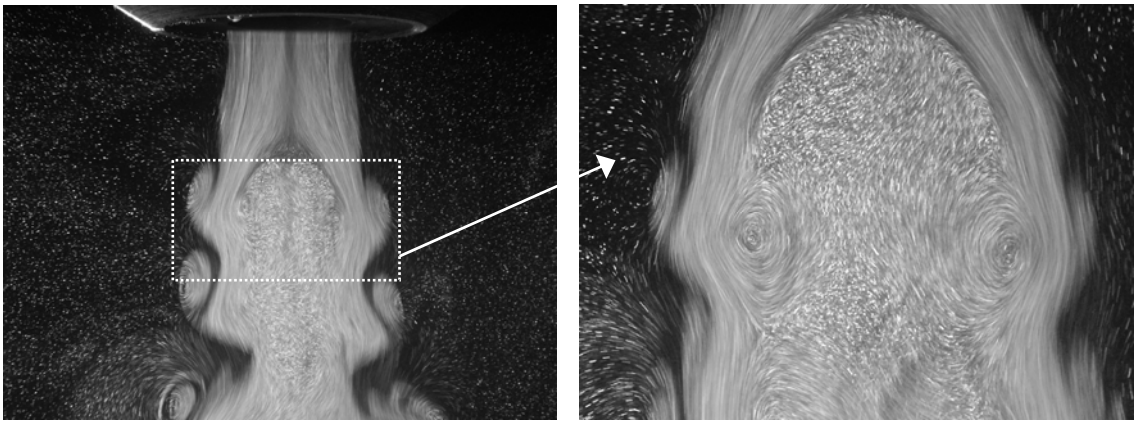

Figure 3.12: Flow visualisation showing streak lines of the transitional bubble including the internal structure at R_e = 600, S = 1.35.

Figure 3.15 shows that during the early stages of the transient bubbles development, the internal structure may contain more than one internal tilted vortex ring. Again these vortex rings coincide with the positions of shear layer ring vortices. It is not clear how multiple internal vortex rings affect the filling and emptying process and is definitely an area open to further investigation; however, it is beyond the scope of this particular investigation.

Comparing the internal structure of the transitional vortex breakdown bubble to that of confined experiments such as those experimentally conducted by Bruecker and Althaus (1992), Faler and Leibovich (1977a), Faler and Leibovich (1977b) have shown only one internal tilted vortex ring in their steady state recirculating bubble, which is similar to the internal structure of this observed transitional bubble when it is in the final stages of development (see for example Figure 3.11a, S = 1.4 (developing)). However, the confined structure in the former case is a closed bubble state which also promotes an

internal recirculating tilted vortex ring. The closed bubble state is more symmetrical due to the effects of confinement limiting asymmetrical instability. Confinement effects also counteract/limit centrifugal instability which gives rise to a steady state cone breakdown in unconfined vortex breakdown experiments.

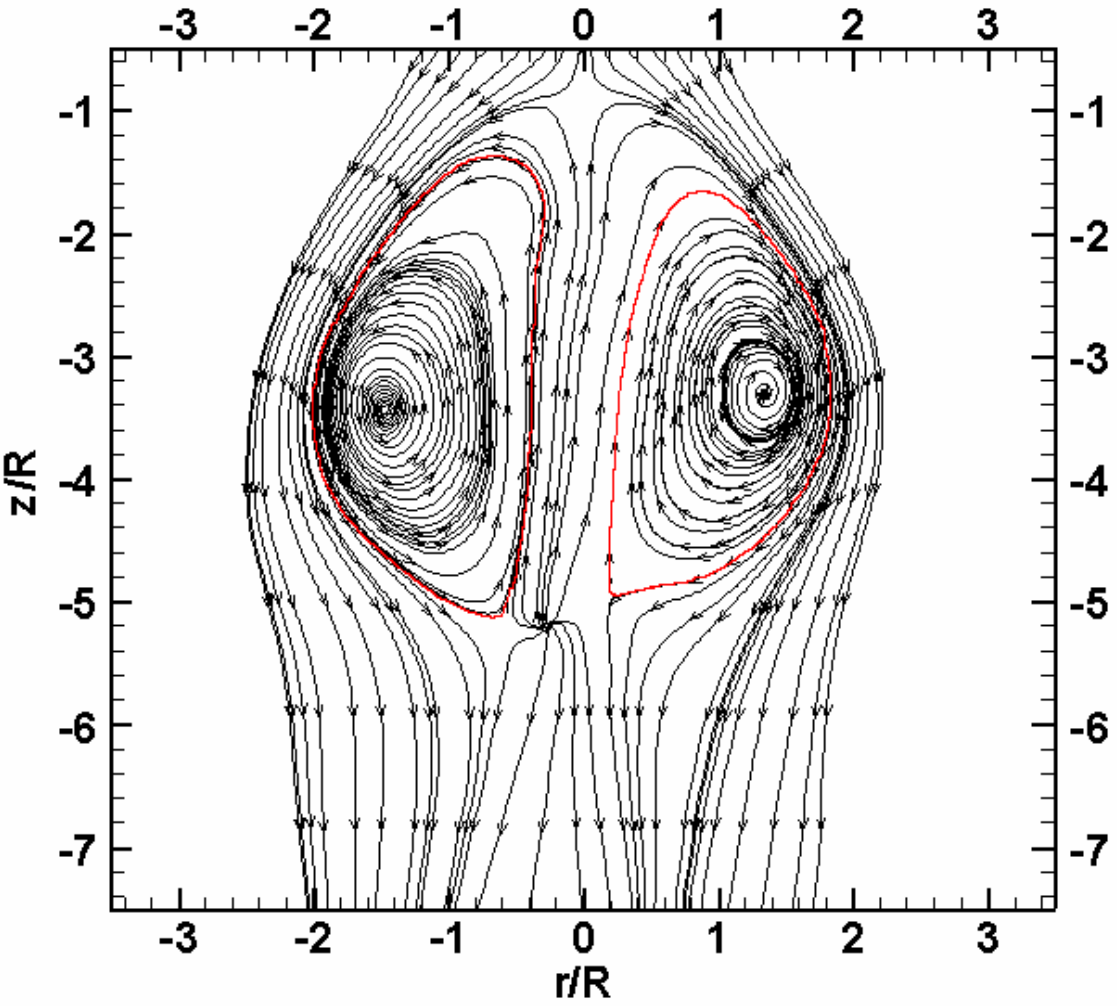

Figure 3.13: **Instantaneous SPIV data at R_e = 600, S = 1.36, showing streamtraces of the transitional bubble including. A central cross-sectional cut of the tilted toroidal vortex ring is highlighted by the red lines.**

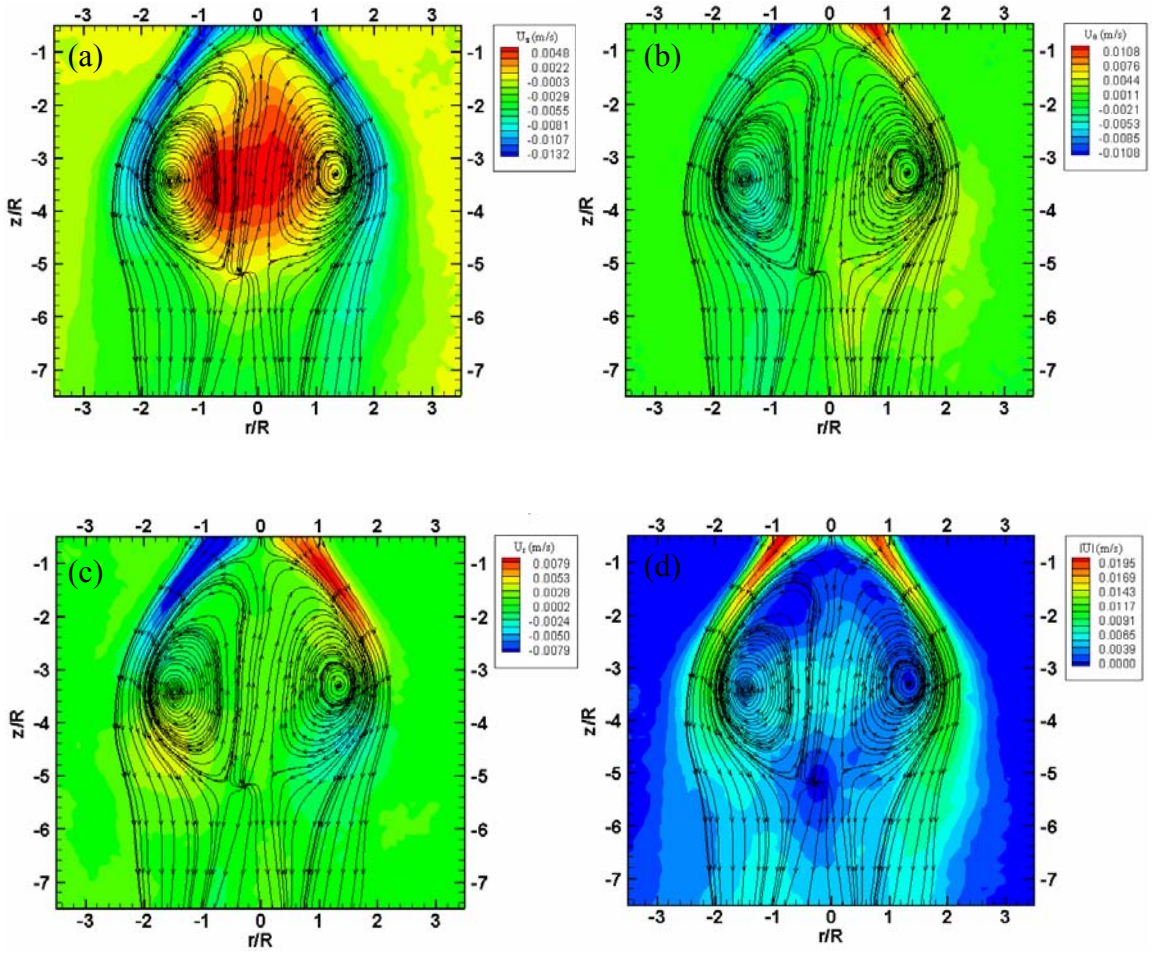

Figure 3.14: **Instantaneous SPIV data at R_e = 600, S = 1.36, showing streamtraces of the transitional bubble and contours of velocity magnitude for all three velocity components, (a) U_z, (b) U_θ, (c) U_r and (d) magnitude of the 3-D velocity vector $|\mathbf{U}| = \sqrt{U_r^2 + U_z^2 + U_\theta^2}$, equation (3.4).**

Also pertinent to the current discussion is the case in which there is co-flow around the swirling jet undergoing breakdown as seen in delta wing experiments (see reviews by Mitchell and Delery (2001), Ozgoren et al. (2002)). In such situations, the breakdown structure is very similar to that of confined breakdown with the co-flow creating a similar confinement effect on the breakdown structure, possibly inhibiting the centrifugal instability and restricting breakdown to the bubble and not the cone state.

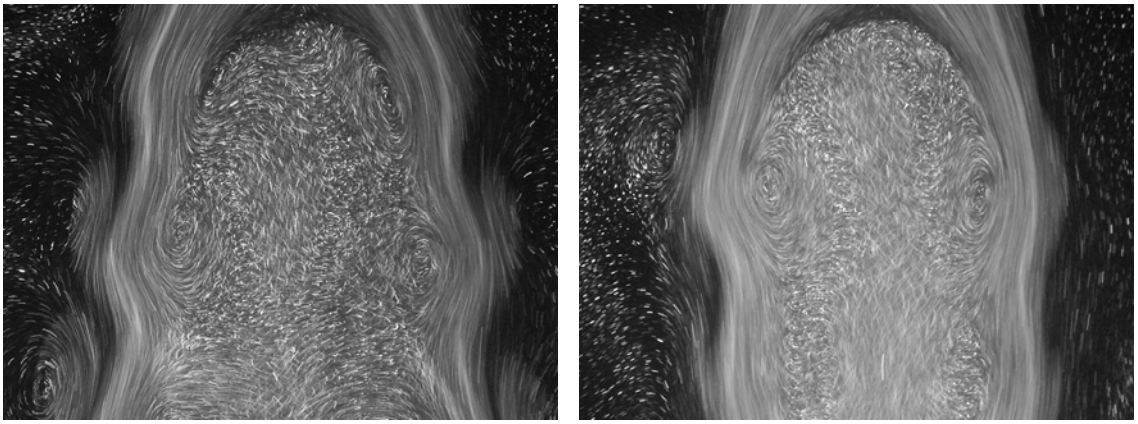

Figure 3.15: Flow visualisation showing streamlines of the transitional bubble including the internal structure at R_e = 600, S = 1.36 at two different times during its upstream movement. More than one tilted internal vortex ring can exist during the breakdowns upstream movement with the location of the vortex ring coinciding with the exterior shear layer shedding axial positions.

Both horizontal and vertical plane cross-sections of the transient bubble reveal that its radial diameter is highly dependent on the initial swirl value. Three factors which influence the horizontal plane diameter are, the initial axial location of the stagnation point, the magnitude of the change in rotational velocity (swirl) and the rate of change of rotational velocity, $\dot{U}_\theta = dU_\theta/dt$, from one setting to the next. To explore this further, it helps to refer to Figure 3.9 recalling that, the initial swirl number, the magnitude of the swirl rate increase/decrease and swirl increment determines the rate and distance over which the stagnation point will move up or downstream. Recall also, that in section 3.2 it was shown that if the Reynolds number is kept constant and the swirl number is increased, the axial velocity along the jet axis begins to increase. This increase is due to the increase of angular velocity through the contraction zone, which leads to a decrease of the pressure near the axis. The increase in axial velocity is not a linearly increasing function with increasing azimuthal velocity and, as a result, the variation of swirl parameter with the rotation rate of the motor tends to plateau. Hence, for the same increment in swirl, the lower the initial swirl number the higher the upstream movement of the stagnation point. Figure 3.16 and Figure 3.17 show flow visualisations which confirm the above argument concerning the cross-sectional diameter of the transitional

bubble. Figure 3.16 reveals a 45% increase in the maximum cross-sectional diameter of the bubble when the swirl increment is halved. Figure 3.17 also shows a 45% increase in the maximum cross-sectional diameter of the bubble when the rate of rotation is halved for a set swirl increment.

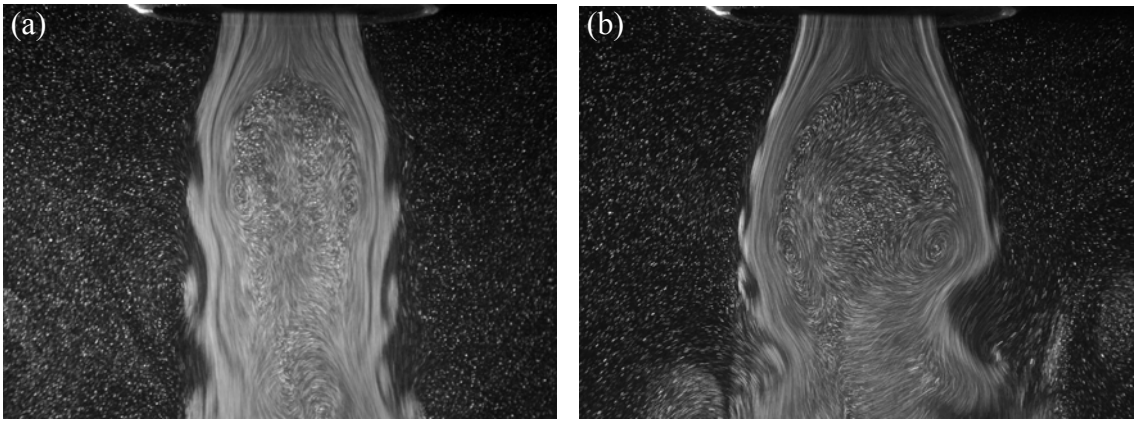

Figure 3.16: Flow visualisation at R_e = 600 showing the different diameter bubbles which result when changing the swirl from (a) S = 1.35 → 1.39 and (b) S = 1.37 → 1.39. Note that the rate of change of rotational velocity was the same in each case. (b) shows a 45% larger diameter than that of (a).

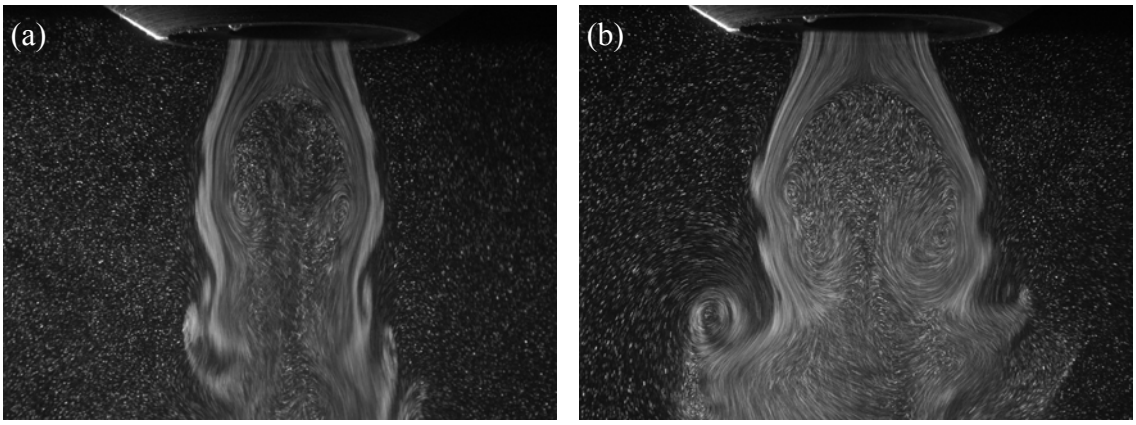

Figure 3.17: Flow visualisation at R_e = 600, showing the different diameter bubbles which result when changing the rate of change of the rotation rate of the vortex generator from (a) $\dot{U}_\theta = 6.2x10^{-4} rad/s^2$ and (b) $\dot{U}_\theta = 1.24x10^{-3} rad/s^2$. For the same increment in swirl S = 1.37 → 1.4, (b) shows a 45% larger diameter than that of (a).

3.4.2 Steady State Cone Breakdown

A closer examination of the steady state cone structure (between $300 \leq R_e < 725$) at various swirl numbers is presented in this section. As the name suggests, the cone breakdown is the steady state structure which results when sufficient time is given for the asymmetric disturbances to diminish and stagnation point movement to settle to its new equilibrium position. In general, the transient times for this particular set of experiments are of the order of 10-15 minutes, during which the transient bubble state ($300 \leq R_e < 725$) is seen. The above description corresponds to the evolutionary process of a swirling jet as shown in Figure 3.11a.

Cone breakdown is identified by its symmetric laminar open core structure, and the existence of a stagnation point on the vortex axis. The cone is an open ended structure which does not contract in diameter further downstream, and contains an extremely slow moving recirculating region. Streamtraces in Figure 3.18 show that the conical sheet thickness is inversely proportional to the downstream distance from the stagnation point, as expected from conservation of mass. As the cone convects downstream, the core radius increases and the conical sheet thickness becomes inversely proportional to r^2. At a downstream axial distance of approximately 2 nozzle diameters, the Kelvin-Helmholtz instability rapidly develops on the very thin, and as a result, unstable conical sheet. This causes the bottom edge of the cone to roll up into small scale vortices prior to breakdown into weak turbulence.

The internal recirculating region of the cone is much broader and far less intense than that of the bubble and all three velocity components are relatively very low (almost negligible), as seen in Figure 3.19. Again considering conservation of mass, we can attribute the negligible internal velocities to the increasing radial expansion of the cone, in contrast to the contracting downstream region of the bubble; this results in significantly slower and weaker velocities than those present within the bubble. It is important to note that the streamtraces within the internals of the cone are time dependant, and due to the negligible internal velocities, streamtraces within this region are very sensitive to PIV errors.

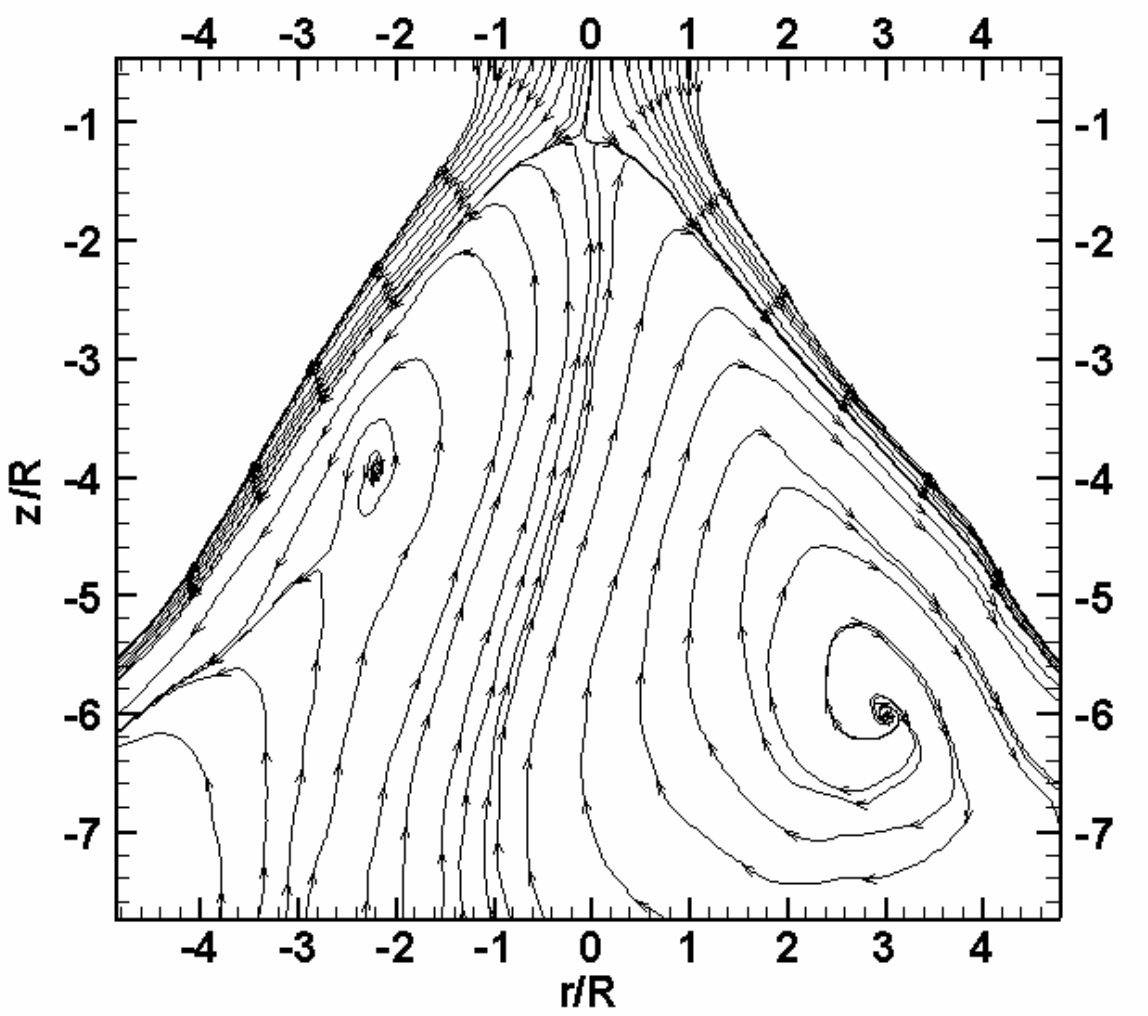

Figure 3.18: Instantaneous SPIV data at R_e = 600, S = 1.34, showing streamtraces of the steady state cone, clearly visible is the thinning conical sheet.

Billant et al. (1998) have found that "the cone angle varies with time in a regular and well-defined fashion while the stagnation point wanders back and forth along the jet axis". This particular phenomenon was not experienced during our sets of experiments, and although both experimental setups are quite similar, there are distinct differences which could account for the difference in behaviour. Firstly, the rig of Billant et al. (1998) contained two "constant-head" tanks in their "semi-open" loop system as opposed to our non-pulsing closed loop system. It is possible that the above mentioned constant-head tanks introduce a low frequency variation in the flow rate due to their inherent mechanism of overflowing in order to maintain constant head at all times. Experimental

simulations of similar low frequency variations in the mass flow rate were conducted via a signal generator controlled inverter on the pump motor. Figure 3.20 shows the variation in the cone breakdown structure when the mass flow is varied by only ±1% (i.e. $m_\upsilon = 1\%$ as previously defined in chapter 2 by equation (2.5)) in a sinusoidal fashion as previously seen in chapter 2 in the form:

$$\dot{m} = \overline{m} + (\dot{m}_{max} - \overline{m})\sin(2\pi f\ t)\,, \qquad \textbf{(2.1)}$$

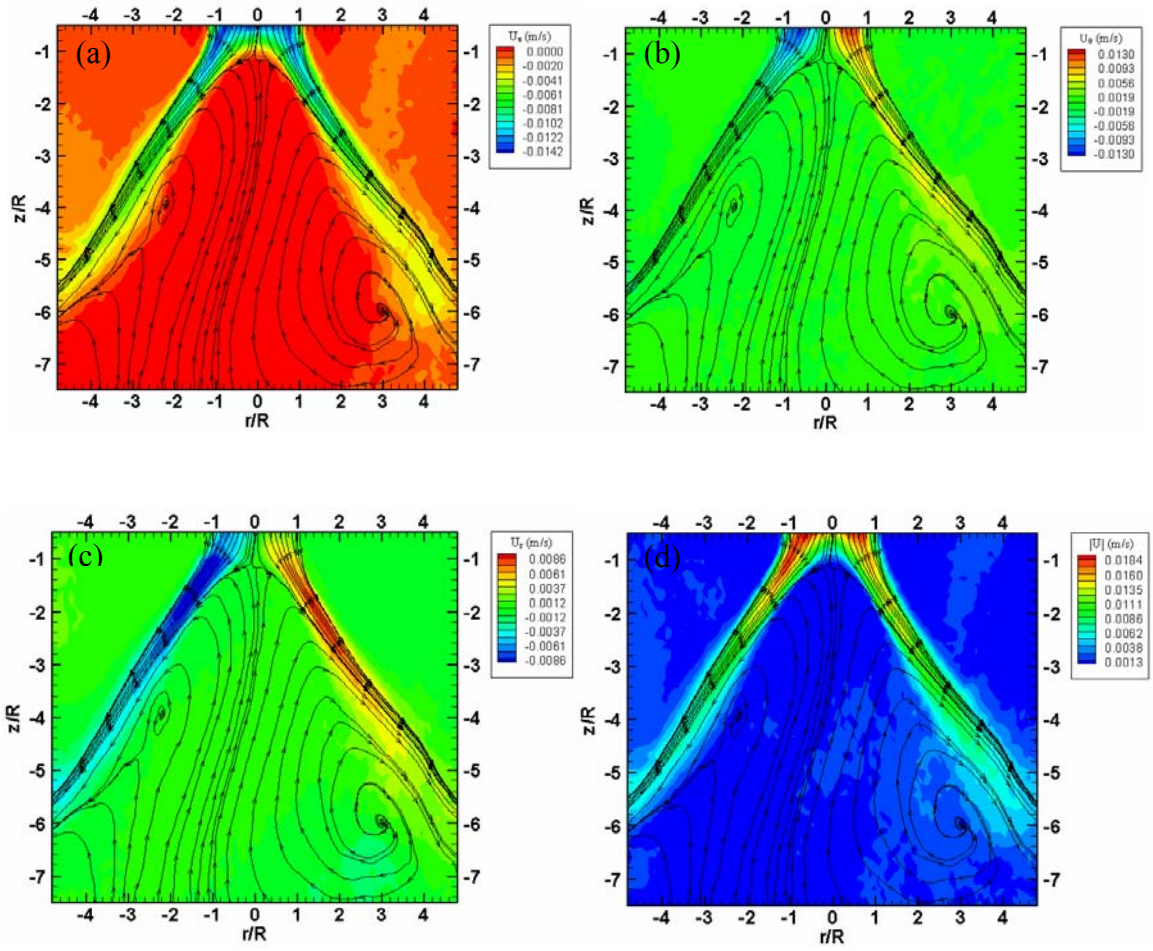

Figure 3.19: **Instantaneous SPIV data at R_e = 600, S = 1.34, showing streamtraces of the steady state cone, and contours of velocity magnitude for all three velocity components, (a) U_z, (b) U_θ, (c) U_r and (d) magnitude of the 3-D velocity vector $|\mathbf{U}| = \sqrt{U_r^2 + U_z^2 + U_\theta^2}$, equation (3.4).**

with a period of T = 1/f = 480 seconds. It is clear that even very small changes in flow rate, which can easily occur in experimental setups, can have a profound effect on breakdown. The effect extends further than just changing the extremities of the cone and stagnation point location. It also affects the shear layer roll up and at worst excite unwanted natural frequencies leading to misleading and or inaccurate results.

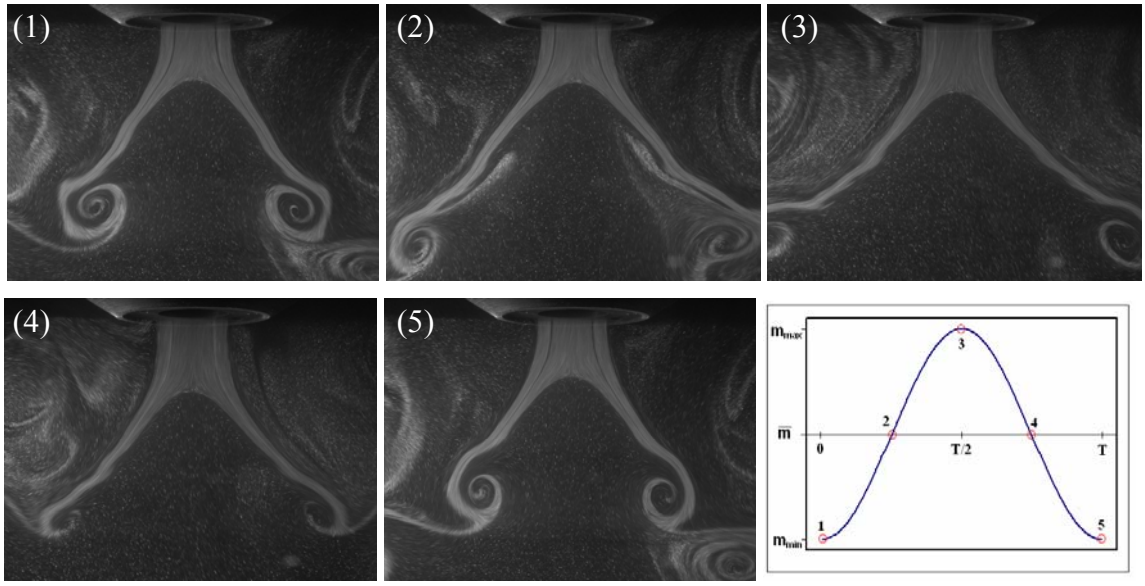

Figure 3.20: **Flow visualisation at R_e = 600, S = 1.34, showing the variance in cone structure with a ±1% (m_υ = 1%) sinusoidal variation in mass flow rate. Each image (1) - (5) corresponds to the mass flow rate as shown in the bottom left graph.**

3.4.3 Asymmetric Breakdown

A closer examination of the asymmetric breakdown structure (between $725 < R_e \leq 900$) at various swirl numbers is presented herein. Asymmetric breakdown, which occurs at higher Reynolds numbers than those of its symmetric counterparts, can be neither classified as a cone or bubble. It differs from the bubble in that it no longer contains a tilted toroidal vortex ring and the internal structure is variable, and as a result, extremely time dependent. This again differs from that of the cone's internal stagnant region, which has almost negligible velocity and recirculation. Observations indicate that the open

ended structure is clearly wider than the bubble and narrower than the cone. The feature that most strongly suggests that this asymmetric breakdown state should have its own classification is the existence of a co-rotating off-axis stagnation point. It is this precessing stagnation point which is the main cause of asymmetry and the highly time dependent nature of the structure.

Figure 3.21 is an example of the asymmetry which higher Reynolds number breakdown exhibits, with the right portion resembling a bubble and the left a cone type breakdown in picture (a). The precession of the stagnation point about the axis causes the configuration to alternate in appearance from right to left as can be seen when comparing (a) and (b) in Figure 3.21.

The asymmetric breakdown type is associated with higher Reynolds numbers. Due to the fact that it contains similarities to that of lower Reynolds number breakdown (see for example Figure 3.21), it is believed that the Reynolds number magnifies the instabilities and causes more intense instantaneous flow structures. Associated with higher instabilities and more intense recirculating shedding vortices is the breakdown of the structure into turbulence in a shorter distance than at lower Reynolds numbers. Asymmetric breakdown will generally break up into small scale turbulence at around 2 to 3 nozzle radii downstream of the stagnation point while a symmetric cone or bubble will undergo the same process at approximately 4 to 6 radii downstream of the stagnation point.

Asymmetry within breakdown at such low Reynolds numbers can easily be falsely attributed to the magnification of asymmetric instabilities if there exist either temperature gradients or asymmetry within the experimental setup. Any asymmetry within an experimental setup which leads to movement of the stagnation point about the axis, and as a result more movement and higher velocities within the internal region of breakdown, gives rise to a more enclosed bubble type breakdown. This is due to the pressure difference created opposing the centrifugal instability within the swirling jet. An in-depth investigation into convection effects due to temperature in-homogeneity is examined in Chapter 4 of this thesis.

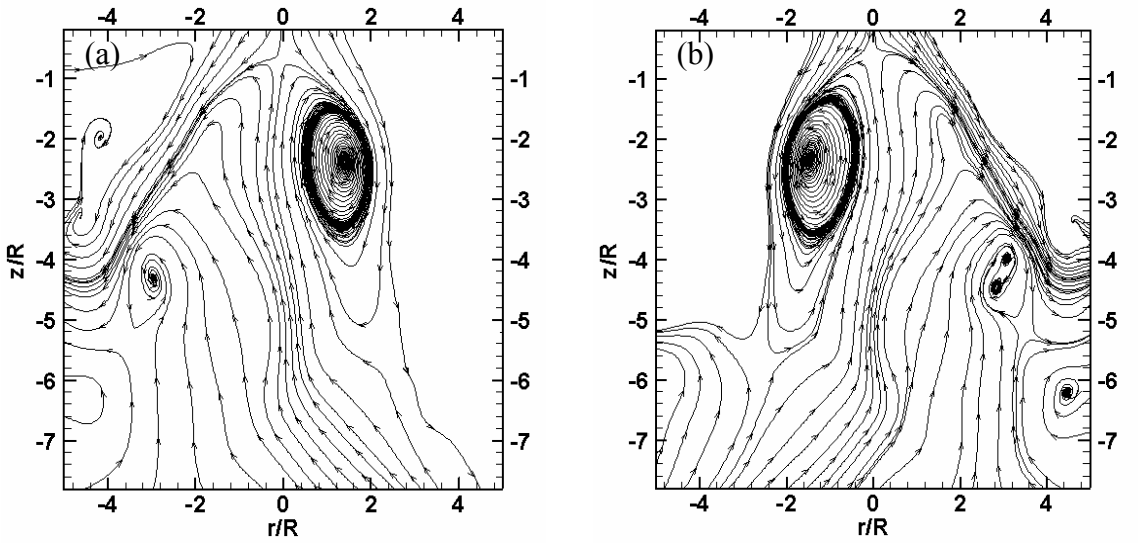

Figure 3.21: Instantaneous SPIV data streamline plots at R_e = 900, S = 1.37, showing the asymmetry of high Reynolds number breakdown as can be seen by (a) the breakdown structure resembling a bubble on the right and cone on the left, and vice versa in (b), which shows the structure at a different time after it has precessed through 180°.

Asymmetric breakdown and the asymmetric bubble identified by Billant et al. (1998), and the 2-D velocity field relating to the spiral breakdown observed by Bruecker (1993), are very similar. A common feature is the regular movement of the stagnation point about the nozzle axis in the same direction as the azimuthal component of the swirling jet velocity. As indicated by Billant et al. (1998), the spiral identified by Bruecker (1993) is simply an asymmetric bubble with an off-axis stagnation point that rotates around the vortex axis. Thompson and Hourigan (2003) suggest that the spiral can be real or simply due to the visualisation technique used. For instance, when a single dye filament is injected, supposedly on the vortex axis of an asymmetric bubble, its path may deviate due to either, a rotating off-axis stagnation point or because of off-centre dye injection, both resulting in the visualisation of a spiral structure. This argument could also explain the famous picture by Lambourne and Bryer (1961), of breakdown over a delta wing, which shows for supposedly identical conditions a spiral exists on one side of the delta wing and bubble on the other side. This could possibly be due to off-axis injection of dye, as in Figure 3.22, slight asymmetry of the delta wing or its orientation to the flow,

and/or an effect of both vortices interacting with each other due to their close proximity resulting in slight changes to the local flow conditions experienced by each vortex. A final note is that experiments have shown that the spiral filament structure can exist without the presence of a stagnation point due to the helical instabilities which vortical flows are so highly prone to.

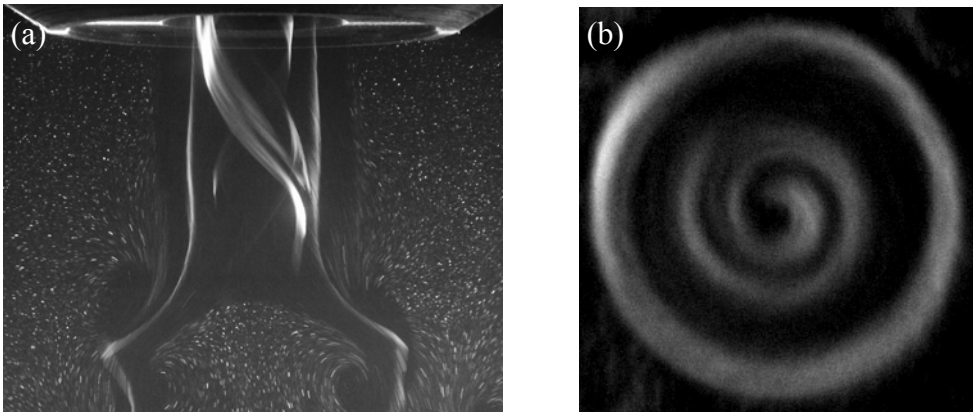

Figure 3.22: Flow visualisation in the (a) vertical plane and (b) horizontal plane at z/R = -2, of an off-axis dye filament revealing a helix structure during the development of breakdown at R_e = 600, S = 1.32.

There are still differing observations and opinions present regarding some critical aspects of vortex breakdown. For example, Billant et al. (1998) have observed that the asymmetric bubble is located in the same range of axial positions as the symmetric bubble. These authors have also found and that the symmetric bubble turns into an asymmetric bubble as the Reynolds number is increased, this is confirmed by the experiments of Brucker and Althaus (1995) and Althaus et al. (1995). In sharp contrast, experiments in confined tubes by Sarkpaya (1971), Faler and Leibovich (1977), Garg and Leibovich (1979) have reported that the spiral breakdown state appears at locations downstream of the symmetric bubble and that, as the Reynolds number is increased, the spiral develops into a bubble. Such conflicting arguments need to be carefully examined in order to find why such critical differences occur. There are several important factors which may be the root cause of these discrepancies. They include the different methods of observation, vortex generation mechanisms and geometrical differences of the various experiments.

3.5 Axial Shear Layer Shedding Frequency

This section presents an examination of the natural shedding frequency of the swirling jet shear layer (i.e. the roll up of semi discrete flow structures from the shear layer) in the axial (vertical) plane. The axial shear layer Strouhal numbers were evaluated for a Reynolds number range of $300 \leq R_e \leq 1000$, and a swirl number range of $0 \leq S \leq 1.45$.

Swirling jets undergo shear layer shedding due to both a combination of axial and azimuthal shear as seen previously in Figure 3.11a and 3.11b. In addition Figure 3.23, shows that shedding occurs both pre and post breakdown. Strictly speaking, it cannot be called Kelvin-Helmholtz shedding due to the additional azimuthal velocity component. A convenient way to express the frequency, f, is via the commonly used Strouhal number, previously defined as:

$$St = \frac{2fR}{\overline{U}_z}. \qquad \textbf{(2.4)}$$

A spectral analysis of the shear layer shedding frequency was examined in a number of ways. One purely visual method included 30 Hz video recording over a duration of 180 seconds, While replaying in slow motion, graphical markers where placed at the first point of shedding (generally at z/R = -2) and a counter was kept for various swirl number and Reynolds number combinations. The other method consisted of examining vorticity level fluctuations at the point of shedding using vertical plane PIV data. The PIV data consisted of 1500 image pairs and the time history of the vorticity concentrations at the first downstream point of shedding was recorded. A Fast Fourier Transform (FFT) was performed on the data to reveal the shear layer shedding frequency as seen in Figure 3.24.

Both methods of shedding frequency evaluation revealed that the shear layer Strouhal number is independent of the swirl number, in agreement with Loiseleux et al. (1998) and Loiseleux and Chomaz (2003). Furthermore, over the Reynolds number range tested, the Strouhal number is independent of Reynolds number (due to the linear effect of Reynolds number on shedding frequency) to within two standard deviations of the mean and is fixed at $St = St_n = 0.78 \pm 0.01$, as seen in Figure 3.25. The Strouhal number

was measured at z/R = -2 (generally the first point of axial shear layer shedding), and that St = St_n = 0.78 ± 0.01 is in excellent agreement with the experimental results of Loiseleux and Chomaz (2003) who also states that "swirl does not seem to affect the value of the frequency associated with the axisymmetric mode (m = 0)", i.e. the natural axisymmetric vortex shedding is independent of the swirl number.

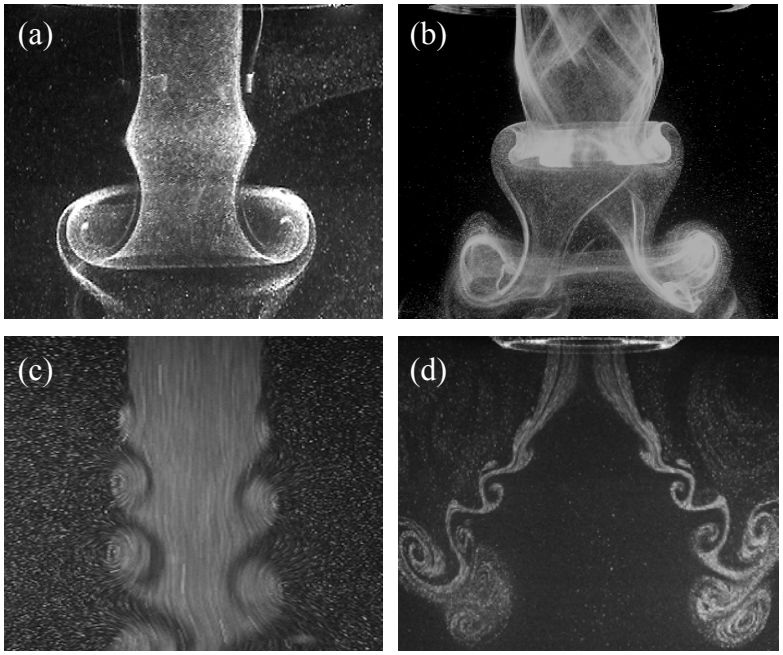

Figure 3.23: Volume flow visualisation at (a) R_e = 300, S = 0.61 and (b) R_e = 600, S = 1.23 and planar flow visualisation at (c) R_e = 900, S = 0.3 and (d) R_e = 600, S = 1.32, showing the shear layer shedding associated with swirling jets.

The shear layer first sheds (i.e. rolls up into semi discrete flow structures) at approximately one nozzle diameter downstream, with slight variation in position depending on whether breakdown had occurred and the proximity of the stagnation point and axial location. It should be noted that for $S \geq S_c$, shedding always begins to occur below the stagnation point of the steady state breakdown structure, and above the stagnation point for transitional breakdown (for which the stagnation point was still moving upstream). Shear layer shedding was present in the entire Reynolds number and swirl number range tested and appeared to periodically shed in small bursts with durations and delays of the same order as the natural shedding frequency of the structure.

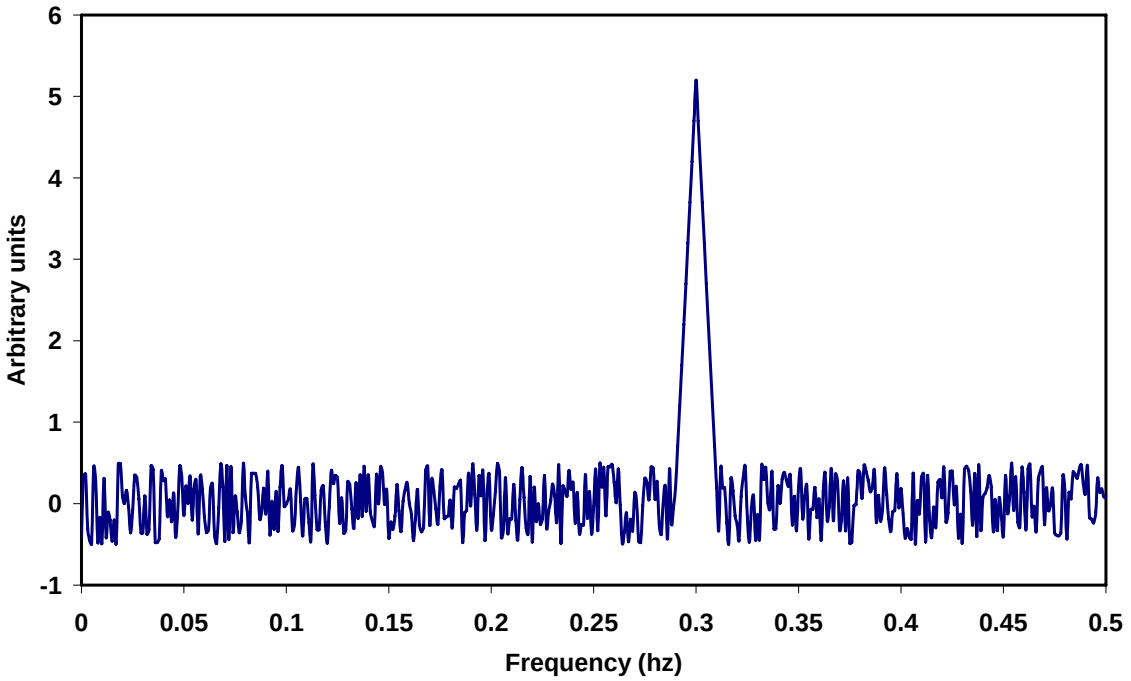

Figure 3.24: **FFT performed on the time varying vorticity data at the point of shear layer shedding. Planar PIV data consisted of 1500 frames, at R_e = 600, S = 0.6.**

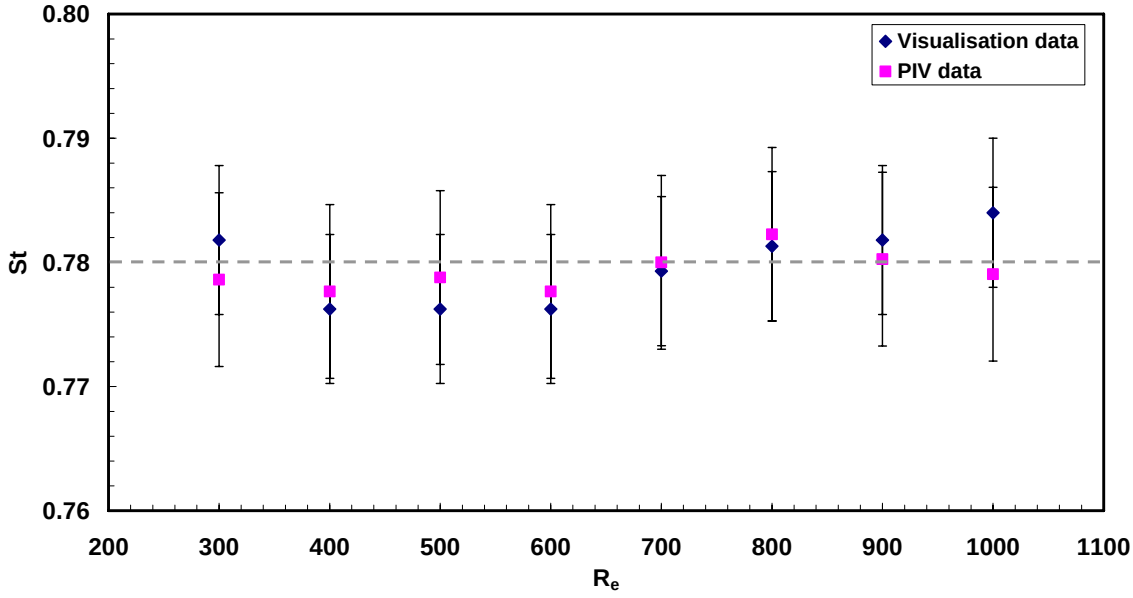

Figure 3.25: **Axial shear layer Shedding frequency at z/R = -2, shows that shedding frequency is independent of swirl ($0 \leq S \leq 1.45$) and Reynolds number within two standard deviations as indicated by the vertical error bars.**

3.6 Azimuthal modes

Horizontal planar cuts of swirling jets reveal various azimuthal modes, m, depending on the Reynolds number, $300 \leq Re \leq 1000$, and swirl number, $0 \leq S \leq 1.45$, combination tested. The azimuthal helical mode dependency on parameter range indicates that these modes are not a by-product of confinement effects as seen in confined tube experiments. Figure 3.26 shows the appearance of mode, m = +2, which exists at $300 \leq Re < 725$, above and below the critical swirl number for breakdown. Figure 3.27 reveals the competing modes, m = +1 and +2, which are present at $725 < Re \leq 1000$, above the onset of breakdown, while below the onset of breakdown there appears an m = +2 mode. For all the above mentioned cases, there exists an underlying axisymmetric mode, m = 0, in the upstream region of the swirling jet, also seen in Figure 3.27. Higher modes always appear downstream of the axisymmetric m = 0 mode, and require more time to develop.

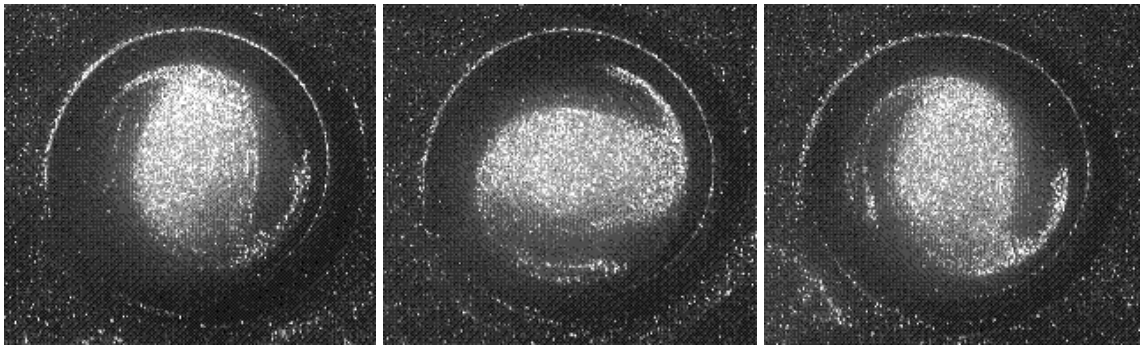

Figure 3.26: Horizontal flow visualisation at R_e = 600, S = 1 and z/R = -4, revealing an azimuthal mode, m = +2, over a half cycle (180°), rotating in a clockwise fashion in the same direction as the swirling jet.

The positive sign in front of the mode number indicates that the helical mode rotates about the same direction as the swirling jet. The two distinct Reynolds number ranges indicated above also coincide with those for symmetric and asymmetric breakdown, and as a result, the appearance of the asymmetric mode m = +1 appears in the range $725 < Re \leq 1000$. The higher-order modes i.e. m = +1 and +2 move further upstream with increasing swirl, indicating that the addition of swirl promotes higher growth rates of the

m = +2 azimuthal instability. At higher Reynolds numbers above the onset of breakdown the co-rotating off-axis stagnation point promotes an asymmetric m = +1 azimuthal mode.

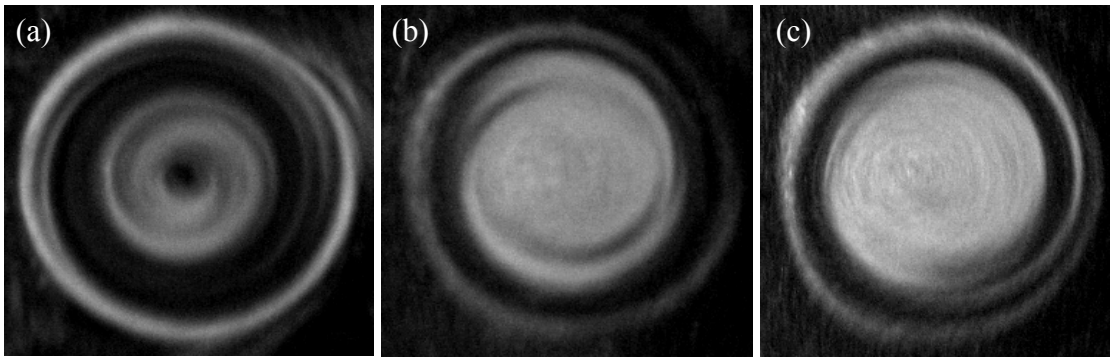

Figure 3.27: Horizontal flow visualisation at R_e = 900 revealing: (a) Axisymmetric mode, m = 0, at S = 1.2 and z/R = -2. (b) Mode, m = +2, at S = 1.2 and z/R = -4. (c) Competition between modes, m = +1 and m = +2, at S = 1.35 and z/R = -1.

3.7 Azimuthal Vorticity Development in Swirling Jets

The azimuthal vorticity component within the swirling jet is defined as:

$$\omega_\theta = \frac{1}{2}\left(\frac{\partial U_z}{\partial r} - \frac{\partial U_r}{\partial z}\right). \qquad \textbf{(3.5)}$$

As previously shown in section 3.4, the flow development leading up to breakdown for both Reynolds number regimes ($300 \leq R_e < 725$ and $725 < R_e \leq 900$) are very similar. As a result of this similarity, the development of azimuthal vorticity is separated into three sub-categories. Figure 3.28a reveals the evolution of azimuthal vorticity within the shear layer for $0 \leq S < S_c$, and is applicable to the entire Reynolds number range, while for $S \geq S_c$, Figure 3.28b is applicable for $300 \leq R_e < 725$, and Figure 3.28c for $725 < R_e \leq 900$.

All the above mentioned azimuthal vorticity plots show that maximum vorticity is, as expected, located at the swirling jet boundary within the shear layer i.e. at r/R = ±1 where the maximum velocity differential/gradient is located. This is also confirmed by

the velocity profiles previously presented in Figure 3.1. Equation (3.5) also reveals that one can check results visually by considering Figure 3.1 and examining the first term, i.e. the radial gradient of the axial velocity, at any location far upstream and downstream if broadening of the jet has not yet occurred. This assumption can be made since the radial velocity component is negligible until breakdown has occurred or in regions where the expansion of the swirling jet has occurred. This was found during SPIV measurements (see for example Figure 3.5) and in previous vortex breakdown studies by Billant et al. (1998), Delery (1994), Green (1995).

Looking at the jet's development pre-breakdown, as shown in Figure 3.28a, reveals that at S = 0 the jet vorticity map is highly symmetrical with narrow bands of high vorticity levels at the jet periphery (r/R= ±1). This is in agreement with Morton (1984), who states that vorticity can only be generated at a boundary. Vorticity gradually diffuses due to viscosity and broadens as it proceeds downstream while still maintaining symmetry. As a low level of swirl is added to the jet in this case (S = 0.25), the jet still remains quite symmetrical and there is no noticeable difference from that of the non-swirling case.

At moderate swirl levels, S = 0.76, diffusion of vorticity in the downstream region of the jet in the axial proximity of $-6 < z/R < -5.5$, begins to occur with a slight thinning of the jet in the same region. The bands of maximum vorticity in the upstream region are more intense than their lower swirl counterparts due to the thinning of the jet as a result of Kelvin-Helmholtz instability, which causes shear layer shedding. The smaller local diameter of the jet in this region causes a local increase in the jet axial velocity and axial velocity gradient, leading to this maintained high band of vorticity.

A closer examination of the central region of the vortex core at S = 0.76 and S = 1.08 reveals the appearance of vorticity at r/R = ± 0.4. This can be attributed to a noticeable axial velocity overshoot along the centreline (as there exists a complex interaction between the axial and azimuthal velocity profiles), which is an effect of our experimental setup, as previously mentioned in section 3.2 and seen in Figure 3.1. The azimuthal vorticity within the central vortical core at r/R = ± 0.4 quickly becomes negligible by z/R = -2 due to the axial velocity overshoot along the centreline rapidly decaying as the jet advects downstream. The downstream portion of the jet becomes

noticeably influenced by the asymmetric instabilities affecting the symmetry of the vorticity in that region. By averaging a large number of PIV frames, symmetry of this vorticity map could be regained, however as the flow in this downstream region is chaotic, it is not feasible to acquire the large number of images required to achieve this near symmetrical average. Concomitant with this asymmetric instability is a broadening of the jet, which is clearly seen in the downstream region at S = 1.08 and 1.17. The broadening of the jet results in a smoothing of the axial velocity profile and gradient in the region, which in turn reduces the maximum azimuthal vorticity, with a considerable decrease in downstream regions at $z/R \leq -4$ to -4.5. Although radial velocities are no longer negligible, their axial gradients are very small (as previously seen in Figure 3.5) and do not considerably contribute to the vorticity within this region. At S = 1.24, the trident state appears, with notable vorticity levels associated with the two outer branches at 2.5 to 3 radii downstream of the nozzle and almost negligible vorticity existing within the central region.

Figure 3.28b displays the development of azimuthal vorticity within the shear layer for the symmetric breakdown Reynolds number range of $300 \leq R_e < 725$. The development of breakdown is shown at selected times, (a) 3 min, (b) 5 min and (c) 9 min after the swirl is abruptly increased from S = 1.25 to S = 1.32 in 1 second. Image (a) reveals the vorticity contour when the expansion of the downstream portion of the jet results in an upstream moving stagnation point. Within the internal viscous core of the swirling jet, the appearance of oppositely signed vorticity to that upstream within the vortex core, is seen downstream of z/R = -5 (i.e. downstream of the upstream moving stagnation point in the expanding core region). Delta wing experiments by Rockwell et al. (2002) and relatively unconfined vortex breakdown experiments by Gallaire et al. (2004) have shown similar results in terms of this internal vorticity swapping sign, due to the proximity of the upstream moving stagnation point. There exists now an axial velocity deficit along the jet centreline, swapping the axial velocity gradient sign and in turn the sign of vorticity. These results are also in agreement with Experiments by Althaus et al. (1995), Brown and Lopez (1990) who found that it is a pre-requisite that negative azimuthal vorticity appear (i.e. the appearance of oppositely signed vorticity) for vortex breakdown to occur. The latter authors believe that vortex breakdown is caused by the

tilting of axial vorticity into the azimuthal plane which appears as negative vorticity as a result of the addition of swirl to the jet. They go on to say that a stagnation point will appear (vortex breakdown) when an adequate amount of negative vorticity in the azimuthal plane is formed. Figure 3.28b, image (b) shows a transitional bubble developing, at which point the upstream vorticity within the swirling jet at $r/R = \pm 0.4$ begins to decrease due to the close proximity of the upstream moving bubble (and stagnation point) and the associated velocity deficit. The decrease in axial velocity with downstream distance associated with the upstream moving stagnation point has the effect of reducing the axial gradient and associated local maximum azimuthal vorticity. The swapping of the sign of the axial velocity downstream, and the strengthening of the recirculating flow is associated with an increase in the opposite signed azimuthal vorticity below the stagnation point (i.e. $z/R < -2$).

The vorticity contours associated with the steady state cone (see Figure 3.28b, image (c)), show intensification of the vortex structures over the transitional bubble structure shown in image (b). Here, as the stagnation point has moved further upstream to its new steady state position, the upstream vorticity within the swirling jet at $r/R = \pm 0.4$ decays further, while the internal opposite signed vorticity bands within the structure (in this case the steady state cone) remain highly intensified.

Figure 3.28b, image (d) shows the transitional bubble when swirl is further increased from $S = 1.32$ to $S = 1.36$ in 1 second before settling to a steady state cone as shown in (e). In both cases, the upstream vorticity within the swirling flow at $r/R = \pm 0.4$ reduces with downstream distance until such a point at which it is no longer visible ($z/R < -4$), (as seen in image (e)), due to the close proximity of the stagnation point and resulting axial velocity deficit. There still remain the highly intense opposite sign vorticity bands within the internal shear layer of the breakdown structure indicating strong recirculation.

Figure 3.28c shows the same development of breakdown as that of Figure 3.28b, but for the asymmetric Reynolds number range of $725 < R_e \leq 900$. The transition from pre-breakdown to breakdown in this Reynolds number range is very similar to that for the symmetric Reynolds number range of $300 \leq R_e < 725$, but with several slight differences. As there is no transitional bubble, the transitional state is simply a chaotically wandering

upstream moving stagnation point (image (a) and (b)). Averaging the data reveals lower intensity bands of vorticity due to the higher degree of velocity fluctuations in the developing structure, hence lower average values. The breakdown to small scale turbulence occurs at a higher upstream location than for the symmetric parametric range, which causes the shorter downstream extent of the intense vorticity bands associated with the shear layer. The appearance of slight asymmetry in Figure 3.28c can be overcome by averaging a much larger number of PIV frames. However, even though the stagnation point precesses in a regular fashion about the vortex axis, the resulting structure below the stagnation point is highly unsteady and chaotic in regions. As a result of these unsteady and chaotic flow regions, an extremely high number of PIV frames are required to average the flow field and produce a symmetrical vorticity map. Due to memory limitations of the available equipment, this was not a feasible option.

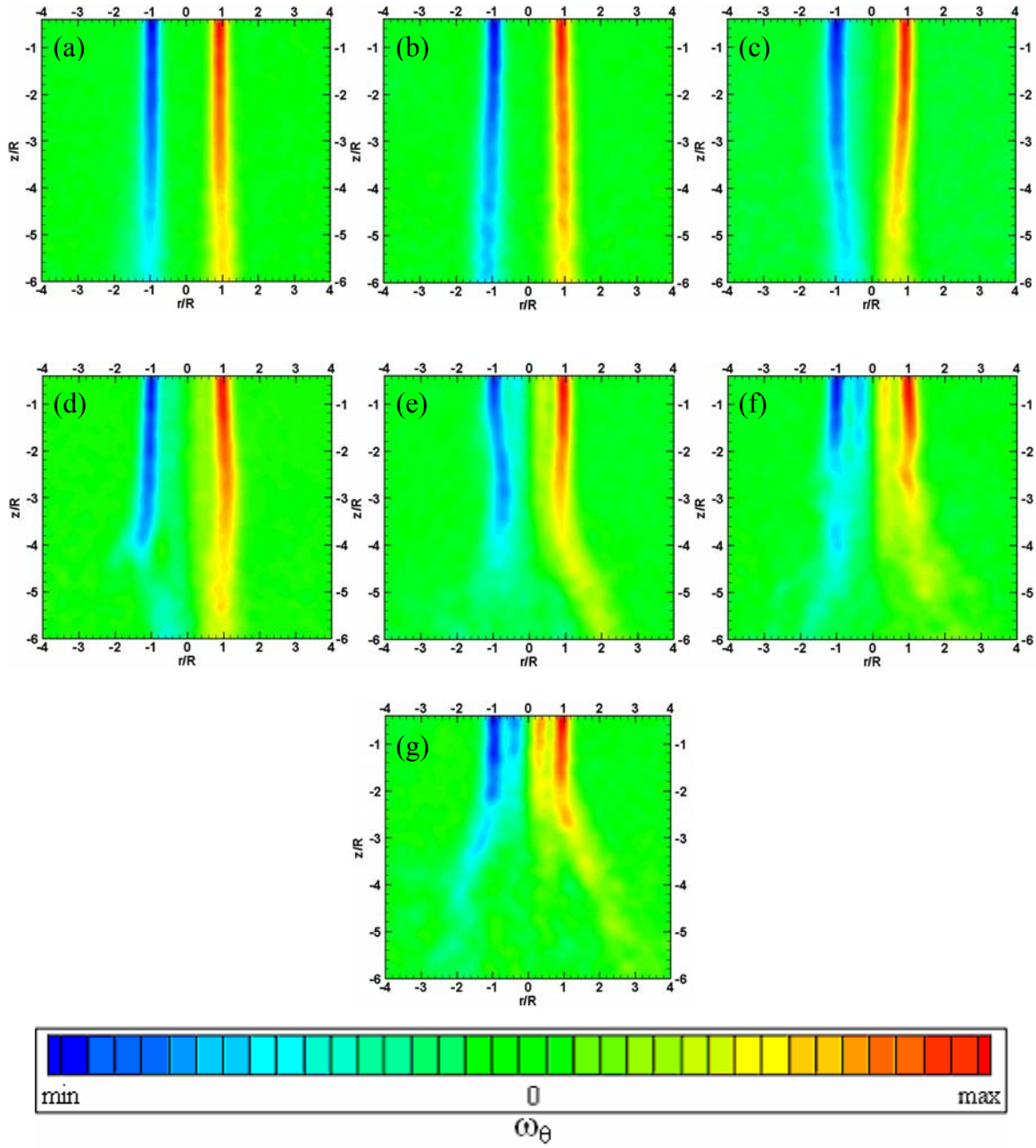

Figure 3.28a: **Steady state azimuthal vorticity plots at a fixed Reynolds number of $R_e = 900$ (representative of, $300 \leq R_e \leq 900$, for $S < S_c$), and various swirl numbers, (a) S = 0, (b) S = 0.25, (c) S = 0.76, (d) S = 0.95, (e) S = 1.08, (f) S = 1.17, (g) S = 1.24. Note: the scale of the colour contour levels are adjusted for each image in order to capture the entire range and not flood the image. Data were obtained via SPIV with an average of 100 images.**

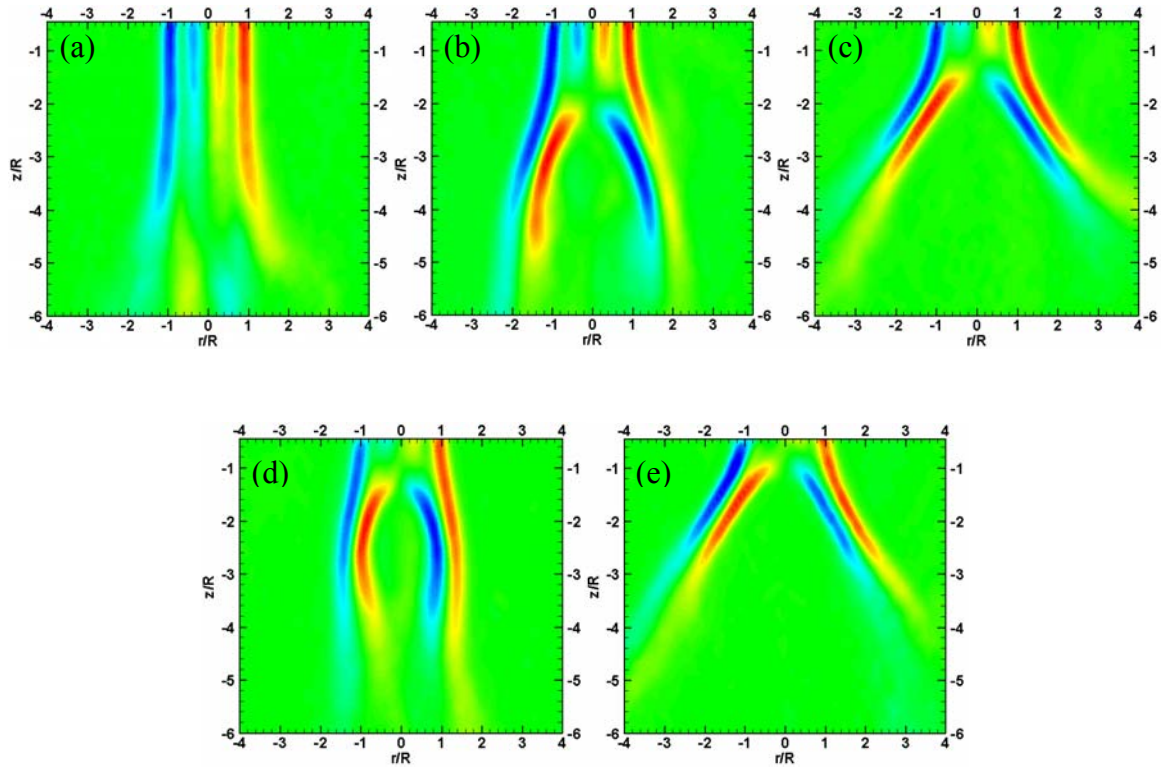

Figure 3.28b: **Azimuthal vorticity plots at $R_e = 600$, representative of, $300 \leq R_e < 725$, for $S \geq S_c$. The development of breakdown is shown at selected times, (a) 3 min, (b) 5 min and (c) 9 min after the swirl is abruptly increased from S = 1.25 to S = 1.32 in 1 second. Vorticity plot (d) shows the transitional bubble when swirl is increased from S = 1.32 to S = 1.36 in 1 second, before settling to a steady state cone as shown in (e). See note in Figure 3.28a and contour legend.**

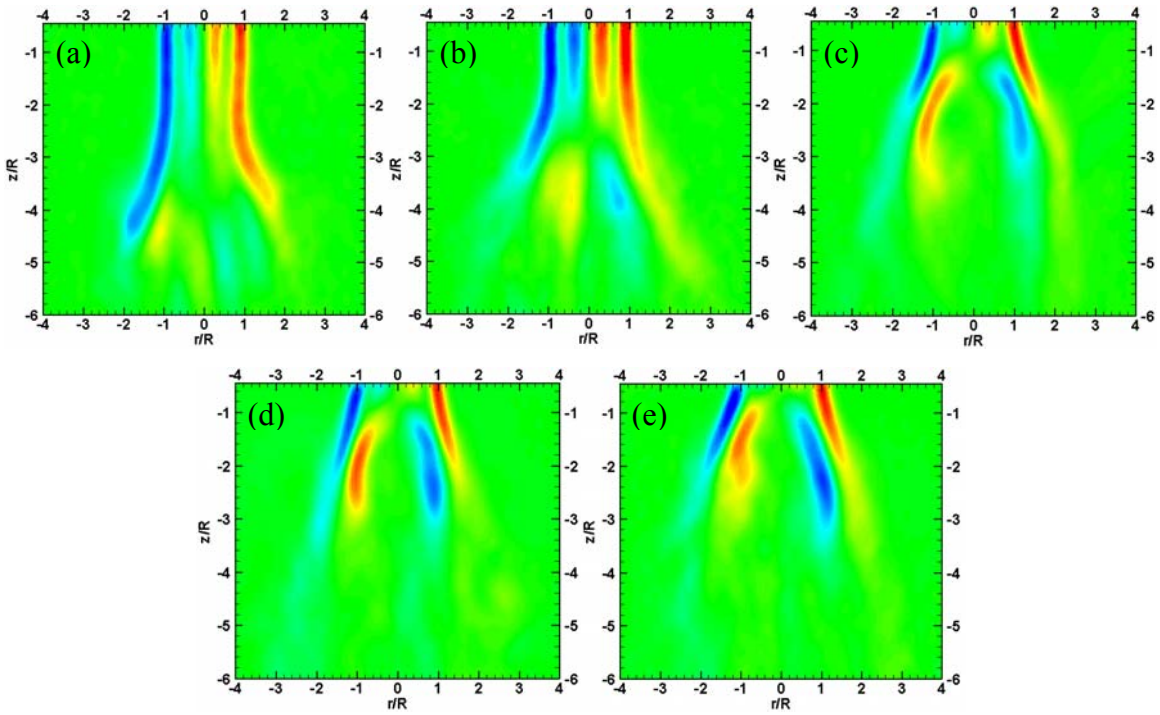

Figure 3.28c: **Azimuthal vorticity plots at R_e = 900, representative of, 725 < R_e ≤ 900, for S ≥ S_c. The development of breakdown is shown at selected times (a) 3 min, (b) 5 min and (c) 9 min after the swirl is abruptly increased from S = 1.24 to S = 1.34 in 1 second. Vorticity plot (d), shows a transitional asymmetric breakdown due to a further abrupt increase in swirl from S = 1.34 to S = 1.38 in 1 second, before settling to a steady state asymmetric breakdown structure, (e). See note in Figure 3.28a and contour legend.**

Chapter 4

Results & Discussion

Convection Effects

4.1 Introduction

Natural (or free) convection is a phenomenon affecting all fluids that experience a temperature difference in any spatial direction. The temperature difference causes density changes within the fluid, which in turn produce buoyancy forces causing motion within the fluid. For our particular case, in which the flow of interest is within a rectangular vertical flow tank, it is essential that we eliminate or reduce convection as far as possible.

This chapter presents a combination of theoretical and experimental results showing the effects of free convection due to temperature differences between the tank wall and working fluid. The extent to which the effect is apparent will depend on the degree of natural convection. This is directly dependent on the temperature difference and is examined in detail within. Later in this chapter, we will examine theoretically the direct effects on breakdown when the swirling jet is at a temperature different to that of the tank

fluid, followed by experimental verification. This is an extremely important influence to which vortex breakdown is very sensitive.

4.2 Part 1: Tank Wall and Working Fluid

4.2.1 Problem Definition

The theoretical analysis within this chapter assumes an axisymmetric approximation to our particular experimental setup, as experiments have shown that the out of plane azimuthal temperature distribution at various fixed radial positions is in fact symmetrical. We will assume the worst case scenario in which the wall temperature, T_w, is the same as the ambient room temperature, T_{amb}. A schematic of the situation is shown in Figure 4.1, which assumes that the wall temperature is higher than the fluid within the tank, leaving a

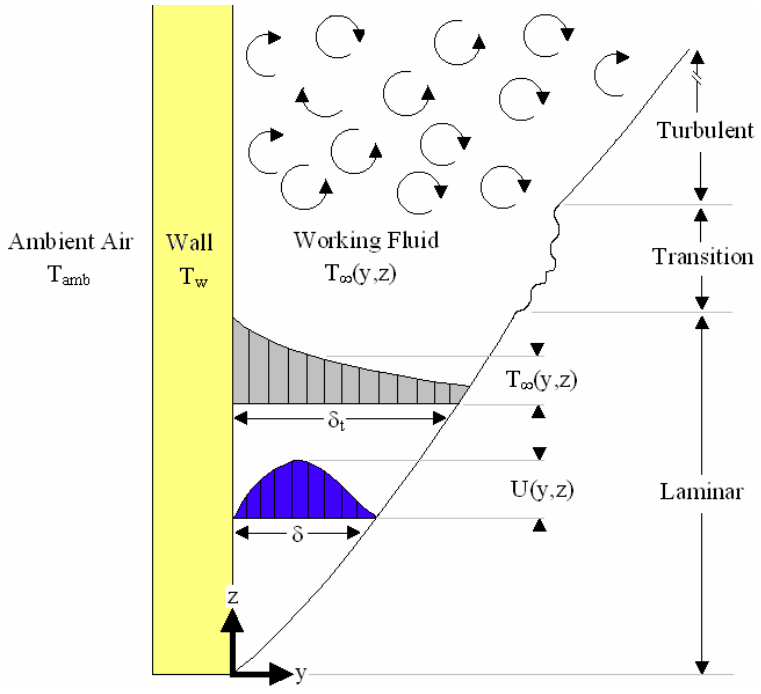

Figure 4.1: Schematic of the thermal boundary layer as a result of the wall surface temperature, T_w, being greater than that of the working fluid, T_∞.

positive differential temperature, $\Delta T = T_w - T_\infty$ (°C). If the fluid were of higher temperature than the wall then the physical problem would simply be inverted, while the mathematical treatment remains unchanged.

Important parameters that are necessary to determine whether or not natural convection will occur include the Prandtl, Grashof, Rayleigh and Richardson numbers. The Prandtl number, which relates the diffusion of momentum to the diffusion of heat is defined as:

$$\mathrm{Pr} = \frac{\nu}{\alpha}, \tag{4.1}$$

where α is the thermal diffusivity and ν is the kinematic viscosity. When Pr = 1, the velocity and thermal boundary layers coincide. The Prandtl number for water is highly temperature dependent and varies from 13.25 at 0°C to 1.76 at 100°C. Since Pr > 1, the heat diffuses more slowly in comparison to the momentum. This means the thickness of the thermal boundary layer is smaller than the velocity boundary layer. The Grashof number is the ratio of buoyancy forces to viscous forces, and is defined as:

$$\mathrm{Gr}_z = \frac{g\beta\Delta T z^3}{\nu^2}, \tag{4.2}$$

where g is the gravitational acceleration at the surface of the earth and β is the volume expansion coefficient. In natural convection, the Grashof number is the equivalent of the Reynolds number for forced convection, in that it determines the flow regime present. For example, the transition to turbulence for vertical plates occurs at $\mathrm{Gr}_z = 109$. The Rayleigh number is the product of Grashof and Prandtl numbers defined as:

$$\mathrm{Ra}_z = \mathrm{Gr}_z \,\mathrm{Pr}. \tag{4.3}$$

The Rayleigh number is an indicator as to when, and at which spatial location (z), natural convection will begin to occur. The Richardson number is another important parameter

for comparing natural to forced convection and is a measure of buoyancy forces to inertial forces, defined as:

$$Ri = \frac{g\beta\Delta T2R}{\overline{U}_z^2}, \qquad \textbf{(4.4)}$$

A highly favourable condition occurs if Ri << 1, indicating that buoyancy forces associated with natural convection are negligible in comparison to inertial forces, consequently, temperature variations are not large enough to significantly alter the flow. Such conditions are generally only achieved for high Reynolds number flows. All of the above dimensionless coefficients are calculated at the average film temperature defined as:

$$T_f = \frac{T_w + T_\infty}{2}. \qquad \textbf{(4.5)}$$

For our purposes it was found that the average film temperature during our experiments was approximately 20 ± 0.1°C.

Before proceeding with an in-depth analysis, it is worthwhile examining whether natural convection is likely to occur. In general, natural convection will only occur above a critical Rayleigh number of $R_{a[crit]} \approx 1100$ according to Holman (1997), for water. This indicates that convection will occur at temperature differences several orders of magnitude smaller than can be measured by the most sensitive equipment available to us. Figure 4.2 illustrates clearly the small size of the temperature difference required for convection to occur, and reveals the disadvantage associated with large experimental rigs and how easily prone they are to natural convection. From equation (4.3), we see that the minimum temperature difference before convection begins varies between 9.5 x 10^{-5} °C and 2.6 x 10^{-8} °C, at the bottom and top of the tank, respectively.

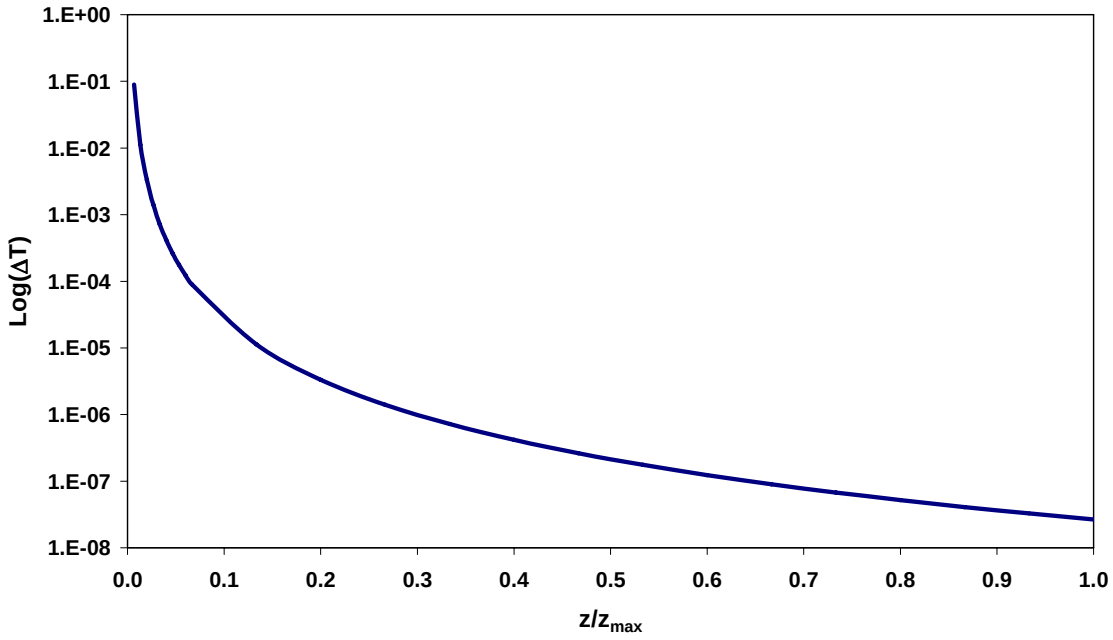

Figure 4.2: Theoretical line of the temperature difference, $\Delta T = T_w - T_\infty$ (°C), required for natural convection to occur based on $Ra_{z[crit]} \approx 1100$ and our particular experimental setup dimensions. Here z_{max} is the maximum tank height.

As with momentum driven flow, natural convection has 2 dominant flow regimes, namely a laminar region, which can further develop through a transition region into a turbulent region, or the flow may begin as fully turbulent in extreme cases. According to Holman (1997), once convection has occurred in a large vertical vessel, the laminar portion of the convected boundary layer occurs between $1 < Ra_z < 10^9$, and a turbulent region between $10^9 < Ra_z < 10^{12}$. Figure 4.3 shows how different temperature differences lead to turbulence transition at different axial positions of the actual experimental tank. In this particular case, the properties were evaluated at a film temperature of $T_f = 20°C$, giving a Prandtl number of Pr = 7.02. Again it is clear from Figure 4.3 that such a large tank causes the progression of the naturally convected boundary layer to become fully turbulent for relatively small temperature differences. Temperature differences of the order of $\Delta T < 0.1°C$, will inhibit the boundary layer from becoming fully turbulent. Fully turbulent flow would adversely affect results due to the higher fluctuating velocities and pressure gradients associated with the turbulent flow.

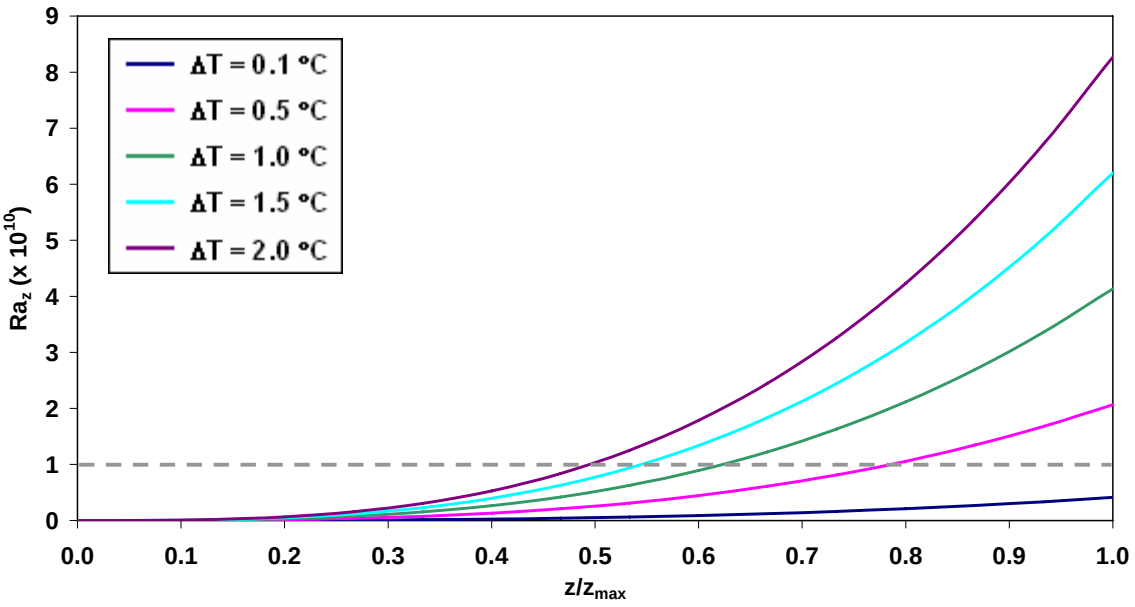

Figure 4.3: **Theoretical axial location at which the thermal naturally convected boundary layer becomes turbulent, as indicated by the point at which the various temperature differences, ΔT (°C), surpass the theoretical critical Rayleigh number for turbulence ($Ra_z = 10^9$), as indicated by the dashed horizontal line.**

4.2.2 Magnitude and Effects of Natural Convection

As natural convection is found to be virtually unavoidable, its magnitude and effect on the system must be examined. The following discussion will look at crucial parameters, such as the Grashof number, that determine whether the flow is primarily governed by forced or natural convection. It will also investigate potential thermal boundary layer velocity profiles and associated mass flow rates.

Effects of buoyancy (or natural convection) can generally be neglected for moderate to high speed flows. However, for low speed flows the effects of free convection can be significant. A measure of the influence of free convection is provided by the ratio:

$$\frac{Gr_z}{R_e^2} \propto \frac{\text{Buoyancy Force}}{\text{Inertia Force}}. \qquad \textbf{(4.6)}$$

It is essential at this point to note that although equation (4.6) is also the definition for the Richardson number (equation (4.4)), it cannot be simplified into the Richardson number form previously presented, as the length scale used for buoyancy force (i.e. indicated by Grashof number) and inertial force (i.e. indicated by the Reynolds number of the swirling jet) are different. Hence for convenience we will leave the ratio as is without simplification.

Holman (1997) states that free convection is significant enough to affect the forced convection if $Gr_z/R_e^2 > 1$. There exist three distinctive regimes based on this ratio, which determine the type of convection governing the flow: free convection when $Gr_z >> R_e^2$; forced Convection when $Gr_z << R_e^2$; and a mixture of free and forced convection when $Gr_z \cong R_e^2$.

The Grashof number for this experiment is evaluated at an average film temperature of 20°C and results in $Gr_z = 1.745x10^9 z\Delta T$. and if we assume a jet Reynolds number of $300 \leq Re \leq 900$, we can see from Figure 4.4 that in order for the flow to be governed by forced convection (i.e. $Gr_z << R_e^2$), ΔT must be much lower than the critical value indicated by the curves, which effectively requires that ΔT approaches zero. This shows that even a slight and almost immeasurable temperature difference will cause natural convection to occur and be the governing/dominant bulk flow in the Reynolds number range we are concerned with (at least in terms of global circulation within the tank).

For our particular experimental setup, the analysis indicates that it would require Reynolds numbers several orders of magnitude greater to ensure that forced convection would be the dominant flow even for the most minute temperature differences, as seen in Figure 4.5. It is clear that this is not only a problem for our particular setup but one which concerns any moderate to low Reynolds number flow in a comparatively large experimental rig. There is a compromise which must be made in such circumstances, high Reynolds number flows require extremely high speed equipment and associated with

such flows are the added turbulence which in our case may mask or make more difficult the ability to elucidate the mechanisms behind the phenomena at hand. Another limitation is the effect of confinement, increasing the Reynolds number of the swirling jet would produce no gains as to maintain a relatively unconfined swirling jet, as the experimental tank would also need to increase in size.

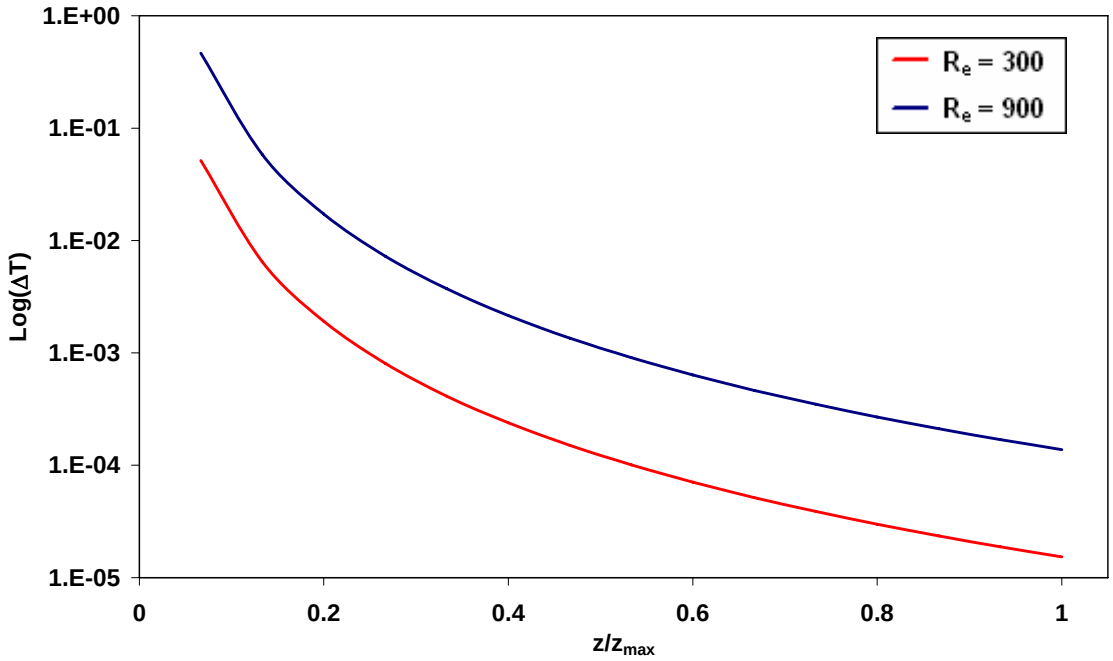

Figure 4.4: **Maximum allowable temperature difference, ΔT (°C), based on equation (4.6) for forced and natural convection to be equally dominant in their effect on the flow, when natural convection is present. For forced convection to be the dominant flow, ΔT must be far less than the critical lines indicate.**

For completeness, the Richardson number as defined by equation (4.4) and based on the nozzle diameter was also graphed in Figure 4.6 (a), while the Richardson number based on the tank width L instead of 2R is shown in (b). It is clear the inappropriateness of the Richardson number in such cases where the natural convection occurs over an area different to that of the forced convection, as can be seen by the dramatically different values in image (a) and (b). In any case, it will be appropriate to use the Richardson number in the following sections of this chapter in which the effects of convection directly at the nozzle exit are examined.

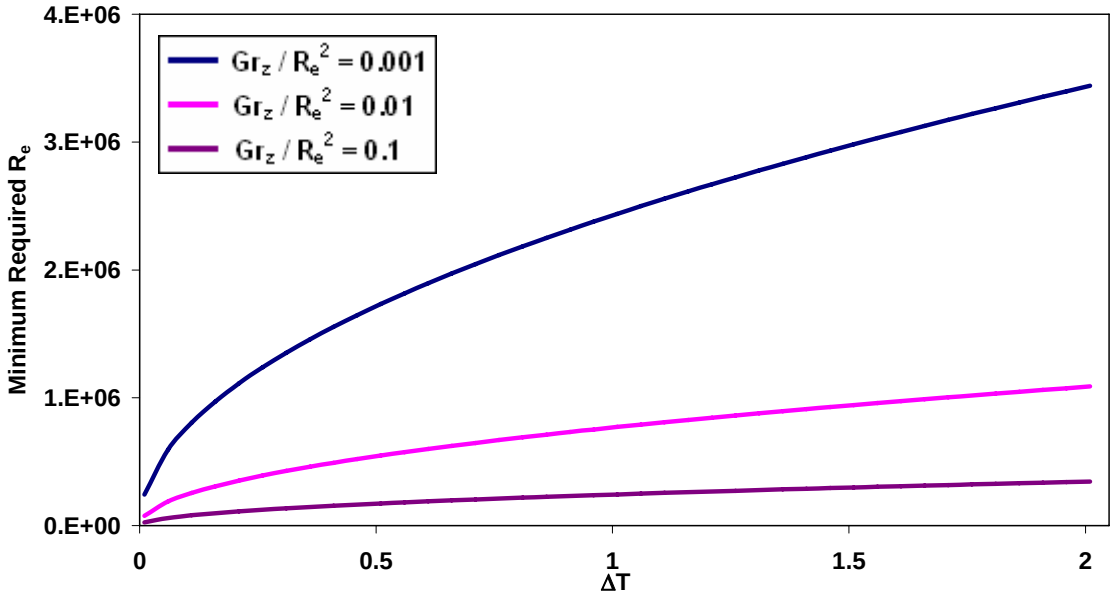

Figure 4.5: **Minimum required Reynolds number for forced convection to be the dominant flow. Note, that it is required that Gr_z/R_e^2 << 1 for forced convection to be the governing flow, hence, one, two and three orders of magnitude less are shown by the purple, pink and blue lines respectively.**

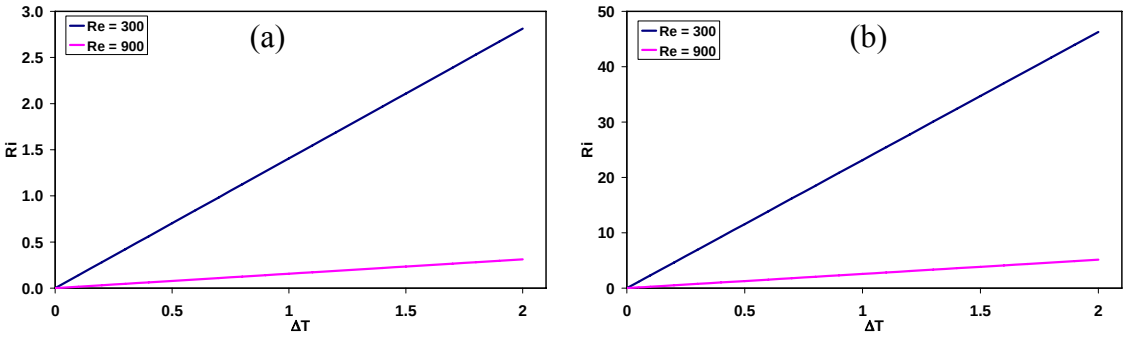

Figure 4.6: **Richardson number at various ΔT, as defined by equation (4.4), based on the nozzle diameter 2R in (a) and tank width L in (b).**

In order to examine more closely exactly how the naturally convected flow will affect the generated vortex (i.e. forced convection), a close examination of the thermal boundary layer, velocity profile and associated mass flow rates for free convection is required. Determining the thermal boundary layer thickness is essential to characterise the velocity profile of the convected flow. It also illustrates visually how the naturally

convected boundary layer develops and the percentage of flow made up by the boundary layer. The general approach of relating a vertical vessel to a vertical flat plate was made by Gebhart (1988). The derivation of the following formulas for vertical flat plates or vertical vessels can be found in Eckert (1950), Eckert (1964), Pitts and Sissom (1997). The laminar or turbulent boundary layer thickness (δ), and velocity profile (u), caused by natural convection are defined as:

Laminar Region ($1 < Ra_z < 10^9$):

$$\frac{\delta_{lam}}{z} = (3.93)\left(\frac{0.952 + Pr}{Gr_z\, Pr^2}\right)^{1/4}, \qquad \textbf{(4.7)}$$

$$\frac{u_{lam}}{V} = \frac{y}{\delta_{lam}}\left(1 - \frac{y}{\delta_{lam}}\right)^2 \qquad 0 \le y \le \delta_{lam}. \qquad \textbf{(4.8)}$$

Turbulent Region ($10^9 < Ra_z < 10^{12}$):

$$\frac{\delta_{turb}}{z} = (0.565)Gr_z^{-1/10}\, Pr^{-8/15}\left(1 + 0.494\, Pr^{2/3}\right)^{1/10}, \qquad \textbf{(4.9)}$$

$$\frac{u_{turb}}{U_1} = \left(\frac{y}{\delta_{turb}}\right)^{1/7}\left(1 - \frac{y}{\delta_{turb}}\right)^4 \qquad 0 \le y \le \delta_{turb}. \qquad \textbf{(4.10)}$$

Here V and U_1 are constants used to non-dimensionalise, the laminar and turbulent velocity profiles, equation (4.8) and (4.10) respectively, and are defined as:

$$V = (5.17)\frac{\nu}{z}\left(\frac{Gr_z}{0.952 + Pr}\right)^{1/2}, \qquad \textbf{(4.11)}$$

$$U_1 = (1.185)\frac{\nu}{z}\left(\frac{Gr_z}{1+0.494\,Pr^{2/3}}\right)^{1/2}. \qquad \textbf{(4.12)}$$

The transition region between the laminar and turbulent boundary layer has no established theoretical formulation, therefore subsequently the transition region will be modelled by a line of best fit between the different regimes. In examining the boundary layer profile, it is advantageous to find where the maximum velocity occurs. This is found by differentiating equations (4.8) and (4.10) with respect to y, equating the derivative to zero and solving for y, at which point the velocity (u_{lam} and u_{turb}) is a maximum. Firstly, considering the laminar velocity profile, differentiating equation (4.8) we obtain:

$$\frac{\partial u_{lam}}{\partial y} = \left(\frac{3V}{\delta_{lam}^3}\right)y^2 - \left(\frac{4V}{\delta_{lam}^2}\right)y + \left(\frac{V}{\delta_{lam}}\right). \qquad \textbf{(4.13)}$$

Equating equation (4.13) to zero and solving for y gives:

$$y = \delta_{lam} \qquad \text{or} \qquad y = \frac{\delta_{lam}}{3}.$$

To test which one of these values is a maximum or minimum, it is simply a matter of looking at the non-dimensional laminar (or turbulent) velocity profiles of Figure 4.7 which clearly shows that $y = \delta_{lam}$ corresponds to a minimum velocity of $u_{lam(min)} = 0$, while $y = \delta_{lam}/3$ corresponds to a maximum velocity of $u_{lam(max)} = (4/27)V$ (obtained from equation (4.8)). A more laborious method of identifying a maximum or minimum would be to test the sign of the derivative at either side of the y value of interest, producing the same result.

The exact location of maximum velocity within the turbulent boundary layer region is found in the same manner as that for the laminar region. This is found by differentiating equation (4.10) with respect to y, equating the derivative to zero and

solving for y, at which point the velocity (u) is a maximum. Differentiating equation (4.10) we obtain:

$$\frac{\partial u_{turb}}{\partial y} = -\frac{4U_1}{\delta_{turb}}\left(\frac{y}{\delta_{turb}}\right)^{1/7}\left(1-\frac{y}{\delta_{turb}}\right)^{3} + \frac{U_1}{7\delta_{turb}}\left(\frac{y}{\delta_{turb}}\right)^{-6/7}\left(1-\frac{y}{\delta_{turb}}\right)^{4}. \qquad \textbf{(4.14)}$$

Equating equation (4.14) to zero and solving for y gives:

$$y = \delta_{turb} \qquad \text{or} \qquad y = \frac{\delta_{turb}}{29}$$

The same test as for the laminar region was conducted to find which value is a maximum or minimum. Here $y = \delta_{turb}$ corresponds to a minimum velocity of $u_{turb(min)}$, while $y = \delta_{turb}/29$ corresponds to a maximum velocity of $u_{turb(max)} = (0.537)U_1$ (obtained from equation (4.10)).

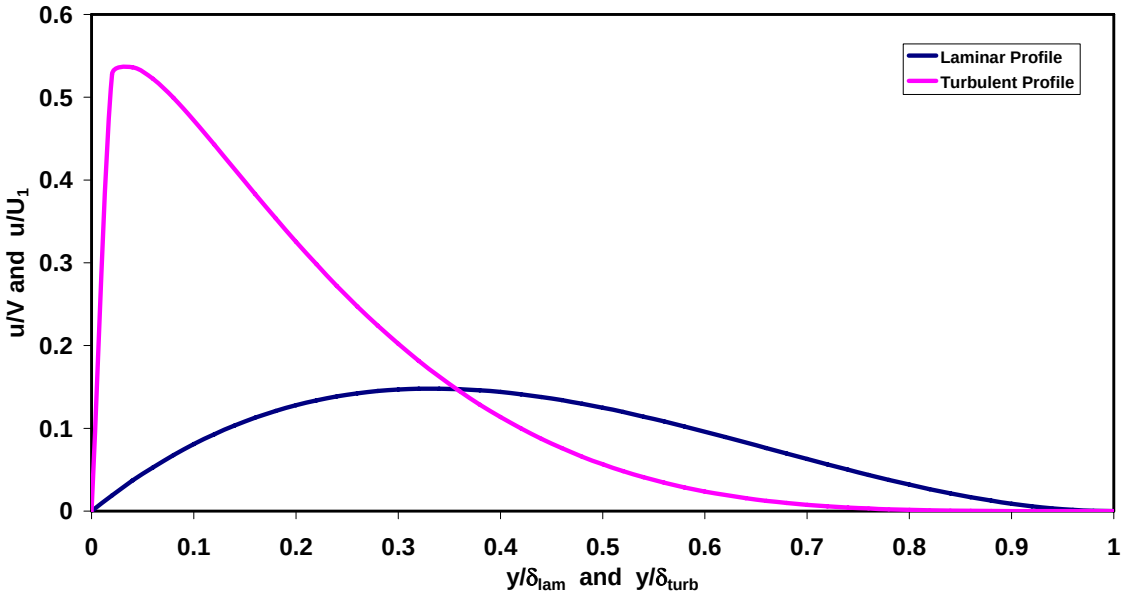

Figure 4.7: **Non-dimensional velocity profile of a laminar and turbulent naturally convected boundary flow, obtained from equation (4.8) and (4.10), respectively.**

Typical representative examples of the velocity profiles within the boundary layer of the experimental tank are presented in Figure 4.8 to help envisage the boundary layer shape and velocity profile dependency on temperature difference and axial location. Figure 4.8(a), as expected, reveals that a strong dependence on axial location exists, even for small temperature differences, showing that both the laminar and turbulent convected boundary layer profiles both increase in magnitude and width with increasing axial location z. Figure 4.8(b) also reveals a high degree of temperature dependency and shows that at a fixed location the convected boundary layer reduces in width (as it transforms into a turbulent profile), while increasing in magnitude as the temperature difference increases.

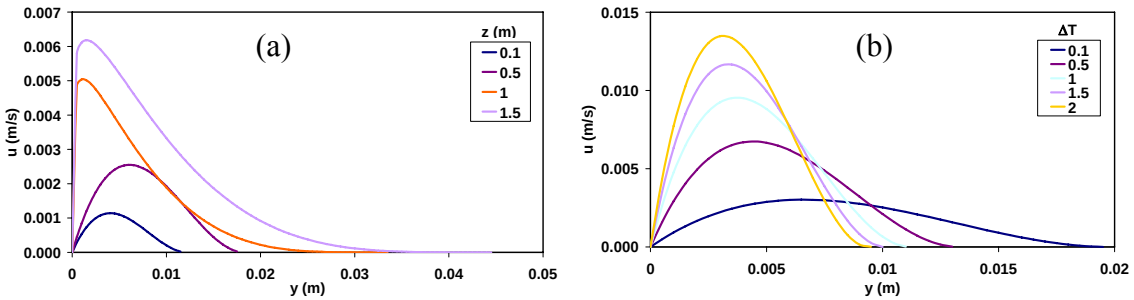

Figure 4.8: **(a) The axial development of a naturally convected boundary layer profile at a fixed ΔT = 0.1°C. (b) The naturally convected boundary layer profile at various ΔT (°C), at a fixed axial location of z = 0.7m.**

Figure 4.9 examines the extent to which the cross-section of the test tank (of width, L) is filled by the convected boundary layer. This is an important consideration. Inturn this determines the location and magnitude the peak velocities within the boundary layer in comparison to those for the jet at y = L/2. At the most extreme position, z = z_{max}, for ΔT = 0.1°C, the boundary layer is at most 13.5% of half the tank width. This indicates that the position of maximum velocity within the boundary layer is far removed from the forced convection/swirling jet located at y = L/2.

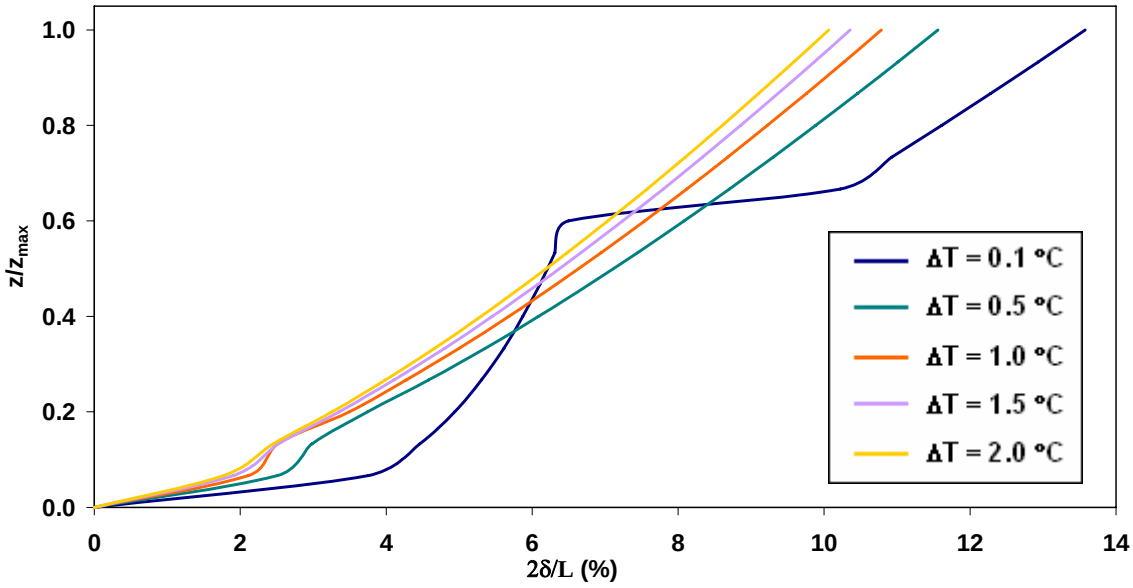

Figure 4.9: **Convected boundary layer thickness as a percentage of half the tank width (L/2).**

To obtain a clearer idea of the velocities within the tank associated with natural and forced convection, the associated mass flow rates and the velocity ratios will be compared. It is not satisfactory to directly compare the ratio of maximum velocity for natural and forced convection as they occur at very distant locations from one another, one being at the centre of the tank and the other close to the wall boundary. A proper theoretical analysis should compare the average velocities and mass flow rates for the free and forced convection as these properties are relevant as the fluid circulates around the tank. It is assumed as the fluid circulates within the tank (which may affect the swirling jet) that the average velocity ratio is the most relevant factor indicating whether the natural convection flow has a significant influence on the jet flow and stability. The natural convection mass flow rate within the test tank is z dependent, as it depends on the boundary layer thickness, δ, and also is dependent on the velocity profile, u. The convected mass flow rate is defined as:

$$\dot{m}_{conv} \cong 8\rho \int_0^{\delta} (y_{max} - y)u(y)dy\,, \qquad \textbf{(4.15)}$$

where the boundary layer area is represented by, $A_\delta = 8(y_{max} - y)dy$, where $y_{max} = L/2$. By substituting the theoretical velocity profiles for the laminar and turbulent convected velocity regions (equations (4.8) and (4.10), respectively) into equation (4.15) and carrying out the integration, the respective laminar and turbulent region mass flow rates can be found:

Laminar Region ($1 < Ra_z < 10^9$):

$$\dot{m}_{conv\,lam} = \frac{-2\rho V\delta(2\delta - 5y_{max})}{15}. \qquad \textbf{(4.16)}$$

Turbulent Region ($10^9 < Ra_z < 10^{12}$):

$$\dot{m}_{conv\,turb} = -0.217825\rho U_1\delta(\delta - 5.375y_{max}). \qquad \textbf{(4.17)}$$

The average convected velocities within the laminar and turbulent regions are calculated as follows:

$$\bar{u} = \frac{\int_0^\delta (y_{max} - y)u(y)dy}{\int_0^\delta (y_{max} - y)dy}. \qquad \textbf{(4.18)}$$

More specifically, by substituting the theoretical laminar and turbulent velocity profiles (equations (4.8) and (4.10), respectively) into equation (4.18), we obtain:

Laminar Region ($1 < Ra_z < 10^9$):

$$\bar{u}_{lam} = \frac{V(2\delta - 5y_{max})}{30(\delta - 2y_{max})}. \qquad \textbf{(4.19)}$$

Turbulent Region ($10^9 < Ra_z < 10^{12}$):

$$\bar{u}_{turb} = \frac{0.054456U_1(\delta - 5.375y_{max})}{\delta - 2y_{max}}. \quad \textbf{(4.20)}$$

The theoretical average velocity for the swirling jet (forced convection case) can be defined in terms of the Reynolds number and jet radius as follows:

$$\bar{U}_z = \frac{R_e \nu}{2R}. \quad \textbf{(4.21)}$$

The associated theoretical mass flow rate of the swirling jet is defined as:

$$\dot{m} = \pi R^2 \rho \bar{U}_z. \quad \textbf{(4.22)}$$

The ratio of average velocities associated with natural and forced convection (equation (4.18) and (4.21), respectively) are compared in Figure 4.10. It is complicated and somewhat speculative to theoretically predict how the recirculating currents associated with this flow will interact and is not considered in this preliminary study of convection effects. Figure 4.10 shows that the average natural convection velocity increases with z (except at the transitional flow regime boundary) as previously seen in Figure 4.8(a). In fact by the top of the tank at $z/z_{max} = 1$, the average natural convection velocity is the same magnitude as the forced convection velocity for $R_e = 300$ and $\Delta T = 2°C$. Interestingly, at low temperature differences ($\Delta T = 0.1°C$) we see that the maximum average velocity occurs at approximately 60% of the tank height, which coincides with boundary layer transition from the laminar to turbulent regime. The lowest achievable velocity ratio for the parameters considered is approximately 8% for $R_e = 900$ and $\Delta T = 0.1°C$. For a fixed temperature difference and similar velocity profiles, i.e. laminar or turbulent, the velocity ratio at $R_e = 300$ is three times greater than that at $R_e = 900$, as the velocity ratio is proportional to the Reynolds number.

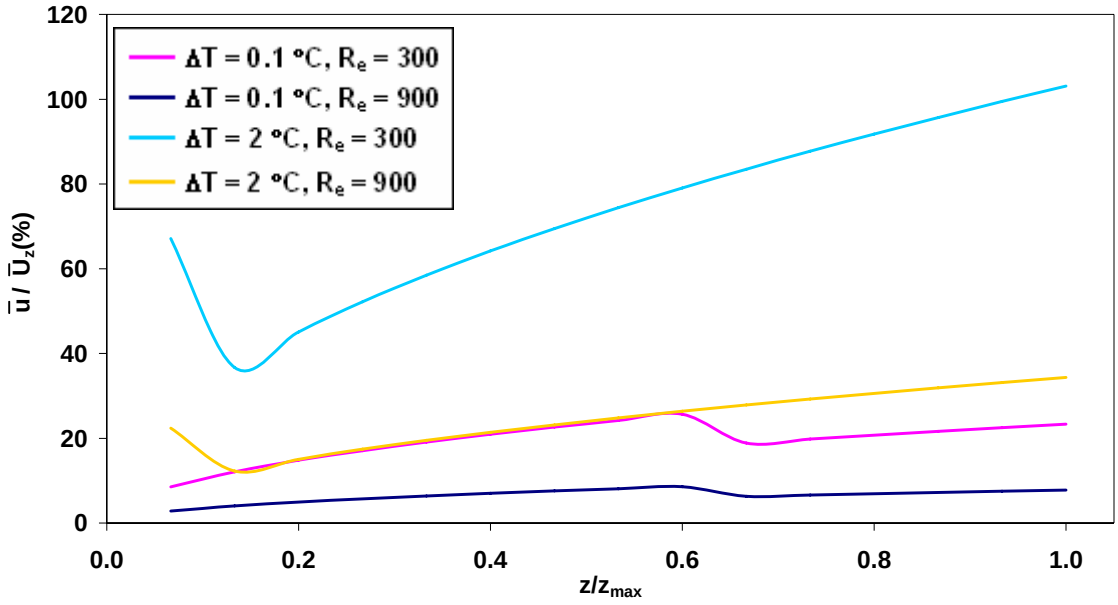

Figure 4.10: Ratio of average natural convection velocity to average forced convection velocity as a function of z.

As the velocity ratio values of Figure 4.10 are only indicative values at localised and different regions within the tank, integrating across the entire horizontal cross-section of the test tank (resulting in the mass flow rate) will give us a better overall picture of the true influence of natural convection. The mass flow rate ratio of natural to forced convection is shown in Figure 4.11. This reveals the mass flow rate associated with natural convection is exceedingly high in comparison to the forced case. While Figure 4.10 shows that the average velocity ratio is equal to 1 for $R_e = 300$ and $\Delta T = 2°C$, if we take into account the area associated with natural convection being far greater than that of the forced flow we obtain peak convected mass flow ratios of the order of 66!

It is clear that convection will always be a major concern of the experiment and minimising its effects will be essential to achieve accurate and meaningful results. Keeping the temperature difference as low as possible with the implementation of the intercooler and long settling times are required. In any case, there are still no accurate means of determining the exact effects that convection has on breakdown i.e. in terms of pressure gradients and recirculating zones, etc. Temperature differences within the test tank can be measured to be $\Delta T \cong 0 \pm 0.1°C$, as previously specified in chapter 2, the experimental setup section of this PhD. Care is taken to ensure that the fluid at all times is

stagnant when the swirling jet is not produced, and both horizontal and vertical plane PIV reveals negligible velocities throughout the entire tank. Hence the measures taken to prevent convection effects within the tank appear to have been successful. As a result of maintaining $\Delta T \rightarrow 0°C$, breakdown seems to be largely unaffected by natural convection, and the above analysis clearly indicates the very serious implications to the reliability of results induced by nominally small temperature differences. However, this global convection is not the only important consideration, of greater importance is to examine the effects of local convection caused by temperature differences between the swirling jet and the almost stagnant tank fluid.

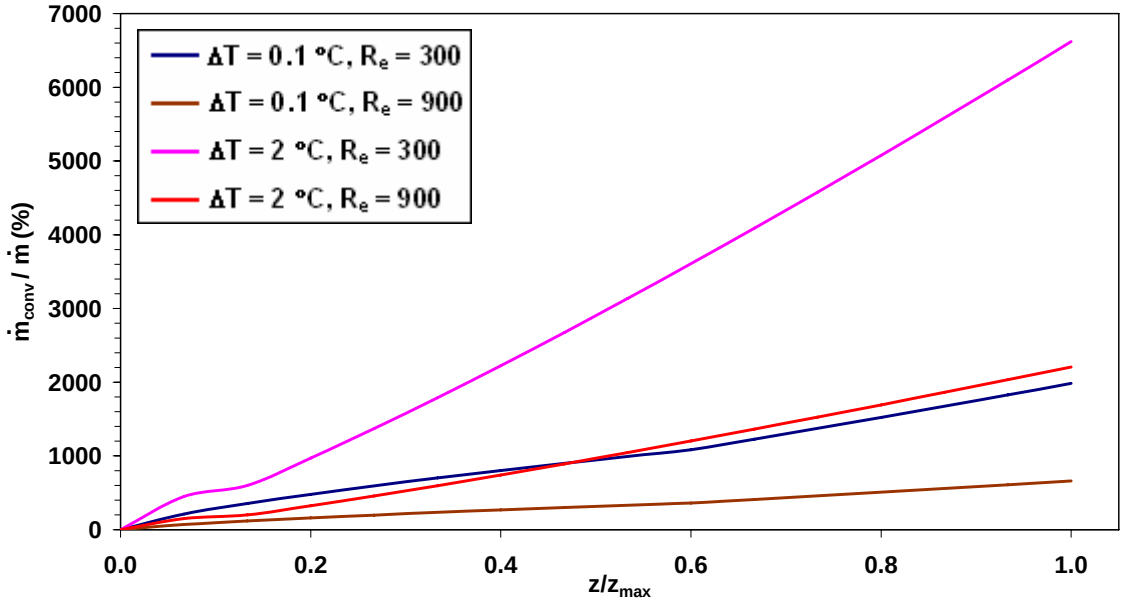

Figure 4.11: Forced to natural convection mass flow rate as a function of axial position.

4.3 Part 2: Jet and Quiescent Surrounding Fluid

4.3.1 Problem Definition

By assuming an incompressible, unconfined symmetrical jet (i.e. independent of θ) undergoing either an open bubble or cone breakdown of different density (ρ), to that of

the surrounding fluid due to temperature differences, $\Delta T = T_{jet} - T_{\infty}$, a more complete criterion for breakdown based on the swirl number will be developed (see Figure 4.12). It should be noted that $\rho_{\infty} = \rho_{jet}$ when $\Delta T = 0$. In this section the average film temperature is defined as:

$$T_f = \frac{T_{jet} + T_{\infty}}{2}. \qquad \textbf{(4.23)}$$

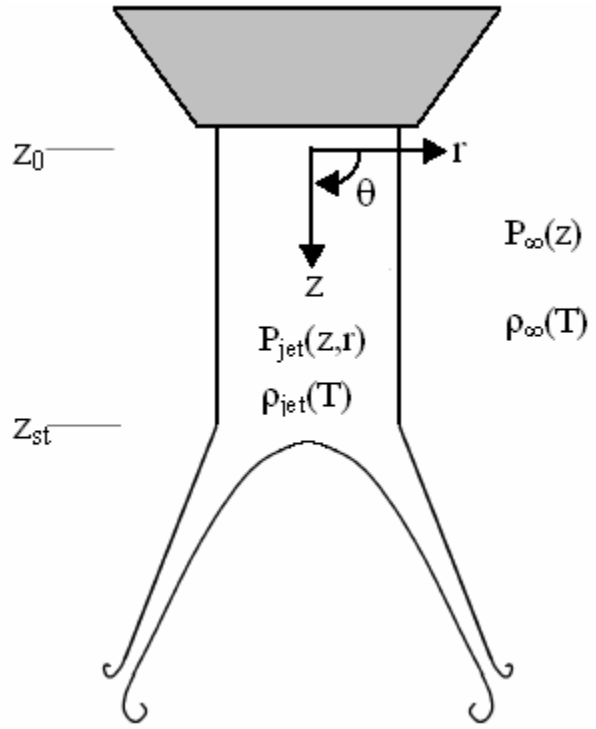

Figure 4.12: Schematic of a swirling jet undergoing cone (open type) breakdown at a temperature difference, ΔT, to that of the quiescent fluid.

4.3.2 Theoretical Criterion and Experimental Verification

By applying Bernoulli's equation along the centreline, r = 0, between the jet exit, z_0, and the stagnation point, z_{st}, of Figure 4.12, we obtain:

$$P_{jet}(z_{st},0) = P_{jet}(z_0,0) + \rho_{jet} g(z_{st} - z_0) + \frac{1}{2}\rho_{jet} U_z^2(z_0,0). \quad \textbf{(4.24)}$$

Applying Bernoulli's equation at the same vertical location, but now at a significant radial distance ($r = \infty$) from the jet (i.e. in the surrounding stagnant tank fluid where $U_z \cong 0$) yields:

$$P_\infty(z_{st},\infty) = P_\infty(z_0,\infty) + \rho_\infty g(z_{st} - z_0). \quad \textbf{(4.25)}$$

At the stagnation point (i.e. $z = z_{st}$), Farokhi et al. (1988) have shown via pressure measurements that:

$$P_{jet}(z_{st},0) \cong P_\infty(z_{st},\infty). \quad \textbf{(4.26)}$$

Finally another pressure relation can be formed by balancing the centripetal forces with the radial pressure gradient well above breakdown at $z = z_0$ where $V_r \cong 0$, to give:

$$P_\infty(z_0,\infty) = P_{jet}(z_0,0) + \rho_{jet}\int_0^\infty \frac{U_\theta^2(z_0,r)}{r} dr. \quad \textbf{(4.27)}$$

Substituting equations (4.25) to (4.27) into (4.24) gives the critical condition for breakdown:

$$\frac{\int_0^\infty \frac{U_\theta^2(z_0,r)}{r} dr}{U_z^2(z_0,0)} + \frac{g(\rho_\infty - \rho_{jet})(z_{st} - z_0)}{\rho_{jet} U_z^2(z_0,0)} \geq \frac{1}{2}. \quad \textbf{(4.28)}$$

The inequality is indicative that this is an absolute minimum condition for breakdown of this type to occur, and accounts for the case in which a bubble breakdown exists or the pressure in the stagnation region is lower, i.e. $P_{jet}(z_{st},0) \leq P_\infty(z_{st},\infty)$, due to recirculation. If

we compare this criterion with that of Billant et al. (1998), we see that it is simply an extension of their criterion to take into account density differences between the jet and surrounding fluid (i.e. if $\Delta T = 0$ then $\rho_\infty = \rho_{jet}$ and the criterion is identical). Assuming that the surrounding fluid is at a different temperature to the jet, a linear approximation of the density variation can be represented as follows:

$$\rho_{jet} = \rho_\infty + \frac{\partial \rho(T_f)}{\partial T}\Delta T . \qquad \textbf{(4.29)}$$

The linear approximation of density variation (equation (4.29)) is highly accurate for small ΔT, as will be seen later in this chapter. Substituting equation (4.29) into (4.28) results in the critical vortex breakdown criterion, which now directly includes the effects of temperature differences, ΔT:

$$\frac{S_{crit-th}}{2} = \frac{\int_0^\infty \frac{U_\theta^2(z_0, r)}{r} dr}{U_z^2(z_0, 0)} - \frac{\frac{\partial \rho(T_f)}{\partial T}\Delta T g(z_{st} - z_0)}{\rho_{jet} U_z^2(z_0, 0)} \geq \frac{1}{2} . \qquad \textbf{(4.30)}$$

The experimental setup temperature range tested was $16°C \leq T \leq 24°C$, within this range the density gradient may be assumed constant at $\partial\rho/\partial T = -0.2062$ (with $R^2 = 0.997$), according to Yaws (2003). The jet Reynolds number was also adjusted by taking into account the linear variation (with $R^2 = 0.998$) in kinematic viscosity due to temperature variation according to Yaws (2003):

$$\nu(T_{jet}) = -2x10^{-8}T_{jet} + 1x10^{-6}. \qquad \textbf{(4.31)}$$

This translates into the following linear relationship for Reynolds number as a function of temperature:

$$R_e(T_{jet}) = (0.0243T_{jet} + 0.5149)R_e(T_{jet} = 20°C). \qquad \textbf{(4.32)}$$

Furthermore, for cases in which the Reynolds number was required to be constant, the axial velocity was adjusted accordingly as in equation (4.21), repeated below:

$$\overline{U}_z = \frac{R_e \nu(T_{jet})}{2R}. \qquad \textbf{(4.21)}$$

Figure 4.13 shows the highly dependent and non-linear nature of the critical (breakdown) swirl number as a function of ΔT. This gives the increased critical swirl number increase or decrease required for breakdown to occur when a temperature difference is imposed. Specifically, the change in the critical swirl number for breakdown to occur is defined as:

$$\Delta S_c = \frac{S_c - S_c(\Delta T = 0)}{S_c(\Delta T = 0)}. \qquad \textbf{(4.33)}$$

It is clear from the experimental SPIV data and flow visualisations that lower Reynolds number flows are greatly influenced by the effects of convection, as can be seen from the second term in equation (4.30) which is inversely proportional to the square of the maximum axial velocity. The effect of a negative ΔT, i.e. when the jet is colder than the surrounding fluid, is much more pronounced than for positive values, as shown in Figure 4.13.

Figure 4.14 shows that criterion given in equation (4.30) holds true experimentally. Taking the least squares line as our best fit to the data it shows that the gradient of both the experimental and theoretical line are visually the same (a variance from the theory of ±2.2%) within the experimental error of ±6%. A clear linear relationship exists between the second convective term, S_{conv}, of equation (4.30) with that of the original swirl number definition (defined as S_T in Figure 4.14).

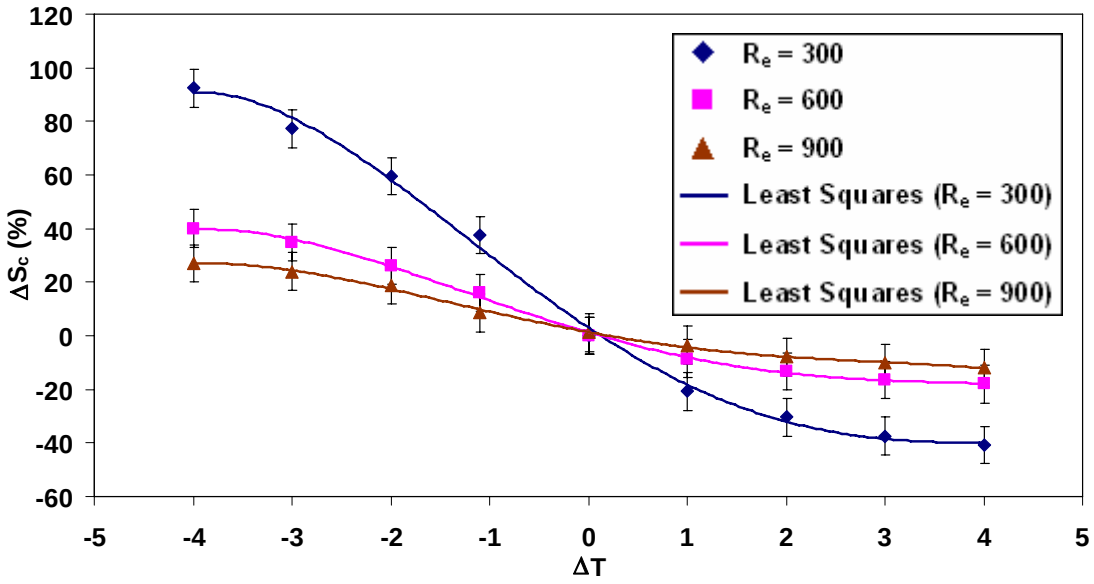

Figure 4.13: **Experimentally determined critical swirl number increase or decrease as a function of ΔT, with least squares fitted polynomial curves as indicated.**

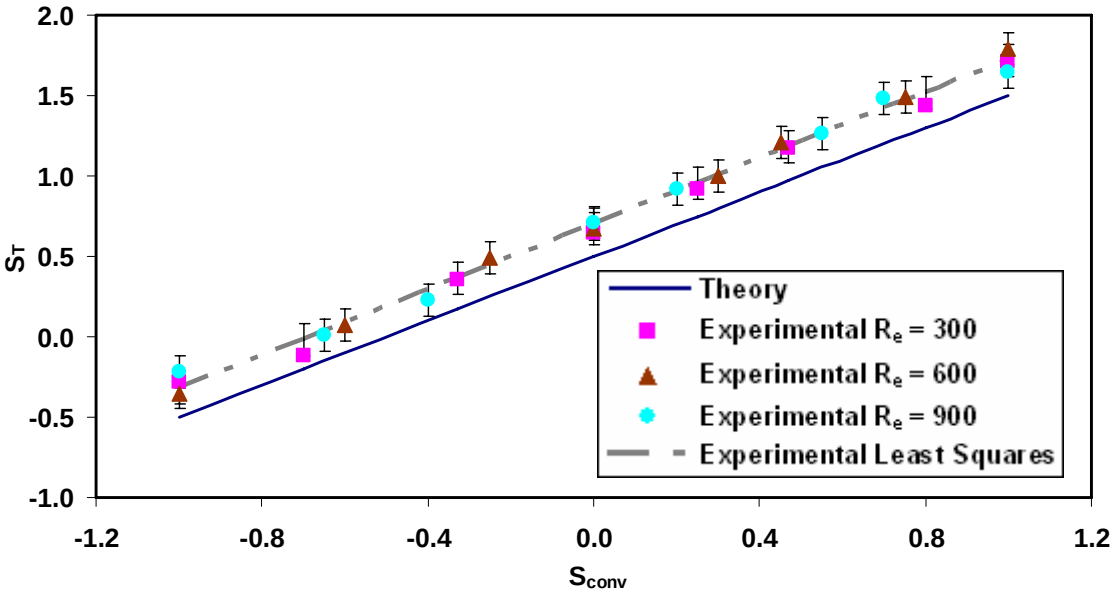

Figure 4.14: **Experimental verification of equation (4.30), where:**

$$S_T = \frac{\int_0^{\infty} \frac{U_\theta^2(z_0, r)}{r} dr}{U_z^2(z_0, 0)} \quad \text{and} \quad S_{conv} = \frac{\frac{\partial \rho(T_f)}{\partial T} \Delta T g (z_{st} - z_0)}{\rho_{jet} U_z^2(z_0, 0)}.$$

The experimental work of Billant et al. (1998) on vortex breakdown, using a very similar experimental setup to the one described here, briefly looked at the effects of convection on the resulting breakdown structure as they found "an extreme sensitivity of the selected breakdown state to small temperature in homogeneities". Using the same working fluid (water) at 20°C, and a relative temperature difference between that of the jet and ambient fluid of 0.1°C, an elementary dimensional argument using the Richardson number was proposed and is worthwhile repeating here. It appeared that buoyancy effects were negligible based on a jet diameter of 0.04m and an average jet velocity of 0.02m/s, which resulted in a Richardson number, Ri_1, of only 0.02. However, when comparing the internal recirculating region pressures of the bubble in which $P_{jet}(z_{st},0) \leq P_{\infty}(z_{st})$, to that of the almost stagnant cone where $P_{jet}(z_{st},0) = P_{\infty}(z_{st})$, we will come to see that in fact buoyancy effects are far from negligible. Using the Richardson number to examine the relative magnitude of buoyancy forces to pressure difference, $P_{\infty}(z_{st}) - P_{jet}(z_{st},0)$, they obtained $Ri_2 = \Delta\rho g2R/(P_{\infty}(z_{st})-P_{jet}(z_{st},0)) = Ri_1 U_z/\Delta U_z$, in which they define $\Delta U_z/U_z$ as the relative difference in velocity between the bubble and the cone upstream of the stagnation point. As a result of $Ri_1 = 0.02$, it is required that the velocity ratio $\Delta U_z/U_z$ also only need be 0.02 in order to produce a critical Richardson number of $Ri_2 = 1$. Given this, buoyancy effects are no longer negligible. This 2% velocity difference between the bubble and cone upstream velocity is found to be of the same order as that observed in their experiments and of the experiments presented within this PhD thesis.

Figure 4.15(a) shows the Richardson number associated with the imposed temperature difference ΔT. At a Reynolds number of 900, it always remains less than unity indicating that that the buoyancy forces associated with convection are small in comparison to the inertial forces. However, as Ri is not << 1 (except for very small ΔT values), it cannot be said that the temperature variations are not large enough to significantly alter the flow. This is especially noticeable in the lower Reynolds number bound at $R_e = 300$, in which the natural convection buoyancy forces are much greater than those of the forced convection of the order of 5.6 times larger at $\Delta T = \pm 4$°C. When comparing the flow visualisation of Figure 4.15 (b) at Re = 300, $\Delta T = 0.2$°C and an associated Ri = 0.3, with that of a typical cone breakdown in Section 3.4.2 of Chapter 3,

it is obvious that even for low Rayleigh numbers (Ri < 1) there is still a significant effect on the breakdown structure. Figure 4.15, in conjunction with SPIV data (which will be detailed below), confirms the observations, and the theoretical and experimental findings of Figure 4.13 and 4.14, which indicate the extent to which convection is Reynolds number dependent. Although the Richardson number dependency on ΔT is linear, its effects on the critical swirl number, as indicated in Figure 4.13, are far from linear.

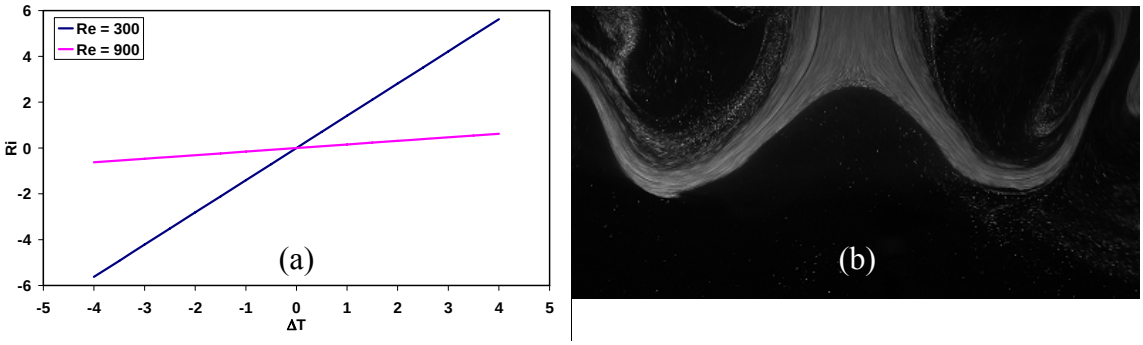

Figure 4.15: **(a) Richardson number bounds for the current imposed experimental conditions of ΔT = ±4°C and 300 ≤ R_e ≤ 900, (b) Flow visualisation at R_e = 300, S = 1.34 and ΔT = +0.2°C, with an equivalent Richardson number of Ri = 0.3.**

As previously stated in the literature review (Chapter 1), vortical flows and especially flows experiencing low Reynolds number vortex breakdown are found to be extremely sensitive to temperature variations. Billant et al. (1998) report that temperature differences of as little as 0.1°C between that of the vortical core and surrounding fluid has considerable effects on the resulting breakdown structure. This was also later confirmed in further experiments by Loiseleux and Chomaz (2003) who found that temperature gradients can lead to a premature loss of axisymmetry of the swirling jet, and an alteration of the dominant mode from the axisymmetric m = 0 mode to the asymmetric m = +1 mode. Herrada and Shtern (2003a) and Herrada and Shtern (2003b) ran numerical simulations in an attempt to investigate the effect of temperature gradients in a closed container with a spinning lid. It was found that axial temperature gradients enabled either suppression or advancement of breakdown. A negative temperature gradient in which negative buoyancy assists the downstream motion of the vertical core suppresses

breakdown while a positive temperature gradient advances breakdown and enlarges the breakdown bubble. Temperature gradients are found to have a much more significant effect on breakdown than increasing the Reynolds number.

The effect of a temperature difference between the swirling jet and the quiescent tank fluid on the breakdown structure is examined in detail with SPIV. Figure 4.16 reveals the considerable change in the breakdown structure and axial location of the stagnation point when a temperature difference between the jet and surrounding fluid is imposed. Figure 4.16(a) shows the symmetric structure of the cone breakdown and the minimal upstream moving flow associated with this structure. The only noticeable region of upstream moving flow is at the extremities of the conical sheet where a roll up of the shear layer occurs, and is of the order of only 10% of the maximum downstream axial velocity. When comparing this to Figure 4.16(b), in which only a small positive temperature difference of $\Delta T = +0.2°C$ is applied, it is clear that the effect of buoyant convection on the structure is dominant. The temperature difference not only widens the cone but also raises the upstream positive axial velocities (by the order of 50%) associated with the extremities of the conical sheet. Asymmetry also appears to be an inherent property of imposing a temperature difference, as previously mentioned and seen by Loiseleux and Chomaz (2003).

Figure 4.16(c) shows an imposed temperature difference of $\Delta T = -0.1°C$ and shows a more closed bubble type breakdown in which the internal recirculation region contains higher velocities than the symmetric cone breakdown of Figure 4.16(a). The position of the stagnation point moves downstream as ΔT decreases below zero until a point at which breakdown does not occur as seen in Figure 4.16 (d).

Figure 4.17 reveals the effect on breakdown structure and the critical swirl number caused by imposing a temperature difference. Figure 4.17(a) shows breakdown occurring prematurely at $S = 1.05$ (i.e. $S < S_c$) due to an imposed ΔT of $+1°C$ opposing the downstream momentum of the jet. This causes the jet to broaden and a stagnation point to appear. The opposite case is shown in Figure 4.17(b) in which a ΔT of $-1°C$ is imposed. Here the swirl number is required to be increased a great deal higher than S_c, in this case $S = 1.8$, in order to achieve breakdown. Associated with this high swirl number breakdown is a more compact recirculating bubble in contrast to an open cone

breakdown. The stagnation point location is also further downstream than for an equivalent breakdown structure at S = 1.8 with no detectable imposed temperature difference.

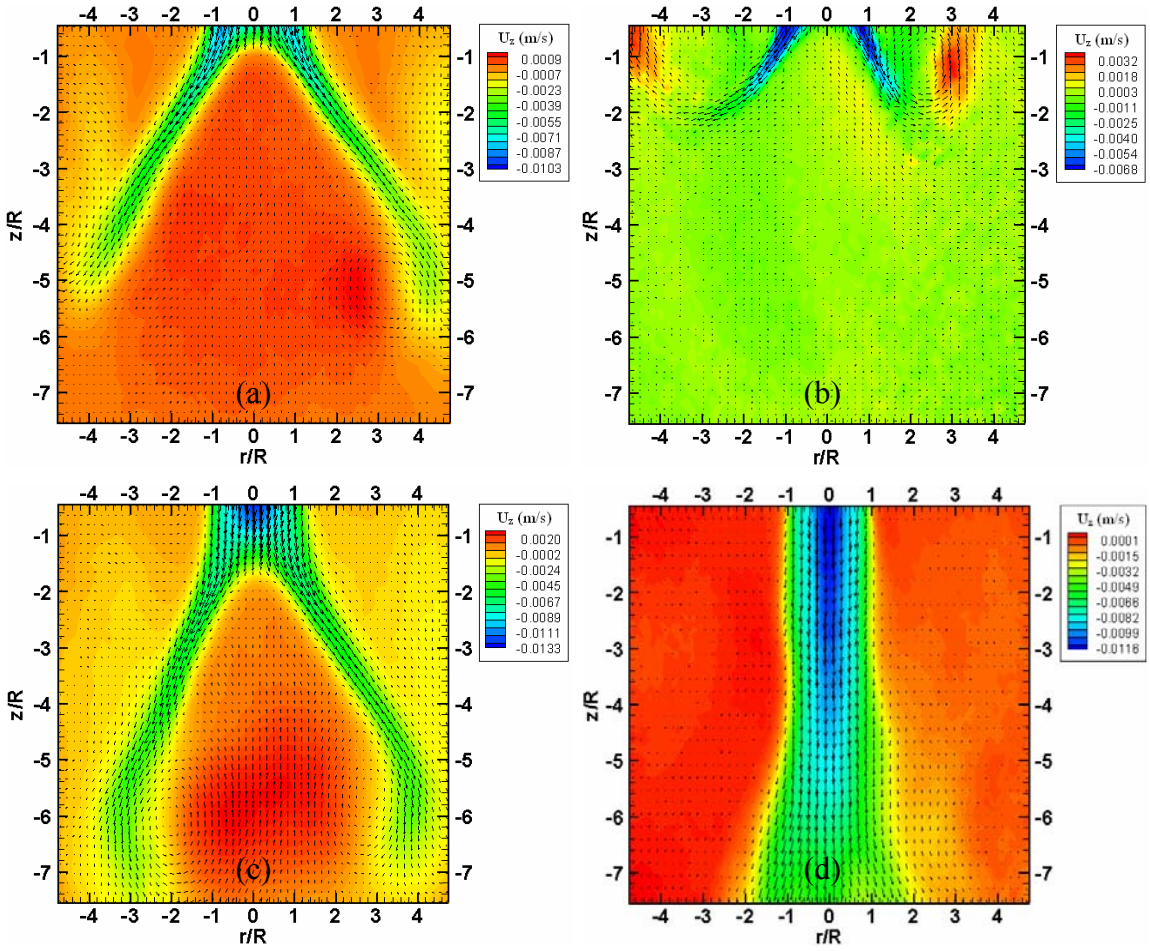

Figure 4.16: Instantaneous SPIV vector and U_z contour plots at R_e = 300, S = 1.35 at (a) ΔT = 0°C, (b) ΔT = +0.2°C, (c) ΔT = -0.1°C and (d) ΔT = -0.2°C.

In view of these findings, the observed sensitivity of breakdown to temperature differences as low as 0.1°C is confirmed by this basic analysis. It has been found both in this experimental study and that of Billant et al. (1998), that if the swirling jet is of a temperature lower than that of the surrounding fluid, a cone breakdown will be suppressed and a more closed bubble type breakdown will be encouraged to form with a lower downstream location of the stagnation point. For the case in which ΔT is positive, the formation of the open cone type breakdown is enhanced in which the extremities of

the conical sheet move upstream, and a wider apex angle exists in the vicinity of the stagnation point along the axis.

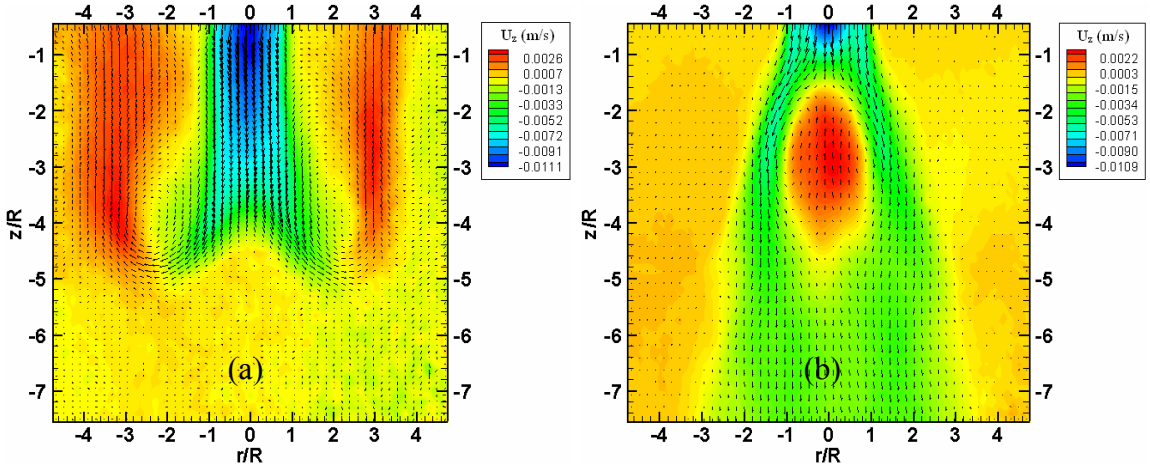

Figure 4.17: **Instantaneous SPIV vector and U_z contour plots at (a) R_e = 300, S = 1.05 and ΔT = 1°C and (b) R_e = 300, S = 1.8 and ΔT = -1°C showing the effects of imposed temperature differences, ΔT, on the critical swirl number, S_c and breakdown structure.**

Chapter 5

Results & Discussion

Effects of Axial Pulsing

5.1 Introduction

This chapter presents results of an experimental investigation undertaken which explores the response of low Reynolds number ($300 \leq R_e \leq 900$) unconfined swirling jets undergoing vortex breakdown to axial pulsing. In particular, particle visualisation in conjunction with PIV and SPIV has allowed a detailed examination of the effect of axial pulsing on shear layer flow structures and vortex breakdown, as the pulsing frequency and amplitude is varied. A range of Reynolds numbers and swirl numbers are considered.

5.2 Mass Flow Variation Characterisation

Following is a recap of important equations relevant to this chapter that have previously been introduced in Chapter 2. The swirling jet characterised in Chapter 3 was subjected to sinusoidal axial pulsing of the mass flow rate, $\dot{m}$, about the mean with variable amplitude and frequency. The mass flow rate was varied in the same form as previously described in Chapter 3 following equation (2.1) and seen in Figure 5.1:

$$\dot{m} = \overline{\dot{m}} + (\dot{m}_{max} - \overline{\dot{m}})\sin(2\pi f\, t)\,. \qquad \textbf{(2.1)}$$

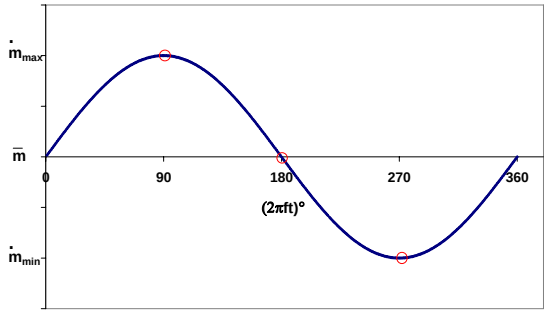

Figure 5.1: Plot of the sinusoidal pulsing function (equation (2.1)) used to force the mass flow rate at various frequencies, f, and amplitudes.

As previously stated in Chapter 2, the sinusoidal variation in mass flow during pulsing is characterised by the Peak Mass Flow Variation (PMFV):

$$m_v = \frac{\overline{\dot{m}} - \dot{m}_{min}}{\overline{\dot{m}}} = \frac{\dot{m}_{max} - \overline{\dot{m}}}{\overline{\dot{m}}}\,. \qquad \textbf{(2.5)}$$

Here, $\dot{m}_{min}$ and $\dot{m}_{max}$ are the minimum and maximum mass flow rates, respectively. Again, the frequency of the natural shedding frequency and axial pulsing frequency, f, can be expressed in terms of the previously defined Strouhal number:

$$St = \frac{2fR}{\overline{U}_z}. \qquad \textbf{(2.4)}$$

Axial pulsing experiments were conducted over the frequency range, 0.01 Hz $\leq$ f $\leq$ 10 Hz in order to cover a range of at least one order of magnitude above and below that of the natural shear layer shedding frequency for the Reynolds number range tested. It was shown in Chapter 3 (section 3.5) that the natural Strouhal number of shear layer shedding remained constant for the Reynolds number range tested ($300 \leq Re \leq 900$) at $St_n = 0.78 \pm 0.01$. Pulsing of the mass flow rate was achieved via two different and independent methods, namely the LabView™ controlled proportional lift solenoid valve and the feedback inverter controlled scotch yolk mechanism outlined in Chapter 2. The frequency of pulsation was able to be controlled to within a maximum error of ±1.5% (at 0.01 Hz $\leq$ f $\leq$ 10 Hz) and ±0.5% (at 0.1 Hz $\leq$ f $\leq$ 10 Hz) for the proportional lift solenoid valve and scotch yolk mechanism, respectively. Both methods produced qualitatively identical results and quantitatively only a maximum error of ±2% for SPIV data and a maximum error of ±1.5% for stagnation point location data.

5.3 Effects of Axial Pulsing on Vortex Breakdown

5.3.1 Shear Layer Receptivity

The frequency at which axial pulsing is applied is a critical factor in determining the effectiveness and receptivity of an otherwise robust structure when axial pulsing of the mass flow rate is applied. Due to the vast number of possible frequencies which may be applied, this study restricted the test range to frequencies close to the natural shedding frequency of the swirling jet, up to an order of magnitude above and below that of the natural shedding frequency.

The vortex shedding frequency was easily controlled when pulsing was conducted at $0.25St_n \leq St \leq 2St_n$, for the entire Reynolds number range tested, ($300 \leq R_e \leq 900$). The

shedding frequency of the swirling jet was found to lock on to low frequencies above approximately one quarter that of the un-pulsed or natural frequency and below approximately twice that of the natural shedding frequency. Outside of this critical range, the flow below the stagnation point, where natural shedding of the breakdown structure becomes apparent, is unresponsive to the imposed perturbation and the jet sheds at its natural frequency independent of the amplitude of the perturbation. As is the case with most stability problems where there is an absolute instability, the shear layer is unreceptive when pulsing is conducted at a frequency far from the natural frequency.

Figure 5.2 shows the shear layer receptivity of a swirling jet undergoing breakdown at $R_e = 600$ and $S = 1.37$ to axial pulsing of the mass flow rate at various Strouhal numbers, with a fixed PMFV of $m_v = 20\%$. It is clear from these figures that axial pulsing of the mass flow rate at PMFV values as low as 20% has a profound effect on the shear layer for the entire Reynolds number range tested ($300 \leq R_e \leq 900$). This shear layer effect is especially noticeable when conducted at Strouhal numbers close to the natural shear layer shedding Strouhal number (St_n). Figure 5.2, image (a) shows the unforced case in which there is an obvious natural shedding frequency associated with the structure, however, it is only clearly visible (without other means such as quantitative SPIV) until approximately $z/R = -2$, which is well below the stagnation point. It is not until $St = 0.25St_n$, as in image (b), that the effect of axial pulsing is seen by concentrated shear layer roll up. Below this critical value of approximately $St = 0.25St_n$, the swirling jet reverts back to its natural shedding frequency with a weak superposition of the low frequency perturbation. By $St = 0.5St_n$ (image (c)), a noticeable locking of the shear layer shedding frequency with the pulsing frequency is observed. With increasing frequency close to the natural (image (d), $St = 0.75St_n$), frequency locking of the shear layer to the pulsing is magnified and noticeable through the intensified shear layer roll up due to the forcing of the axisymmetric Kelvin-Helmholtz instability.

Forcing at the natural Strouhal number, $St = St_n$ (Figure 5.2, image (e)) has the most prominent effect on the shear layer. At the natural resonance shear layer shedding becomes highly periodic and SPIV measurements show that it also results in the most intense shear layer roll up of all. A noticeable reduction in vortex core diameter upstream of the breakdown stagnation point occurs. Observations also reveal that when axial

pulsing is applied, the shear layer no longer begins to shed at approximately z/R = -2 downstream, but instead is clearly visible at the nozzle exit, z/R = 0. By $St = 1.25St_n$ and $St = 1.5St_n$ (image (f) and (g)), the intensity of the shear layer vortices is reduced, with intensity varying inversely to the frequency difference between the forced and unforced/natural frequencies. Locking of the shear layer shedding still occurs, as can be seen by the higher frequency of shed ring vortices.

A rapid reduction of the intensity and in the ability to lock the shear layer shedding to the forcing frequency in the downstream region of breakdown is observed at $St = 1.75St_n$ and $St = 2St_n$, as seen in image (h) and (i), respectively. Above this critical threshold for vortex locking of $St = 2St_n$, the breakdown structure reverts back to its unforced shedding frequency as seen at $St = 2.25St_n$ in image (j) of Figure 5.2.

There exists a special case at the lower Reynolds number bound of our flow at $R_e = 300$ and low swirl values near the critical swirl number for vortex breakdown. Figure 5.3 reveals the change in the shear layer shedding from the jet periphery to internally within the jet at r/R = ±0.5, when forcing is conducted at $4St_n \leq St \leq 6St_n$ (with the strongest response observed at $St = 4St_n$), for all PMFV values tested $6\% \leq m_v \leq 40\%$. It appears as if the shear layer at the periphery is unreceptive to the applied forcing at high frequencies as the shear layer still sheds at the natural shedding frequency. It is unknown the exact reason for the ability of the swirling jet to support/sustain high frequencies within the internal region of the shear layer at r/R = ±0.5. However, it does indicate that higher frequencies (4 to 6 times higher than that of the natural shear layer shedding) do exist within the swirling jet shear layer.

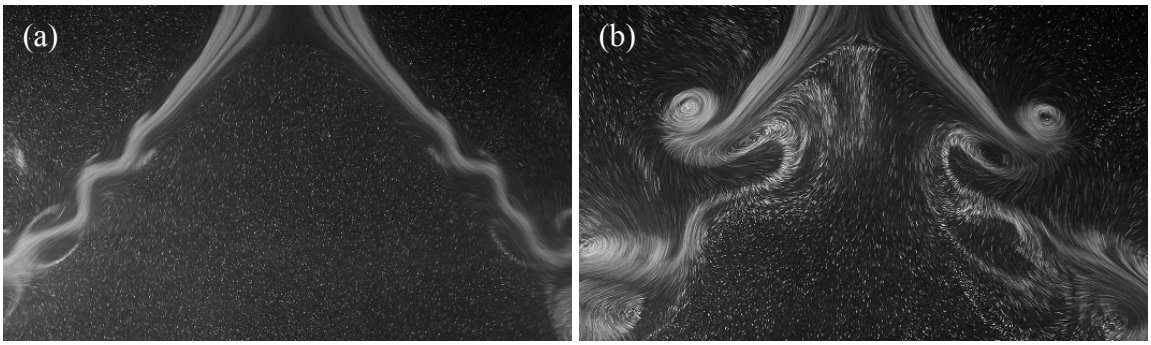

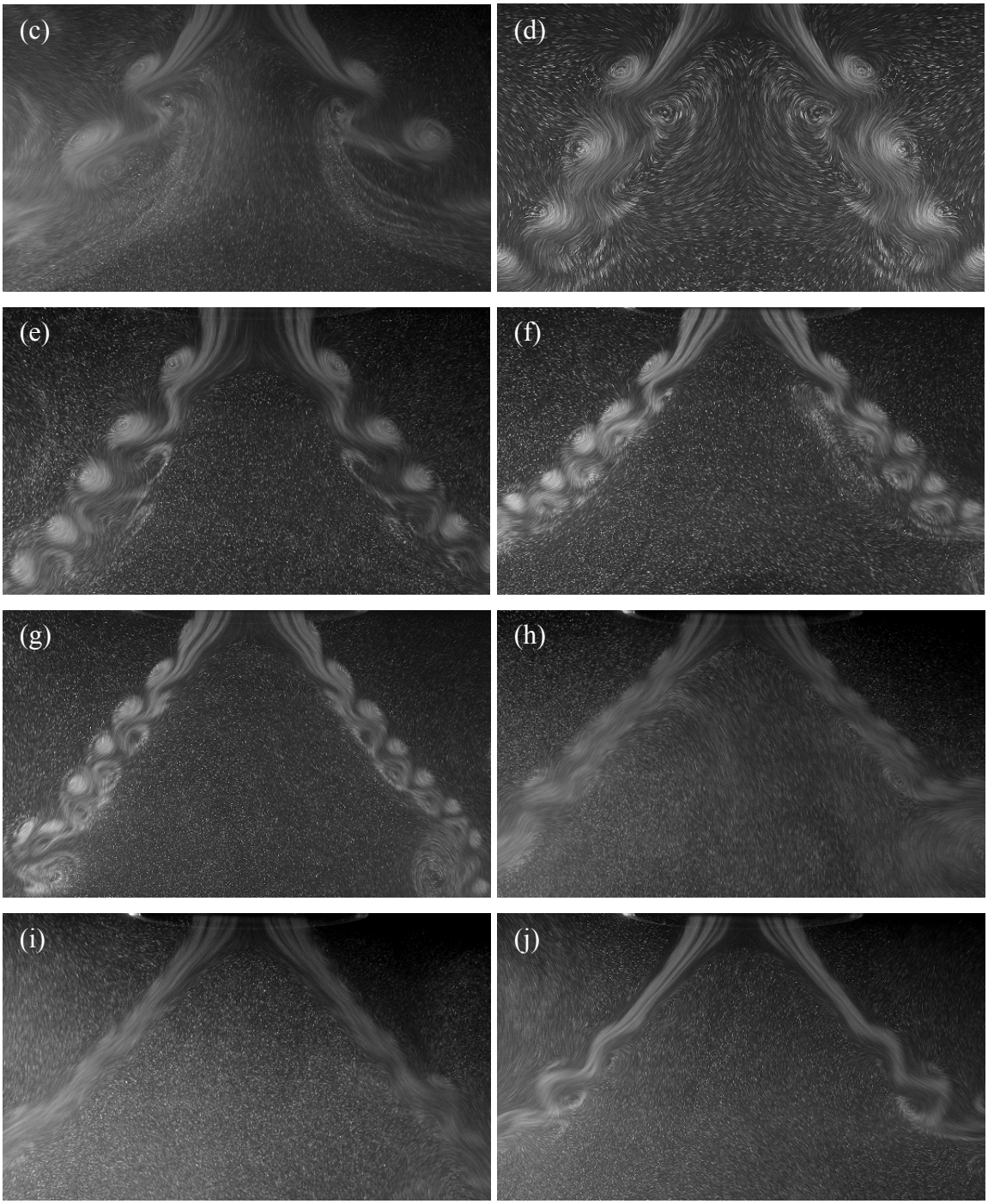

Figure 5.2: **Flow visualisation showing the receptivity of a swirling jet shear layer undergoing breakdown at R_e = 600, S = 1.32 to axial pulsing of the mass flow rate at various Strouhal numbers, (a) St = 0 (un-forced) (b) St = 0.25St_n (c) St = 0.5St_n (d) St = 0.75St_n (e) St = St_n (f) St = 1.25St_n (g) St = 1.5St_n (h) St = 1.75St_n (i) St = 2St_n, (j) St = 2.25St_n, with a fixed PMFV of m_v = 20%.**

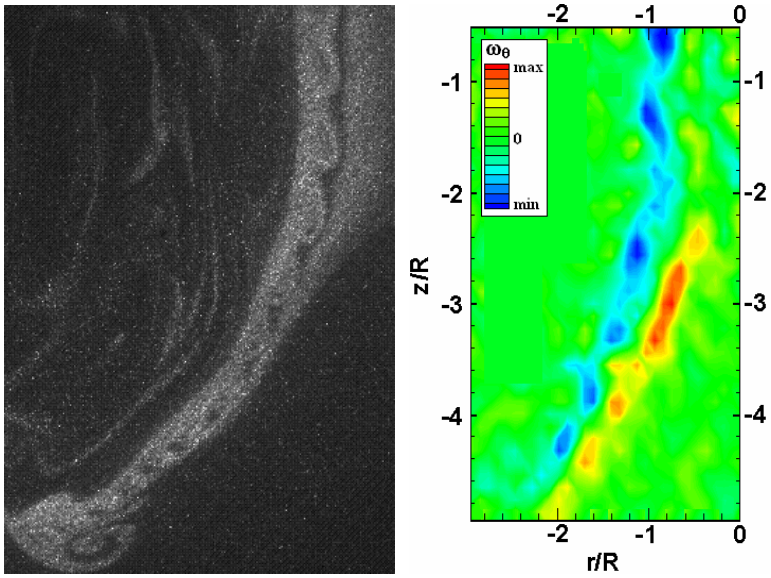

Figure 5.3: **(a) Flow visualisation and (b) instantaneous vorticity contour plot, showing a special case (not seen in other cases tested) of the receptivity of a swirling jet shear layer undergoing breakdown at R_e = 300, S = 1.31 to axial pulsing of the mass flow rate at St = $4St_n$ and m_v = 15%. Flow is from top to bottom and as the flow is symmetrical only the left portion is shown. The vorticity contour plot is equi-spaced with max = 0.37 s^{-1} and min = -0.37 s^{-1}. Images are at $\dot{m} = \overline{\dot{m}}$.**

Instantaneous SPIV data in Figures 5.4, 5.5 and 5.6 show the variation in velocity vector plots (a), streamtracers (b) and vorticity contours (c) of the unforced and forced cases, respectively, at R_e = 300, 600 and 900. In conjunction with the flow visualisation of Figure 5.2, the SPIV data reveal that it is possible to alter the distribution of the vorticity within the shear layer, and hence alter the vortex-shedding frequency at the point of its conception. Axial pulsing induces both radial and axial velocity gradients within the swirling jet. Therefore, as expected, when referring back to equation (3.5) for vorticity in the axial plane:

$$\omega_\theta = \frac{1}{2}\left(\frac{\partial U_z}{\partial r} - \frac{\partial U_r}{\partial z}\right), \qquad \textbf{(3.5)}$$

it is clear that the vorticity distribution within the swirling jet shear layer is greatly affected.

Figure 5.4 ($R_e = 300$) and Figure 5.5 ($R_e = 600$), both show very similar trends for the forced and unforced cases as they both lie in the symmetric/laminar Reynolds number range ($300 \leq R_e < 725$) as previously described in chapter 3. However, in the case of Figure 5.6 ($R_e = 900$), which lies within the asymmetric/turbulent Reynolds number domain of, $725 < R_e \leq 900$, the effects of the off-axis co-rotating stagnation point displays several differences from that of the lower Reynolds number counterpart. These effects will be discussed in further detail below.

Looking at the shear layer vector (image a) and streamtracer (image b) plots of Figure 5.4 and 5.5 reveals the emergence of shed vortices from the shear layer near the nozzle exit for the forced case, as opposed to below the stagnation point for unforced breakdown. This is typified by much larger and more intensified shedding of vortices in the shear layer at the jet periphery as indicated by the larger diameter ring vortices. This intensified and enlarged shedding of the shear layer has a profound effect on an otherwise extremely robust and stable structure. By exciting resonance, as is the case here, by sinusoidally pulsing the mass flow rate at $St = St_n$, we again confirm the frequency of shear layer shedding locking onto the forcing frequency, as previously seen in Figure 5.2. A local decrease in the jet diameter at the point of shedding is observed and an increase in the axial jet velocity within the region also occurs. Previously, this type of increased velocity at the point of shear layer shedding was only observed below the vortex breakdown stagnation point in unforced cases.

Figure 5.6 vector (image a) and streamtracer (image b) plots reveal a much greater irregularity and asymmetry within the breakdown structure at a Reynolds number of $R_e = 900$. Unlike the lower Reynolds number band breakdown, there is clearly an off-axis stagnation point which causes an irregular and highly time-dependent structure as previously seen in Chapter 3. By forcing this particular structure, we again observe vorticity levels high enough to induce shear layer shedding at the nozzle exit on the swirling jets periphery. Concomitantly, there is a reduction in the local jet diameter at the point of shedding and increased velocities within the region. A more regular and well-defined shedding pattern is also produced when axial pulsing is applied, with the effects

felt for a shorter distance downstream than for the lower Reynolds number range, due to its inherently more turbulent nature, which causes more rapid decay through small-scale turbulence in the downstream regions of the breakdown structure.

Vorticity plots for the symmetrical cone breakdown at both $R_e = 300$ (Figure 5.4 (c)) and $R_e = 600$ (Figure 5.5 (c)) reveal that even at very low forcing inputs of $m_v = 15\%$, the vorticity within the shear layer is dramatically different, especially upstream of the breakdown stagnation point. Not only are vorticity levels within the shear layer of the forced case up to 50% higher than for the unforced case, the shed vortices are also larger in size. This suggests large changes in velocity profile and gradient are produced when axial pulsing is applied, even with very low PMFV values of $m_\upsilon = 6\%$. As the mean mass flow remains constant during pulsing (i.e. maintaining a zero net change in mass flux), there must exist particular radial regions within the symmetrical jet in which axial velocity increases and decreases occur and are most concentrated, which in turn lead to such a dramatically different vorticity field due to large velocity gradient changes within the jet. This phenomenon will be further examined later in this chapter in section 5.3.3 where a detailed look at velocity profiles will be studied. Vorticity levels consistently remain higher for a further downstream distance when the swirling jet with vortex breakdown is pulsed, due to shear layer shedding locking. The frequency of shedding and magnitudes of velocity and vorticity become highly regular and consistent when forcing is applied. Intensity levels of the opposite-signed (positive) vorticity within the internal structure of the steady state cone for the unforced case are of similar magnitude to those of the vorticity within the outer periphery of the swirling jet. When forcing is applied, both oppositely signed high level vorticity regions are intensified, however, the outer peripheral negative vorticity regions are much more receptive to the effects of pulsing as evidenced by the more prominent/larger shear layer vortex rings and their associated vorticity.

For the case of the higher Reynolds number ($R_e = 900$), forced asymmetric breakdown of Figure 5.6, we find that pulsing creates a much more symmetrical vorticity field, very similar to that of the previously discussed lower Reynolds number forced cone breakdown cases. Although being visually very similar, forcing at higher Reynolds numbers does not create the same increases in vorticity, with increases of the order of

only 30% being found for the forced case over that of the unforced. This can be attributed to the high radial and out of plane velocities and inherent gradients present in the unforced structure due to the co-rotating stagnation point. Axial forcing increases axial and radial velocity gradients, and hence vorticity, which to a certain degree suppresses asymmetry within this asymmetric breakdown state. The resulting vorticity increases are not as great as for the steadier forced breakdown states in the lower Reynolds number regime. However, in the unforced case, high vorticity levels are associated only with the first point of shear layer shedding before quickly deteriorating due to the decay of the structures into small-scale turbulence. This is in strong contrast to the forced case, in which high levels of vorticity are maintained for comparatively large downstream distances, $z/R \leq -5$, as opposed to maximum vorticity rapidly deteriorating by, $z/R \cong -2$ to -3, for the unforced case.

Figure 5.7 shows horizontal cross-sections of the unforced and forced Kelvin-Helmholtz shear layer induced shedding at $z/R = -2$, for a cone breakdown at $R_e = 600$, $S = 1.32$. The unforced shedding reveals a much weaker radial velocity than that associated with the forced case as seen by the associated vector and streamtracer plots. The horizontal cross-sections confirm the added intensity and enlargement of the shear layer shedding previously seen in the vertical plane SPIV data of Figures 5.4, 5.5 and 5.6.

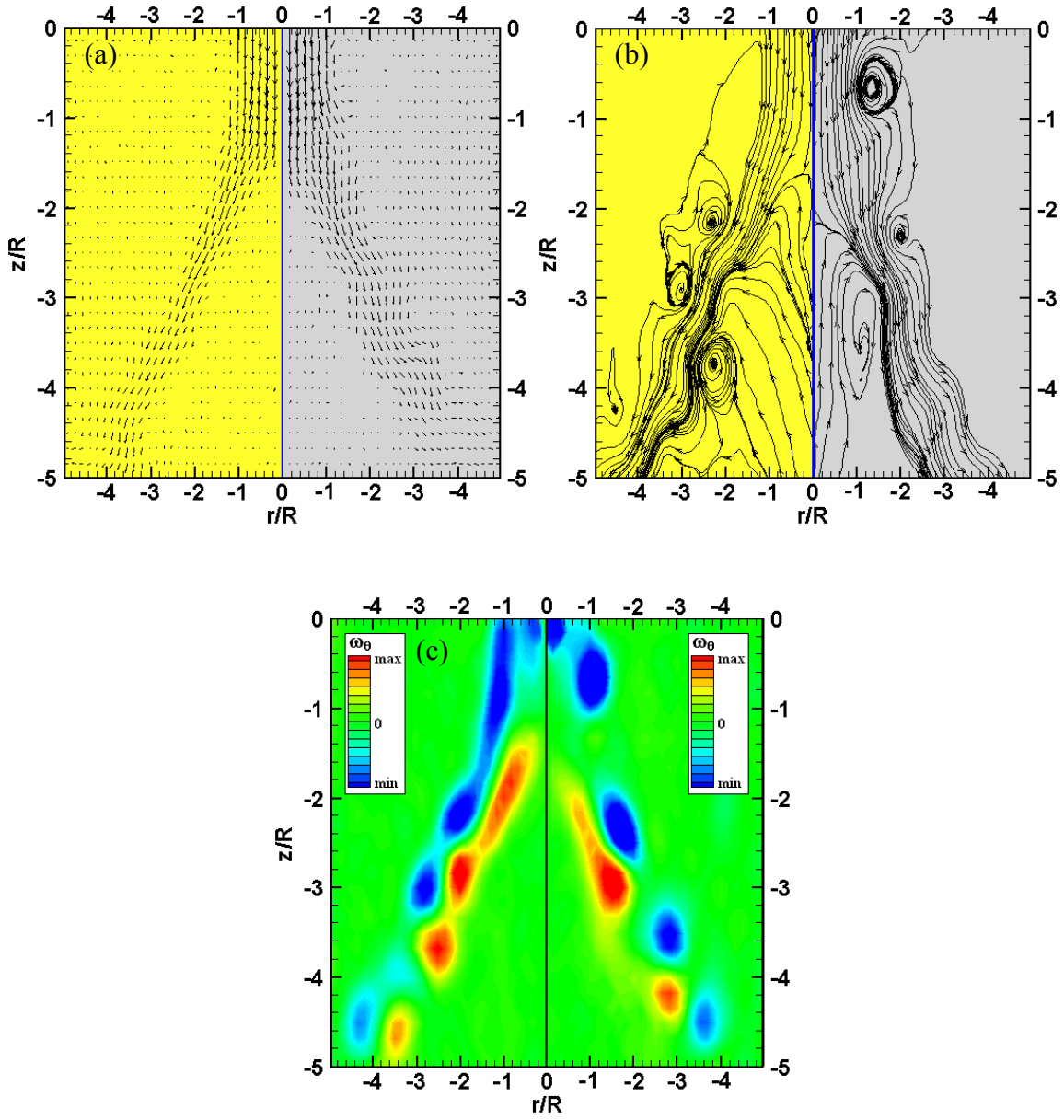

Figure 5.4: **Instantaneous SPIV data showing a comparison of unforced (left), and forced (right) vortex breakdown at R_e = 300 and S = 1.32 by a vector plot (a), which is accompanied by its associated streamtracers (b), in conjunction with a vorticity plot (equi spaced, max = 0.4 s^{-1} and min = -0.4 s^{-1}) (c). The forced case was conducted at a fixed PMFV value of m_v = 15% and St = St_n, with the instantaneous image taken at $\dot{m} = \overline{\dot{m}}$. The vorticity plot (c) was scaled equally for the unforced and forced cases.**

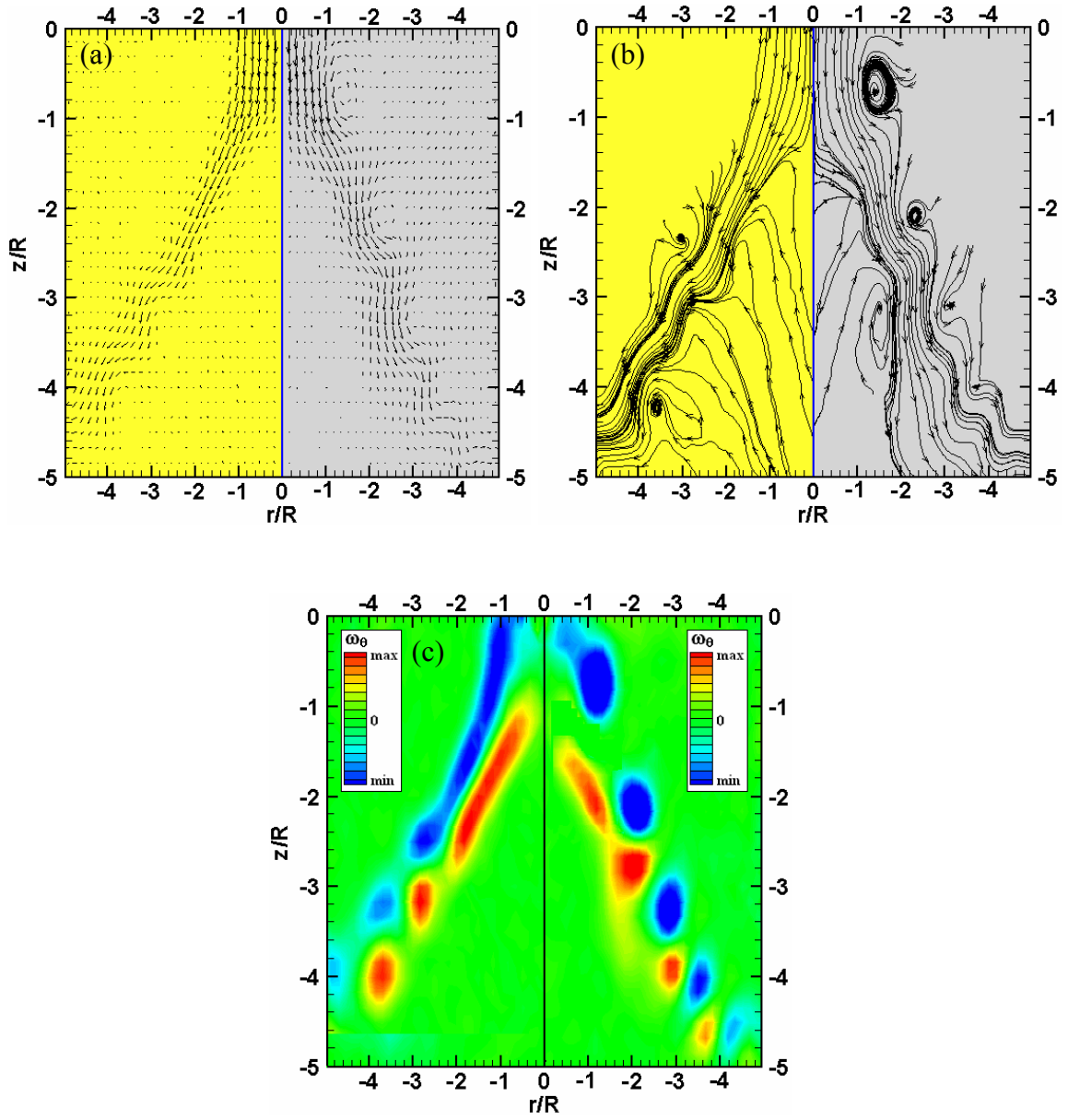

Figure 5.5: **Instantaneous SPIV data showing a comparison of unforced (left), and forced (right), vortex breakdown at R_e = 600 and S = 1.32 by a vector plot (a), which is accompanied by its associated streamtracers (b), in conjunction with a vorticity plot (equi spaced, max = 0.9 s^{-1} and min = -0.9 s^{-1}) (c). The forced case was conducted at a fixed PMFV of m_v = 15% and St = St_n, with the instantaneous image taken at $\dot{m} = \overline{m}$. The vorticity plot (c) was scaled equally for the unforced and forced cases.**

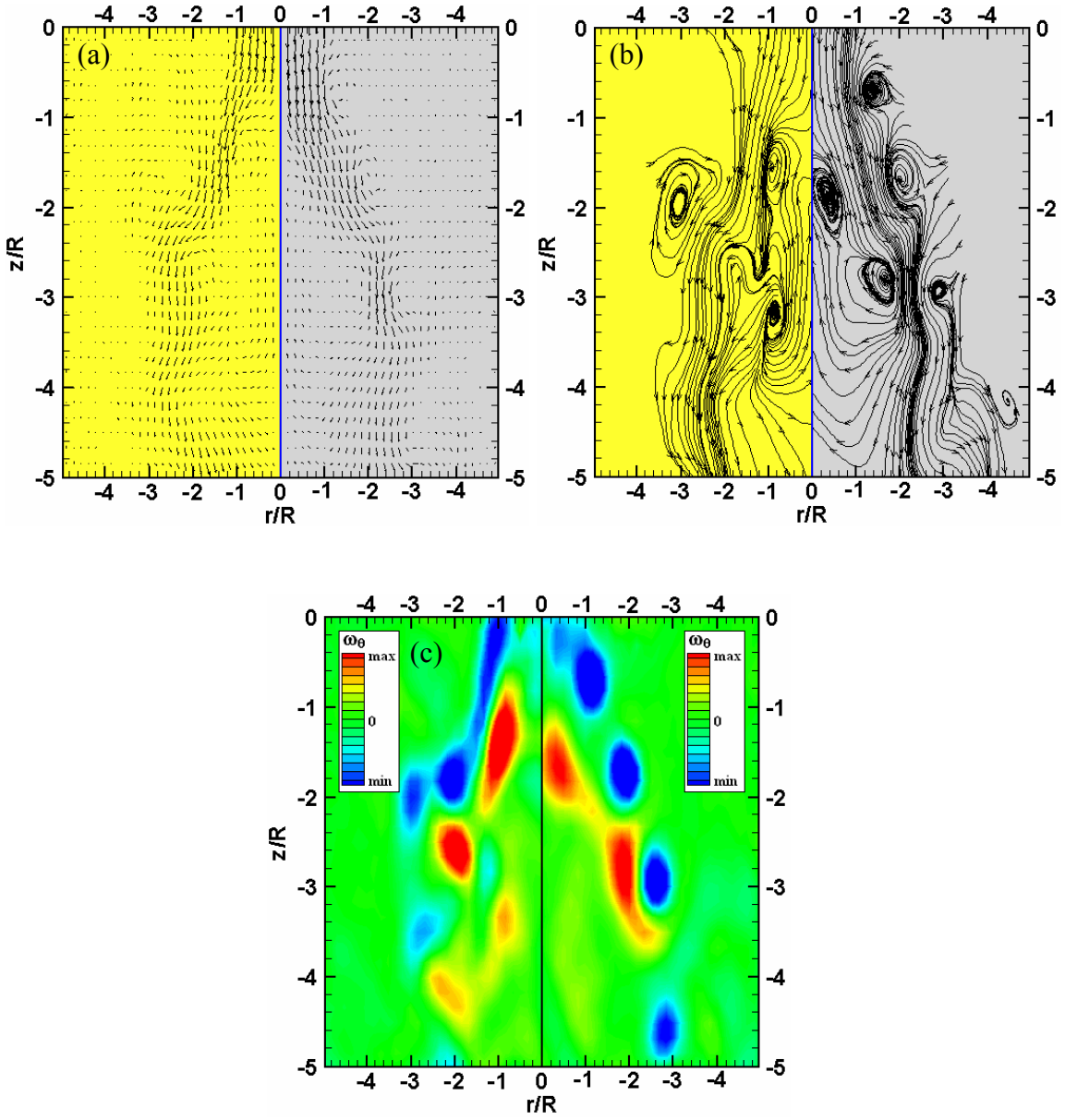

Figure 5.6: **Instantaneous SPIV data showing a comparison of unforced (left), and forced (right) vortex breakdown at R_e = 900 and S = 1.35 by a vector plot (a), which is accompanied by its associated streamtracers (b), in conjunction with a vorticity plot (equi spaced, max = 2.05 s^{-1} and min = -2.05 s^{-1}) (c). The forced case was conducted at a fixed PMFV of m_v = 15% and St = St_n, with the instantaneous image taken at $\dot{m} = \overline{m}$. The vorticity plot (c) was scaled equally for the unforced and forced cases.**

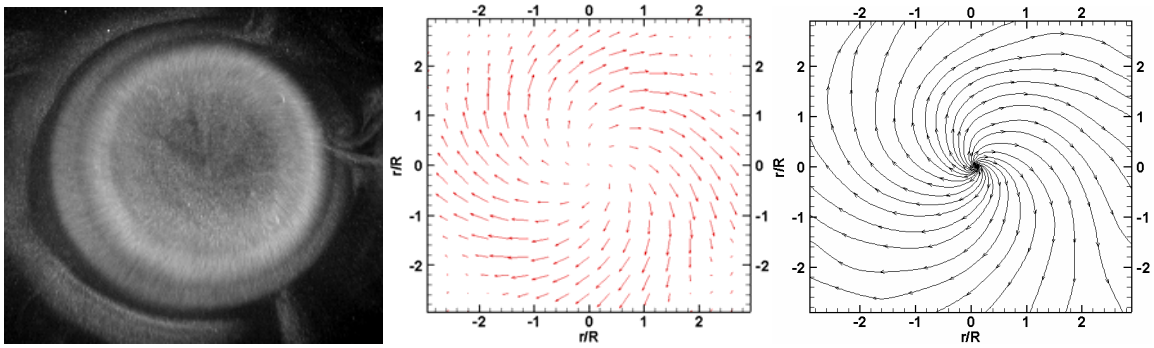

Unforced

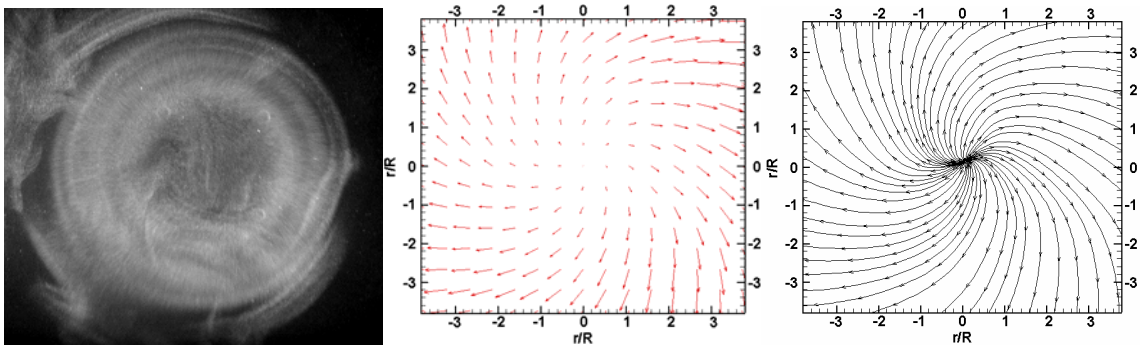

Forced

Figure 5.7: **Flow visualisation (left) in conjunction with instantaneous PIV data in the form of vector (middle) and streamtracer (right) plots showing a cross-section at z/R = -2 of a swirling jet undergoing cone breakdown at R_e = 600, S = 1.32, during shear layer shedding. The top row of figures are representative of the unforced case, while the bottom row, of the forced case conducted at a PMFV of m_v = 15% and St = St_n, with the instantaneous image at $\dot{m} = \overline{m}$.**

5.3.2 Forcing of Symmetry

As seen in section 5.3.1, forcing brings about a more coherent shedding and symmetrical breakdown structure. The extent of this coherency and the reasons behind it will be discussed in this section. Axial pulsing of the mass flow rate forces the excitation of the m = 0 mode and, as a result, forces an otherwise helical shedding pattern to become more

symmetrical. This is similar to that of a non-swirling jet as seen in experiments by Bera et al. (2001).

Considering the horizontal plane of symmetry, Figure 5.8 demonstrates the ability of axial pulsing to aid in inhibiting the development of the asymmetric m = +1 mode within the vortex core. Within the higher Reynolds number regime, axial pulsing enabled the delay of the asymmetric instability m = +1 within the upstream portion of the swirling jet, i.e. above the stagnation point. However, in the vicinity and downstream of the stagnation point, the effects of the co-rotating off-axis stagnation point were too great to entirely overcome. The effects of pulsing in retarding the development of the asymmetric mode decreases as the swirl is increased. This is indicated by the higher-order modes i.e. m = +1, +2, moving further upstream with increasing swirl. The addition of swirl promotes higher growth rates of the asymmetric m = +1 azimuthal mode along with the m = +2 mode. It is not known if the off-axis co-rotating stagnation point is a by-product of an inherent asymmetric instability within the swirling jet or is due to slight asymmetry within the vortex generator due to manufacturing tolerances, which could as a result cause the excitation/forcing of the development of the asymmetric m = +1 mode. Numerical simulations by Thompson and Hourigan (2003) reveal that for a confined breakdown (spinning-lid setup), even the slightest misalignment of the rotating lid can cause a dramatic change in the resulting breakdown structure and bring about noticeable asymmetry. This is an area that requires further investigation, however, preliminary evidence reveals that it is an inherent instability within the jet as its appearance takes some time to develop downstream. This would possibly not otherwise occur if the instability was generated due to asymmetry within the vortex generator. However, there is an opposing point of view that the asymmetric instability growth rate is low and as a result requires some time downstream before the mode is amplified sufficiently for its effects on the swirling jet to be observed. Again, these arguments are just speculative and in fact, the asymmetry could be a combination of the two. Any definite conclusions would require further investigation, which is beyond the scope of this present study. It should be noted however, that this instability was also found in a similar experimental setup to the present, by Billant et al. (1998).

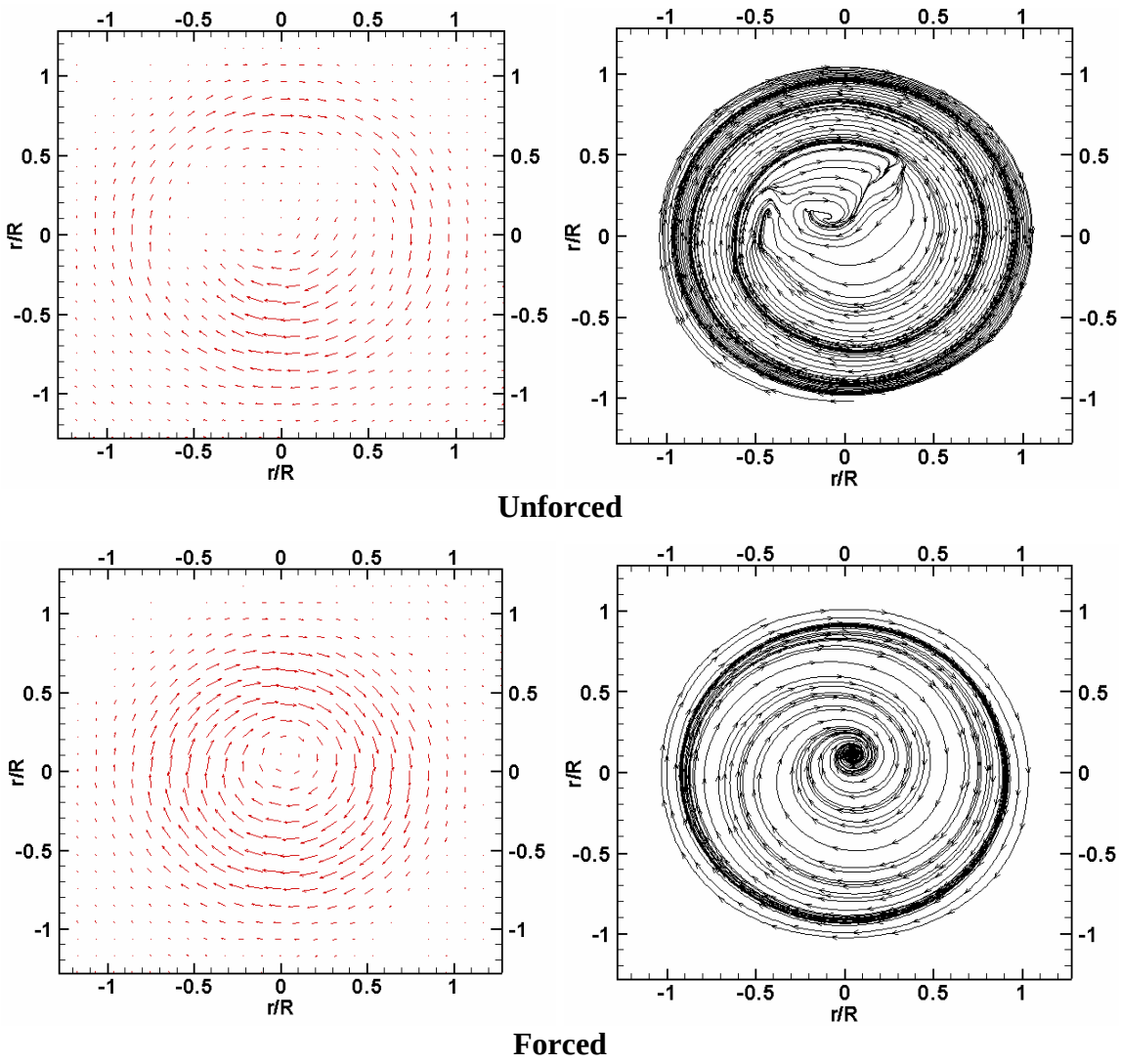

Figure 5.8: **Instantaneous PIV data in the form of vector (left), and streamtracer (right) plots showing a cross-section at z/R = -1, of an unforced (top), and forced (bottom) swirling jet undergoing asymmetric breakdown at R_e = 900, S = 1.35. The unforced case reveals a mode, m = +1 instability within the core at, -0.5 $\leq$ r/R $\leq$ 0.5, while the forced case reveals a symmetric, m = 0 mode at the same axial and radial locations. The forced case was conducted at a PMFV of m_v = 15%, St = St_n, with the instantaneous image at $\dot{m} = \overline{m}$.**

The symmetric m = +2 mode was affected in a manner similar to that of the above mentioned asymmetric mode across the entire Reynolds number range tested, 300 $\leq$ R_e $\leq$ 900, as seen by the flow visualisation images of Figure 5.9. Axial pulsing of the mass

flow rate in general promotes the growth of the axisymmetric m = 0 mode, which is present for non-swirling jets and in the upstream region of swirling jets (i.e. above the point of vortex breakdown), while inhibiting the growth rates of the higher modes m = +1 and +2, but not entirely destroying them. This also leads to the conclusion that due to the limited ability of axial pulsing to inhibit the growth rate of the asymmetric mode, m = +1, (possibly due to the downstream moving helical instability within the jet) and the co-rotating off-axis stagnation point (which both occur in the higher Reynolds number regime), the resultant asymmetry of the breakdown structure cannot be overcome by the present means of axial pulsing of the swirling jet.

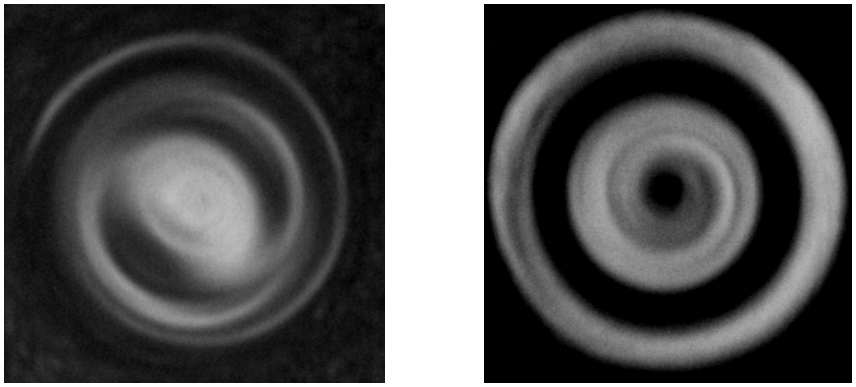

Unforced **Forced**

Figure 5.9: **Flow visualisation showing a horizontal cross-section at z/R = -1 of an unforced (left), and forced (right) swirling jet undergoing cone breakdown at R_e = 600, S = 1.34. The unforced case reveals a mode, m = +2 instability within the core at, -0.5 $\leq$ r/R $\leq$ 0.5, while the forced case reveals a symmetric, m = 0 mode at the same axial and radial locations. The forced case conducted at a PMFV of m_v = 20%, St = St_n, with the instantaneous image at $\dot{m} = \overline{\dot{m}}$.**

Recalling that at low Reynolds numbers, (300 $\leq$ R_e < 725), the flow remains highly symmetrical and symmetry is not affected by the addition of axial pulsing of the mass flow rate as previously seen in Figure 5.2. For the asymmetric high Reynolds number range where asymmetry appears below the co-rotating stagnation point, pulsing the flow, as previously discussed, aids in reducing the growth rate of the helical

disturbance and retards the magnitude of the off-axis rotation of the stagnation point. A comparison of vortex breakdown symmetry in the vertical plane is shown in Figure 5.10 for the turbulent high Reynolds number regimes ($725 < R_e \leq 900$). Figure 5.10 demonstrates the increased symmetry obtained when the current forcing method is applied to an otherwise asymmetric structure. Although the off-axis stagnation point is not entirely destroyed, its effect of causing asymmetry to the structure deteriorates rapidly with increasing amplitude (PMFV) of pulsing. In general, the forced breakdown structure becomes highly symmetrical to such an extent that it now resembles the open cone type

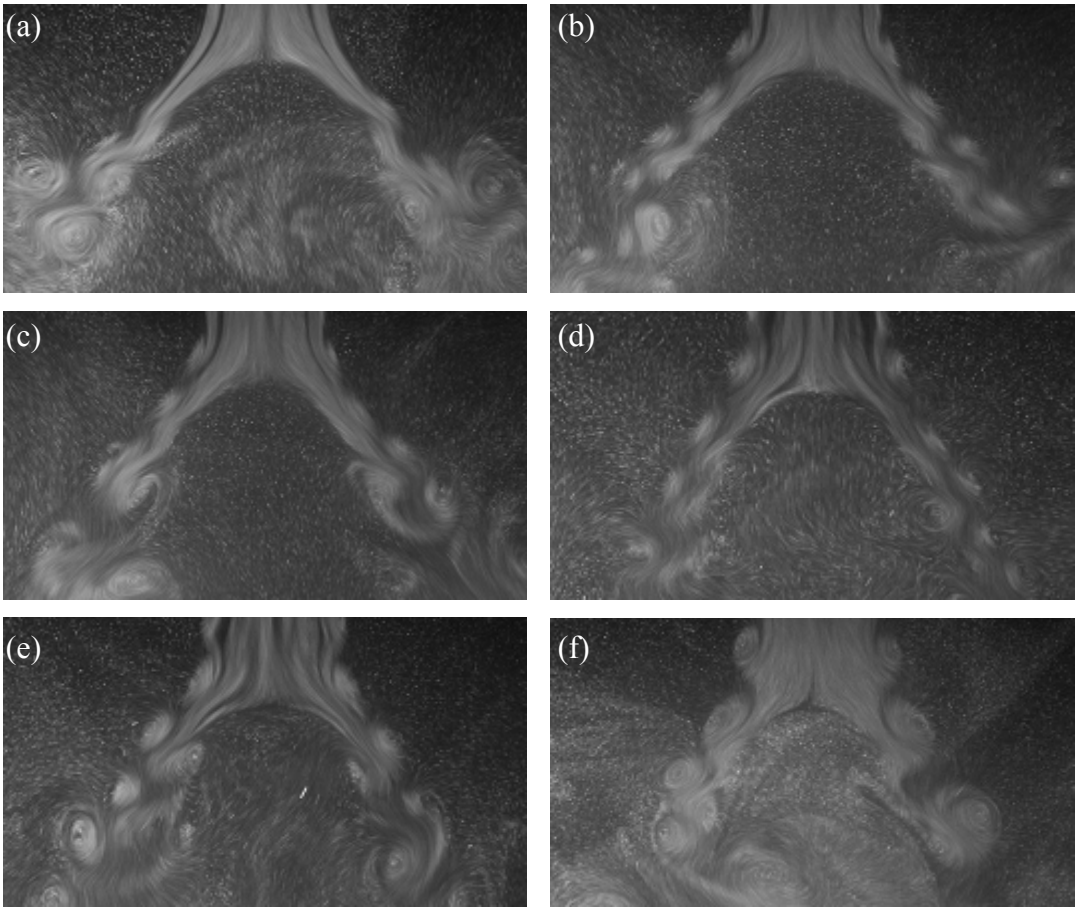

Figure 5.10: Flow visualisation showing the reduction in asymmetry when forcing is applied to an otherwise asymmetric breakdown structure at $R_e = 900$ and $S = 1.34$. Forcing is applied at a fixed frequency of $St = St_n$, at various PMFV values, (a) $m_v = 0$ (un-forced), (b) $m_v = 10\%$, (c) $m_v = 15\%$, (d) $m_v = 25\%$, (e) $m_v = 30\%$ and (f) $m_v = 35\%$.

breakdown, previously only seen in the lower Reynolds number domain of $300 \leq R_e < 725$. Increasing swirl has the effect of increasing the helical instability and amplifying the co-rotating stagnation point hence promoting asymmetry within the breakdown structure. As a result, the effects of pulsing in promoting symmetry in the asymmetric breakdown structure become less successful as swirl is increased.

5.3.3 Axial Location of Forced Vortex Breakdown

Figure 5.11 and previous figures within this chapter (namely, Figures 5.2, 5.4, 5.5, 5.6 and 5.10) clearly show that not only does forcing at the natural frequency of the swirling jet affect the shear layer structure, but also causes a downstream shift/delay of the axial position of the breakdown structure. The effect of pulsing at various Strouhal numbers on the vortex breakdown position (more precisely the stagnation point location) was quantitatively determined via flow visualisation in conjunction with vertical plane PIV and SPIV.

The stagnation point location was determined by extracting the velocity data along the centreline of SPIV data averaged over a minimum of 200 frames. The stagnation point location is obtained by examining the extracted velocity data for the point at which the velocity is zero (indicating a stagnation point) and the velocity upstream and downstream of this location switches sign. This switching of sign indicates that we have passed from the downstream moving swirling jet through the stagnation point to the internal upstream moving recirculating region of the breakdown structure. As a secondary check for stagnation point location, a visual check of the streamtracers of the averaged SPIV image is undertaken in conjunction with the inspection of a long exposure image of the breakdown structure which reveals the streamlines and clearly shows the stagnation point. It is convenient at this point to non-dimensionalise the forced/pulsed breakdown position Z_{bp} as a fraction of the un-pulsed breakdown position Z_b:

$$\Delta Z_{bp} = \frac{Z_{bp} - Z_b}{Z_b}. \qquad \textbf{(5.1)}$$

As previously seen, the most effective Strouhal number at which the shear layer is receptive, is that which matches the natural shedding frequency, St_n. It is at this natural shedding frequency where maximum gains in the downstream shift of the stagnation point are obtained. This is in excellent agreement with experiments conducted using delta wings by Johari and Moreira (1996) and confirm that, in fact, maximum gains in downstream movement of the stagnation point occur at the natural shear layer shedding frequency of the vortical core.

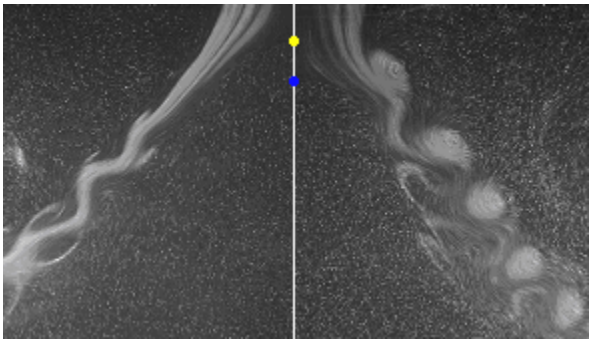

Figure 5.11: Flow visualisation showing the receptivity of a swirling jet shear layer undergoing breakdown at R_e = 600, S = 1.32 to axial pulsing of the mass flow rate at St = St_n and a fixed PMFV of m_v = 20%. The yellow and blue dots indicate the axial stagnation point location of the unforced (left) and forced (right) breakdown states respectively.

The 3-D carpet plots of Figure 5.12 reveal the dependency of the downstream stagnation point movement on swirl number for various Strouhal and PMFV values. It is clear that the addition of swirl has a stabilising effect on breakdown, in that it makes the structure more robust and less receptive to the effects of axial pulsing. This is seen by the inversely proportional trend of downstream stagnation point movement with increasing swirl. This is most likely due to the fact that increasing swirl also increases centrifugal forces (proportional to U_θ^2), hence the effects of axial pulsing in overcoming such forces are less effective. It is also this same centrifugal instability which is the primary reason for vortex breakdown and the upstream movement of breakdown with increasing swirl.

The 3-D carpet plots of Figure 5.13 reveal the dependency of the downstream stagnation point movement on Reynolds number for various Strouhal and PMFV values.

The downstream movement of the forced breakdown structure is only very slightly Reynolds number dependent, showing that this manipulation method is equally applicable to the low Reynolds number laminar breakdown regime and the higher Reynolds number turbulent range. This is as expected, recalling that Mitchell et al. (2000) have shown that the natural Strouhal frequencies at high Reynolds number ($2x10^6 \leq R_e \leq 20x10^6$) vortex breakdown are "similar to those determined at much lower Reynolds number", hence the effects and applicability of the current forcing mechanism should remain similar throughout an extremely broad Reynolds number range, much broader than that tested in the current study.

Figure 5.14 shows the maximum downstream shift, ΔZ_{bpmax}, at various swirl and Reynolds numbers. This further confirms the fact that breakdown delay is only very slightly Reynolds number dependent when we take into account the error bars which show the maximum relative differential location of the stagnation point over an average of 5 runs. This differential stems from experimental error, including minute temperature gradients and inherent errors in mass flow and rotational rates of the pump and vortex generator, respectively. However, the biggest error in measuring stagnation point movement occurs at the point when the downstream shift of an established breakdown begins to plateau at $m_\upsilon > 30$ - 40% due to the appearance of time-varying axial position of the stagnation point, as indicated by the larger error bars. For higher amplitudes, large fluctuations in the stagnation point position are observed in the order of 10% to 20%. As a result of the unsteadiness of the axial stagnation point location and the clear plateau effect with increasing PMFV values, our study was restricted to PMFV values of $m_\upsilon \leq$ 40%.

Both Figures 5.12 and 5.13 reveal some very interesting findings. The increase in stagnation point movement downstream occurs as the forcing frequency approaches that of the natural shedding frequency in a symmetrical fashion above and below St_n. In order to obtain significant downstream movement of the breakdown position, pulsing must be conducted at $St = St_n \pm 10\%$, independent of swirl or Reynolds number for the range tested. It is not uncommon to experience relative shifts of $\Delta Z_{bp} > 50\%$ at $S = S_c$ and St = 0.78, with higher swirl stabilising the structure, in agreement with Loiseleux et al. (1998), and lowering ΔZ_{bp}. Axial pulsing within the hysteretic range at which breakdown exists

has the ability to revert the core to the non-breakdown state, with PMFV values as low as m_υ = 6% to 12%. Axially pulsing a swirling jet which has not yet undergone breakdown ($S < S_c$) can delay the formation of breakdown by raising the threshold critical swirl number for breakdown to occur. An in-depth study of the effects of axial pulsing on swirling jets at $S < S_c$ was not conducted as it was beyond the scope of this particular PhD, but is well suited for future work in this area.

If we consider the relative shift in breakdown as a result of forcing at the natural shear layer shedding frequency, we see that even shifts of $\Delta Z_{bp} > 50\%$ do not seem large in absolute terms as opposed to the relative axial movement, considering that breakdown generally first forms at an approximate downstream axial location of $z/R \cong -2$, when $S = S_c$. However if we take into account our current experimental setup, we realise just how effective axial forcing is in shifting breakdown downstream. The large and rapid expansion of the jet issuing from the nozzle results in a very robust vortex breakdown close to the nozzle. Changes in the stagnation point location, although not large in comparison to systems where the expansion occurs more gradually (e.g., flow over delta wings), are significant and smoothly varying. Hence, from an application view point in which for most systems the expansion generally occurs smoothly, substantial gains in axial location can be easily achieved with minimal energy input while maintaining a zero net change in mass flux.

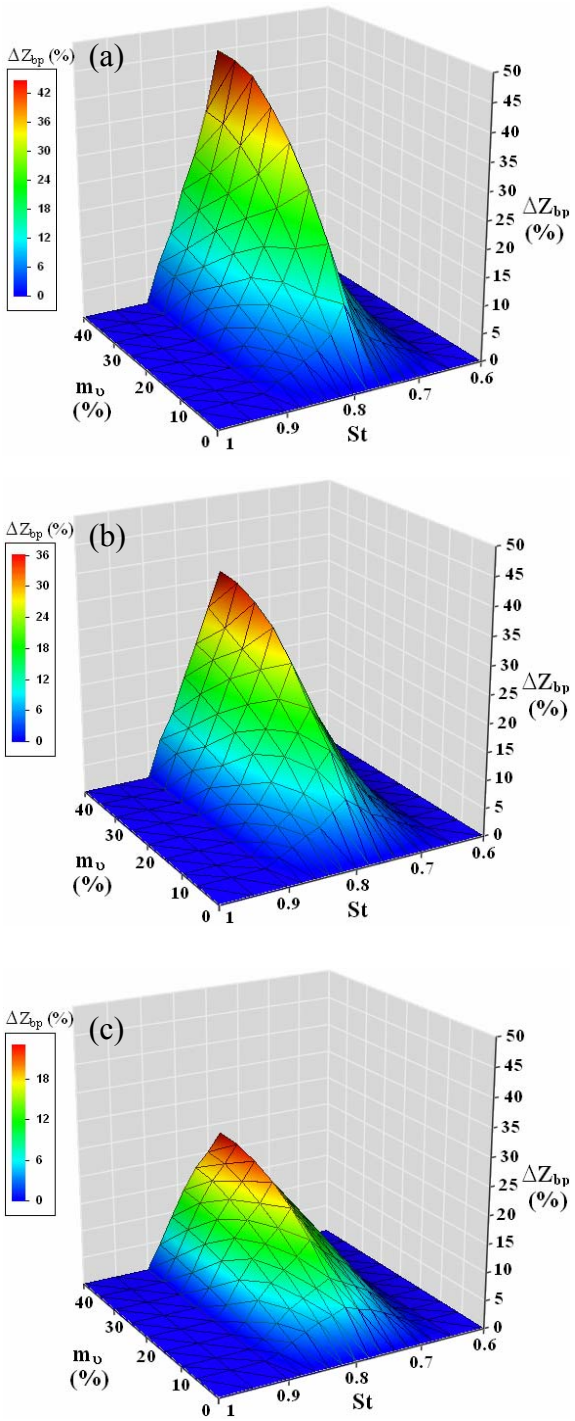

Figure 5.12: **3-D carpet plots of ΔZ_{bp}, showing the dependency on swirl number at, (a) S = 1.35, (b) S = 1.4, (c) S = 1.45 at R_e = 600 and various Strouhal numbers and PMFV values. The maximum deviations in ΔZ_{bp} are indicated by the error bars in Figure 5.14.**

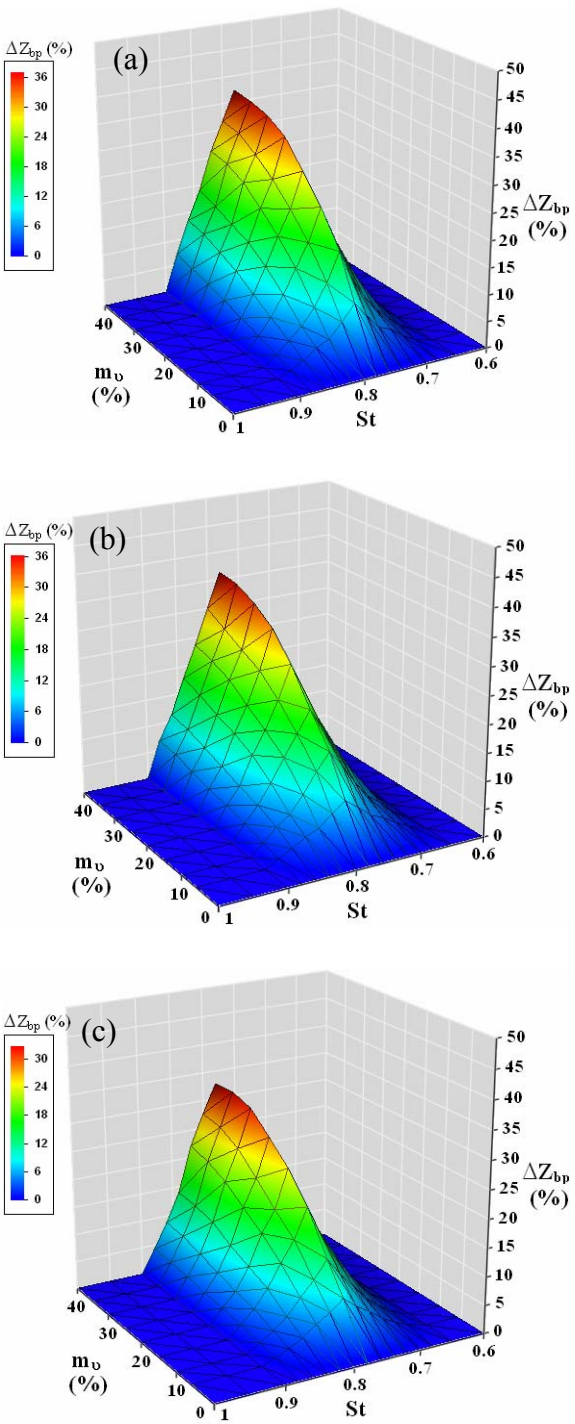

Figure 5.13: **3-D carpet plots of ΔZ_{bp}, showing the dependency on Reynolds number at, (a) R_e = 300, (b) R_e = 600, (c) R_e = 900 at S = 1.4 and various Strouhal numbers and PMFV values. The maximum deviations in ΔZ_{bp} are indicated by the error bars in Figure 5.14.**

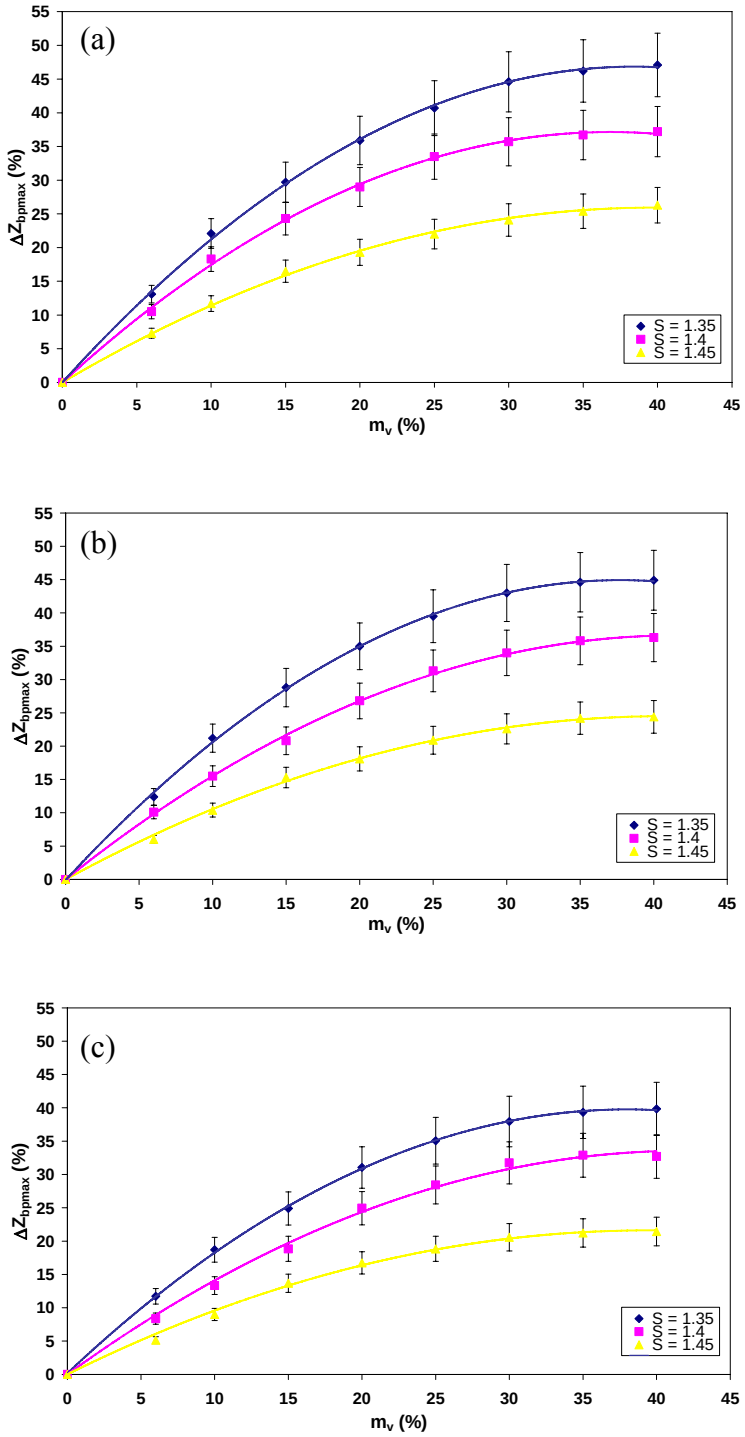

Figure 5.14: **Maximum ΔZ_{bp} achieved by forcing at St = St_n, shown for various swirl numbers, S = 1.35, 1.4 and 1.45 and Reynolds numbers, (a) R_e = 300, (b) R_e = 600 and (c) R_e = 900. Second order least squares polynomials are fitted to the data.**

When forcing is applied at $St = St_n$ (as previously seen in Figures 5.2, 5.4, 5.5, 5.6, 5.10 and 5.11), increases in the concentration of vorticity within the shear layer are observed and excitation of shear layer resonance occurs. Besides the associated highly periodic shedding, shedding of the shear layer now begins to occur much further upstream at the point of vortex conception (i.e. at the nozzle exit), well above the stagnation point in comparison to the unforced case, which occurs at approximately 2 radii downstream of the nozzle and always downstream of the stagnation point. It is these bursts of increased vorticity concentration at regular intervals which is enough to transfer the momentum in the shear layer to the central core of the vortex. This results in effectively modifying the axial and azimuthal velocity profiles in such a way as to lower the average swirl number over a period of time, causing a downstream shift in the breakdown structure or delaying the formation of breakdown altogether.

A typical example of the modification to the axial and azimuthal velocity profile as a result of forcing is shown in Figure 5.15. Firstly, it should be realised that as breakdown has occurred, the close proximity of the stagnation point to the jet exit now means that the data set is no longer an accurate predictor of the swirl number as previously mentioned in Chapter 3. The inaccuracy in obtaining an accurate prediction of the swirl number in such situations is due to the inability to obtain the axial and azimuthal velocity profiles far upstream enough to be sure that it is unaffected by the stagnation point. However, it serves to elucidate the mechanism responsible for the downstream shift in breakdown position when axial pulsing is applied at $St = St_n \pm 10\%$. Two extremes on the forced axial and azimuthal velocity plots of Figure 5.15, labelled “Forced - max” and “Forced - min”, indicate the velocity profiles which coincide with the maximum and minimum mass flow rates, respectively, at $z/R = -1$. The axial profiles of Figure 5.15 (a), reveal that pulsing in this particular manner causes a deficit at $r/R = \pm 0.6$, in the region of minimal shear stress, and an axial increase along the centreline at $r/R = 0$, again a region of minimal shear stress, which is in agreement with theoretical investigations into pulsed flows by Womersley (1955).

As mentioned in Chapter 3, there exists a complex interaction between the two velocity components which determine the swirl number, namely, the axial and azimuthal velocity. Examining Figure 5.15 (b) reveals a very small relative change in azimuthal

velocity when comparing it to the axial component. Overall the swirl number decreases as a result of forcing, as axial velocity deficits are small/negligible along the centreline where maximum velocities exist, when compared to the large axial gains in the same region. As part of the well proven swirl number definition (equation (2.2)), the maximum velocity component in both the axial and azimuthal directions must be determined when calculating the swirl number. Overall, the average swirl number is reduced significantly when forcing is applied at $St = St_n$, as the percentage increase in maximum axial velocity over the increase in azimuthal velocity is far greater in comparison. The exact decrease in swirl number cannot be quantified with much certainty due to the close proximity of the stagnation point. However, relatively speaking, the gains in axial velocity far outweigh their reduction along the centreline (where maximum velocities occur and are required to determine the swirl number), hence the lowering of the swirl number has the effect of shifting the stagnation point downstream.

The reason why velocity gains and deficits are located in the position seen in Figure 5.15 can be attributed to the complicated effects of increased concentrated vortices shed from the shear layer during forcing well upstream of breakdown. Figure 5.16 shows the downstream movement of a shed shear layer vortex ring as it proceeds downstream and the resulting effect on the vortical core. As previously seen in Figures 5.4, 5.5 and 5.6, the intensification of vorticity within the shear layer due to forcing at the natural shear layer shedding frequency, results in a reduction of the vortical core in the immediate vicinity of the shed vortex ring. This ultimately results in increased axial velocities within the vortex core, not only as a result as conservation of mass and the reduced vortex core cross-sectional area, but also due to the shed vortices transferring the momentum in the shear layer to the central core of the vortex. This is confirmed by the velocity profiles in Figure 5.15, which show that the momentum transfer and axial velocity increase is concentrated along the centreline hence lowering the local swirl number and shifting the established breakdown structure downstream.

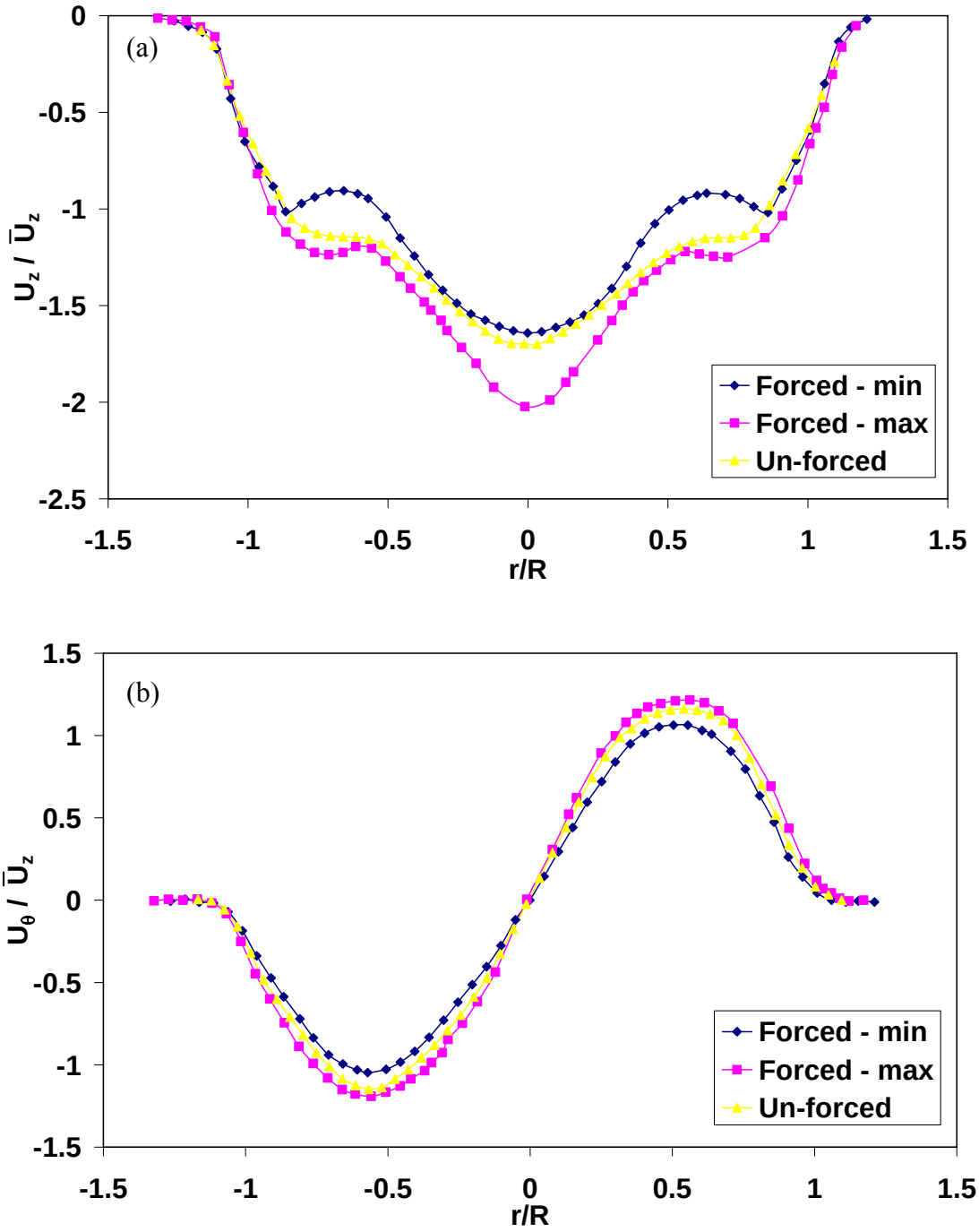

Figure 5.15: **Typical unforced and forced axial (a) and azimuthal (b) velocity profiles at R_e = 600, S = 1.34. Showing that forcing results in an axial velocity increase along the centreline (r/R = 0) and deficit at r/R = ±0.6, while only a minimal change in azimuthal velocity occurs. Forcing was conducted at St = St_n, with a fixed PMFV value of m_v = 30%. All data was deduced from instantaneous SPIV data at z/R = -1.**

Figure 5.17 shows flow visualisation, instantaneous velocity vector fields overlaid on contours of axial velocity, U_z, and vorticity contour fields at R_e = 900, S = 1.35 and m_v = 25%. It is clear that the axial velocity along the centreline (r/R = 0) for the minimum and median times of pulsing remains relatively constant as seen in image (a) and (b) respectively. However, there is a noticeable increase in centreline axial velocity as the maximum point in forcing/mass flow rate is reached. As was the case with the lower Reynolds number range, the increased intensity of the shed vortices causes a reduction in the vortical core diameter and a transfer of momentum from the periphery of the jet to the jet centreline.

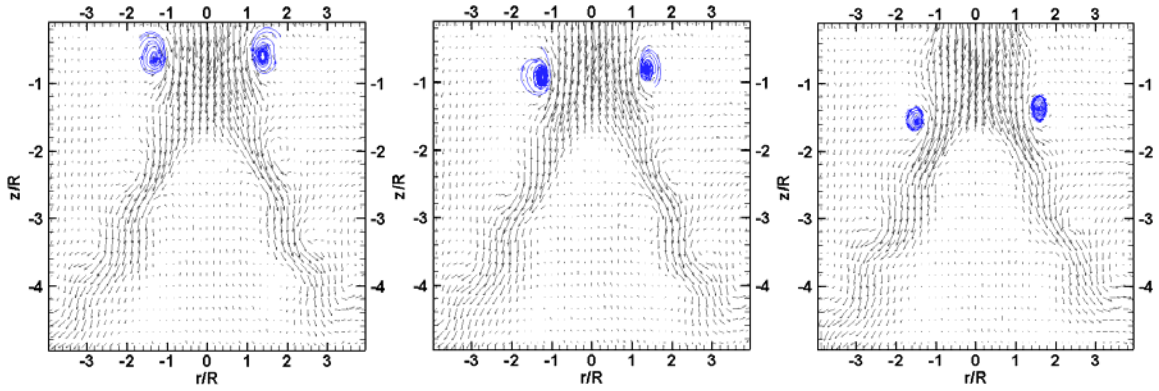

Figure 5.16: Velocity vector plots showing the downstream motion of a shed vortex ring from the shear layer generated at the nozzle exit over one period of pulsing at R_e = 600, S = 1.34 and m_v = 30%. Blue streamtracers highlight the downstream moving vortex ring.

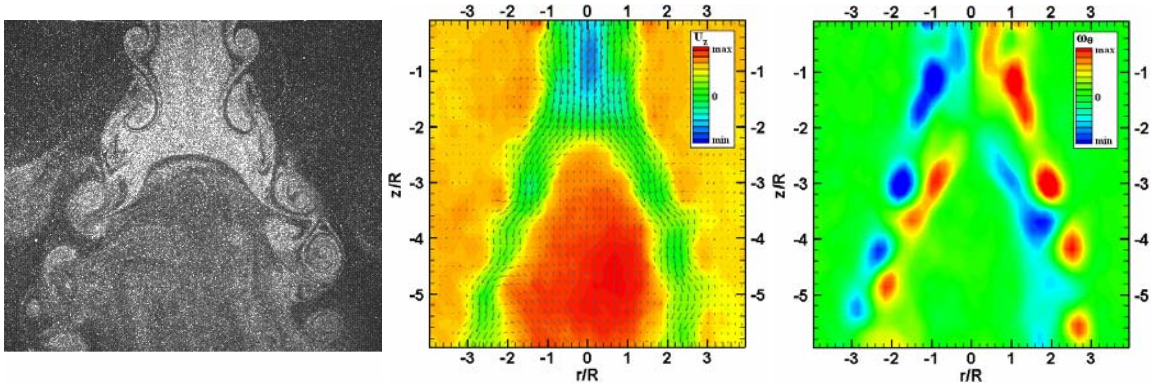

(a) Minimum

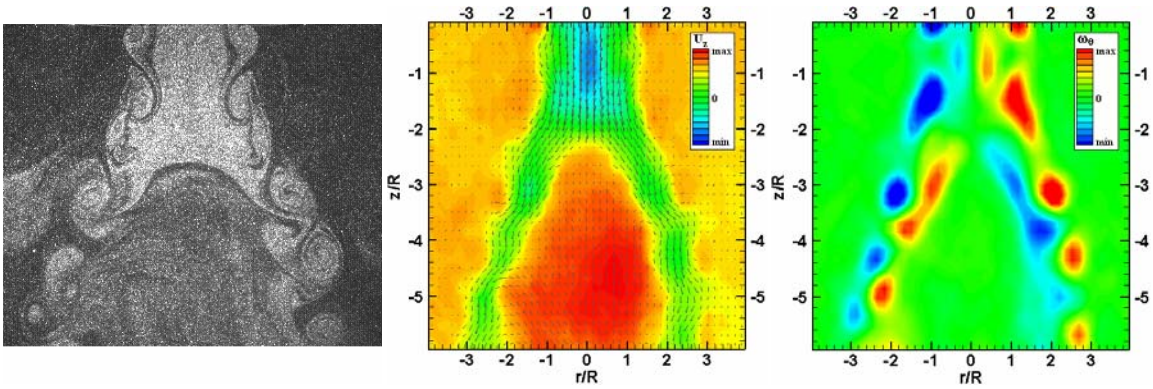

(b) Median

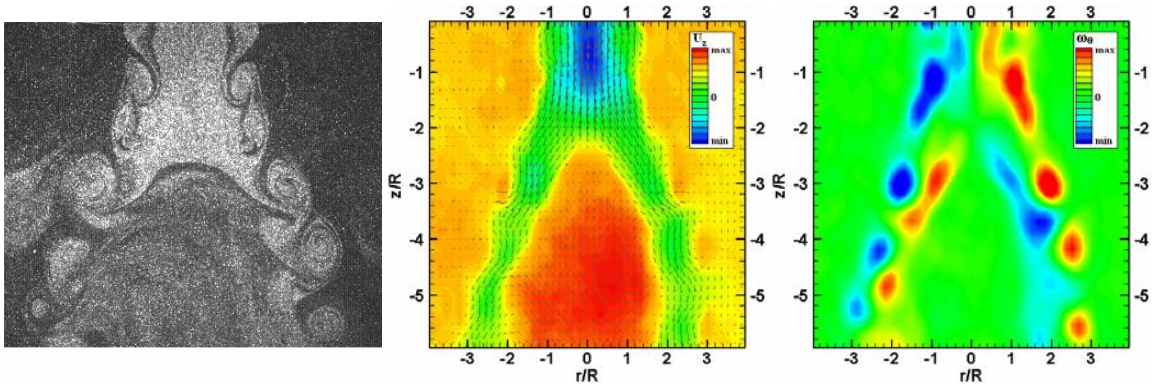

(c) Maximum

Figure 5.17: **Flow visualisation (left) in conjunction with an instantaneous velocity vector field overlayed on contours of axial velocity (middle) and vorticity contour field (right) at, (a) minimum, (b) median and (c) maximum phases of mass flow rate and velocity pulsation at R_e = 900, S = 1.35 and m_v = 25%. This figure clearly indicates the effect on centreline maximum velocity due to the intensified vorticity within the shear layer shedding as a result of axial pulsing. The equi-spaced colour contours for velocity are: max = 0.04 ms^{-1} and min = -1.5 x 10^{-3} ms^{-1}, and vorticity are: max = 2 s^{-1} and min = -2 s^{-1}.**

Chapter 6

Conclusions

Concluding Remarks and Future Work

6.1 Introduction

This Chapter will bring together a concise summary of the work completed within this PhD thesis and the important conclusions which can be drawn from this experimental investigation. In order to facilitate coherency, this chapter will be broken into five main sections outlining general conclusions regarding this PhD thesis as whole, followed by conclusions specific to each of the three experimental results chapters and a final section outlining suggestions for future work.

6.2 General Conclusions

This PhD thesis has covered an experimental investigation into various aspects of vortex breakdown and vortex breakdown control, a topic which has been, and remains, of immense interest and importance in a wide array of industries. Several novel experiments have produced results which contribute to the knowledge within this field of research. Several new findings have been discovered along with results which agree with, and some which contradict, previous studies throughout the literature regarding various aspects of this phenomenon.

In order to examine the effects of thermal convection and sinusoidally forcing the flow, on vortex breakdown, a base study into the development of a swirling jet undergoing breakdown was conducted in order to obtain qualitative and quantitative results for comparison. The various swirling jet and breakdown states which arise in a parametric study of swirl and Reynolds number have been extensively documented for a Reynolds number range of $300 \leq R_e \leq 900$. A detailed look at 3-D vector fields using SPIV has allowed an in-depth analysis of the velocity and vorticity fields associated with vortex breakdown. This work has enabled the identification of the principal factors which lead to breakdown and the key features of the three main types of breakdown structures identified. From this study, proposed explanations as to why different breakdown structures are observed with different experimental setups and conditions have been put forward.

A theoretical investigation with experimental verification into the effects of temperature difference induced natural convection has shed new light into this particular area of research. An analysis of the global effects of convection in terms of a temperature difference between the tank walls and working tank fluid was examined with startling results. The effects of Reynolds number and Grashof number has shown the profound influence and dominance over flow properties which convection can have on such experimental setups if care is not taken. The effects on breakdown when a temperature difference is imposed or exists between the swirling jet and tank fluid confirm the extent to which convection is a critical factor in controlling and predicting vortex breakdown. A theoretical criterion derived to predict the onset of breakdown when convection is taken

into account was successfully verified by experimental results, further revealing the extent to which breakdown is sensitive to the effects of convection caused by temperature differences.

A final look at the effects of axial sinusoidal forcing of an unconfined swirling jet undergoing breakdown has not only been a novel experiment but has also revealed some very interesting findings. In the same manner as the previous chapter, these results are extremely useful for industry purposes and contribute greatly to the knowledge within this particular field of fluid mechanics. This method of vortex breakdown control proves to be an extremely promising method of controlling vortex breakdown with minimal energy input.

6.3 Chapter 3 Conclusions: Vortex Breakdown

A swirling jet undergoing breakdown has been extensively researched using PIV, SPIV and flow visualisation. The swirling jet consisted of a jet-like axial velocity profile and is characterised by high levels of vorticity at its core periphery due to the associated azimuthal shear. This type of vortex was found to promote both axisymmetric centrifugal instability and Kelvin-Helmholtz instability, causing a destabilisation of the azimuthal modes. As a possible result of the experimental setup (mainly the contracting nozzle arrangement), there exists a non-linear relationship between the axial and azimuthal velocities, increasing or decreasing the azimuthal velocity causes an increase or decrease in the axial velocity component respectively, and vice versa.

The circulation differs greatly to that of a Batchelor or Rankine vortex which is used in the majority of theoretical studies on trailing line vortices, in that their circulation remains constant and does not decay to zero as in our case. Secondly, it is still unknown whether the region of decreasing circulation (in a vertical plane along the vortex axis) is a sufficient criterion alone to declare this a centrifugally unstable flow. Hence the available theory does not accurately represent and describe the results obtained throughout this experimental investigation.

In general, the minimum swirl number for breakdown to occur is in the range of $1.31 \leq S_c \leq 1.35$ for the Reynolds numbers tested ($300 \leq R_e \leq 1200$). There is however a slight increasing trend in the critical swirl number with increasing Reynolds number. This slight increase in swirl number could be attributed to the asymmetry and unsteadiness associated with higher Reynolds number vortex breakdown. This requires an increase in the centrifugal instability (by increasing the swirl) to overcome the opposing higher negative internal pressure arising from the unsteadiness and higher internal velocities.

Above a Reynolds number of approximately 650 to 725, hysteresis no longer exists and is only a low Reynolds number effect. The transitional boundary for hysteresis also coincides with that of the Reynolds number boundary for axisymmetric and asymmetric breakdown. This boundary lies in the region of $R_e = 725 \pm 19$. It is this coinciding of R_e boundaries which leads to the most plausible reason for the lack of hysteresis at higher Reynolds numbers as being due to the asymmetry and unsteadiness in this Reynolds number regime that results in disturbances, which preclude such a sensitive breakdown region to exist.

The progression of a swirling jet leading to breakdown consists of four distinct regimes. At $S = 0$, the non-swirling jet is highly structured and characterised by strong axisymmetric deformations due to Kelvin-Helmholtz instability at the jet periphery. The addition of low to moderate swirl, $0 < S < 1$, intensifies the shed vortex rings due to an interaction and transfer of vorticity between the axial and azimuthal components resulting in a modified type of Kelvin-Helmholtz instability. This intensification of shed vortices also causes an increase in the entrainment rate of the shear layer. At $1 < S < 1.3$, distinct pinching of the jet downstream occurs and moves upstream with increasing swirl. Above the point of pinching, a broadening of the jet begins to take place, causing its dissipation into small scale turbulence. Once this balance of asymmetric and axisymmetric instabilities has had sufficient time to reach equilibrium, a coherent and steady trident state appears before the onset on vortex breakdown in the final regime, $S > 1.3$.

Once breakdown occurs, two regimes exist, axisymmetric breakdown ($300 \leq R_e < 725$), and asymmetric breakdown ($725 < R_e \leq 900$). The axisymmetric Reynolds number range is typified by the formation of a stagnation point downstream, which gradually travels upstream creating a small open ended transitional bubble breakdown state in its

wake, containing a tilted toroidal vortex ring within its internal recirculating flow. Given sufficient time, the disturbances settle and result in a steady cone type breakdown. The tilted vortex ring is responsible for the filling and emptying of the transitional bubble. The near axis region draws the downstream flow upstream, before it is expelled and passed into the outer perimeter region of the internal structure. The asymmetric Reynolds number breakdown regime tested includes a more open ended breakdown state which is almost a mix of a bubble and a cone state (the transitional bubble state no longer exists). Asymmetry is due to the precession of the off-axis stagnation point about the central axis, in the same rotational direction as the vortex core. The existence of a bubble state as only being a transitional breakdown state is contradictory to observations by a few other researchers with similar experimental setups (see for example Billant et al. (1998)), who believe that the bubble is a steady state breakdown structure. This is possibly due to fine differences in the control of the axial velocity in which any unsteadiness causing axial movement of the stagnation point gives rise to an open ended bubble as opposed to a steady state cone breakdown. The axial movement in breakdown position is not a linear function of the swirl number, even across the entire hysteretic range. For an unforced swirling jet (in the Reynolds number range investigated, $300 \leq R_e \leq 900$), the Strouhal number of shedding is independent of Reynolds number and swirl number, and is fixed at $St = St_n = 0.78 \pm 0.01$.

Mode m = +2 appears in the range $300 \leq R_e < 725$, straddling the critical swirl number for breakdown. Modes m = +1 and +2 are present at $725 < R_e \leq 900$, above the onset of breakdown while below the onset of breakdown, there appears an m = +2 mode. For all the above mentioned cases, there exists an underlying axisymmetric mode m = 0 in the upstream region of the swirling jet.

Azimuthal vorticity plots reveal that the transition from a swirling jet to breakdown is identified by an internal vorticity sign swap within the viscous core of the swirling jet. This internal vorticity sign swapping as a prerequisite for vortex breakdown to occur is in agreement with experiments by Althaus et al. (1995), Brown and Lopez (1990).

6.4 Chapter 4 Conclusions: Convection Effects

Convection is an important and unavoidable part of most experiments; and due to the sheer size required for this experimental rig, extreme care is required to minimise its effects. Convection will occur at temperature differences several orders of magnitude smaller than can be measured by the most sensitive equipment available to us.

For similar experimental setups in which moderate to low Reynolds number flows in a comparatively large experimental rig are tested, it is effectively required that ΔT approach zero. Even a slight and almost immeasurable temperature difference will cause natural convection to occur and be the governing/dominant bulk flow in the Reynolds number range with which we are concerned (at least in terms of global circulation within the tank). If temperature control is not adequate, our theoretical analysis indicates that Reynolds numbers several orders of magnitude greater than that used are required to ensure that forced convection would be the dominant flow even for the most minute temperature differences.

When trying to overcome this problem, it is obvious that the effects of confinement limit the possible solutions. Increasing the Reynolds number of the swirling jet would produce no gains as to maintain a relatively unconfined swirling jet, the experimental tank would also need to increase in size. Hence it is clear that on a global scale of thermal effects, the only way to control this phenomenon is to maintain a uniform test temperature throughout the experimental rig and its surroundings.

Although the position of maximum convected velocity within the boundary layer is far removed from the forced convection/swirling jet located at $y = L/2$, the effects of recirculating currents are of major concern. The lowest achievable velocity ratio for the parameters considered is approximately 8% for $R_e = 900$ and $\Delta T = 0.1°C$, which is the lowest accurately measurable temperature difference.

A theoretical criterion for the onset of vortex breakdown which includes the effects of convection due to temperature differences was developed and experimentally verified for a temperature range of $16°C \leq T \leq 24°C$. This criterion along with successful experimental verification shows the highly dependent and non-linear nature of the critical

(breakdown) swirl number as a function of ΔT. It is clear from the experimental SPIV data and flow visualisation that lower Reynolds number flows are greatly influenced by the effects of convection. The effect of a negative ΔT (i.e. when the jet is colder than the surrounding fluid) is much more pronounced than for positive values.

It was found that even if the Richardson number associated with the imposed temperature difference, ΔT, was considerably less than unity (indicating that the buoyancy forces associated with convection are small in comparison to the inertial forces), the temperature variations are still large enough to significantly alter the flow. Vortical flows and especially flows experiencing low Reynolds number vortex breakdown are found to be extremely sensitive to temperature variations. Temperature gradients can lead to a premature loss of axisymmetry, and an alteration to the dominant mode from the axisymmetric m = 0 mode, to the asymmetric m = 1 mode.

Axial temperature gradients enabled either the suppression or advancement of breakdown. A negative temperature gradient, in which negative buoyancy assists the downstream motion of the vertical core, suppresses breakdown while a positive temperature gradient advances breakdown and enlarges the breakdown bubble. An imposed positive temperature difference not only widens the cone but also raises the upstream positive axial velocities (of the order of 50%) associated with the extremities of the conical sheet. A positive temperature difference can also cause premature breakdown at values much less than the critical swirl number for breakdown in a uniform temperature environment, due to convective flow opposing the downstream momentum of the jet. The opposite case, in which a negative temperature difference is imposed, causes the required critical swirl number to increase dramatically for breakdown to occur. Associated with this high swirl number breakdown is a more compact recirculating bubble in contrast to an open cone breakdown. Temperature gradients are found to have a much more significant effect on breakdown than increasing the Reynolds number.

If the swirling jet is of a temperature lower than that of the surrounding fluid, a cone breakdown will be suppressed and a more closed bubble type breakdown will be encouraged to form with a lower downstream location of the stagnation point. For the case in which ΔT is positive, the formation of the open cone type breakdown is enhanced

in which the extremities of the conical sheet move upstream, and a wider apex angle exists in the vicinity of the stagnation point along the axis.

6.5 Chapter 5 Conclusions: Effects of Axial Pulsing

An experimental investigation into the effects of sinusoidally forcing a swirling jet undergoing breakdown has resulted in several key findings. Results have been obtained that clearly reveal that pulsing at the natural shedding frequency leads to a substantial downstream shift of the mean breakdown position. Furthermore, application of low level forcing at the natural frequency intensifies the shear layer vortices considerably.

The application of axially pulsing swirling jets undergoing vortex breakdown can have some profound effects on the flow structure. For the forced case, the shedding frequency of the swirling jet was found to lock onto low frequencies up to approximately $0.25St_n \leq St \leq 2St_n$. Above this critical range, the flow below the stagnation point is not receptive to the higher frequency pulsing and the jet sheds at its natural frequency, independent of the amplitude of the forcing.

To obtain downstream movement of the breakdown position, pulsing must be conducted close to the natural frequency, i.e. at $St = St_n \pm 10\%$. Axial pulsing within the hysteretic range over which breakdown exists has the ability to destroy the breakdown structure altogether with Peak Mass Flow Variation (PMFV) values as low as m_U = 6-10%. It is possible to shift the breakdown structure by up to 50% at $S = S_c$ and $St = St_n$ = 0.78. The increased vorticity concentrations within the shear layer and the highly periodic shedding at St = 0.78 ± 10% has the effect of forcing the stagnation point further downstream, delaying breakdown as shedding now occurs closer to the nozzle exit.

Axial pulsing of the mass flow rate in general promotes the growth of the axisymmetric m = 0 mode, which is present for non-swirling jets and in the upstream region of swirling jets (i.e. above the point of vortex breakdown), while inhibiting the growth rates of the higher modes m = +1 and +2, but not entirely destroying them. As a result, the resultant asymmetry of the breakdown structure can only be reduced and cannot be totally overcome by the present means of axial pulsing of the swirling jet.

Bursts of increased vorticity concentrations at regular intervals, as a result of axial pulsing, cause a reduction in the jet diameter in the vicinity of the shedding vortex ring. The intensified shedding is also enough to transfer the momentum in the shear layer to the central core of the vortex. As a result, the axial and azimuthal velocity profiles are effectively modified in such a way as to lower the average swirl number over a period of time and delay the onset of breakdown and/or shift the breakdown structure downstream.

The large and rapid expansion of the jet issuing from the nozzle results in a very robust vortex breakdown close to the nozzle. Changes in the stagnation point location, although not large in comparison to systems where the expansion occurs more gradually (e.g. flow over delta wings), are significant and smoothly varying. Hence from an application view point in which for most systems the expansion generally occurs smoothly, substantial gains in axial location can be easily achieved with minimal energy input while maintaining a zero net change in mass flux.

6.6 Suggestions for Future Work

Suggestions for future work in such a broad ranging area such as vortex breakdown and control can be too numerous to mention. It is for this reason that we will limit our discussion to areas of interest relating specifically to the study undertaken within this PhD.

An in-depth study into the effects of experimental apparatus on the observed breakdown states is required to resolve the numerous aspects of breakdown which receive differing observations and opinions. This could also include a study into the effects of differing velocity profiles and their effects on the breakdown structures due to the differing instabilities they promote, in essence an extension of the work already done by Ruith et al. (2003).

The development of a complete theory for breakdown which can describe all that is observed in the literature is required in order to obtain a fundamental understanding of the exact physics behind this phenomenon. This would have to include a theoretical vortex model which accurately replicates the experimental observations, as the current

models available such as the Batchelor or Rankine vortices are found to be inadequate and unrepresentative. Such an investigation could include whether or not a region of decreasing circulation is a sufficient criterion alone to declare a swirling jet as centrifugally unstable.

The effects of convection on vortex breakdown have been well documented for this particular experimental setup, however, there is a great gap in the literature regarding its effects in other experimental setups. The development of a practical method of implementing imposed temperature differences to induce convective flow as a form of controlling breakdown would be highly desirable for industry purposes.

An investigation into how to implement the current method of pulsing into various industrial applications is required. This could include combustion chambers (this would include an investigation into its effectiveness when compression is a major factor in the process), mixing vessels and delta wings for efficient control of the vortex breakdown structure. To further extend this vortex breakdown control method, a closed loop real time system must be developed to account for the flexibility and continual variation experienced in the swirling jet properties when implemented over delta wings during manoeuvring. An additional study of the effects of axial pulsing on swirling jets for $S < S_c$, would also be an advantageous extension to the work presented within this PhD thesis.

References

Adams, B., Jones, M., Hourigan, K., and Thompson, M. C.(1999). "Hysteresis in the Open Pipe Flow with Vortex Breakdown." *Second International Conference on CFD in the Minerals and Process Industries*, CSIRO, Melbourne, Australia, 325-330.

Adrian, R. J. (1988). "Statistical Properties of Particle Image Velocimetry Measurements in Turbulent Flow." *Laser Anemometry in Fluid Mechanics*, 3, 115-129.

Adrian, R. J., and Yao, C. S. (1985). "Pulsed Laser Technique Application to Liquid and Gaseous Flows and the Scattering Power of Seed Materials." *Applied Optics*, 24, 44-52.

Akilli, H., and Sahin, B. (2001). "Control of Vortex Breakdown by a Transversely Oriented Wire." *Physics of Fluids*, 13(2), 452-463.

Akilli, H., Sahin, B., and Rockwell, D. (2003). "Control of Vortex Breakdown by a Coaxial Wire." *Physics of Fluids*, 15(1), 123-133.

Alexander, A. J. (1963). "Experiments on a Delta Wing Using Leading-Edge Blowing to Remove Secondary Separation." Aeronautical Research Council. *249963.*

Althaus, W., Brucker, C., and Weimer, M. (1995). "Breakdown of Slender Vortices." Fluid Vortices - Fluid Mechanics and Its Applications, S. I. Green, ed., Dordrecht: Kluwer Academic, 373-426.

Anders, H., and McCulskey, D.(1994). "The Accuracy and Reliability of Piv Measurements." *Proceedings of the Seventh International Symposium on Applications of Laser Techniques to Fluid Mechanics*, Lisbon, Portugal, 891-897.

Arnold, W., and Hinsch, K. D. (1989). "Parallel Optical Evaluation of Double Exposure Records in Optical Metrology." *Applied Optics*, 28(4), 726-729.

Behrbohn, H. (1965). *Basic Low-Speed Aerodynamics of the Short-Coupled Canard Configuration of Small Aspect Ratio*, SAAB, Sweden.

Benjamin, T. B. (1962). "Theory of the Vortex Breakdown Phenomenon." *Journal of Fluid Mechanics*, 14, 593-629.

Bera, J. C., Michard, M., Grosjean, N., and Comte-Bellot, G. (2001). "Flow Analysis of Two Dimensional Pulsed Jets by Particle Image Velocimetry." *Experiments in Fluids*, 31(5), 519-532.

Bhattacharyya, S., and Pal, A. (1998). "Axisymmetric Vortex Breakdown in a Filled Cylinder." *International Journal of Engineering Science*, 36, 555-563.

Billant, P., Chomaz, J. M., and Delbende, I. (1994). "Tridents, Bubbles and Cone-Like States in Swirling Jets." *Bulletin of American Physics Society*, 39, 921-935.

Billant, P., Chomaz, J. M., and Huerre, P. (1998). "Experimental Study of Vortex Breakdown in Swirling Jets." *Journal of Fluid Mechanics*, 376, 183-219.

Bornstein, J., and Escudier, M. P. (1984). "Lda Measurements within a Vortex Breakdown Bubble." Laser anemometry in fluid mechanics, Ladoan-Instituto Superior Tecnico.

Bradley, R. G., and Wray, W. O. (1974). "A Conceptual Study of Leading-Edge-Vortex Enhancement by Blowing." *Journal of Aircraft*, 11(1), 33-38.

Breuer, M., and Hanel, D.(1989). "Solution of the 3d Incompressible Ns Equations for the Simulation of Vortex Breakdown." *Proceedings of the Eighth GAMMM Conference on Numerical Methods in Fluid Mechanics*.

Breuer, M., and Hanel, D. (1993). "Dual Time Stepping Method for 3-D, Viscous, Incompressible Vortex Flows." *Computers & Fluids*, 22(4), 467-484.

Brown, G. L., and Lopez, J. M. (1990). "Axisymmetric Vortex Breakdown. Part 2: Physical Mechanism." *Journal of Fluid Mechanics*, 221, 553-76.

Brucker, C. (2002). "Some Observations of Vortex Breakdown in a Confined Flow with Solid Body Rotation." *Flow, Turbulence and Combustion*, 69(1), 63-78.

Bruecker, C. (1993). "Study of Vortex Breakdown by Particle Tracking Velocimetry. Part 2: Spiral-Type Vortex Breakdown." *Experiments in Fluids*, 14, 133-139.

Bruecker, C. (2002). "Some Observations of Vortex Breakdown in a Confined Flow with Solid Body Rotation." *Flow, Turbulence and Combustion*, 69, 63-78.

Bruecker, C., and Althaus, W. (1992). "Study of Vortex Breakdown by Particle Tracking Velocimetry. Part 1: Bubble-Type Vortex Breakdown." *Experiments in Fluids*, 13, 339-349.

Bruecker, C., and Althaus, W. (1995). "Study of Vortex Breakdown by Particle Tracking Velocimetry (Ptv) Part 3: Time-Dependent Structure and Development of Breakdown-Modes." *Experiments in Fluids*, 18(3), 174-186.

Caflisch, R. E., Xiaofan, L., and Shelley, M. J. (1993). "The Collapse of an Axi-Symmetric, Swirling Vortex Sheet." *Physics of Fluids*, 6(6), 843-867.

Campbell, J. F. (1976). "Augmentation of Vortex Lift by Spanwise Blowing." *Journal of Aircraft*, 13(9), 727-732.

Cassidy, J. J., and Falvey, H. T. (1970). "Observations of Unsteady Flow Arising after Vortex Breakdown." *Journal of Fluid Mechanics*, 41(4), 727-736.

Chanaud, R. C. (1965). "Observations of Oscillatory Motion in Certain Swirling Flows." *Journal of Fluid Mechanics*, 21, 111-127.

Cheng, Y., and Lu, Z. (1993). "Forms of Unsteady Concentrated Vortex-Breakdown and Its Reactions to Disturbance." *Journal of Beijing University of Aeronautics and Astronautics*, 1, 95-100.

Cho, S. K., Yoo, J. Y., and Choi, H. (2000). "Resonance in Axisymmetric Jet under Controlled Helical, Fundamental, and Axisymmetric Subharmonic Forcing." *American Institute of Aeronautics and Astronautics Journal*, 38(3), 434-441.

Cho, Y. C., and Park, H.(1990). "Instantaneous Velocity Field Measurement of Objects in Coaxial Rotation Using Digital Image Velocimetry." *Proceedings of the International Society for Optical Engineering*, San Diego, CA, USA, 740-748.

Cornish, J. J.(1970). "High Lift Applications of Spanwise Blowing." *7th Congress of the International Council of the Aeronautical Sciences, ICAS*, Rome, Italy, Paper no. 70-09.

Cornish, J. J.(1983). "Vortex Flows." *American Institute of Aeronautics and Astronautics Applied Aerodynamics Conference*, Danvers, MA, AIAA-83-1812.

Delery, J. M. (1994). "Aspects of Vortex Breakdown." *Progress in Aerospace Sciences*, 30, 1-59.

Deng, Q., and Gursul, I. (1996). "Effect of Leading-Edge Flaps on Vortices and Vortex Breakdown." *Journal of Aircraft*, 33(6), 1079-1086.

Dixon, C. J. (1969). "Lift Augmentation by Lateral Blowing over a Lifting Surface." AIAA/AHS VTOL Research, Design, and Operations Meeting, Atlanta, GA.

Dixon, C. J., Dansby, T., and Poisson-Quinton, P.(1978). "Benefits of Spanwise Blowing at Transonic Speeds." *11th International Congress of Aeronautical Sciences (ICAS)*, Lisbon, Portugal, 430-436.

Eaton, J. K., and Fessler, J. R. (1994). "Preferential Concentration of Particles by Turbulence." *International Journal of Multiphase Flow*, 20, 169-209.

Eckert, G. (1950). "Analysis of Turbulent Free-Convection Boundary Layer on Flat Plate." *Report 1015.*

Eckert, G. (1964). "Regimes of Flow in Horizontal Tubes." *Journal of Heat Transfer*, 86, 295-304.

Er-El, J., and Seginer, A.(1986). "Effects of Spanwise Blowing on Pressure Distribution and Leading-Edge Vortex Stability." *15th Congress of the International Council of the Aeronautical Sciences*, London, ICAS-86-2.5.1.

Escudier, M. P. (1984). "Observations of the Flow Produced in a Cylindrical Container by a Rotating Endwall." *Experiments in Fluids*, 2(4), 189-196.

Escudier, M. P. (1988). "Vortex Breakdown: Observations and Explanations." *Progress in Aerospace Sciences*, 25(2), 189-229.

Escudier, M. P., Bornstein, J., and Maxworthy, T. (1982). "The Dynamics of Confined Vortices." *The Royal Society of London. Proceedings. Series A. Mathematical, Physical and Engineering Sciences*, 382, 335-360.

Escudier, M. P., and Keller, J. J.(1983a). "Vortex Breakdown: A Two-Stage Transition." *AGARD CP no. 342, aerodynamics of vortical type flows in 3D*.

Escudier, M. P., and Keller, J. J.(1983b). "Vortex Breakdown: A Two-Stage Transition." *AGARD CP No.342 Aerodynamics of Vortical flows in Three Dimensions, Paper no. 25*.

Escudier, M. P., and Keller, J. J.(1985). "Essential Aspects of Vortex Breakdown." *Proceedings of the Colloquium on Vortex Breakdown*, 119-144.

Escudier, M. P., and Zehnder, N. (1982). "Vortex-Flow Regimes." *Journal of Fluid Mechanics*, 115, 105-121.

Faler, J. H., and Leibovich, S. (1977a). "Disrupted States of Vortex Flow and Vortex Breakdown." *Physics of Fluids*, 20, 1385-1400.

Faler, J. H., and Leibovich, S. (1977b). "An Experimental Map of the Internal Structure of a Vortex Breakdown." *Journal of Fluid Mechanics*, 86, 313-335.

Faler, J. H., and Leibovich, S. (1978). "Experimental Map of the Internal Structure of Vortex Breakdown." *Journal of Fluid Mechanics*, 86(2), 313-335.

Farokhi, S., Taghavi, R., and Rice, E. J. (1988). "Effect in Initial Swirl Distribution on the Evolution of a Turbulent Jet." *American Institute of Aeronautics and Astronautics Journal*, 27(6), 700-706.

Farokhi, S., Taghavi, R., and Rice, E. J. (1998). "Effect of Initial Swirl Distribution on the Evolution of a Turbulent Jet." *American Institute of Aeronautics and Astronautics Journal*, 27, 700-706.

Fouras, A. (1997). "Development of a Cross-Correlation Piv Image Recording Technique and Analysis of Velocity and Vorticity Measurement Error Applied to an Unsteady Separated Flow," Masters Thesis, Monash University.

Gallaire, F., Rott, S., and Chomaz, J. M. (2004a). "Experimental Study of a Free and Forced Swirling Jet." *Physics of Fluids*, 16(8), 2907-2917.

Gallaire, F., Rott, S., and Chomaz, J. M. (2004b). "Experimental Studyof a Free and Forced Swirling Jet." *Physics of Fluids*, 16(8), 2907-2917.

Garg, A. K., and Leibovich, S. (1979). "Spectral Characteristics of Vortex Breakdown Flow Fields." *Physics of Fluids*, 22(11), 2053-2064.

Gatsky, T. B., and Spall, R. E.(1991). "Numerical Studies of Vortex Breakdown: From Helices to Bubbles." *Fourth Intl Symp. on Computational Fluid Dynamics*, 418-423.

Gebhart, B. (1988). "Transient Response and Disturbance Growth in Vertical Buoyancy-Driven Flows." *Journal of Heat Transfer*, 110(4), 1166-1174.

Goldshtik, M. (1979). "On Swirling Jets." *Fluid Dynamics*, 14, 19-26.

Goldshtik, M., and Hussain, F. (1998). "Analysis of Inviscid Vortex Breakdown in a Semi-Infinite Pipe." *Fluid Dynamics Research*, 23, 189-234.

Grabowski, W. J., and Berger, S. A. (1976). "Solutions of the Navier-Stokes Equations for Vortex Breakdown." *Journal of Fluid Mechanics*, 75, 525-544.

Grant, I.(1997). "Particle Image Velocimetry: A Review." *Proceedings of the Institution of Mechanical Engineers*, 55-76.

Green, S. I. (1995). *Fluid Vortices (Fluid Mechanics and Its Applications)*, Kluwer Print on Demand.

Grobel, M., and Merzdirch, W.(1988). "Measurement of Natural Convection by Speckle Photography." *Preceedings Conference on Optical Methods in Flow and Particle Diagnostics*, San Diego, CA, USA, 728-735.

Gu, W., Robinson, O., and Rockwell, D. O. (1993). "Control of Vortices on a Delta Wing by Leading-Edge Injection." *American Institute of Aeronautics and Astronautics Journal*, 31(7), 1177-1186.

Guillot, S., Gutmark, E. J., and Garrison, T. J.(1998). "Delay of Vortex Breakdown over a Delta Wing Via near-Core Blowing." *35th Aerospace Sciences Meeting and Exhibit*, Reno, NV, AIAA-98-0315.

Gursul, I. (1996). "Effect of Nonaxisymmetric Forcing on a Swirling Jet with Vortex Breakdown." *Journal of Fluids Engineering, Transactions of the ASME*, 118(2), 316-321.

Gursul, I., Srinivas, S., and Batta, G. (1995a). "Active Control of Vortex Breakdown over a Delta Wing." *American Institute of Aeronautics and Astronautics Journal*, 33(9), 1743-1745.

Gursul, I., and Xie, W. (2001). "Interaction of Vortex Breakdown with an Oscillating Fin." *AIAA Journal*, 39(3), 438-446.

Gursul, I., Yang, H., and Deng, Q.(1995b). "Control of Vortex Breakdown with Leading-Edge Devices." *33rd American Institute of Aeronautics and Astronautics Aerospace Sciences Meeting and Exhibit*, Reno, NV, AIAA-95-0676.

Guy, Y., Morrow, J. A., and McLaughlin, T. E.(1999). "Control of Vortex Breakdown on a Delta Wing by Periodic Blowing and Suction." *37th American Institute of Aeronautics and Astronautics Aerospace Sciences Meeting and Exhibit*, Reno, NV, AIAA-99-0132.

Guy, Y., Morrow, J. A., McLaughlin, T. E., and Wygnanski, I.(2000a). "Parametric Investigation of the Effects of Active Flow Control on the Normal Force of a Delta Wing." *38th American Institute of Aeronautics and Astronautics Aerospace Sciences Meeting and Exhibit*, Reno, NV, AIAA-2000-0549.

Guy, Y., Morrow, J. A., McLaughlin, T. E., and Wygnanski, I.(2000b). "Velocity Measurements on a Delta Wing with Periodic Blowing and Suction." *38th American Institute of Aeronautics and Astronautics Aerospace Sciences Meeting and Exhibit*, Reno, NV, AIAA-2000-0550.

Hafez, M., Ahmad, J., Kuruvila, G., and Salas, M. D. (1987). "Vortex Breakdown Simulation." *American Institute of Aeronautics and Astronautics Journal*, 87, 1343-1361.

Hall, M. G. (1966). "The Structure of Concentrated Vortex Cores." *Progress in Aerospace Sciences*, 7, 53-110.

Hall, M. G. (1972). "Vortex Breakdown." *Annual Review of Fluid Mechanics*, 4, 195-218.

Harvey, J. K. (1962). "Some Observations of the Vortex Breakdown Phenomenon." *Journal of Fluid Mechanics*, 14, 585-592.

Hebbar, S., Platzer, M., and Alkhozam, A. (1994). "Experimental Study of Vortex Flow Control on Double-Delta Wings Using Fillets." *Journal of Aircraft*, 33(4), 743-751.

Helin, H., and Watry, C. W. (1994). "Effects of Trailing-Edge Jet Entrainment on Delta Wing Vortices." *American Institute of Aeronautics and Astronautics Journal*, 32(4), 802-804.

Herrada, M. A., and Shtern, V. (2003a). "Control of Vortex Breakdown by Temperature Gradients." *Physics of Fluids*, 15(11), 3468-3477.

Herrada, M. A., and Shtern, V. (2003b). "Vortex Breakdown Control by Adding near-Axis Swirl and Temperature Gradients." *Physical Review E*, 68(4 1), 41202-1.

Hites, M., Nagib, H., and Sytsma, B. (2002). "Lift Enhancement Using Pulsed Blowing at Compressible Flow Conditions." 306, Moscone Center, Israel (TAU). *Session Ef - Vortex Dynamics. [Ef.08]*.

Holman, J. P. (1997). *Heat Transfer*, Mc-Graw Hill.

Hong, J., Celik, Z., and Roberts, L. (1996). "Effects of Leading-Edge Lateral Blowing on Delta Wing Aerodynamics." *American Institute of Aeronautics and Astronautics Journal*, 34(12), 2471-2478.

Hopfinger, E. J., and Heijst, G. V. (1993). "Vortices in Rotating Fluids." *Fluid Mechanics Annual Review*, 25, 241-260.

Hourigan, K., Graham, L.J.W. and Thompson, M.C. (1995), “Spiral Streaklines in Pre-Vortex Breakdown Regions of Axisymmetric Swirling Flows.” *Physics of Fluids*, 7, 3126-3128.

Howard, L. R., and Gupta, A. S. (1962). "On the Hydrodynamic and Hydromagnetic Stability of Swirling Flows." *Journal of Fluid Mechanics*, 14, 463-475.

Huntley, J. M. (1989). "Speckle Photography Fringe Analysis: Assesment of Current Algorithms." *Applied Optics*, 28(20), 4316-4322.

Husain, H., Shtern, V., and Hussain, F. (2002). "Control of Vortex Breakdown by Addition of near-Axis Swirl." *Physics of Fluids*, 15(2), 271-279.

Husain, H. S., Shtern, V., and Hussain, F. (2003). "Control of Vortex Breakdown by Addition of near-Axis Swirl." *Physics of Fluids*, 15(2), 271-279.

International Association for the Properties of Water and Steam, I. (1997). "Release on Refractive Index of Ordinary Water Substance as a Function of Wavelength, Temperature and Pressure."

Iwanski, K., Ng, T. T., and Nelson, R. C.(1989). "An Experimental Investigation of Delta Wing Vortex Flow with and without External Jet Blowing." *27th American Institute of Aeronautics and Astronautics Aerospace Sciences Meeting*, Reno, NV, AIAA-89-0084.

Johari, H., and Moreira, J. (1996). "Delta Wing Vortex Manipulation Using Pulsed and Steady Blowing During Ramp-Pitching." *Journal of Aircraft*, 33(2), 452-453.

Johari, H., Olinger, D. J., and Fitzpatrick, K. C. (1995). "Delta Wing Vortex Control Via Recessed Angled Spanwise Blowing." *Journal of Aircraft*, 32(4), 804-810.

Jones, J. P.(1964). "On the Explanation of Vortex Breakdown." *Symposium on vortex motion*, IUTAM, 121-127.

Jones, M., Hourigan, K., and Thompson, M. C.(1998). "An Investigation of Wave Trapping as a Cause of Vortex Breakdown in the Torsionally Driven Cylinder." *13th Australasian Fluid Mechanics Conference*, Monash University, Melbourne, Austrralia, 230-241.

Jones, M., Hourigan, K., and Thomson, M. (1999). "Azimuthal Vorticity Dynamics in the Torsionally Driven Cylinder." *American Institute of Aeronautics and Astronautics Journal*, 38(7), 233-238.

Jones, M. C., Hourigan, K., and Thompson, M. C.(2001). "Toward a Geometry Independent Criterion for Vortex Breakdown." *14th Australasian Fluid Mech. Conference*, Adelaide University, Adelaide, Australia.

Keller, J. J., Egli, W., and Exley, J. (1985). "Force-Free and Loss-Free Transitions between Flow States." *Journal of Applied Mathematical Physics*, 36(6), 854-889.

Keller, J. J., and Escudier, M. P. (1980). "Theory and Observations of Waves on Hollow-Core Vortices." *Journal of Fluid Mechanics*, 99(3), 495-511.

Khoo, B. C., Yeo, K. S., Lim, D. F., and He, X. (1997). "Vortex Breakdown in an Unconfined Vortical Flow." *Experimental Thermal and Fluid Science*, 14(2), 131-148.

Khorrami, M. R. (1991). "On the Viscous Modes of Instability of a Trailing Line Vortex." *Journal of Fluid Mechanics*, 225, 197-212.

Khorrami, M. R. (1995). "Stability of a Compressible Axisymmetric Swirling Jet." *American Institute of Aeronautics and Astronautics Journal*, 30, 650-667.

Klute, S. M., Rediniotis, O. K., and Telionis, D. P.(1993). "Flow Control over Delta Wings at High Angles of Attack." *11th American Institute of Aeronautics and Astronautics Applied Aerodynamics Conference*, AIAA-93-3494.

Klute, S. M., Vlachos, P. P., and Telionis, D. P. (2005). "High-Speed Digital-Particle-Image-Velocimetry Study of Vortex Breakdown." *American Institute of Aeronautics and Astronautics Journal*, 43(3), 642-650.

Kopecky, R. M., and Torrance, K. E. (1973). "Initiation and Structure of Axisymmetric Eddies in a Rotating Stream." *Computational Fluids*, 1, 289-300.

Kostas, J. D., Fouras, A., and Soria, J.(1996). "The Application of Image Shifting to Piv." *1st Australian Conference on Laser Diagnostics in Fluid Mechanics and Combustion*, Sydney, Australia, 326-332.

Krause, E. (1990a). "The Solution to the Problem of Vortex Breakdown." Lecture notes in Physics, Berlin, 35-50.

Krause, E.(1990b). "Vortex Breakdown: Physical Issue and Computational Simulation." *Proceedings of the Third International Congress on Fluid Mechanics.*, Cairo, 335-344.

Krause, E., and Menne, S.(1987). "Investigation of Vortex Breakdown by Numerical Solution of the Navier-Stokes Equation." *Vortex control and breakdown behaviour, Second International Colloquium on Vortical Flows*, 43-57.

Krause, E., Shi, X., and Hartwich, P. M. (1983). "Computation of Leading Edge Vortices." *American Institute of Aeronautics and Astronautics Journal*, 83, 1907-1922.

Kuo, C. H., and Lu, N. Y. (1998). "Unsteady Vortex Structure over Delta-Wing Subject to Transient Along Core Blowing." *American Institute of Aeronautics and Astronautics Journal*, 36(9), 1658-1664.

Kuo, C. H., Lu, N. Y., and Lin, D. C. (1997). "Evolution of Vortical Structure over Delta Wing with Transient Along-Core Blowing." *American Institute of Aeronautics and Astronautics Journal*, 35(4), 617-624.

Kuo, C. H., and Rockwell, D. O. (1991). "Control of Vortex Structure on a Delta Wing by Small Amplitude Perturbations of Angle-of-Attack." *Journal of the Chinese Society of Mechanical Engineers*, 12(1), 1-7.

Kurosaka, M., Kikuchi, M., Hirano, K., Yuge, T., and Inoue, H. (2003). "Interchangability of Vortex-Breakdown Types." *Experiments in Fluids*, 34, 77-86.

Lambourne, N. C. (1965). "The Breakdown of Certain Types of Vortex." Aeronautical Research Council.

Lambourne, N. C., and Bryer, D. W. (1961a). "The Bursting of Leading-Edge Vortices." Aeronautical Research Council, R and M 3282.

Lambourne, N. C., and Bryer, D. W. (1961b). "The Bursting of Leading-Edge Vortices-Some Observations and Discussion of the Phenomenon." ARC. *R&M no. 3282 (22775).*

Landreth, C., Adrian, R., and Yao, C. (1988). "Double Pulsed Particle Image Velocimetry with Directional Resolution for Complex Flows." *Experiments in Fluids*, 6, 119-123.

Lawson, N. J., and Wu, J. (1997). "Three-Dimensional Particle Image Velocimetry: Error Analysis of Stereoscopic Techniques." *Measurement Science Technology*, 8, 1455-1464.

Leibovich, S. (1978). "Structure of Vortex Breakdown." *Annual Review of Fluid Mechanics*, 10, 221-246.

Leibovich, S. (1983). "Vortex Stability and Breakdown: Survey and Extension." *American Institute of Aeronautics and Astronautics Journal*, 22(9), 1192-1206.

Leibovich, S., and Stewartson, K. (1983). "A Sufficient Condition for the Instability of Columnar Vortices." *Journal of Fluid Mechanics*, 126, 335-356.

Lessen, M., and Paillet, F. (1974a). "Stability of a Trailing Line Vortex Part 2: Viscous Theory." *Journal of Fluid Mechanics*, 65(4), 769-779.

Lessen, M., and Paillet, F. (1974b). "The Stability of a Trailing Line Vortex. Part 2. Viscous Theory." *Journal of Fluid Mechanics*, 65, 769-799.

Lessen, M., Pawan, J. S., and Paillet, F. (1974). "The Stability of a Trailing Line Vortex. Part 1: Inviscid Theory." *Journal of Fluid Mechanics*, 63, 753-763.

Liang, H., and Maxworthy, T. (2005). "An Experimental Investigation of Swirling Jets." *Journal of Fluid Mechanics*, 525, 115-59.

Lin, S. J., and Corcos, G. M. (1984). "Mixing Layer: Deterministic Models of a Turbulent Flow. Part 3. The Effect of Plane Strain on the Dynamics of Streamwise Vortices." *Journal of Fluid Mechanics*, 141, 139-178.

Liu, Y., Koyama, H. S., and Chen, H. (2003). "Experimental Investigation of Vortex Breakdown in Spin-up and Spin-Down Processes Via Piv." *Journal of Hydrodynamics*, 15(2), 58-63.

Loehrke, R. I., and Nagib, H. M. (1976). "Control of Free-Stream Turbulence by Means of Honeycombs: A Balance between Suppression and Generation." *Transactions of the ASME*, 98, 342-353.

Loiseleux, T., and Chomaz, J. M. (2003). "Breaking of Rotational Symmetry in a Swirling Jet Experiment." *Physics of Fluids*, 15(2), 511-523.

Loiseleux, T., Chomaz, J. M., and Huerre, P. (1998). "Effect of Swirl on Jets and Wakes: Linear Instability of the Rankine Vortex with Axial Flow." *Physics of Fluids*, 10(5), 1120-1134.

Long, R. R. (1961). "A Vortex in an Innite Viscous Fluid." *Journal of Fluid Mechanics*, 11, 611-625.

Lourenco, L.(1991). "Recent Advances in Lsv, Piv and Ptv." *Flow Visualisation and Image Analysis, EuroMech Colloquium*, 81-99.

Lowson, M. V. (1964). "Some Experiments with Vortex Breakdown." 68, 343-365.

Lowson, M. V., and Riley, A. J. (1995). "Vortex Breakdown Control by Delta Wing Geometry." *Journal of Aircraft*, 32(4), 832-838.

Lucca-Negro, O. (1999). "Modelling of Swirl Flow Instabilities," PhD Thesis, University of Wales, UK.

Lucca-Negro, O., and O'Doherty, T. (2001). "Vortex Breakdown: A Review." *Progress in Energy and Combustion Science*, 27(4), 431-481.

Lynch, D. K., and Livingston, W. (2001). *Color and Light in Nature*.

Maines, B. H., Moeller, B., and Rediniotis, O. K.(1999). "The Effects of Leading-Edge Suction on Delta Wing Vortex Breakdown." *37th American Institute of Aeronautics and Astronautics Aerospace Sciences Meeting and Exhibit*, Reno, NV, AIAA-99-0128.

Marchman, J. F., and Grantz, A. C.(1982). "Trailing Edge Flap Influences on Leading Edge Vortex Flap Aerodynamics." *20th American Institute of Aeronautics and Astronautics Aerospace Sciences Meeting*, Orlando, FL, AIAA-82-0128.

Martin, J. E., and Meiburg, E. (1996). "Nonlinear Axisymmetric and Three-Dimensional Vorticity Dynamics in a Swirling Jet Model." *Physics of Fluids*, 8(7), 1917-1928.

Martin, J. E., and Melburg, E. (1994). "On the Stability of the Swirling Jet Shear Layer." *Physics of Fluids*, 6(1), 424-426.

Maxworthy, T., Hopfinger, E. J., and Redekopp, L. G. (1985a). "Wave Motions on Vortex Cores." *Journal of Fluid Mechanics*, 151, 141-165.

Maxworthy, T., Mory, M., and Hopfinger, E. J.(1985b). "Waves on Vortex Core and Their Relation to Vortex Breakdown." *Aerodynamics of Vortical Type Flows in 3D*, Paper no. 342.

McComb, W. D. (1990). *The Physics of Turbulence*, Clarendon Press, Oxford.

McCormick, S., and Gursul, I. (1996). " Effect of Shear-Layer Control on Leading-Edge Vortices." *Journal of Aircraft*, 33(6), 1087-1093.

Merzkirch, W. (1987). *Flow Visulisation*, Academic Press, New York.

Miller, S., and Gile, B.(1992). "The Effects of Blowing on Delta Wing Vortices During Dynamic Pitching at High Angles of Attack." *30th American Institute of Aeronautics and Astronautics Aerospace Sciences Meeting and Exhibit*, Reno, NV, AIAA-92-0407.

Mitchell, A. M., Barberis, D., Molton, P., and Delery, J. (2000). "Oscillation of Vortex Breakdown Location and Blowing Control of Time-Averaged Location." *American Institute of Aeronautics and Astronautics Journal*, 38(5), 793-803.

Mitchell, A. M., and Delery, J. (2001). "Research into Vortex Breakdown Control." *Progress in Aerospace Sciences*, 37(4), 385-418.

Mitchell, A. M., Molton, P., Barberis, D., and Délery, J.(1999a). "Control of Leading-Edge Vortex Breakdown by Trailing-Edge Injection." *17th American Institute of Aeronautics and Astronautics Applied Aerodynamics Conference*, Norfolk, VA, AIAA-99-3202.

Mitchell, M., Molton, P., Barberis, D., and Délery, J.(1999b). "Control of Vortex Breakdown Location by Symmetric and Asymmetric Blowing." *30th American Institute of Aeronautics and Astronautics Fluid Dynamics Conference*, Norfolk, VA, AIAA 99-3652.

Morton, B. R. (1984). "The Generation and Decay of Vorticity." *Geophysics Fluid Mechanics*, 28, 277-308.

Morton, S. A., Guy, Y., Morrow, J. A., and Blake, D. C.(1999). "Numerical Simulation of Periodic Suction and Blowing Control of Vortex Breakdown on a Delta Wing." *17th American Institute of Aeronautics and Astronautics Applied Aerodynamics Conference*, Norfolk, VA, AIAA-99-3195.

Mununga, L., Hourigan, K., Thompson, M. C., and Leweke, T. (2004). "Confined Flow Vortex Breakdown Control Using a Small Rotating Disk." *Physics of Fluids*, 16(12), 4750-4753.

Nawrocki, D.(1995). "Differential and Vectored Trailing-Edge Jet Control of Delta Wing Vortices." *33rd American Institute of Aeronautics and Astronautics Aerospace Sciences Meeting and Exhibit*, Reno, NV, AIAA-95-0008.

Neu, J. C. (1984). "Dynamics of Stretched Vortices." *Journal of Fluid Mechanics*, 143, 253-276.

Novak, F., and Sarpkaya, T. (2000). "Turbulent Vortex Breakdown at High Reynolds Numbers." *American Institute of Aeronautics and Astronautics Journal*, 38(5), 825-834.

Owen, F. K., and Peake, D. J. (1986). "Vortex Breakdown and Control Experiments in the Ames-Dryden Water Tunnel." Fluid Dynamics Panel Symposium on Aero and Related Hydrodynamic Studies Using Water Facilities, Monterey, CA.

Owens, D. B., and Perkins, J.(1995). "Vortex Suppression on Highly-Swept Wings by Suction Boundary-Layer Control." *33rd AIAA Aerospace Sciences Meeting and Exhibit*, Reno, NV, AIAA-95-0683.

Ozgoren, M., Sahin, B., and Rockwell, D. (2002). "Vortex Structure on a Delta Wing at High Angle of Attack." *American Institute of Aeronautics and Astronautics Journal*, 40(2), 285-292.

Panda, J., and McLaughlin, D. K. (1994). "Experiments on the Instabilities of a Swirling Jet." *Physics of Fluids*, 6(1), 263-276.

Panton, R. L. (1990). "Effects of a Contoured Apex on Vortex Breakdown." *Journal of Aircraft*, 27(3), 285-288.

Parmenter, K., and Rockwell, D. O. (1990). "Transient Response of Leading-Edge Vortices to Localized Suction." *American Institute of Aeronautics and Astronautics Journal*, 28(6), 1131-1132.

Payne, F. M., Ng, T. T., Nelson, R. C., and Schiff, L. B. (1988). "Visualisation and Wake Surveys of Vortical Flow over a Delta Wing." *American Institute of Aeronautics and Astronautics Journal*, 26(2), 137-143.

Peckham, D. H., and Atkinson, S. A. (1957). "Preliminary Results of Low Speed Wind Tunnel Test on a Gothic Wing of Aspect Ratio 1.0." British Aeronautical Research Council.

Pelletier, A., and Nelson, R. C. (2000). "Prediction of Vortex Breakdown Location on a Banked Delta Wing." *Journal of Aircraft*, 37(4), 738-740.

Pickering, J. D., and Halliwell, N. A. (1984). "Speckle Photography in Fluid Flows: Signal Recovery with Two Step Processing." *Applied Optics*, 23(8), 1128-1129.

Pilkington, D. J., and Wood, N. J.(1994). " Unsteady Aerodynamic Effects of Trailing Edge Controls on Delta Wings." *19th Congress of the International Council of the Aeronautical Sciences*, Anaheim, CA, ICAS-94-10-1.1.

Pitts, D., and Sissom, L. (1997). *Heat Transfer*, Mc-Graw Hill.

Prasad, A. K. (2000). "Stereoscopic Particle Image Velocimetry." *Experiments in Fluids*, 29, 103-116.

Prasad, A. K., and Jensen, K. (1995). "Scheimpflug Stereocamera for Particle Image Velocimetry in Liquid Flows." *Applied Optics*, 34, 7092-7099.

Raffel, M., and Kompenhans, J.(1994). "Error Analysis for Piv Recording Utilizing Image Shifting." *Proc. of the 7th Int. Symp on Laser Applications in Fluid Mechanics*, Lisbon, Portugal, 204-215.

Randall, J. D., and Leibovich, S. (1973). "The Critical State: A Trapped Wave Model of Vortex Breakdown." *Journal of Fluid Mechanics*, 58(3), 495-515.

Rao, D. M. (1979). "Leading-Edge Vortex Flap Experiments on a 74° Delta Wing." NASA. *NASA CR 159161.*

Rao, D. M.(1980). "Leading-Edge `Vortex Flaps' for Enhanced Subsonic Aerodynamics of Slender Wings." *12th Congress of the ICAS*, Munich, Germany, ICAS-80-13.5.

Rao, D. M., and Buter, T. A.(1983). "Experimental and Computations Studies of a Delta Wing Apex-Flap." *American Institute of Aeronautics and Astronautics Applied Aerodynamics Conference*, Danvers, MA, AIAA-83-1815.

Rao, D. M., Sharma, G., and Telionis, D.(1995). "Active Control of Vortex Lift at High Angles of Attack." *33rd American Institute of Aeronautics and Astronautics Aerospace Sciences Meeting and Exhibit*, Reno, NV, AIAA 95-0653.

Rayleigh, L. (1916). "On the Dynamics of Revolving Fluids." *Proceedings of the Royal Society of London*, 93, 148-156.

Reynolds, G., and Abtahi, A.(1989). "Three-Dimensional Vortex Development, Breakdown and Control." *Second American Institute of Aeronautics and Astronautics Shear Flow Conference*, Tempe, AZ, AIAA-89-0998.

Rockwell, D., Ozgoren, M., and Sahin, B. (2002). "Vortex Breakdown from a Pitching Delta Wing Incident Upon a Plate: Flow Structure as the Origin of Buffet Loading." *Journal of Fluids Structures*, 16, 295-303.

Ruith, M. R., Chen, P., Meiburg, E., and Maxworthy, T. (2003). "Three-Dimensional Vortex Breakdown in Swirling Jets and Wakes: Direct Numerical Simulation." *Journal of Fluid Mechanics*, 486, 331-378.

Salas, M. D., and Kuruvila, G. (1989). "Vortex Breakdown Simulation: A Circumspect Study of the Steady, Laminar, Axisymmetric Model." *Computers & Fluids*, 17(1), 247-262.

Sarpkaya, T. (1971a). "On Stationary and Travelling Vortex Breakdowns." *Journal of Fluid Mechanics*, 45(3), 545-559.

Sarpkaya, T. (1971b). "Vortex Breakdown in Swirling Conical Flows." *American Institute of Aeronautics and Astronautics Journal*, 9(9), 1792-1799.

Sarpkaya, T. (1974). "Effect of the Adverse Pressure Gradient on Vortex Breakdown." *American Institute of Aeronautics and Astronautics Journal*, 12(5), 602-607.

Sarpkaya, T. (1995). "Turbulent Vortex Breakdown." *Physics of Fluids*, 7(10), 2301-2303.

Satran, D. R., Gilbert, W. P., and Anglin, E. L. (1985). "Low-Speed Stability and Control Wind Tunnel Investigation of Effects of Spanwise Blowing on Fighter Flight Characteristics at High Angles of Attack." NASA. *NASA TP-2431.*

Schaeffer, N. W., Rediniotis, O. K., and Telionis, D. P.(1993). "Controlling of Delta Wing Leading-Edge Vortex with Cavity Flaps." *ASME Flow, Acoustics, Interaction and Fluid Flow Control Symposium of the 1993 Winter Annual Meeting*, ASME Paper 93-WA/NCA-27.

Schaeffler, N. W., Hoang, N. T., and Telionis, D. P.(1993). "Controlling of Delta Wing Vortices with Vortex Cavity Flaps." *Proceedings of the ASME Winter Conference*, New Orleans, LA, USA, 1-8.

Seginer, A., and Salomon, M. (1983). "Augmentation of Fighter Aircraft Performance by Spanwise Blowing over the Wing Leading Edge." NASA. *NASA-TM-84330.*

Serre, E., and Bontoux, P. (2002). "Vortex Breakdown in a Three-Dimensional Swirling Flow." *Journal of Fluid Mechanics*, 459, 347-370.

Shi, X.(1985). "Numerical Simulation of Vortex Breakdown." *Proceedings of the Colloquium on Vortex Breakdown*, 69-80.

Shi, X., and Shan, X.(1987). "Relation between the Quasi-Cylinderical Approximation and the Critical Theory for Swirling Flow." *Vortex Control and Breakdown Behaviour, Second International Colloquium on Vortical Flows*, 72-82.

Shi, Z., Wu, J. M., and Vakili, A. D.(1987). "An Investigation of Leading-Edge Vortices on Delta Wings with Jet Blowing." *25th AIAA Aerospace Sciences Meeting*, Reno, NV, AIAA-87-0330.

Shih, C., and Ding, Z. (1996). "Trailing-Edge Jet Control of Leading Edge Vortices of a Delta Wing." *American Institute of Aeronautics and Astronautics Journal*, 34(7), 1447-1456.

Shtern, V., and Hussain, F. (1993). "Hysteresis in a Swirling Jet as a Model Tornado." *Physics of Fluids*, 5(9), 2183-2192.

Simpkins, P., and Dudderar, T. (1978). "Laser Speckle Measurement in Transient Bernard Convection." *Journal of Fluid Mechanics*, 89, 665-671.

Singh, P. I., and Uberoi, M. S. (1976). "Experiments on Vortex Stability." *Physics of Fluids*, 19, 18-58.

Sinha, S., and Kuhlman, P. (1992). "Investigating the Use of Stereoscopic Particle Streak Velocimetry for Estimating the Three Dimensional Vorticity Field." *Experiments in Fluids*, 12, 377-384.

Smith, C. W., Ralston, J. N., and Mann, H. W. (1979). "Aerodynamic Characteristics of Forebody and Nose Strakes Based on F-16 Wind Tunnel Test Experience." *NASA CR-3053.*

Sotiropoulos, F., and Ventikos, Y. (2001). "The Three-Dimensional Structure of Confined Swirling Flows with Vortex Breakdown." *Journal of Fluid Mechanics*, 426, 155-175.

Spall, R. E., and Gatski, T. B.(1987). "Numerical Simulation of Vortex Breakdown." *Forum on Unsteady Flow Separation*, Cincinnati,OH,Engl, 25-33.

Spall, R. E., and Gatski, T. B. (1990). "A Computational Study of the Taxonomy of Vortex Breakdown." *American Institute of Aeronautics and Astronautics Journal*, 90, 16-24.

Spall, R. E., and Gatski, T. B. (1995). "Numerical Calculations of 3d Turbulent Vortex Breakdown." *International Journal of Numerical Methods in Fluids*, 20, 307-318.

Spall, R. E., Gatski, T. B., and Ash, R. L. (1990). "The Structure and Dynamics of Bubble-Type Vortex Breakdown." *Proceedings of the Royal Society of London*, 429, 613-637.

Spedding, G., and Rignot, E. (1993). "Performance Analysis and Application of Grid Interpolation Technichues for Fluid Flows." *Experiments in Fluids*, 15, 417-430.

Spillman, J., and Goodridge, M. (1972). "Flow Characteristics About a Delta Wing at 15° Incidence with and without Edge Blowing." Cranfield Report Aero, 9.

Spohn, A., Mory, M., and Hopfinger, E. J. (1998). "Experiments on Vortex Breakdown in a Confined Flow Generated by a Rotating Disc." *Journal of Fluid Mechanics*, 370, 73-99.

Stuart, J. T.(1987). "A Critical Review of Vortex Breakdown Theory, Vortex Control and Breakdown Behaviour." *Second International Colloquium on Vortical Flows*, 131-154.

Sun, D. J., Hu, G. H., Gao, Z., and Yin, X. Y. (2002). "Stability and Temporal Evolution of a Swirling Jet with Centrifugally Unstable Azimuthal Velocity." *Physics of Fluids*, 14(11), 4081-4084.

Tedeschi, G., and Menon, R. K.(1996). "Frequency Response of Solid Particles in Oscillating Flows." *Proceedings of Eighth International Synopsis on Application of Laser Techniques to Fluid Mechanics*, Lisbon, 615-623.

Thompson, M. C., and Hourigan, K. (2003). "The Sensitivity of Steady Vortex Breakdown Bubbles in Confined Cylinder Flows to Rotating Lid Misalignment." *Journal of Fluid Mechanics*, 496, 129-38.

Uchida, S., Nakamura, Y., and Ohsawa, M. (1985). "Experiments on the Axisymmetric Vortex Breakdown in a Swirling Air Flow." *Transactions of the Japan Society for Aeronautical and Space Sciences*, 27(78), 206-216.

Visser, K. D., Iwanski, K. P., Nelson, R. C., and Ng, T. T.(1988). "Control of Leading Edge Vortex Breakdown by Blowing." *26th American Institute of Aeronautics and Astronautics Aerospace Sciences Meeting*, Reno, NV, AIAA 88-0504.

Vorobieff, P. V., and Rockwell, D. O. (1996a). "Multiple-Actuator Control of Vortex Breakdown on a Pitching Delta Wing." *American Institute of Aeronautics and Astronautics Journal*, 34(10), 2184-2186.

Vorobieff, P. V., and Rockwell, D. O. (1996b). "Multiple-Actuator Control of Vortex Breakdown on a Pitching Delta Wing." *AIAA J*, 34(10), 2184-2186.

Vorobieff, P. V., and Rockwell, D. O. (1998). " Vortex Breakdown on Pitching Delta Wing: Control by Intermittent Trailing-Edge Blowing." *American Institute of Aeronautics and Astronautics Journal*, 36(4), 585-589.

Wang, J. J., Li, Q. S., and Liu, J. Y. (2003). "Effects of a Vectored Trailing Edge Jet on Delta Wing Vortex Breakdown." *Experiments in Fluids*, 34(5), 651-654.

Wang, S., and Rusak, Z. (1997). "The Dynamics of a Swirling Flow in a Pipe and Transition to Axisymmetric Breakdown." *Journal of Fluid Mechanics*, 340, 177-223.

White, F. M. (1999). *Fluid Mechanics*, McGraw-Hill.

Womersley, J. R. (1955). "Method for the Calculatuion of Velocity, Rate of Flow and Viscous Drag in Arteries When the Pressure Gradient Is Known." *Journal of Physiology*, 127, 553-563.

Wood, N. J., Lee, K. T., and Roberts, L.(1988). "Dynamic Control of Vortical Flow on Delta Wings at High Angles of Attack." *American Institute of Aeronautics and Astronautics Atmospheric Flight Mechanics Conference*, Minneapolis, MN, AIAA-88-4333.

Wood, N. J., and Roberts, L. (1988). "Control of Vortical Lift on Delta Wings by Tangential Leading-Edge Blowing." *Journal of Aircraft*, 25(3), 236-243.

Wu, M. M., Garcia, A., Chomaz, J. M., and Huerre, P. (1992). "Instabilities in a Swirling Jet." *Bulletin of the American Physics Society*, 37(8), 1789-1790.

Xu, Y., and Wang, J. (2002). "Effect of Apex Flap Length on Leading Edge Vortex Breakdown over Delta Wings." *Journal of Beijing University of Aeronautics and Astronautics*, 28(5), 543-546.

Yaws, C. L. (2003). *Yaws' Handbook of Thermodynamic and Physical Properties of Chemical Compounds*, Knovel.

Zang, W., and Prasad, A. K. (1997). "Performance Evaluation of a Scheimpflug Stereocamera Particle Image Velocimetry." *Applied Optics*, 36, 8738-8744.